Biological Polymers

Confined, Bent, and Driven

José Alvarado

This thesis was reviewed by
Prof. dr. Stephan Grill (MPI CBG & MPI PKS, Dresden)
Prof. dr. Jasper van der Gucht (Wageningen UR)
Prof. dr. Martin van Hecke (U Leiden)
Prof. dr. Frederick MacKintosh (VU Amsterdam)
Dr. Manos Mavrakis (CNRS/Aix-Marseille U)
Prof. dr. Bela Mulder (Wageningen UR)
Dr. Greg Stephens (VU Amsterdam)

ISBN 978-90-77209-74-5

FOM Institute
AMOLF

The work described in this thesis was performed at the FOM Institute AMOLF, Science Park 104, 1098 XG Amsterdam, The Netherlands. This work is part of the research programme of the Foundation for Fundamental Research on Matter (FOM), which is financially supported by the Netherlands Organisation for Scientific Research (NWO).

For digital copies:
www.ubvu.vu.nl/
www.amolf.nl/

For printed copies:
library@amolf.nl

Printed by Wöhrmann Print Service

VRIJE UNIVERSITEIT

Biological Polymers: Confined, Bent, and Driven

ACADEMISCH PROEFSCHRIFT

ter verkrijging van de graad Doctor aan
de Vrije Universiteit Amsterdam,
op gezag van de rector magnificus
prof.dr. F.A. van der Duyn Schouten,
in het openbaar te verdedigen
ten overstaan van de promotiecommissie
van de Faculteit der Exacte Wetenschappen
op maandag 17 juni 2013 om 13.45 uur
in de aula van de universiteit,
De Boelelaan 1105

door

José Ramón Alvarado

geboren te Panamá City, Panamá

promotor: prof.dr. G.H. Koenderink

Contents

1. Introduction 11
2. Tunable symmetry in confined colloidal liquid crystals 41
3. Alignment in confined semiflexible polymer networks 81
4. Septins bundle and curve actin filaments 121
5. Molecular motors robustly drive active gels to a critically connected state 171
6. Phase behavior of contractile active gels 211
Summary 261
Samenvatting 263
References 267


1

1. Introduction

Cells exert and resist mechanical forces. This ability allows them to perform many essential tasks. Some cells can crawl across surfaces and through small pores, pulling themselves forward while pushing against their environment. Some cells swim by beating long appendages which push the surrounding fluid. Most cells proliferate by dividing into two daughter cells, which is accomplished by pinching the cell membrane at (most often) the mother cell's equator. Many cells maintain their internal components organized by a combination of internal pushing and pulling forces. Cell growth, division, and changes in shape allow fast-growing embryos to properly develop into organisms with a well-defined anatomy. But how can cells exert and withstand such forces?

In order to accomplish force-related tasks, cells rely on a variety of *biological polymers*. The kind of biological polymer used depends on cell type. Most plant, yeast, and bacterial cells maintain relatively constant, rod-like shapes. These cells possess an outer *cell wall* composed of rigid polymers, which provide robust mechanical stability. In contrast, many animal cells are soft and deformable. This allows them to move and change shape. Rather than possessing a static, rigid cell wall, animal cells rely on the *cytoskeleton* to provide resistance to external forces. However, at the same time the cytoskeleton itself also actively generates forces. These dynamic, adaptable proteins greatly contribute to the structural complexity of cells. Understanding the physical properties of biological polymers like cytoskeletal filaments is thus crucial in order to resolve the role of forces in cell mechanics.

In order to resolve how biological polymers regulate cell shape and mechanics, researchers in recent years have turned to quantitative experiments on purified biological polymers in a simplified, cell-free environment (Bausch and Kroy, 2006; Fletcher and Geissler, 2009).

The advantage of such biomimetic systems is that their molecular and structural complexity can be precisely controlled. The reduced complexity compared to living cells makes it easier to develop physical theories that predict the macroscopic physical properties in terms of the molecular properties of the components.

Yet our current knowledge of the mechanical properties of cytoskeletal polymers does not suffice in providing a complete mechanical description of how cells resist and exert forces. So far, much research has focused on the mechanical properties of single polymers, entangled networks and liquid crystals, crosslinked networks, and motor-driven systems. Yet there are many aspects of these polymer systems that remain poorly understood. Experiments so far have addressed the properties of macroscopic networks of biological polymers, yet we know little about how these networks are affected when spatially restricted to cellular dimensions. Furthermore, the formation of constricting rings is essential for cell division, yet how biological polymers form rings remains a mystery. Finally, the ability of biological polymers to exert forces is well understood at the microscopic level of single molecules, but how these forces can be integrated over long distances to give rise to larger forces remains poorly understood.

In this thesis, we aim to better understand the properties of the organization and force-generating capabilities of biological polymers. In order to achieve this goal, we investigate how biological polymers organize in cell-size confinement, how they can be bent into rings by crosslinks, and how they can actively exert forces over long distances. In all these cases, we present experimental results which current physical models fail to predict. A better theoretical understanding of our findings should lead to a more quantitative understanding of how forces influence cell behavior.

In this chapter, we present the state of the art in our understanding of biological polymers. First, we shall look at examples of biological polymers in living systems. Next, we shall investigate the properties of individual polymers, networks of polymers, crosslinked polymers, and actively driven polymers. Finally, the chapter will end with an outline of this thesis.

1.1 The cytoskeleton

The cytoskeleton is a network of biological polymers which provides cells with mechanical strength and the ability to generate active forces. Cytoskeletal polymers associate with a variety of accessory proteins to form different structures which execute distinct tasks. Despite the large number of possible cytoskeletal structures, the cytoskeleton primarily comprises only three types of polymers. In this section, we will introduce these cytoskeletal polymers and highlight some of the structures which they form. In later sections, we will investigate the properties of these polymers and some of their accessory proteins in more detail.

Microtubules are stiff polymers which help organize the interior of the cell. Microtubules act as tracks for accessory proteins called *molecular motors*, which move along microtubules to transport intracellular cargo. In interphase animal cells, microtubules usually radiate from the nucleus and extend toward the cell membrane, enabling transport between different parts of the cell (Barlan et al., 2013; Vale, 2003). For example, many amphibians and fish possess cells called *melanophores* which allow them to change color (Tuma and Gelfand, 1999). This is accomplished by molecular motors, which spatially rearrange vesicles containing the pigment melanin across microtubules. Before cell division, microtubules reorganize to form the *mitotic spindle*, an assembly of microtubules, molecular motors, and other accessory proteins which reliably separates chromosomes to the two daughter cells (Walczak and Heald, 2008). Fission yeast cells similarly use microtubules and molecular motors to separate chromosomes and transport cargo (Hagan, 1998). However, unlike in animal cells, interphase microtubules only extend to the two ends of the rod-shaped yeast cell. This allows molecular motors to deliver growth factors specifically to these two ends, maintaining yeast cells' rod-like shape (Chang and Martin, 2009). Some eukaryotic cells swim by beating *flagella* or *cilia*. These are long appendages which comprise an ordered arrangement of microtubules which slide past one another, causing the entire appendage to lash back and forth (Brokaw, 1994). In many plant cells, microtubules form an ordered *cortex*, or thin layer underneath the cell membrane. These microtubules help guide the

ordered production of the cell wall, which is essential in maintaining plant cells' elongated shape (Bringmann et al., 2012).

Actin filaments are more flexible polymers which can form either fine meshworks, branched networks, or stiff bundles. The most well-known example of actin filaments in organisms is found in muscle cells (Rayment et al., 1993). A well-organized array of actin filaments and molecular motors can exert contractile forces, allowing organisms to move, change shape, and drive essential functions like heartbeats and breathing. But non-muscle cells also possess an actin cytoskeleton, which can be used to exert forces, both internally and externally. In many animal cells, actin filaments form a thin *cortex* meshwork. This actin cortex allows molecular motors to exert forces which control cell shape (Salbreux et al., 2012). Furthermore, the actin cortex allows tissues of epithelial cells to exert forces on each other, maintaining tissue integrity (Cavey and Lecuit, 2009) and determining tissue shape (Rauzi and Lenne, 2011). The actin cortex also assists yeast and animal cells during *endocytosis*, the process whereby cells internalize foreign objects or fluids (Engqvist-Goldstein and Drubin, 2003). One example is *phagocytosis*, where immune cells engulf and destroy invasive pathogens like bacteria (May and Machesky, 2001). During eukaryotic cell division, cortical actin filaments and molecular motors organize into a *contractile ring*, which constricts to pinch off the mother cell into two daughter cells (Guertin et al., 2002). Apart from a thin cortex, some large cells such as oocytes additionally have a three-dimensional, cytoplasmic network of actin filaments (Field and Lénárt, 2011) which can be used for transporting chromosomes (Lénárt et al., 2005). Crawling cells like fish keratocytes, amoebas, and metastatic cancer cells can move across surfaces using a combination of actin-based structures (Abercrombie, 1980; Ananthakrishnan and Ehrlicher, 2007; Rafelski and Theriot, 2004). At the front of crawling cells, a thin, two-dimensional array of actin filaments called the *lamellipodium* pushes the cell membrane forward. Actin bundles called *filopodia* often accompany the lamellipodium, which can sense environmental cues that guide the direction of cell motion (Davenport et al., 1993). At the back of crawling cells, a network of actin filaments and molecular motors exerts retraction forces which allows the cell body to move forward. Inside the ear, inner hair cells project *stereocilia*, bundles of actin which participate in the transduction

of sound waves to neuronal impulses (Manor and Kachar, 2008). Interestingly, most plant cells lack an actin cortex. Rather, actin bundles usually radiate from the nucleus towards the cell membrane (Hussey et al., 2013) and assist in properly positioning the nucleus (Starr and Han, 2003).

Intermediate filaments provide animal cells with mechanical strength. They are encoded by 70 genes in the human genome, which are divided into six groups based on sequence homology (Szeverenyi et al., 2008). Different intermediate filaments are expressed in different cell types (Helfand et al., 2003; Herrmann et al., 2007). For example, epithelial cells such as skin cells resist deformation by a network of *keratin filaments* (Omary et al., 2009). Eukaryotic cells use *lamin filaments* to not only provide the nucleus with with mechanical strength, but also to regulate nuclear events such as chromosome replication and cell death (Gruenbaum et al., 2000). Fiber cells of the vertebrate eye lens contain *beaded filaments* which not only provide the lens with mechanical strength, but also maintain its transparency (Song et al., 2009).

Septin filaments have only recently begun to gain recognition as a fourth component of the cytoskeleton (Mostowy and Cossart, 2012). In budding yeast cells, septins form rings at the bud neck which separate the membranes of the mother and daughter cells (Byers, 1976; Hartwell, 1971). In animal cells, septins are core components of the contractile ring that are essential for proper cell division (Glotzer, 2005). However, their role in cytokinesis remains poorly understood.

1.2 Single filaments

So far we have seen many examples of cytoskeletal polymers and the structures they form inside living cells. In this section, we will introduce the properties of polymer filaments. We will see that cytoskeletal polymers possess unique properties that distinguish them from other biological polymers as well as synthetic polymers.

Macromolecular polymers. Many materials nowadays are made of plastics, which are *polymers* (Rubinstein and Colby, 2003), such as polyethylene, polystyrene, and polyvinyl chloride (PVC). The word "poly" in these names refers to a fundamental property of polymers: they comprise many copies of the same building block. These subunits assemble into long, linear chains. Polymer subunits within a chain are held together by strong covalent bonds. Individual polymer chains are thus large molecules, and often referred to as *macromolecules*.

Cells also produce macromolecular polymers, using sugars, nucleic acids and amino acids as building blocks. Plant cells produce cellulose fibers, built from linked glucose chains, which form a strong cell wall (Somerville, 2006). Bacterial colonies secrete extracellular polysaccharide chains which maintain cohesion and contribute to the formation of biofilms such as dental plaque (Costerton et al., 1999). Cells store their genetic information in the form of deoxyribonucleic acid (DNA), which are chains built from four different types of interchangeable nucleic acids (Alberts, 2008). Cells express DNA to produce proteins, which are macromolecules composed of one or more polypeptide chains, which themselves are long chains of up to twenty interchangeable amino acids (Alberts, 2008).

Supramolecular polymers. Many types of biological polymers are built up from many protein subunits. Unlike man-made plastics, these *supramolecular polymers* are formed via weak interactions such as electrostatic interactions, hydrophobic interactions, and hydrogen-bonding. The specificity of these interactions results in highly ordered structures. The non-covalent nature of these interactions lead to dynamic, regulatable structures. Collagen proteins assemble into thick fibrils that form the connective tissues of animals (Prockop and Kivirikko, 1995). Fibrinogen proteins also assemble into thick fibrils that form clots at wounds which stop bleeding (Weisel, 2008). Both of these fibril types are stabilized by covalent crosslinks, forming stable structures that often span far beyond cellular length scales.

Cytoskeletal polymers are also supramolecular polymers, but unlike collagen and fibrin polymers they are not covalently crosslinked. Because the subunits are held together by many weak, non-covalent interactions, cytoskeletal polymers can assemble and disassemble in response to biochemical signals. They can form dynamic and

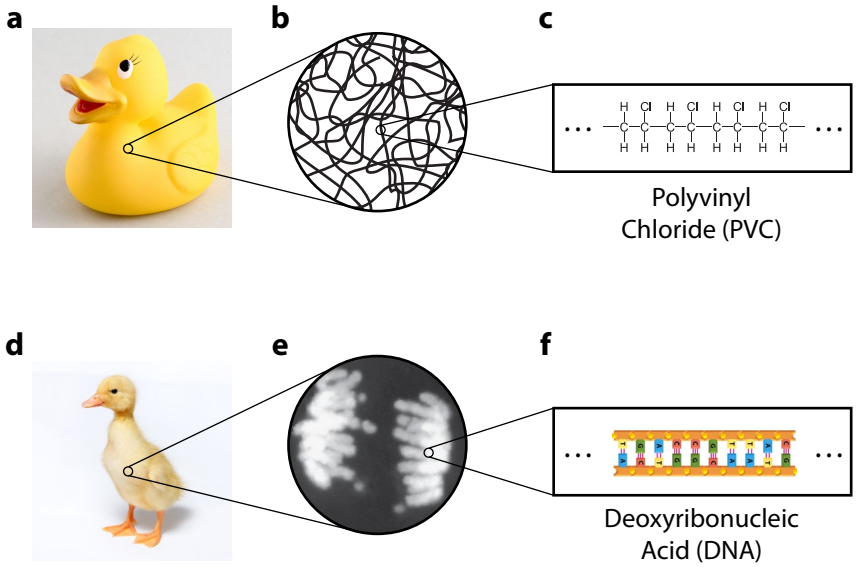

Figure 1. Common examples of polymers. **a**. A duck made of synthetic polymers. **b**. Polymers are long, linear chains. **c**. The structure of polyvinyl chloride (PVC), which comprises a long chain of vinyl chloride molecules. **d**. A duck made of biological polymers (among other materials). **e**. The nucleus of a dividing cell. **f**. The structure of an example strand of deoxyribonucleic acid (DNA), one of the most prevalent biological polymers. (Panels a, d © Wikimedia Commons. Panels e, f © Garland Science.)

adaptable structures that can allow cells to quickly respond to changing environments.

Polymer and subunit structure. Actin filaments comprise globular actin protein monomers. Actin monomers comprise two domains separated by a cleft, which binds a divalent cation as well as either adenosine triphosphate (ATP) or adenosine diphosphate (ADP). Monomers assemble head-to-tail to form linear polymer filaments. The ligand-binding cleft is directed toward the so-called "minus end" or "pointed end" of the filament. The opposite side is directed toward the "plus end" or "barbed end". Apart from assembling head-to-tail, actin

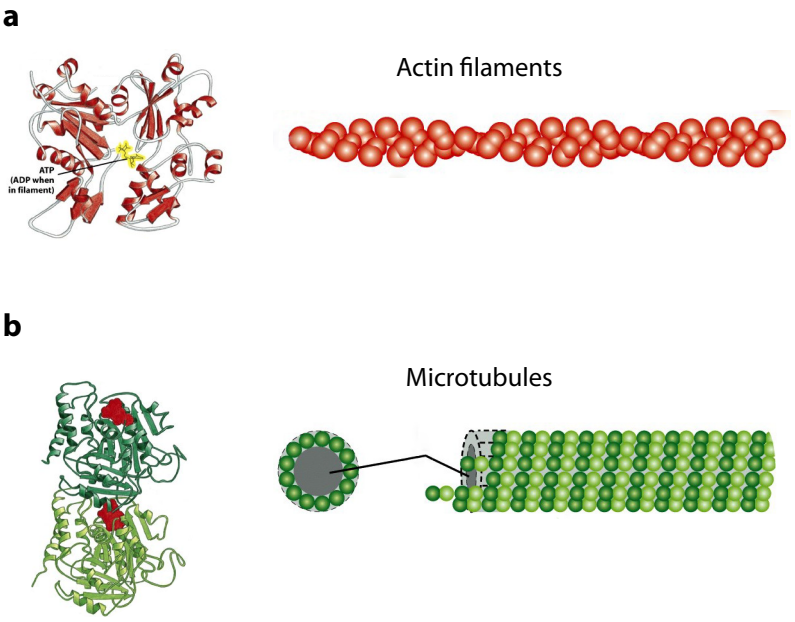

Figure 2. Actin and microtubules. **a**. Molecular structure of actin monomers, which assemble into actin filaments. **b**. Molecular structure of α- and β-tubulin, which form dimers that assemble into microtubules. (Panels a, b © Garland Science.)

monomers associate via side-by-side contacts, forming a two-stranded helical structure with a 37-nm pitch.

Microtubules comprise α- and β-tubulin proteins, which form stable heterodimers. β-tubulin proteins bind guanine triphosphate (GTP) or guanine diphosphate (GDP). Although α-tubulin proteins bind guanine triphosphate (GTP), this binding site is buried at the dimer interface. Dimers of α-β-tubulin assemble head-to-tail to form linear protofilaments, with α-tubulin at the "plus end" and β-tubulin at the "minus end". Thirteen protofilaments associate side-by-side to form a hollow, cylindrical microtubule. This stable, tubular structure makes microtubules stiffer than actin filaments by a factor of approximately 300 (Gittes et al., 1993).

The notion of head-to-tail assembly indicates a special property of actin filaments and microtubules. S*tructural polarity* refers to the fact that the two ends of the filament can be distinguished from each other. Other examples of polymers with structural polarity are DNA (5' and 3' ends) and protein polypeptide chains (N- and C-termini). This is in strong contrast to many other synthetic and biological polymers, which exhibit *structural symmetry*. In structurally symmetric filaments, both ends of the filament are identical and indistinguishable. Intermediate filaments and septin filaments are structurally symmetric.

The amino acid sequences of actin and tubulin proteins are surprisingly well conserved across many eukaryotic species (Mitchison, 1995; Sheterline and Sparrow, 1994). Intermediate filaments and septin filaments also maintain a large degree of evolutionary conservation, although species-specific variation is greater than with actin and tubulin. Even in prokaryotes, various actin, tubulin, and intermediate-filament homologues been identified which can also assemble into polymers to perform a variety of tasks (Shih and Rothfield, 2006).

Polymerization and enzymatic activity. The process by which monomer subunits join a polymer is called *polymerization*. For supramolecular polymers such as actin, this process is characterized by the rate of monomer addition, k_{on}, as well as the rate of monomer dissociation, k_{off}. In equilibrium, these rates are identical. For structurally polar filaments, the on/off rates vary for the two different ends. The end with the higher rate is conventionally called the "plus end", while "minus end" refers to the end with the slower rate. Structurally symmetric filaments have identical on/off rates at both ends.

Actin and microtubules, apart from possessing structural polarity, also possess enzymatic activity. These proteins bind the nucleoside triphosphates ATP or GTP. Shortly after subunits join polymers, hydrolysis occurs. Continuous addition of fresh ATP- or GTP-bound monomers therefore results in a so-called *ATP cap* or *GTP cap* at the plus end, while the rest of the filament contains ADP- or GDP-bound monomers. The presence of such a cap allows for faster polymerization kinetics at the plus end, which can lead to dynamic, non-equilibrium processes such as treadmilling (Pollard and Borisy, 2003) and dynamic instability (Gardner et al., 2011). Specialized tip-tracking molecules can selectively bind at the plus end of microtubules, though it remains

unclear whether they bind specifically to the GTP cap or to other nucleotide-bound states (Bowne-Anderson et al., 2013; Maurer et al., 2012; Seetapun et al., 2012). These dynamic properties allow cytoskeletal filaments to exert polymerization and depolymerization forces, which we will discuss later in this chapter.

Although intermediate filaments lack structural polarity and enzymatic activity, evidence suggests that intermediate filaments exhibit fast polymerization and depolymerization kinetics (Helfand et al., 2003). Septin filaments lack structural polarity but exhibit enzymatic activity (Weirich et al., 2008). Septin subunits bind and slowly hydrolyze GTP, and septin subunits can form filaments via the GTP-binding domain (or also at an interface containing N- and C-termini). However, the role of enzymatic activity in regulating filament formation remains poorly understood.

Worm-like chain model. So far we have seen how molecular structure can determine many of the special properties of cytoskeletal filaments. Yet physical theories accounting for the mechanical properties of polymer filaments often ignore fine structural detail. The *worm-like chain model* is the most common theoretical model used to describe the mechanics of cytoskeletal polymers. This model was originally developed by Kratky and Porod (Kratky and Porod, 2010). It approximates polymers by a smooth linear contour which resists bending with a bending modulus κ. In the absence of thermal fluctuations, polymers assume a linear shape. But at finite temperatures, random forces from thermal fluctuations can cause the polymer to bend. These thermal bending undulations have been observed experimentally for actin filaments by fluorescence microscopy (Gittes et al., 1993; Isambert et al., 1995; Ott et al., 1993) and have been used to measure κ. This was achieved by measuring a length scale l_p called the *persistence length*, which is defined as the decay length of angular correlations along the polymer contour. Roughly speaking, the persistence length is the distance over which the polymer contour appears straight. In equilibrium, the persistence length is related to the bending modulus by the relation $\kappa = kT\, l_p$, where k is Boltzmann's constant and T is temperature.

Using the persistence length l_p and the contour length L, we can distinguish between three classes of polymers. If the polymer backbone offers little resistance to bending ($l_p \ll L$), thermal fluctuations

dominate, bending the polymer so strongly that it crumples to a highly bent conformation well described by a fractal contour (de Gennes, 1979). Such polymers are called *flexible polymers*, and are suitable for describing many synthetic macromolecular polymers. In the opposite scenario ($l_p \gg L$), *stiff polymers* strongly resist thermal fluctuations and can be modeled as rigid rods (Landau et al., 1986). A third intermediate regime occurs when $l_p \sim L$. In this regime, thermal fluctuations cannot be neglected, though the polymer retains a well-defined, mostly straight shape with long, wavelike undulations. Polymers in this intermediate regime are called *semiflexible polymers*. Many biological polymers are semiflexible. Double-stranded DNA has a persistence length of 50 nm (Hagerman, 1988). Cytoskeletal filaments have a much larger persistence length ranging from 0.5-1 μm for intermediate filaments, to 8 μm for actin filaments and 5 mm for microtubules (Kasza et al., 2007).

Response to pulling forces. So far we have seen that the mechanical properties of semiflexible filaments can be characterized by the persistence length. This quantity describes how filaments respond to thermal forces. But how do semiflexible polymers respond to external pulling forces? Given an infinitely strong force, we should expect the polymer to assume a straight shape: such a taut filament would not bend due to thermal forces. Theoretical models have accounted for the reduction of thermally-induced bends due to external pulling forces (MacKintosh et al., 1995). The amplitude of thermally induced bends in the polymer depends on wavelength, given by the wave vector $q = n\,\pi / L$, where $n = 1, 2, 3\ldots$ If the polymer experiences tension due to an external pulling force f, the amplitude u_q of bending mode q is given by

$$\left\langle \left| u_q \right|^2 \right\rangle = \frac{2kT}{L\left(\kappa q^4 + f q^2\right)}$$

Long-wavelength bends (lower q) have the largest bending amplitudes in equilibrium. Short-wavelength bends (higher q) decay quickly, as q^{-4}. This formula also shows that applying a pulling force f to the polymer reduces bending amplitudes u_q. This reduction in thermal modes results in an effective restoring force:

$$f \sim \frac{l_p \kappa}{L^4} x$$

where x denotes the displacement of the end-to-end-distance vector of the polymer contour from its equilibrium position. The effective spring constant is thus $l_p\, \kappa\, L^{-4}$. Because semiflexible polymers bend in response to thermal forces, their response to a pulling forces is entropic in origin. This effect is often called the *entropic spring*. The force-extension relation was experimentally verified with DNA in optical tweezers (Bustamante et al., 1994), as well as for actin and microtubules (van Mameren et al., 2009).

So far we have considered how pulling forces decrease the bending amplitudes of polymer fluctuations. Note that this expression only takes into account the bending response of the polymer. Interestingly, this result is valid even though we have completely neglected the enthalpic response of the polymer chain itself to stretch deformations. However, the above equations are only valid under the assumption of small forces and linear responses. For strong pulling forces the thermal undulations are pulled out, and this assumption breaks down. In this case, we must account for stretch deformations of the polymer chain, which slightly elongates their contour. This has been accomplished by introducing a stretch modulus μ in the worm-like chain model (Odijk, 1995; Storm et al., 2005). The result is the emergence of two different force-response regimes with distinct spring constants. For low deformations, the effective spring constant is dominated by the bending modulus κ according to the entropic spring. For high deformations, the effective spring constant is dominated by the stretching modulus μ, corresponding to the enthalpic stretch of the polymer contour.

Response to pushing forces. We have investigated how individual semiflexible polymers respond to pulling forces. But how do they respond to pushing forces? Given small forces and linear responses, the stretch modulus μ determines the compressive deformation of elastic rods. Long, semiflexible rods can readily undergo a *buckling* instability when pushing forces exceed the critical Euler force f_c (Landau et al., 1986):

$$f_c \sim \kappa\, L^{-2}$$

This force is the maximal protrusive force that a rod can exert. Increased external pushing forces do not result in further compressive deformations. Rather, the rod bends and gives way, ultimately resulting in its collapse.

Microtubules are stiff polymers and can withstand rather high compressive forces. Actin filaments buckle at forces 300 times smaller, owing to their reduced bending stiffness (Gittes et al., 1993). This results in an *asymmetry in mechanical response*: single actin filaments can withstand and propagate pulling forces but not pushing forces. Yet despite this asymmetry, we will later see that cells can overcome this limitation and use actin filaments to exert substantial pushing forces (see "Force generation", below)

1.3 Filament networks

In cells, biological polymers are generally present at high density. So far we have encountered mechanical descriptions of single filaments. In this section, we will describe the collective properties of materials composed of many filaments. In order to accomplish this, we shall first investigate the phase behavior of suspensions of rigid rods. These model systems have been theoretically well characterized, and form the basis of understanding the properties of filament networks.

Rigid rods: dilute, entangled, and nematic regime. Consider a molecular rod of length L and thickness d diffusing freely in solution. As it translates and rotates, it sweeps out a volume $\sim L^3$. Thus, for a suspension of rods with concentration $c \ll L^{-3}$, neighboring rods are spaced far enough apart that they do not significantly interfere with each other's motions. In this *dilute* regime, the rotational diffusion constant $D_{\circlearrowleft}$ scales with rod length (with a prefactor that depends on temperature and viscosity) (Riseman and Kirkwood, 1950):

$$D_{\circlearrowleft,\text{dilute}} \sim L^{-3} \ln(L/d)$$

If the rod concentration c increases beyond L^{-3}, rods interact via steric repulsion: two rods cannot overlap in space, and therefore repel each other upon contact. In this *entangled* regime, the diffusion of a rod is constrained by its neighbors. Early theory by Doi and Edwards modeled the effect of entanglements for concentrated suspensions of rods by

proposing the tube model (Doi and Edwards, 1978). In this model, a rod of interest cannot diffuse freely in a volume $\sim L^3$, but is rather confined to an elongated virtual tube formed by the presence of neighboring rods. This results in a drastically reduced rotational diffusion constant for the entangled regime:

$$D_{\circlearrowleft,\text{entangled}} \sim L^{-6} D_{\circlearrowleft,\text{dilute}}$$

If the rod concentration c increases further towards $d^{-1}L^{-2}$ (where $d\ L^2$ is the volume of a single rod), the packing of rods cannot be neglected. Early theory by Onsager in this dense limit found that rods self-align to decrease their mutual excluded volume (Onsager, 1945). At concentrations below a critical concentration c^*, rod orientations are isotropically distributed to maximize rotational entropy. At concentrations above c^*, rod orientations are distributed about a preferred direction. Although this orientational alignment decreases rotational entropy, it is compensated by an increase in translational entropy due to a decrease in the mutual excluded volume. In the limit of infinitely long rods, the critical concentration c^* depends only on the inverse of the rod aspect ratio D / L. This phase of matter is called a *nematic* phase. The orientational anisotropy of rods in the nematic phase results in an anisotropy in optical properties, giving the appearance of a crystal. Hence, materials in the nematic phase form one of many possible *liquid-crystalline* phases.

Polymer networks. So far, we have considered theories which treat suspensions of diffusing rigid rods of uniform length. These theories have successfully predicted the phase behavior of suspensions of rod-shaped colloidal objects, including the rodlike viruses tobacco-mosaic virus (Graf and Löwen, 1999) and bacteriophage fd (Dogic and Fraden, 2006). However, polymers are usually neither rigid nor uniform in length. Theories have been developed to predict the changes in phase behavior arising from these deviations. In particular, the critical concentration c^* needed to form a nematic phase increases for both flexible filaments (Khokhlov, 1982) as well as filaments with nonuniform lengths (Odijk, 1986; Odijk and Lekkerkerker, 1985).

Yet despite these quantitative differences, the overall phase behavior predicted by theories on uniform, rigid rods provides a good description of the phase behavior of networks of rigid polymers such as actin and microtubules. For entangled actin filament networks with

actin concentrations between 0.1 to 2 mg mL^{-1}, the tube model was confirmed experimentally (Käs et al., 1996): labeled filaments were observed to fluctuate within a virtual, confining tube formed by the unlabeled surrounding filaments. Above concentrations of ~2 mg mL^{-1}, networks of actin filaments can form nematic phases (Käs et al., 1996; Suzuki et al., 1991). Shortening actin filaments by adding the capping protein gelsolin increases c^*, consistent with Onsager's theory (Suzuki et al., 1991).

Mechanical properties of entangled polymer networks. Entangled networks of polymer filaments form *viscoelastic* gels, which exhibit behavior characteristic of both solids and fluids. Rheology experiments quantify the mechanical properties of such viscoelastic materials. In these experiments, gels are grown between two large surfaces, which are moved relative to one another to apply shear stresses on the material. The response of a viscoelastic material to these shear stresses is given by two quantities (Meyers and Chawla, 2009): the storage modulus G', which measures elastic, or solid-like behavior; and the loss modulus G'', which measures viscous, or fluid-like behavior. These two quantities can be expressed as a single complex shear modulus $G = G' + i\,G''$.

For entangled actin networks, the primary determinant of the mechanical properties is the filament density. The storage modulus scales with concentration according to $G \sim \varphi^{7/5}$, where φ is the polymer volume fraction (Gisler and Weitz, 1999; Hinner et al., 1998). Theoretical scaling arguments, which consider two length scales, can account for this experimental result. The first length scale is the mesh size ξ, which is defined as the typical spacing between filaments. It scales as $\xi \sim \varphi^{-1/2}\, a$, where a is the thickness of a single filament (Schmidt et al., 1989). The second relevant length scale is the entanglement length l_e, which describes the typical length over which filament entanglements restrict thermal fluctuations. It scales as $l_e \sim (a^4\, l_p)^{1/5}\, \varphi^{-2/5}$, where l_p is the persistence length (Hinner et al., 1998; Isambert and Maggs, 1996). These two length scales determine the properties of networks of semiflexible filaments, with $G \sim kT / (\xi^2\, l_e)$. Substituting this expression with ξ and l_e yields the experimentally determined scaling relation $G \sim \varphi^{7/5}$. Interestingly, the two length scales, and thus the shear modulus

G, do not depend strongly on the stiffness of single filaments, given by l_p.

Entropic forces. So far we have explored how steric repulsion between filaments can account for different material phases, including entangled networks and nematic liquid crystals. In cells, the organization of actin filaments is further affected by steric interactions with other cytoplasmic components and with the cell membrane.

First, adding inert globular polymers can cause filaments to aggregate into bundles via the so-called *depletion attraction*. Globular polymers can be thought of as diffusing, impenetrable spheres. They interact with filaments mainly via steric repulsion. At a low concentration c of the globular polymer, filaments and polymers diffuse without significantly affecting each other. However, above a critical concentration c^* of polymer, filaments bundle together in order to maximize the free volume available to the globular polymers, thereby maximizing translational entropy (Lekkerkerker and Tuinier, 2011). Experiments have shown that actin filament networks indeed become bundled when sufficient amounts of inert polyethylene glycol (PEG) polymers are added (Hosek and Tang, 2004).

Second, filament organization can be strongly affected by the presence of external boundaries, leading to *confinement* effects. Initial theoretical work has addressed confinement effects by studying suspensions of rigid rods in the isotropic phase near an impenetrable planar surface. Rods were found to align along the surface, forming a so-called orientational wetting layer (van Roij et al., 2000). This effect only occurs for rods close to the surface, with an effective layer depth on the order of one rod length. In the case of semiflexible polymer networks, experiments investigated the effect of actin filament networks grown close to a rigid planar surface. The density of the network was found to decrease close to surfaces, forming a *depletion layer* whose thickness compares with the average filament length (Fisher and Kuo, 2009). Interestingly, the opposite effect was found when filaments were confined in three dimensions. Actin filaments grown in emulsion droplets were found to *accumulate* at the droplet surface, forming a cortex-like layer when droplets were smaller than the persistence length of actin filaments (Claessens et al., 2006b). Similarly, microtubules

grown in confining microchambers were found to coil and wrap around the chamber edges (Cosentino Lagomarsino et al., 2007).

Note that the depletion attraction and confinement effects induce only effective interactions between filaments. These interactions are mediated by the maximization of entropy of the entire system, similarly to the alignment of filaments in the nematic phase. For this reason, these indirect effects are referred to as *entropic forces*.

Entropic forces likely contribute to the organization of cytoskeletal structures inside cells. The environment inside most cells is crowded with soluble proteins which comprise 20–30% of the cell's volume (Ellis, 2001). For this reason, the depletion interaction has been suggested to contribute to actin filament bundling, amyloid fibril formation, and DNA looping (Marenduzzo et al., 2006). Similarly, confinement effects should also play a significant role in cytoskeletal organization. Cytoskeletal filaments have contours and persistence lengths that often compare with cellular dimensions, especially in thin compartments such as lamellipodia and filopodia. However, the extent to which these entropic forces determine intracellular organization remains poorly understood.

1.4 Crosslinks

So far, we have investigated how steric interactions affect the structure and mechanical properties of biological polymer networks. We neglected the effect of other important physical forces that can strongly affect phase behavior, including electrostatic attraction and repulsion, van der Waals interactions, and the free energy of hydration (Leckband and Israelachvili, 2001). In addition, cells possess *crosslink* proteins which specifically connect filaments to each other as well as to other cellular structures such as the plasma membrane. By tightly regulating the density and activity of these crosslink proteins, cells can create different cytoskeletal structures without significantly affecting the

physical properties of the filaments themselves. In this section, we will focus on *actin-binding proteins*, accessory proteins which crosslink actin filaments. We will describe their structural properties and consequences for the organization and mechanical properties of actin filament networks.

Crosslink structure. Most crosslink proteins contain at least two actin-binding domains. Each domain can independently bind a separate filament, thereby creating a mechanical link between filament pairs. Different types of actin-binding domains have been identified. The most common kind is the calponin-homology domain, which is found across a broad class of crosslink proteins, including spectrin, filamin, fimbrin, and α-actinin (Korenbaum, 2002). Fascin proteins bind actin filaments through β-trefoil domains (Jansen et al., 2011). Some crosslinks such as fascin and fimbrin can only bind pairs of parallel filaments, whereas other crosslinks such as α-actinin and filamin can bind actin filaments over a wide range of angles, forming isotropic rigid networks (Courson and Rock, 2010; Stossel et al., 2001).

Crosslink binding. Crosslinks bind with typical dissociation constants of 0.1–3 μM (Chen et al., 1999; Goldmann and Isenberg, 1993; Meyer and Aebi, 1990; Ono et al., 1997; Skau et al., 2011; Wachsstock et al., 1993; Yamakita et al., 1996). This corresponds to binding free energies of 32–42 kJ mol^{-1}, or 13–17 kT at room temperature. In equilibrium, crosslinks also unbind, with typical timescales of 10 s (Courson and Rock, 2010). Stresses acting on crosslinks usually accelerate crosslink unbinding (Evans and Ritchie, 1997). Such crosslinks are known as *slip bonds*. However, thecrosslink α-actinin 4 exhibits different stable conformations (Galkin et al., 2010a), which can expose additional actin binding domains buried inside the crosslink (Volkmer Ward et al., 2008) when subject to stress (Yao et al., 2011). Remarkably, these crosslinks therefore bind more tightly under tension, and are known as *catch bonds* (Thomas et al., 2008).

Crosslinked meshworks and bundles. Adding crosslinks to entangled actin networks can result in a variety of structures, including fine crosslinked meshworks, pure bundle networks, bundle cluster networks, and composite meshwork-bundle networks (Lieleg et al., 2010). However, predicting network structure given the local crosslink structure and binding mechanism remains elusive.

Mechanical properties of crosslinked networks. Introducing crosslinks in an actin filament network introduces a new length scale, called the crosslink distance l_c. This distance is the average separation between crosslinks. Similar to the entanglement l_e, this length scale determines the mechanical properties of crosslinked polymer networks. In particular, l_c determines whether a network deformation results in predominantly filament stretching or filament bending. WWhen a macroscopic shear strain results predominantly in filament stretching, the network experiences *affine* deformations (or *uniformly*). For affine thermal deformations, the shear modulus of the network depends on the concentration c_x of crosslinks (Gardel et al., 2004):

$$G_{\text{affine}} \sim c_x \kappa l_p l_c^{-3}$$

When filaments are very stiff, or when the network connectivity is low, filaments or bundles significantly bend when a macroscopic shear stress is applied, resulting in *nonaffine* deformations. In this case, the shear modulus of the network is insensitive to the concentration of crosslinks and instead depends strongly on the concentration of actin filaments c (Kroy and Frey, 1996):

$$G_{\text{nonaffine}} \sim \kappa \xi^4 \sim c^2$$

1.5 Force Generation

So far we have encountered passive physical forces that determine the organization and mechanical properties of biological polymers. But unlike many polymers, actin filaments and microtubules are out of equilibrium because of consumption of chemical energy in the form of the nucleotides ATP and GTP. We have already seen that these polymers exhibit enzymatic activity, which leads to polarized polymerization, treadmilling, and dynamic instability. These non-equilibrium properties allow actin filaments and microtubules to exert forces as they grow or shrink. Furthermore, motor proteins can slide filaments past one another, leading to generation of pushing and pulling forces. In this

section, we review the mechanisms whereby biological polymers can actively exert force.

Polymerization and depolymerization forces. Actin filaments and microtubules polymerize asymmetrically due to differences in the free energy of monomer binding between the plus-end and the minus-end. This free energy difference can be harnessed as filaments grow against a barrier to exert pushing forces (Hill, 1981; Theriot, 2000). Single microtubules are stiff and can exert forces of up to 3–4 pN as they polymerize (Dogterom and Yurke, 1997), though forces of up to ~50 pN should be possible (Dogterom et al., 2005). These forces are essential for maintaining the internal organization of the cell (Tolić-Nørrelykke, 2008), including the proper positioning of the kinetochore and chromosomes in the mitotic spindle in animal cells (Inoué and Salmon, 1995). Actin, too, exerts pushing forces. Despite the fact that single actin filaments alone are more flexible than microtubules and should buckle readily under compression at forces of ~0.1 pN (Landau et al., 1986), actin filaments have been measured to exert polymerization forces of up to 1 pN (Footer et al., 2007). Furthermore, actin-based structures can exert larger forces when organized by accessory proteins. Filopodia in the growth cones of migrating neurons, which contain actin bundles crosslinked by the protein fascin, can exert pushing forces of up to 3 pN (Cojoc et al., 2007). Such weak force generation may potentially serve to sense mechanical cues and preferentially grow along soft substrates (Betz et al., 2011). In the lamellipodium of crawling fish keratocytes, a dense array of short actin filaments branched by the Arp2/3 complex at the leading edge polymerize against the membrane and push it forward (Mogilner and Oster, 1996; 2003), exerting forces of about 100 pN (Roure et al., 2005). A similar mechanism is used by the bacterium *Listeria monocytogenes* (Cameron et al., 2001; Tilney and Portnoy, 1989). This pathogen uses the actin machinery of infected cells to propel itself with forces of 10–100 pN (McGrath et al., 2003; Wiesner, 2003). More dramatically, during the acrosomal process of the horseshoe crab *Limulus polyphemus*, a stiff bundle of actin filaments crosslinked by the protein scruin extends from sperm cells to break open the egg cell wall with a force of 2 nN (Shin et al., 2003; 2007).

Other biological polymers are similarly capable of exerting pushing forces. Sperm cells of the nematode *Ascaris suum* migrate using major

sperm protein (MSP) polymers, which elongate and pack in a similar fashion to the actin cytoskeleton in the lamellipodium (Miao et al., 2008; Roberts and Stewart, 2000). In *Escherichia coli* bacteria, the actin homologue ParM (Bork et al., 1992) polymerizes to push chromosomes apart to cell poles before division (Garner et al., 2007).

Apart from exerting pushing forces during polymerization, actin filaments and microtubules can exert pulling forces during depolymerization. In the case of microtubules, these forces are transmitted through tip-tracking proteins, which selectively bind the plus end of microtubules (Schuyler and Pellman, 2001). As microtubules shrink, tip-tracking proteins can remain bound to the retreating plus end (Lombillo et al., 1995). These forces are believed to underlie some of the pulling forces necessary for proper positioning of chromosomes during cell division (Dickinson et al., 2004; Hill, 1981; Joglekar et al., 2010; McIntosh et al., 2010). In the case of actin, filament depolymerization is essential during the constriction of the actomyosin ring during cytokinesis in the budding yeast *Saccharomyces cerevisiae* (Mendes Pinto et al., 2012).

Molecular motors. In addition to the ability of actin filaments and microtubules to exert polymerization and depolymerization forces, cells also possess specialized proteins called *molecular motors*. These proteins can exert forces by again coupling the free energy of ATP hydrolysis to mechanical work. This mechanical work can be harnessed for a wide variety of tasks, including DNA replication and expression, protein translocation, cell migration, chromosome separation, and cytokinesis (Bustamante et al., 2004).

Here we focus on the cytoskeletal motor proteins, which can exert forces while moving along cytoskeletal filaments. There are three classes of cytoskeletal motor proteins (Howard, 1997). *Myosin* motors bind actin filaments and most of the ca. 20 types of myosins move towards the plus-end. *Kinesin* and *dynein* motors bind microtubules and move towards the plus- and minus-end, respectively. Although there can be considerable variation among molecular motor types (Goodson et al., 1994; Thompson and Langford, 2002), cytoskeletal motor proteins share a few common design principles (Howard, 1997; Schliwa and Woehlke, 2003). They possess one or two head domains which bind filaments as well as ATP or ADP. Upon ATP hydrolysis, motor proteins undergo

conformational changes, manifested in a "power stroke" that results in step-wise motion of the motor along the filament. Step sizes typically vary between 8 and 30 nm, generating forces of up to ~10 pN (Burgess et al., 2003; Finer et al., 1994; Ishijima et al., 1998; La Cruz et al., 1999; Mehta et al., 1999; Visscher et al., 2000). Motor proteins also possess tail domains, which can bind to the tail domains of other motors to form oligomeric motor complexes (Bresnick, 1999), or to the cell cortex (Dujardin and Vallee, 2002), or to intracellular cargo (Hirokawa, 1998).

Many cells and organisms rely on molecular motors to exert forces that are stronger than by polymerization or depolymerization alone. Unicellular organisms such as the alga *Chlamydomonas reinhardtii* beat two long flagella composed of microtubules and dynein and kinesin motors (Bernstein and Rosenbaum, 1994), allowing the cell to propel itself with a force of 30 pN (McCord et al., 2005). Fish keratocytes glide on surfaces powered by myosin contraction, exerting traction forces of 45 nN (Harris et al., 1980; Oliver et al., 1995). Similar traction forces between kidney epithelial cells maintain tissue integrity and reach 100 nN (Maruthamuthu et al., 2011). Even higher forces can be achieved with dedicated muscle cells, which organize actin filaments and myosin motors in a sarcomeric structure dedicated to integrating the power strokes of many myosin motors (Gautel, 2011; Huxley and Niedergerke, 1954; Huxley and Hanson, 1954). Individual cardiac muscle cells have been measured to exert forces of 10 μN (Lin et al., 2000; Tarr et al., 1983; Yin et al., 2005).

Motor activity and spatial organization. Apart from exerting forces on their surroundings, cells use molecular motors to organize transient internal structures such as the mitotic spindle (Dumont and Mitchison, 2009; Tolić-Nørrelykke, 2008). Understanding how forces produced by single motors translate into cell-scale forces and cell-scale spatial organization remains an enormous challenge. Forces re-organize the cytoskeleton, but the spatial organization of the cytoskeleton in turn influences force generation. Addressing this feedback in living cells is hindered by their inherent complexity. Recent experiments with reconstituted cytoskeletal networks driven by molecular motors have started to address how spatial organization and force generation can affect each other.

Microtubules driven by kinesin and dynein motors exhibit fascinating structural patterns in solution, including vortices and asters (Nédélec et al., 1997). Similar asters have also been reported in the case of actin bundles driven by myosin motors (Backouche et al., 2006). In confined geometries, microtubule asters can be reliably centered by either pushing forces from microtubule polymerization (Holy et al., 1997) or pulling forces from dynein motors (Laan et al., 2012). In all these cases, self-organization arises from a feedback between force generation and the motion of stiff filaments. Meanwhile, single actin filaments are relatively flexible and readily buckle under compressive forces. This property is likely the reason why actin filament meshworks driven by myosin motors have not been reported to exhibit the same pattern formation as microtubules (Soares e Silva et al., 2011b). Buckling of actin filaments under compressive loads leads to an asymmetry in the response of actin networks to local internal forces generated by motors, biasing towards motor pulling forces and leading to contraction (Lenz et al., 2012b; Liverpool et al., 2009; Murrell and Gardel, 2012; Vogel et al., 2013).

Material properties of motor-driven systems. Apart from exerting forces and affecting spatial organization, molecular motors can also strongly affect the material properties of the polymer systems with which they interact. Myosin activity enhances fluctuations of crosslinked actin networks at frequencies below 10 Hz which violate the fluctuation-dissipation theorem (Mizuno et al., 2007) and cause strong non-Gaussian displacements of embedded probe particles (Stuhrmann et al., 2012). In suspensions of clusters of actin bundles, myosin motors can regulate cluster size (Köhler et al., 2011a) and lead to superdiffusive behavior (Köhler et al., 2011b). Stresses resulting from myosin activity stiffen crosslinked actin networks by a factor of 100 or more in a manner consistent with the response to an externally applied stress (Koenderink et al., 2009; Mizuno et al., 2008). The ability of force-generating elements to bring systems out of equilibrium has led to a lot of recent theoretical effort in predicting the phase behavior of actively driven matter using generalized statistical-mechanical frameworks (Marchetti et al., 2012). Moreover, theoretical studies of actin network mechanics have shown that these networks stiffen in response to internal, motor-induced stresses in a manner similar to the response to an external

stress (Sheinman et al., 2012a), unless these networks are poised near the rigidity percolation threshold (Sheinman et al., 2012b).

1.6 Thesis Outline

The goal of this thesis is to establish experimental systems which address major shortcomings in our current understanding of the properties of assemblies of biological polymers. A better grasp of the physical forces which organize biological polymers is necessary to account for the mutual interplay between cellular organization and force generation. In order to address these shortcomings, we perform experiments on model systems of reconstituted biological polymers which are 1. confined to cellular dimensions, 2. curved by crosslinks, and 3. driven by molecular motors. In all these cases, we lack a comprehensive theoretical understanding of the underlying physical mechanisms. The results we present should help advance our understanding of the role of the cytoskeleton in generating forces that underlie cellular organization.

In Chapters 2 and 3, we confine biopolymer systems to micrometer-sized spaces that mimic the spatial confinement that the cytoskeleton experiences within cells. Little is known about how polymers collectively organize when packed into a confined space with length scales similar to the contour length of the polymers themselves. In order to investigate the effect of an external geometry on polymer organization, we confine biopolymer systems in customized microchambers. In Chapter 2, we report experiments on nematic suspensions of the rod-like virus bacteriophage fd confined to shallow, donut-shaped microchambers. We quantify the nematic director field patterns and compare to predictions of Monte Carlo simulations accounting for the finite particle size. We find two patterns which are expected on the basis of continuum theory, but one pattern—with a striking three-fold-symmetry—is predicted to occur only for rods of finite length. In Chapter 3 we report experiments of actin networks confined to shallow, rectangular microchambers. We

quantify the nematic director field and find that nematic and bundled networks preferentially align along either the diagonal axis of the chambers, or parallel to chamber walls.

In Chapter 4, we investigate the actin-organizing capabilities of septins. A close interplay between septins and the actin cytoskeleton has been previously suggested, but little is known about the nature of this interaction. We report experiments which show that septins directly bind and bundle actin filaments, overthrowing prevailing assumptions that they do not interact directly. Surprisingly, we also find rings of actin bundles. Our observations demonstrate that septins alone are sufficient for actin ring formation, which may explain recent *in-vivo* experiments showing that septins are necessary for proper contractile ring formation in *Drosophila* embryos undergoing cellularization.

In Chapters 5 and 6, we investigate how myosin motors exert contractile forces on crosslinked actin filament networks. Little is known about the mechanisms whereby crosslinks transmit forces generated by molecular motors over macroscopic length scales. In Chapter 5, we show experimentally that myosin motors contract actin networks crosslinked by fascin to clusters with a scale-free size distribution. This critical behavior occurs over an unexpectedly broad range of crosslink concentrations. To understand this robustness, we compare our experimental results to a quantitative model of contractile networks. This model takes into account *network restructuring*: motors reduce connectivity by forcing crosslinks to unbind. Paradoxically, to coordinate global contractions, motor activity should be low. Otherwise, motors drive initially well-connected networks to a critical state where ruptures form across the entire network. In Chapter 6, we extend the results in Chapter 5 by comparing the effect of different crosslink proteins (fascin, fimbrin, and α-actinin). We furthermore vary motor activity by varying ATP and salt concentrations in the buffer, and vary network connectivity by varying actin filament density and length. We propose a phase-space diagram of connectivity-governed contractile active gels.

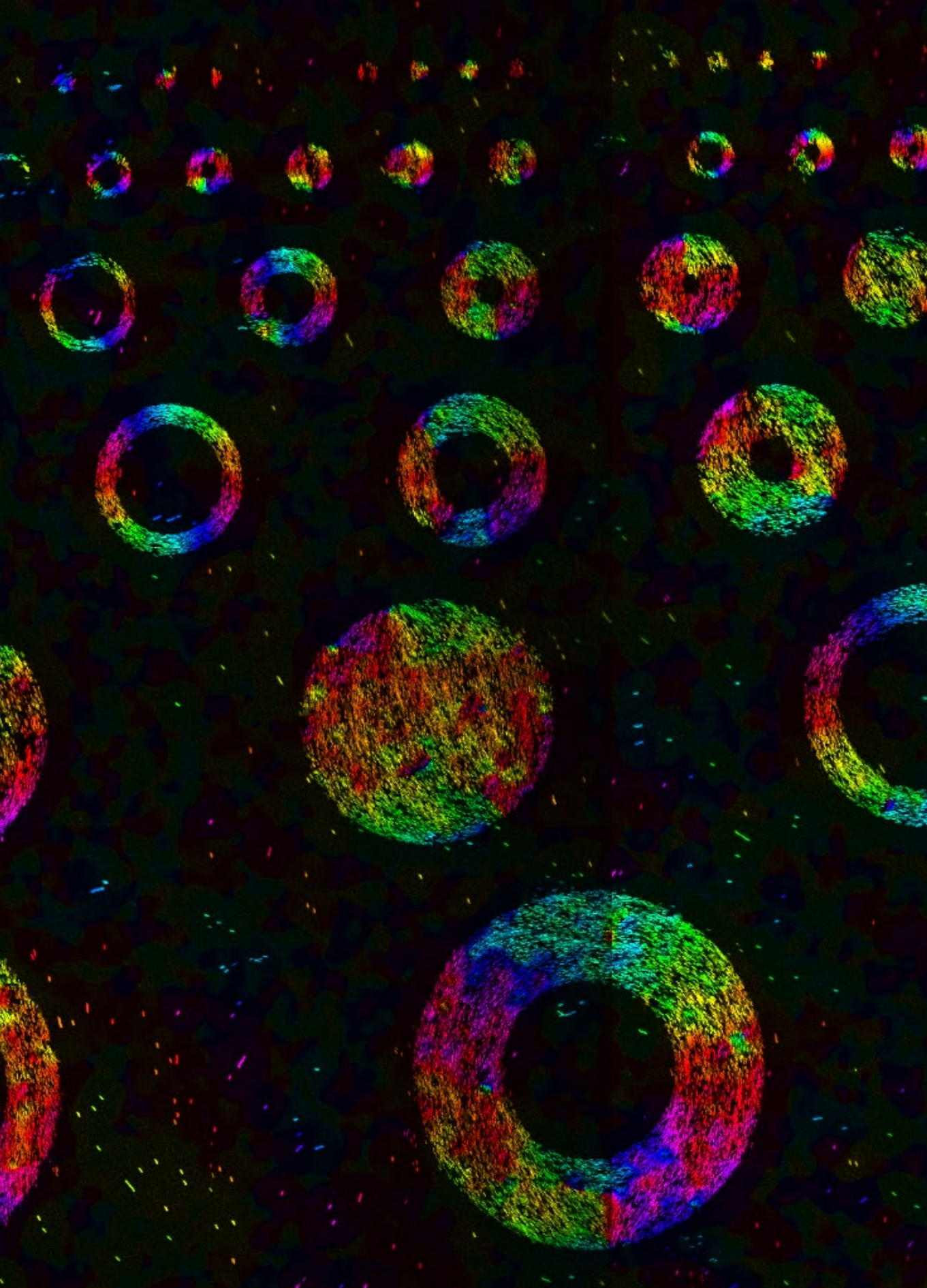

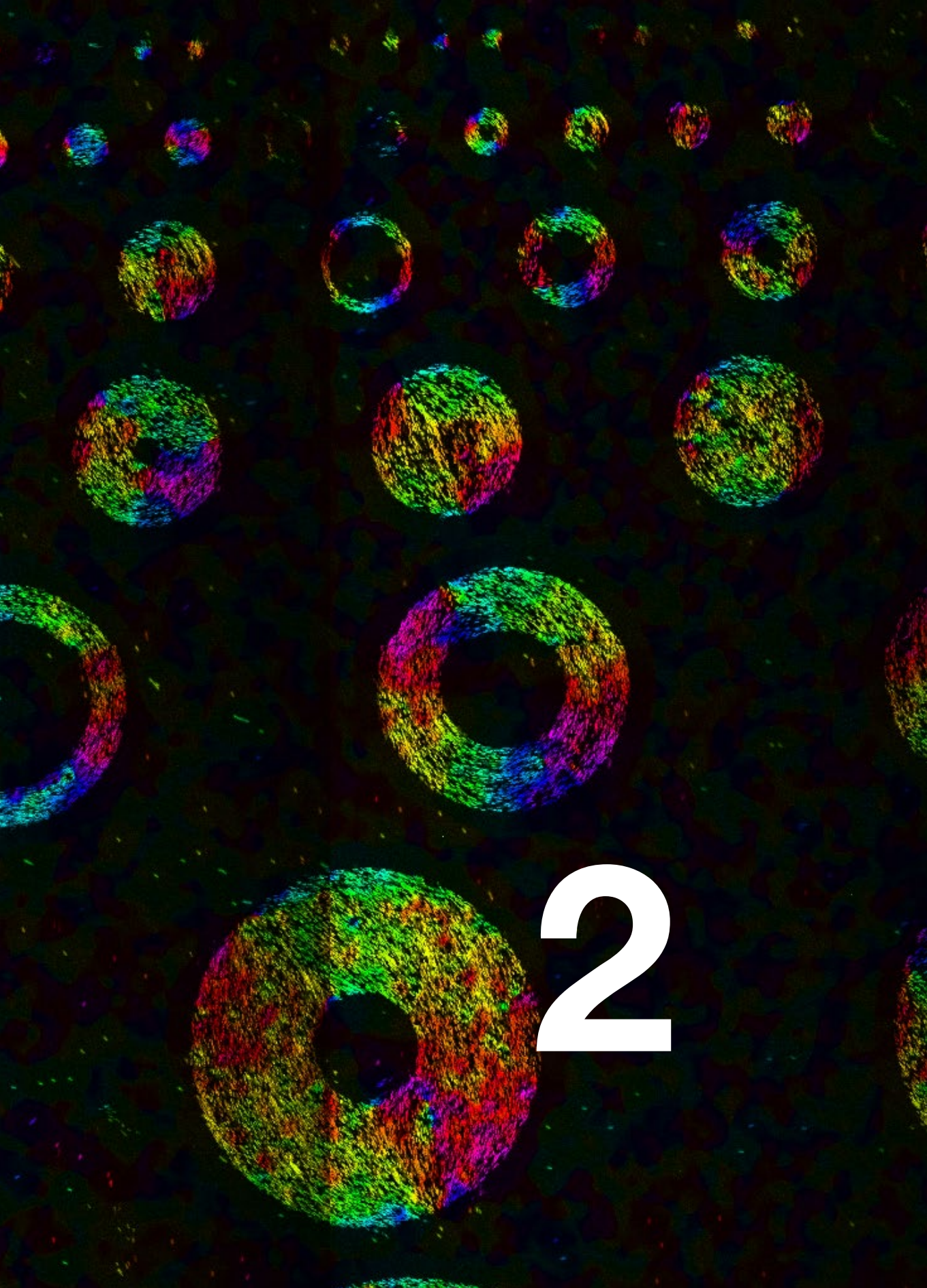
2

2. Tunable symmetry in confined colloidal liquid crystals

Modern display technology relies on molecular liquid crystals, often confined to cells with boundaries that orientationally "anchor" the mesogenic molecules and control the optical properties of the cell. Biological molecules like virus rods and cytoskeletal polymers also exhibit liquid crystalline phases that are spatially confined. But in contrast to the liquid crystals used in displays, the sizes of these biopolymers are often on a similar length scale as the confinement. This raises the question how the finite length of the polymers influences the competition between bulk liquid crystalline ordering and boundary ordering. To answer this question, we confine nematic liquid crystals of monodisperse bacteriophage fd-virus rods inside shallow, donut-shaped microchambers. The doughnut geometry allows us to specifically address the question how colloidal nematics resolve topological constraints when singularities are no longer negligible in size. We quantify the nematic director fields by fluorescence time-lapse microscopy and custom-written image analysis software and compare the patterns with predictions of continuum theory as well as Monte Carlo simulations accounting for the finite particle size. We observe patterns that can be classified into categories based on their symmetries and defect patterns. Two of these patterns are expected on the basis of continuum theory, but one pattern—with a striking three-fold-symmetry—is predicted to occur only for rods of finite length. The remaining patterns may represent metastable states. At the end of the chapter, we also report first tests of packing of fd-rods in square chambers, where we find diagonal alignment of the rods, consistent with continuum theory. We propose that the interplay between bulk and surface ordering under

ultra-confined conditions can lead to novel liquid crystals with tunable symmetry.

2.1 Introduction

Modern display technology would be unthinkable without *nematic liquid crystals* (Castellano, 2005). This fluid phase of matter differs from typical liquids by exhibiting orientational molecular order, which affects the polarization of light (Sluckin et al., 2003). Liquid crystalline materials may have various types of molecular structure, but they have in common that the molecules interact via anisotropic attractive and repulsive forces. Often, the molecules are rod-shaped. Liquid crystalline phase transitions can be well-modeled by continuum theories such as the phenomenological theory of Landau and de Gennes (de Gennes and Prost, 1995), which account for the system's change in symmetry. However, isotropic-nematic phase transitions have also been modeled by microscopic models (Singh and Dunmur, 2002), including the Maier-Saupe theory (Maier and Saupe, 1958) that attributes nematic ordering to anisotropic attractive interactions and the Onsager theory that considers exclusively repulsive interactions (Onsager, 1949).

Most applications of liquid crystals require these materials to be confined to cells with boundaries specifically treated to orientationally "anchor" the mesogenic molecules, allowing the optical properties of the cell to be controlled. The equilibrium director field is now determined by a competition between the mutual packing of the molecules and the surface anchoring conditions. This competition can lead to an interesting range of defect patterns when thermotropic nematics are confined in thin spherical shells (Fernandez-Nieves et al., 2007; Lopez-Leon et al., 2011; 2012). In shallow, square microchambers and in channels, molecular liquid crystals can adopt bi-stabile director fields, with two distinct, stable alignment states (Davidson et al., 2010; Tsakonas et al., 2007). Such bistability is advantageous for display applications, since it

allows one to use simply a pulse voltage to switch between "on" and "off" states.

Confinement-mediated ordering of molecular liquid crystals is commonly described by Frank elastic theory and Landau-de Gennes theory (de Gennes and Prost, 1995; Majumdar et al., 2007; Tsakonas et al., 2007). These are continuum theories, which account for the competition between the elastic free energy of the liquid crystal and the surface anchoring imposed by the confinement. For low molecular weight mesogens, continuum descriptions are indeed well-suited, since the lengths of these molecules are in the nm-range, well below the micron-sized dimensions of typical confining geometries (for reference, current state-of-the-art in displays employ ~70 μm pixels).

Nature, however, provides us with many examples of large-molecular weight mesogens that measure several microns in length, such as actin and microtubules (Bras et al., 1998; Buxbaum et al., 1987; Coppin and Leavis, 1992; Furukawa et al., 1993; Suzuki et al., 1991), DNA (Strzelecka et al., 1988), and rod-like viruses (Bawden et al., 1936; Bernal and Fankuchen, 1941; Dogic and Fraden, 2006; Fraden et al., 1989; Lapointe and Marvin, 1973). Often, these rod-like polymers are confined in cellular (sub)volumes with micron-sized dimensions, comparable to the contour length and persistence length of the particles themselves. Actin and microtubules are for instance packed within cellular compartments such as lamellipodia and filopodia (Medalia et al., 2002) and DNA is packed at high density inside virus capsules (Speir and Johnson, 2012). These strongly confined conditions raise the question how the competition between mutual packing interactions and confinement play out when both effects share the same length scale.

Mutual packing interactions in bulk liquid crystals of colloidal rods are well-understood experimentally and theoretically. For rods interacting exclusively through hard-core repulsive interactions, the isotropic-nematic phase transition is usually described by models based on seminal theory by Onsager (Onsager, 1949). For hard rods, the free energy of the system consists only of entropic terms, in particular the orientational and translational entropy of the molecules. These two terms compete, since orientational entropy is maximized when the rods point in all directions with equal probability, whereas translational entropy is maximized when rods are aligned, since alignment maximizes

the total free volume in which rods can diffuse. At low rod volume fractions, rotational entropy dominates and the suspension is isotropic, but above a critical volume fraction, excluded-volume (or packing) entropy dominates and the orientations of the rods are distributed about a preferred direction. Onsager considered the limiting case where the ratio of rod length L over diameter D tends to infinity. In this case, the I-N phase transition may be treated with a virial expansion of the free energy truncated at the second virial coefficient. The entropic transition from an isotropic to a nematic state is predicted to take place at a critical volume fraction $\varphi_{crit} = 3.340\ D / L$. This prediction is exact in the limit of infinite aspect ratio, but remains surprisingly accurate for aspect ratios down to about 100 (Frenkel, 1987). For shorter rods, high-order virial coefficients become increasingly important (Bolhuis and Frenkel, 1997). Modifications of the Onsager theory exist, for instance to account for rod semi-flexibility (Chen, 1993; Khokhlov, 1982), the soft repulsive interactions between charged rods (Stroobants et al., 1986), attractive van der Waals interactions (van der Schoot and Odijk, 1992), and polydispersity in rod length and diameter (Odijk, 1986; Vroege and Lekkerkerker, 1992).

The Onsager theory describes orientational ordering in bulk (unconfined) liquid crystals. It is much less well understood what happens when confining walls pose additional packing constraints on liquid crystals of finite-sized particles. Continuum theories have been applied, but these do not account for the finite size of the rods (Galanis et al., 2006; 2010b; Vitelli and Nelson, 2006). Numerical Monte-Carlo simulations have been reported to describe ordering of nematic fluids of colloidal rods in spherical cavities and shells (Dzubiella et al., 2000) and wetting of these suspensions at planar or curved hard walls (Dijkstra et al., 2001; Holyst and Poniewierski, 1987; Poniewierski and Holyst, 1988; van Roij et al., 2000). However, these simulations again did not directly address the question of how finite rod size influences the competition between bulk and surface ordering.

Meanwhile, experiments on confined colloidal rods have mostly addressed dilute suspensions. Individual biopolymers have been shown to orient along the longest axis of microchambers (Cosentino Lagomarsino et al., 2007) due to a competition between configurational entropy and bending enthalpy. For the same reason, isotropic entangled

networks of actin filaments organize into peripheral shells when confined in spherical droplets and vesicles (Claessens et al., 2006a; Limozin et al., 2003). Confinement of nematic phases has been reported for actin filaments in microchambers (Deshpande and Pfohl, 2012; Soares e Silva et al., 2011a) and fd-virus rods in wedges (Dammone et al., 2012). However, these studies again did not directly address the question how finite rod size influences the competition between bulk and surface ordering.

Here we investigate the director fields of colloidal nematic liquid crystals in shallow, circular microwells whose diameters are comparable to the rod length. We use rod-shaped bacteriophage fd-virus as a model liquid crystal system, since these rods are monodisperse, their interactions are hard-core like when the charges are screened, and their phase behavior in bulk is well-known (Dogic and Fraden, 2000; Dogic et al., 2004; Purdy and Fraden, 2004; Purdy et al., 2003; Tombolato et al., 2006). We use standard photolithography to produce non-adhesive doughnut-shaped SU-8 chambers whose overall diameter and width of the annulus is varied. This doughnut shape allows us to specifically address the question how colloidal nematics resolve topological constraints when singularities are no longer negligible in size.

In Section 2, we briefly summarize theoretical results of numerical simulations performed by Pieter Mulder, Ioana Garlea, and Bela Mulder (Mulder, 2012). These simulations predict liquid crystals with special symmetries that emerge as a consequence of the finite-size of the rods. In Section 3, we present director fields obtained experimentally by performing confocal time-lapse imaging of a low density of fluorescently labeled rods in the nematic background of unlabeled rods. Since fd-rods have a length of 0.88 μm, diameter of 6.6 nm (L / D ~ 130), and persistence length of 2.2 μm, we can observe individual virus particles and their anisotropic (mostly axial) diffusion in the nematic background (Lettinga et al., 2007). To compute director fields, we analyze the time-averaged orientations of the rods by custom-written software. We confirm the existence of the special symmetries predicted by numerical simulations, in particular the occurrence of a liquid crystal pattern with three-fold symmetry that is a direct result of the finite length of the rods. We propose that the interplay between optimal packing and confinement could lead to novel liquid crystals with tunable symmetry.

2.2 Theory

In order to investigate the optimal packing of colloidal rods in confined spaces, we examine the following problem: consider a suspension of stiff, thermally agitated rods of length L in a nematic liquid crystal phase (Fig. 1a). The rod orientations are distributed around one preferred direction known as the nematic director, but the rod positions are disordered. Next, consider these rods in a two-dimensional, annular chamber of outer diameter d_o and inner (or hole) diameter d_i. Wall-anchoring results in rods aligning parallel to the circular contours of the edges of the chamber. As long as the rod length L is much smaller than both the chamber and the hole diameter, this boundary condition establishes a nematic field devoid of defects, exhibiting infinite-fold rotational symmetry which we will denote as $U(1)$ (see Fig. 1b). However, when the hole is removed ($d_i = 0$), a topological problem arises in the center of the chamber: although wall-anchoring should dictate that rods follow the circular contour, this would result in a thermodynamically unfavorable +1 singularity at the center (Fig. 1c). Instead, the system tends towards a configuration with two $+\frac{1}{2}$ singularities located at polar opposites of the chamber (Fig. 1d). The director field thus exhibits two-fold rotational symmetry denoted as $D(2)$.

These two problems can be mapped to each other by taking the limit $d_i \to 0$. But in order to realize this limit, d_i must eventually compare to the length L of the rods. In such a regime, the small-rod assumption breaks down and continuum theory does not apply. We hypothesize that when transitioning from the infinite-fold symmetry state to the two-fold symmetry state, intermediate states occur which are somehow determined by the length scale L. Such intermediate states might possess symmetries of intermediate order, considering that an abrupt break in symmetry order (from infinite-fold to two-fold) occurs only when $d_i = 0$ is realized under the small rod assumption.

This hypothesis was tested in numerical Monte-Carlo simulations performed by Ioana Garlea and Pieter Mulder in the group of Bela Mulder (AMOLF). In these simulations, rigid spherocylinders of length L and thickness D diffuse in quasi-two-dimensional chambers of outer diameter d_o, inner (hole) diameter d_i, and vertical height d_z (Fig. 2).

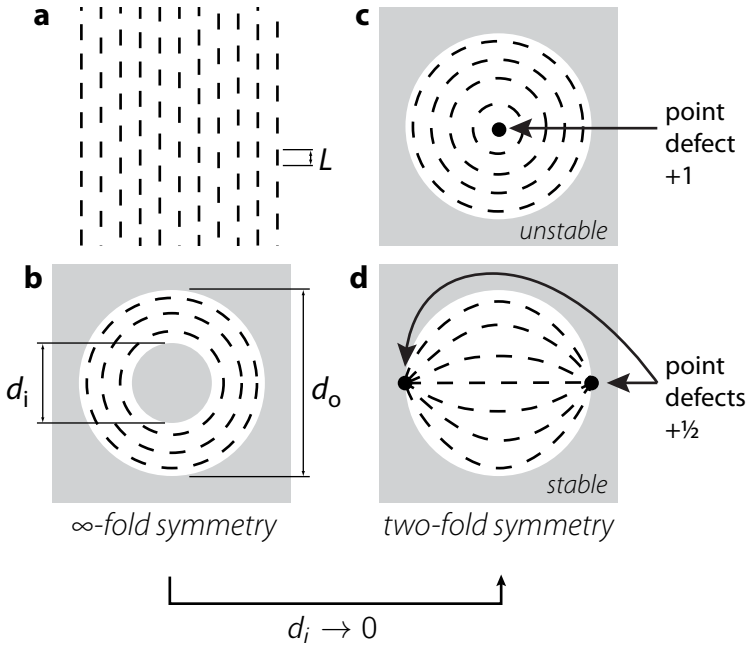

Figure 1. Prediction of continuum theory of the effect of boundary conditions on orientational ordering of a two-dimensional nematic liquid crystal. **a**. Schematic of rod-shaped molecules of length L in a nematic liquid-crystalline phase. **b**. The nematic liquid crystal organizes to follow boundaries and exhibit infinite-fold symmetry when confined to a donut-shaped chamber of outer diameter d_o and inner (hole) diameter d_i. **c**. Removing the hole reveals a thermodynamically unfavorable +1 defect. **d**. Instead, the stable configuration in the disk-shaped chamber contains two +½ defects, resulting in two-fold rotational symmetry.

Rods interact with other rods and with chamber boundaries via hard-core steric repulsions.

Rods align to form higher-order symmetric states. For disk-shaped chambers without a hole, the simulations produce a two-fold symmetric state identical to that predicted by continuum theory (Fig. 2a, compare to Fig. 1d). Strikingly, introducing a hole with diameter d_i results in higher-order symmetries. The smallest holes result in a liquid crystal with three-fold symmetry (Fig. 2b). Increasing the hole diameter

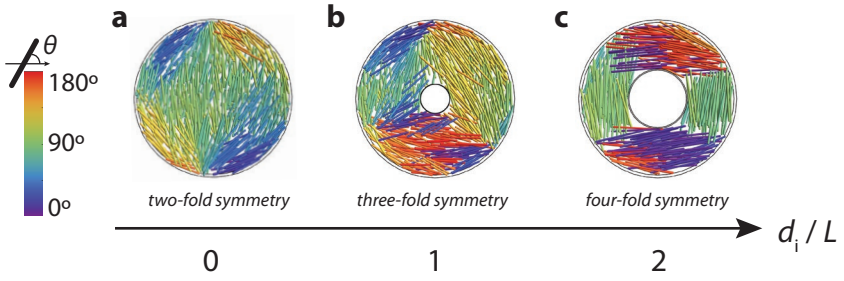

Figure 2. Monte-Carlo simulations of finite-length rods in annular confinement predict two-fold symmetric patterns consistent with continuum theory but also higher-order symmetries emerging from the finite size of the rods compared to the chamber dimensions. Snapshots of equilibrated suspensions of rods in disk-shaped chambers. **a**. Two-fold symmetry occurs in chambers without a hole (inner hole diameter $d_i / L = 0$), **b**. three-fold symmetric patterns occur in chambers with $d_i / L = 1$, and **c**. four-fold symmetry occurs in chambers with $d_i / L = 2$. Chamber vertical height $d_z = 6\ D$. Rod color corresponds to orientation θ (calibration bar, left). Figure courtesy of P. Mulder, I. Garlea, and B. Mulder.

results in four-fold symmetry (Fig. 2c). Five-, six-, seven-, and eight-fold symmetries can also occur, depending on the hole diameter d_i and vertical chamber height d_z (see Fig. 4). These higher-order symmetries are not predicted to be thermodynamically favorable according to continuum theory, which neglects rod length. Because the simulations explicitly account for finite rod length, these higher-order symmetries are a direct consequence of the optimal packing of finite-sized rods in a confined, annular geometry.

Geometric correspondence occurs in 2D chambers. Thin chambers whose vertical height d_z equals the rod thickness D exhibit particularly interesting behavior. These shallow chambers confine rods to a two-dimensional environment by completely suppressing out-of-plane rotations. In this case, the relationship between hole diameter d_i and rod length L controls the symmetry order. For size ratios $d_i / L = 3^{-1/2} = 0.58$, rods can form an equilateral triangle around the hole; concomitantly, a three-fold symmetric pattern emerges for $d_i / L \approx 0.58$ (Fig. 3a). For

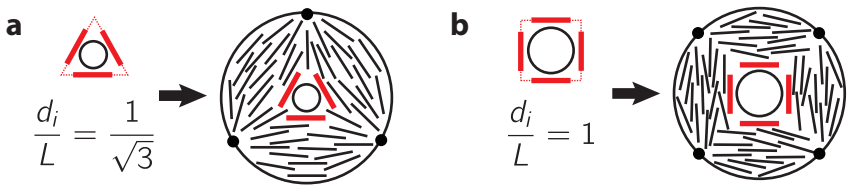

Figure 3. Geometric correspondence occurs if the polygon that is accommodated by rods of length L packing around a hole of diameter d_i has the same symmetry as the resulting liquid crystal. **a**. For $d_i / L = 3^{-1/2}$, the innermost rods (red) can arrange around the inner hole in a triangle. If geometric correspondence holds, a three-fold-symmetric liquid crystal should emerge. **b**. For $d_i / L = 3^{-1/2}$, the innermost rods can arrange around the inner hole in a square. If geometric correspondence holds, a four-fold-symmetric liquid crystal should emerge.

$d_i / L = 1$, rods can form a square around the hole; concomitantly, a four-fold symmetric pattern emerges for $d_i / L \approx 1$ (Fig. 3b). More generally, the number n of rods that can form a regular polygon around the hole, given rod length L and inner diameter d_i, is given by the formula

$$\frac{d_i}{L} = \cot\left(\frac{\pi}{n}\right).$$

We use the term *geometric correspondence* to refer to situations where the number of rods n is equal to the symmetry order of the resulting nematic texture. As shown in Fig. 4, simulations (yellow circles) show that geometric correspondence (blue lines) also holds for higher-order symmetries.

Thicker chambers result in lower-order symmetry. Chambers with a larger vertical height relative to the rod diameter ($d_z / D = 3$ and 6) were also investigated by numerical simulations. As shown in Fig. 4, already at $d_z = 3\,D$, the symmetry order (green circles) is greatly reduced compared to values expected from geometric correspondence (blue lines). Increasing chamber thickness to $d_z = 6\,D$ (red circles) further decreases symmetry order. These results show that thicker chambers which do not fully prohibit out-of-plane rod orientations result in symmetries whose order can be far lower than that expected from geometric correspondence.

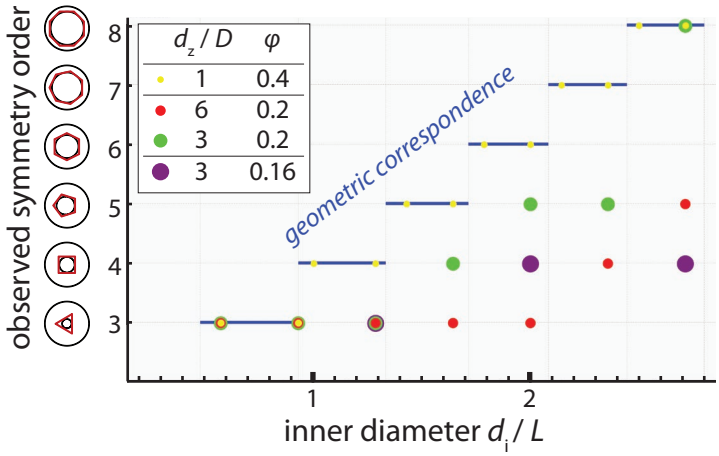

Figure 4. Dependence of observed symmetry order on chamber inner diameter, d_i / L (where rod length L is 15× rod diameter D). Circles denote simulations performed with different chamber heights (d_z / D) and rod volume fraction (φ), as indicated in the legend. Blue lines denote expected symmetry order based on geometric correspondence. Figure courtesy of P. Mulder, I. Garlea, and B. Mulder.

2.3 Results

Two-, three-, and infinite-fold symmetries occur depending on chamber shape. Based on the simulations, we anticipate that liquid crystals of finite-sized rods in annular geometries should exhibit symmetries that cannot be accounted for by continuum theory. In order to test this hypothesis, we prepare non-adhesive microchambers with a donut shape and fill them with suspensions of rod-like fd-virus in the nematic phase (Fig. 5). We systematically varied the chamber outer diameter d_o (from 10 μm to 100 μm) and the diameter of the inner hole d_i (from 0 to 0.7 times the outer diameter d_o). The chambers have vertical heights in the range of d_z = 1–3 μm, which is the minimal thickness that was experimentally attainable. We note that this chamber thickness is still much larger than the diameter of the fd-rods, 6.6 nm (Dogic and Fraden, 2006). Nevertheless, time-lapse imaging of fluorescently

labeled particles in the otherwise unlabeled background nematic phase showed that particles diffused mostly in-plane. Additionally, 3D *z*-scans confirmed that the cholesteric twist normally observed in bulk nematic phases of fd-rods (Dogic and Fraden, 2000; Grelet and Fraden, 2003; Purdy and Fraden, 2004; Tang and Fraden, 1995) was suppressed. To examine the nematic patterning, we acquired time-lapse image series of chambers containing fd-rods with a small tracer fraction that was fluorescently labeled. We developed a customized image analysis program (see Image Analysis) to quantify the orientation of the nematic director for each image pixel. By visual inspection of the rotational symmetry of the resulting nematic director fields and the location and number of defects, we categorize the patterns into 7 different types.

One commonly observed pattern is a nematic pattern with infinite-fold rotational symmetry that does not exhibit any obvious singularities (Fig. 6a). A second pattern is one with three-fold rotational symmetry, showing three +½ singularities (Fig. 6b). A third pattern is one with two-fold rotational symmetry, showing two +½ singularities at

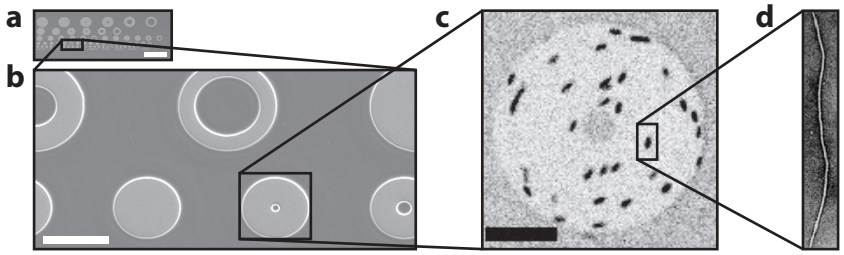

Figure 5. The experimental model system. **a**. Image of a glass substrate patterned with SU-8 microchambers, acquired by scanning-electron microscopy. Scale bar 200 μm. **b**. Close up of the region indicated by the black box in panel a. Scale bar 20 μm. **c**. Fluorescence confocal image of an annular microchamber (d_o = 20 μm, d_i = 0.4 μm) filled with a suspension of partially labeled fd-virus rods (inverted grayscale lookup-table). Scale bar 5 μm. **d**. Image of a single fd-virus rod, acquired by transmission electron microscopy (reprinted from (Dogic and Fraden, 2006)). The rod length is 0.88 μm and the diameter is 6.6 nm (L / D ~ 130).

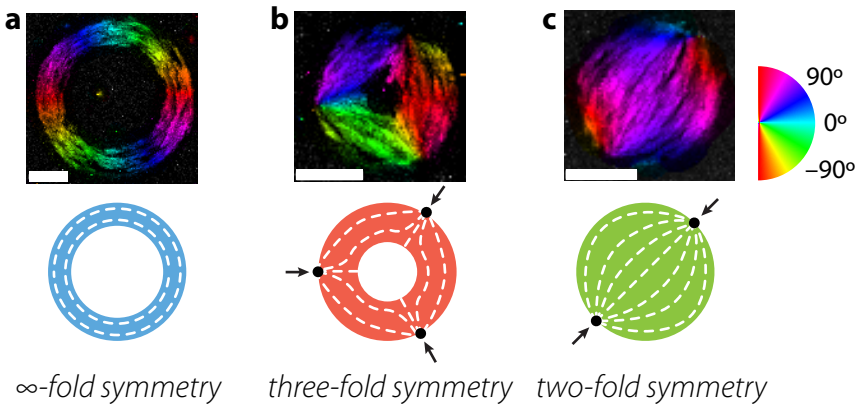

Figure 6. Three types of experimentally observed nematic patterns. **Top row**: Representative instances of the three patterns. Brightness corresponds to a maximum intensity projection of 2000 frames. Color corresponds to the average orientation $<\theta>$ of the nematic director (calibration wheel, right). Bottom row: Schematic diagrams of the nematic pattern types, showing singularities as black points, further indicated by the arrows. **a**. A pattern of infinite-fold symmetry in narrow annular chambers exhibiting no singularities. **b**. A pattern of three-fold symmetry in wider annular chambers exhibiting three singularities. **c**. A pattern of two-fold symmetry in disc-shaped chambers exhibiting two singularities.

two opposite poles (Fig. 6c). The first and third patterns agree well with continuum theory (cf. Figs 6a,c and 1b,d). The second pattern is not predicted by continuum theory, but is consistent with the three-fold-symmetrical state predicted by the simulations (cf. Figs 6b and 2b). The simulated pattern arose from the finite size of diffusing rods, suggesting that the three-fold symmetric pattern we observe in experiment is a direct consequence of the finite length of the fd-rods. The occurrence of the observed nematic patterns depends strongly on the shape and dimensions of the confining chambers, as shown in Fig. 7, where the probability of occurrence of the three nematic patterns (see Methods) is plotted against the inner hole diameter d_i (in units of outer diameter d_o).

The pattern with infinite-fold symmetry is most likely to occur in narrow ring-shaped chambers with a large hole in the middle with

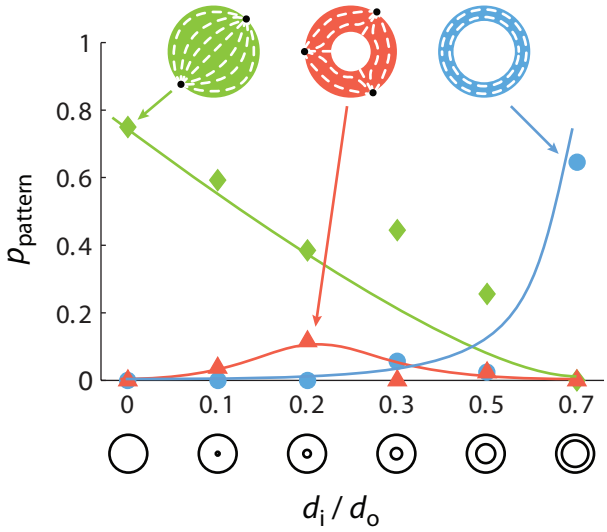

Figure 7. Comparison of the probability of occurrence of the three patterns shown in Figure 6 as a function of the ratio of inner (hole) diameter d_i to outer diameter (d_0) Blue circles correspond to the infinite-fold symmetric pattern, green diamonds correspond to the three-fold symmetric pattern, and red triangles correspond to the two-fold symmetric pattern. Lines are guides to the eye.

$d_i / d_o = 0.7$ (blue circles in Fig. 7, see also Fig. 8c). We denote this pattern with the symbol $U(1)$, which corresponds to the infinite-fold rotational symmetry of the unit circle given by the unitary group of degree 1 (Cornwell, 1984) (Fig. 8a). Two typical examples of the $U(1)$ pattern are shown in Fig. 8b. The pattern occurs exclusively in the smallest chambers with diameters up to 50 μm (Fig. 8d).

The two-fold symmetric pattern with two +½ singularities on opposite ends of the chamber is most probable in disk-shaped chambers without a central hole ($d_i / d_o = 0$, see green diamonds in Fig. 7, see also Fig. 9b). We denote this pattern with the symbol D_2, which corresponds to the two-fold rotational symmetry of the dihedral group of order two (Atkins and de Paula, 2009) (Fig. 9a). D_2 patterns do form also in chambers with a hole ($d_i / d_o > 0$), but with a probability that decreases sharply with increasing hole size (Fig. 9c). The occurrence of the D_2

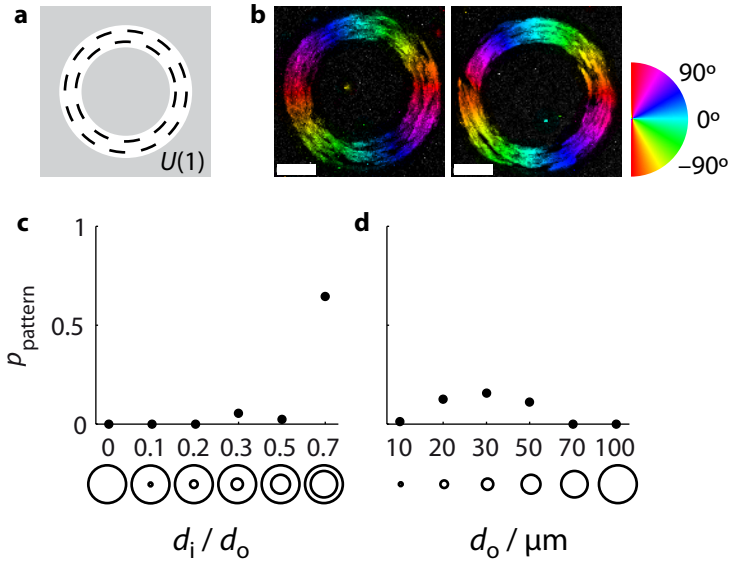

Figure 8

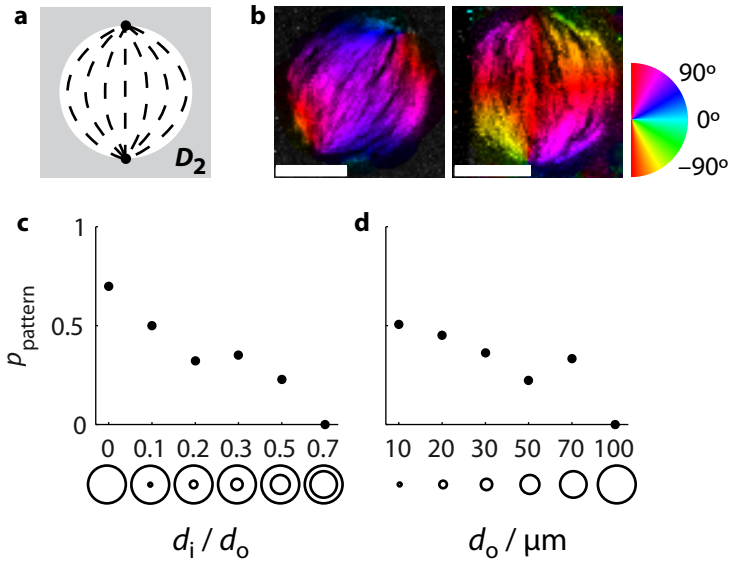

Figure 9

pattern also depends on the chamber size, decreasing with increasing d_o and being zero for the largest chambers of 100 μm (Fig. 9d).

The three-fold symmetric pattern only occurs for chambers with a small but finite hole size (d_i / d_o = 0.2, red triangles in Fig. 7, see also Fig. 10c). This pattern has three evenly spaced +½ singularities (Fig. 10a). Two examples are shown in Fig. 10b. We denote this pattern D_3, which corresponds to the three-fold rotational symmetry of the dihedral group of order three. Hole sizes d_i for chambers with D_3 patterns varied in the range 2–6 μm, corresponding to 1 to 3 fd-rod lengths. Furthermore, D_3 occurred mainly for smaller chambers up to 30 μm (Fig. 10d).

Alternative nematic patterns. So far we focused on only three out of the seven different nematic patterns we observed for confined fd-rod liquid crystals. The additional four nematic patterns, which we will describe below, are not predicted by either the continuum theory (which predicts 2 patterns) or the simulations (which predict only three patterns in the parameter range that we used). Here we describe each pattern type and quantify their probability of occurrence as a function of both outer diameter and inner (hole) diameter.

***N* occurs for small chambers**. In the smallest chambers (outer diameter d_o = 10 μm) we observed nematic liquid crystals where rods aligned with each other but not along the circular contour of the chamber (Fig. 11a,b). We denote this pattern, which resembles a bulk

---

Figure 8. Pattern $U(1)$. **a**. Schematic. **b**. Representative instances of $U(1)$. Brightness corresponds to maximum intensity projection of 2000 frames. Color corresponds to the average orientation $\langle\theta\rangle$ of the nematic director (calibration wheel, right). Scale bars 5 μm. **c**-**d**. Probability of occurrence of $U(1)$, given inner diameter d_i (c) and outer diameter d_o (d).

Figure 9. Pattern D_2. **a**. Schematic. **b**. Representative instances of D_2. Brightness corresponds to maximum intensity projection of 2000 frames. Color corresponds to the average orientation $\langle\theta\rangle$ of the nematic director (calibration wheel, right). Scale bars 5 μm. **c**-**d**. Probability of occurrence of D_2, given inner diameter d_i (c) and outer diameter d_o (d).

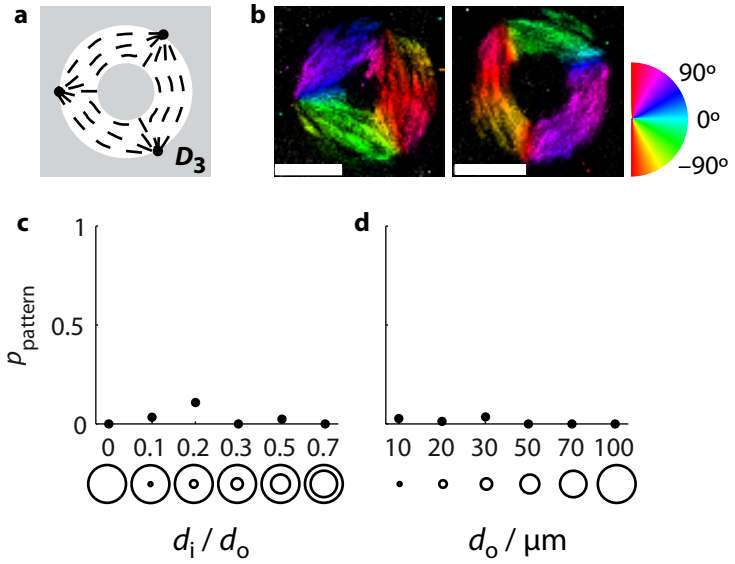

Figure 10

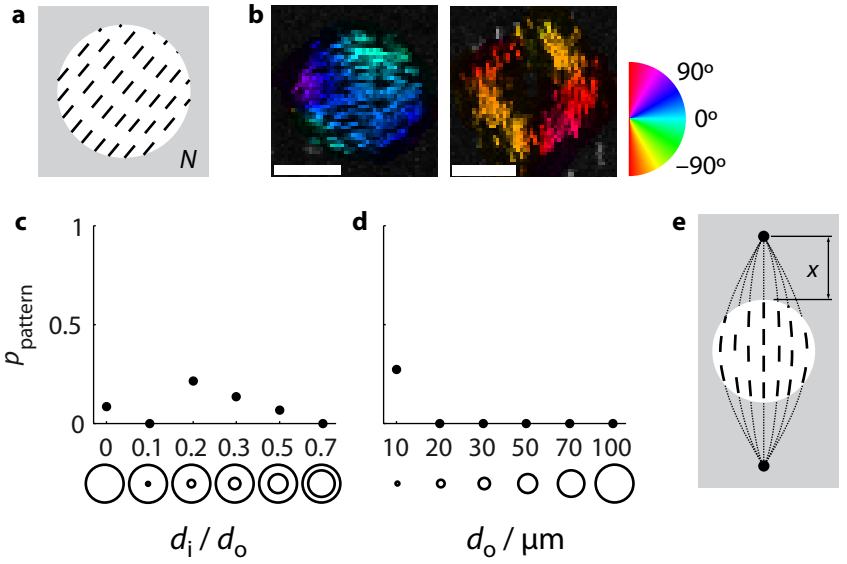

Figure 11

nematic state, with the symbol *N*. These patterns occur over a broad range of hole sizes (Fig. 11c), but occur only when d_o = 10 μm (Fig. 11d). *N* patterns may be related to the D_2 patterns, in that we anticipate that there are two opposite singularities displaced at a distance *x* beyond the chamber edge (Fig. 11e).

Asymmetric *S* patterns. Asymmetric patterns were also observed. Some chambers exhibited only one singularity (Fig. 12a,b). Because of the lack of non-trivial rotational symmetry, we denote this pattern S_1 for "one singularity". This pattern was mostly observed in thin, ring-like chambers (d_i / d_o = 0.5 and 0.7, Fig. 12c). The probability of finding S_1 increases somewhat with increasing chamber size, but is observed over the entire range of chamber sizes (10-100 μm) (Fig. 12d).

Another asymmetric pattern exhibited two singularities, similar to D_2, but unlike in the D_2 pattern, the defects were not positioned at polar opposites (Fig. 13a,b) We call this pattern S_2, which denotes a pattern with two singularities exhibiting no particular rotational symmetry. This pattern occurred over a wide range of hole and chamber sizes with no particular preference (Fig. 13c,d). We quantify the relative angular positions of the two singularities for S_2 patterns by the angle β (Fig. 13e), and find a broad angle distribution ranging from 90 to 160°, with a peak

---

Figure 10. Pattern D_3. **a**. Schematic. **b**. Representative instances of D_3. Brightness corresponds to maximum intensity projection of 2000 frames. Color corresponds to the average orientation $<\theta>$ of the nematic director (calibration wheel, right). Scale bars 5 μm. **c**-**d**. Probability of occurrence of D_3, given inner diameter d_i (c) and outer diameter d_o (d).

Figure 11. Pattern *N*. **a**. Schematic. **b**. Representative instances of *N*. Brightness corresponds to maximum intensity projection of 30 frames. Color corresponds to the average orientation $<\theta>$ of the nematic director (calibration wheel, right). Scale bars 5 μm. **c**-**d**. Probability of occurrence of *N*, given inner diameter d_i (c) and outer diameter d_o (d). **e**. Schematic of hypothetical point defects displaced beyond the chamber edge by a distance *x*.

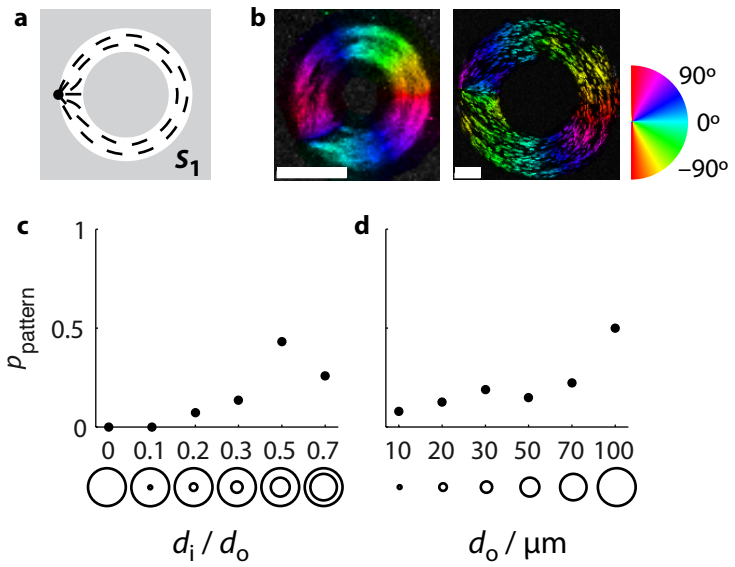

Figure 12. Pattern S_1. **a**. Schematic. **b**. Representative instances of S_1. Brightness corresponds to maximum intensity projection of 2000 frames (left) and 30 frames (right). Color corresponds to the average orientation $\langle\theta\rangle$ of the nematic director (calibration wheel, right). Scale bars 5 μm. **c**-**d**. Probability of occurrence of S_1, given inner diameter d_i (c) and outer diameter d_o (d).

at β = 140° (Fig. 13f). (Note that this distribution excludes chambers which have been classified D_2 and therefore exhibit β = 180°.)

Disordered *B* patterns occur in large chambers. Sometimes, multiple singularities were scattered across the interior of the chamber, and the nematic director field exhibited chaotic-looking patterns (Fig. 14a,b). We denote such structures with the symbol *B*. This type of pattern was mostly observed in chambers with small holes (d_i / d_o = 0.1, Fig. 14c) and in large chambers with d_0 > 50 μm (Fig. 14d).

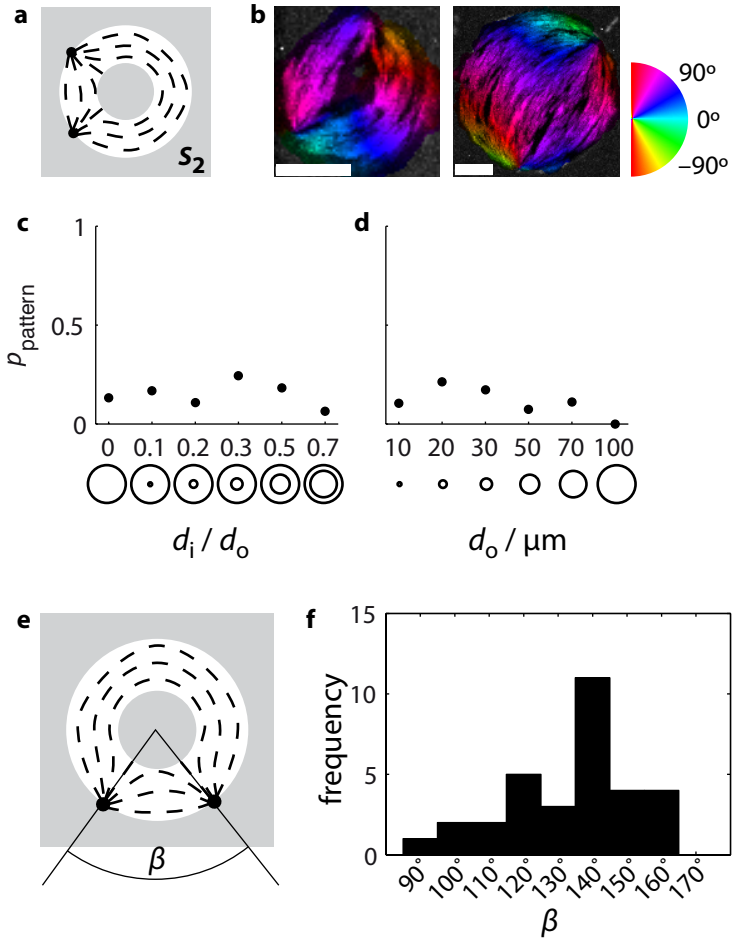

Figure 13. Pattern S_2. **a**. Schematic. **b**. Representative instances of S_2. Brightness corresponds to maximum intensity projection of 2000 frames. Color corresponds to the average orientation $\langle\theta\rangle$ of the nematic director (calibration wheel, right). Scale bars 5 μm. **c**-**d**. Probability of occurrence of S_2, given inner diameter d_i (c) and outer diameter d_o (d). **e**. Schematic representing the angle β formed by the two point defects and the center of the circle. **f**. Histogram of observed values of β for S_2 patterns.

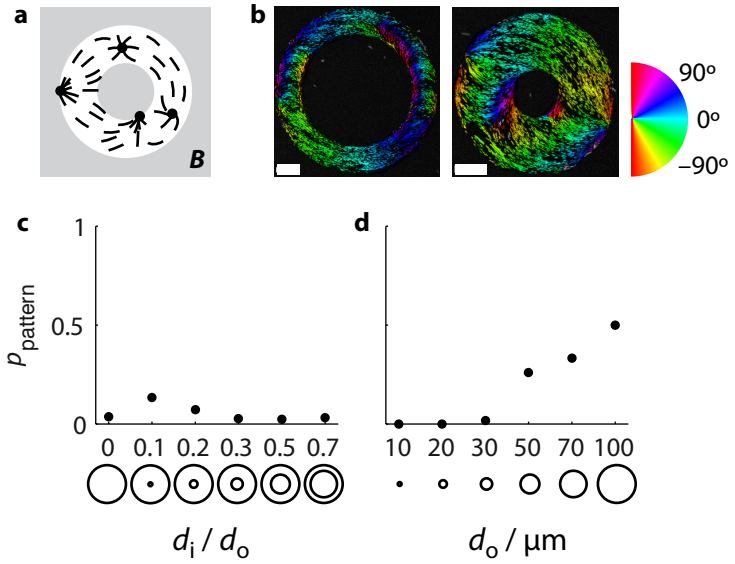

Figure 14. Pattern *B*. **a**. Schematic. **b**. Representative instances of *B*. Brightness corresponds to maximum intensity projection of 30 frames. Color corresponds to the average orientation $\langle\theta\rangle$ of the nematic director (calibration wheel, right). Scale bars 10 μm. **c**-**d**. Probability of occurrence of S_1, given inner diameter d_i (c) and outer diameter d_o (d).

2.4 Discussion

We confined nematic suspensions of fd-virus rods in shallow donut-shaped chambers and reported experimental evidence of a three-fold rotationally symmetric pattern which we denote D_3. We propose that this pattern arises from the optimal packing of confined, colloidal rods, whose sizes cannot be neglected. The main argument to support this interpretation is that the D_3 pattern is identified as a thermodynamically favorable configuration in simulations accounting for finite particle size, whereas it is not predicted by continuum theory. Moreover, the pattern exhibits intermediate properties that suggest it occurs in a transition from $U(1)$ to D_2. First, the three-fold symmetry of D_3 is of an order that lies between the two-fold symmetry of D_2 and the infinite-fold symmetry

of $U(1)$. Second, D_3 was most likely in chambers with intermediate hole diameters $d_i / d_o = 0.2$, in between the hole diameters where D_2 ($d_i / d_o = 0$) and $U(1)$ ($d_i / d_o = 0.7$) patterns were observed (cf. Fig. 7).

Although the existence of D_3 in experiment and simulation indicates consistency, experiment and simulation could not be performed with identical parameters, as detailed in Figure 15. In particular, the confinement in the z-direction was much less stringent in the experiments (1.1–3.4 rod lengths) than in the simulations (1-6 rod diameters). This likely explains why D_3 patterns occurred for different values of d_i / L: in experiment, D_3 occurred for $d_i / L = 2.5–7.5$. These values are greater than expected from geometric correspondence (cf. Fig. 3), where we should expect $d_i / L \approx 3^{-1/2} = 0.58$. Experimentally, we cannot rule out that D_3 is not a thermodynamically favorable condition based solely on consistency with simulation data. However, simulation found that thicker (more three-dimensional) chambers exhibited lower-order symmetries (cf. Fig. 4). In particular, D_3 occurred over a broad range of parameters, up to $d_i / L \approx 1.7$, which approaches the experimentally observed interval of 2.5–7.5. The chambers investigated in simulation had vertical height d_z that were at most equal to about half a rod length L, while in experiment the chamber height was 1.1–3.4 times the rod length L. It will be interesting to extend the computational work with calculations over a broader region of parameter space, to identify when D_3 is a thermodynamically favorable state. Furthermore, experiments on thicker colloidal rods such as microtubules may lead to the direct observation of higher-order symmetry states.

Despite differences in parameters, simulation and experiment furthermore agreed on the occurrence of N patterns. In experiment, we found patterns that resembled D_2, but with expelled singularities (cf. Fig. 11). This N pattern also occurred in simulation when rod length L or density φ were increased (Mulder, 2012) (results not shown here). Prior theoretical work on colloidal rods in tactoidal droplets, where two virtual defects occur outside the droplet, similarly observed a transition to a bipolar state where defects approached the droplet surface to become true defects as droplet size increased (Prinsen and van der Schoot, 2004). These predictions agree well with experiment, where we find tactoid-like N patterns for small outer diameters d_o. This agreement suggests

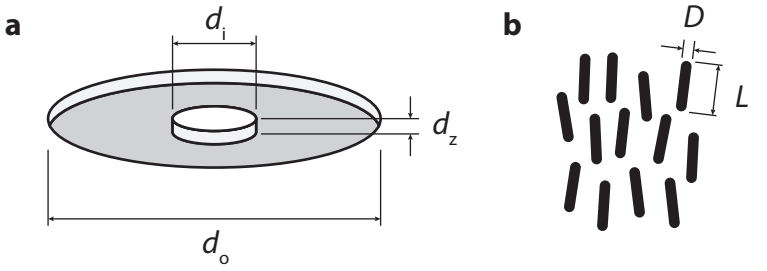

c

	Simulation	Experiment
d_0	40 / D	10–100 μm
d_i	0–0.5 d_o	0–0.7 d_o
d_z	1–6 D	1–3 μm
L	15–25 D	133 D
D	1	6.6 nm

Figure 15. Comparison of length scales probed in simulations and experiments. **a**. Schematic of an annular chamber with outer diameter d_o, inner diameter d_i, and vertical height d_z. **b**. Schematic of rods with thickness D and length L. **c**. Table comparing values of d_o, d_i, d_z, D, and L between simulation and experiment.

that the control parameter d_o / L determines a crossover between D_2 and N.

Further agreement between experiment and simulation occurred with the asymmetric pattern S_2. This pattern was also observed in simulation, albeit as a transient state while simulated systems were approaching equilibrium (Garlea and Mulder, 2013). Simulated systems that exhibited transient S_2 patterns ultimately equilibrated to D_3 symmetries. The two singularities in S_2 occurred at two vertices of an equilateral triangle. This observation roughly agrees with experiment: we found a wide distribution of angles β with a peak at β = 140°. This experimental value is in reasonable agreement with the value of β = 120°, which corresponds to the intermediate state observed in simulations. This suggests that experimental S patterns may represent a metastable precursor to D-type symmetries.

This hypothesis raises the important question whether the experimentally observed patterns represent thermodynamic equilibrium. Although we cannot strictly rule out the possibility of nonequilibrium behavior, the nematic patterns we observed were stable over the course of 1–24 h after sample assembly and were reproducible over a large number of chambers. Furthermore, many of the experimental patterns correspond to predicted equilibrium configurations by simulations. Interestingly, $U(1)$, D, N, and S_2 patterns were most likely in small chambers ($d_o \leq 30$ μm, cf. panel d of Figs 8, 9, 10, 11, and 13), whereas the potentially metastable B and S_1 patterns were most likely in large chambers ($d_o \geq 50$ μm, cf. panel d of Figs 12 and 14). This observation suggests that smaller chambers may be more likely to produce equilibrium structures.

2.5 Outlook: Square Chambers

So far we investigated the breakdown of continuum theory arising from the optimal packing of hard rods of finite size in annular geometries. Previous experiments with actin filaments (Soares e Silva et al., 2011a) and vibrofluidized rods (Galanis et al., 2006; 2010a) suggest that finite-size effects also influence packing of rods in microchambers with a different shape, such as square chambers. Here we report first tests of packing of fd-rods in square chambers and examine how finite-rod-size effects could manifest in these geometries. Continuum theory predicts that rods close to the chamber edges align along the walls, while rods at the center align along the long axis of the chamber, which is one of the two diagonals (Fig. 15a). The competition between bulk and surface ordering leads to diagonal alignment, with splay deformations in two diagonally opposing corners, and bend deformations in the other two opposing corners.

Recent simulations by Ioana Garlea and Bela Mulder address the limit of finite rod size. Similar to the simulations summarized in Section

2, hard rods diffuse in boxes with dimensions $d_z = 3\ D$ and $d_x = d_y = 73\ D$, where D is the rod diameter. As before, box vertical height d_z was chosen such that rods cannot freely rotate out of the xy-plane. In sharp contrast to continuum theory, the simulations predict that the liquid crystal adopts a line in place of a bend deformation, since the rods are unable to bend. At the line defect, the orientations of the rods change in a discontinuous manner (Fig. 16b).

To test whether such line defects can be observed experimentally, we confined nematic liquid crystals of fd-virus rods in shallow square- and rectangular-shaped chambers. As in Section 3, we acquire time-lapse image series of chambers containing fd-rods with a small tracer fraction that was fluorescently labeled. Again, we quantify the orientation of the nematic director using the customized image analysis routine described in Section 7. The nematic field director closely resembles predictions from continuum theory, with parallel alignment of rods near the walls and diagonal alignment in the chamber center (Fig. 16c). This alignment also resembles the patterning we find for nematic liquid crystals of actin filaments (Chapter 2). However, the data do not clearly reveal a sharp discontinuity in rod orientation at the corners, as predicted by the finite rod simulations. Because the line defect in simulation was predicted to have a size on the order of the rod length L, the discontinuity should manifest itself on length scales of 0.88 μm for fd-virus rods. In principle, a discontinuity of this length scale should be detectable. However, the square chambers in simulation have perfectly sharp corners, whereas the edges of the experimental chambers are rounded due to the limited (~1 μm) resolution of the photolithographic techniques used to produce them. The rounded edges may assist in the formation of a continuous bend structure rather than a discontinuous line defect. Future experiments which employ either chambers with sharper corners (for instance made by electron beam lithography), or suspensions of longer rods (for instance actin or microtubules), should be capable of experimentally verifying the line defect predicted by simulations of diffusing rods in square chambers.

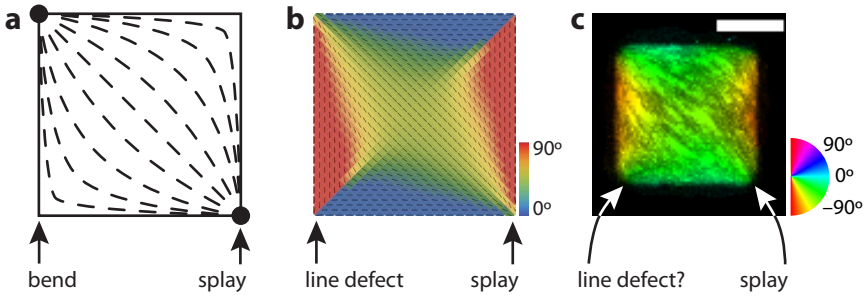

Figure 16. Nematic director fields of nematic liquid crystals of rods confined in square microwells. **a**. Schematic depicting a thermodynamically favorable configuration as predicted by continuum theory. **b**. Thermodynamically favorable configuration predicted by simulations of finite-length rods. Color denotes average rod orientation $<\theta>$ (see color calibration bar). **c**. Experimentally determined director field for fd-virus rods confined in a square microchamber (width d_x = height d_y = 10 μm, thickness d_z = 3 μm). Scale bar 5 μm. Color denotes average rod orientation $<\theta>$ (see color calibration wheel).

2.6 Methods

Bacteriophage fd-virus preparation. fd-virus rods were grown using a standard protocol (Dogic and Fraden, 2005) and stored in fd-buffer (20 mM tris pH 8.15, 100 mM sodium chloride, 15% ethanol). Assay suspensions were prepared at concentrations of 24 mg mL^{-1}, slightly above the bulk isotropic-nematic biphasic region, which occurs at ~20 mg mL^{-1}, in agreement with Onsager theory (Tang and Fraden, 1995). Suspensions were biphasic, as evidenced by visual inspection through crossed polarizers. fd-rods have a molecular weight of $1.64 \cdot 10^7$ Da (Zimmermann et al., 1986). We chose the lowest possible nematic concentration, in order to minimize the energy cost to re-arrange from one director field to another and thus reduce the probability of getting stuck in high energy metastable states. Fluorescently labeled rods were prepared by incubation with Alexa-488 succinimidyl ester (Dammone et al., 2012) (Invitrogen). A small amount of labeled rods (2–4% v/v)

was mixed with unlabeled rods in order to make individual labeled rods distinguishable by fluorescence microscopy.

Microchamber preparation. Microchambers were assembled using a standard photolithographic technique. In short, glass cover slips were spin-coated with a layer of photoresist and exposed to UV light patterned by a customized mask. Before spin-coating, cover slips (thickness #1, Menzel Gläser) were cleaned with base piranha (water, 30% ammonium hydroxide, 30% hydrogen peroxide at a ratio of 5:1:1; 75 °C for 15 min), followed by rinsing with water and baking (200 °C, 5 min). Cover slips were spin-coated (Delta 80 GYRSET, SUSS MicroTec; spin speed 3000 rpm) with a negative photoresist (SU-8 2005, MicroChem). Layer thickness was adjusted by diluting photoresist with cyclopentanone by approximately 10–20% and measured by a profilometer (Alpha-Step 500, KLA-Tencor). Coated cover slips were then baked (95 °C, 5 min) before exposure to ultraviolet light (only wavelengths above 365 nm, BG-12 bandpass filter, Schott) in a mask aligner (MJB, Karl Süss; typical dosage: 50–100 mJ cm^{-2}). Patterning was achieved through custom-designed mask of chromium features printed on soda-lime glass (DeltaMask). The mask design included circular and annular geometries with outer diameters d_o of 10, 20, 30, 50, 70, and 100 μm. For each outer diameter, geometries with inner diameters d_i of 0, 0.1, 0.2, 0.3, 0.5, and 0.7 times the outer diameter d_o were made, resulting in 36 different geometries.

Exposed cover slips were baked (95 °C, 5 min), developed (2-methoxy-1-methylethyl acetate, MicroChem; 1–2 min), rinsed with isopropanol, and ultimately hard-baked (150°C, 2h). This process results in a glass substrate with a layer of photoresist patterns that form the basis of microchambers. Next, microscope slides (Menzel Gläser) were coated with a layer (~1 mm thick) of polydimethylsiloxane rubber (Sylgard 184, Dow Corning; 10:1 base:curing-agent w/w ratio; 120 °C, 5 min). Rubber-coated glass was rendered hydrophilic by corona discharge (BD-20V high-frequency generator, Electro-Technic Products) and soaked overnight in fd-buffer containing 0.1 wt% of the amphiphilic block copolymer Pluronic F-127 (Sigma-Aldrich), which effectively blocked nonspecific adsorption of fd-rods as confirmed by time-lapse imaging of rod diffusion. Saturation of the PDMS with buffer prevented drying of the sample for at least 24 hours.

We used the same lithography technique to prepare rectangular microwells with short edges of length 2–50 μm and aspect ratios of 1 to 18. We used chamber heights of 0.7, 3 and 5 μm. However, the cells of height 0.7 μm were difficult to fill, thus we used 3 μm for the majority of the experiments.

Confinement assay. A drop of fd-virus suspensions was placed on a glass-photoresist substrate and pressed against rubber-coated glass to form microchambers. After hermetically sealing glass edges with VALAP (equal parts vaseline, lanolin, and paraffin wax), samples were left to equilibrate for at least 30 mins and subsequently visualized by fluorescence microscopy. Only chambers that were well-sealed were considered, amounting to approximately 40% of all chambers. Chambers that were not well-sealed were evident by diffusion of fluorescently labeled rods escaping from the chamber (Fig. 17). The rods rapidly organized in steady-state nematic patterns within 30 minutes after filling the chambers. When we filled the chambers with the isotropic phase below the biphasic region, a nematic was not formed and the sample remained isotropic. This observation implies that the filling (and confinement) were not sufficient to induce a nematic.

Fluorescence microscopy. Microchambers were visualized using two microscope setups: (1) a spinning disk confocal scanner (CSU 22, Yokogawa) on an inverted microscope (DMIRB, Leica) with a cooled, electron-multiplying charged-coupled device (C9100, Hamamatsu) and (2) a Nikon C1 confocal point scanner on an inverted microscope (Ti, Nikon) with a photomultiplier tube detector (A1, Nikon). Labeled rods were excited with 488 nm laser light (Coherent). A series of images were recorded over a long enough time interval such that viruses diffused across the entire chamber. The average diffusion constant of virus rods in the nematic phase is $D_{\parallel} \approx 1$ μm^2 / s along the nematic director and $D_{\perp} \approx 0.1$ μm^2 / s perpendicular to the nematic director (Lettinga et al., 2007). These diffusion constants result in diffusion timescales of tens of seconds for diffusion by one particle length and minutes for diffusing over inter-particle distances between fluorescently labeled rods (~ a few μm). The anisotropy in diffusion constants is apparent in Figure 18, where tracks of fluorescently labeled rods are clearly elongated along the direction of the nematic director. For spinning disk data, ~ten movies of 200 frames each were acquired at a fast imaging rate (0.1 frames per

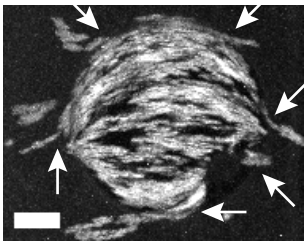

improperly sealed

Figure 17. Improperly sealed chambers are clearly evident by rods escaping chambers at the interface between the chip and the lid. Image represents a maximum time projection over 50 s. Escape events are visible as tracks of fluorescence that extend past chamber boundaries (white arrows). Scale bar 5 μm.

second), which were separated by 2 minutes to allow rods to diffuse completely across the chamber (Fig. 18). For point-scanning confocal data, ~15–30 frames were acquired at a slower rate (1 frame per ~1–2 minutes) over several fields of view which were automatically acquired and stitched (NIS Elements, Nikon). A customized image analysis technique was developed to determine the average nematic director orientation $\langle\theta\rangle$ given average orientations θ of labeled fd-rods across all images acquired (see Image Analysis).

Identification of nematic patterns. Rods formed a variety of liquid crystal patterns. Pattern type was determined by visual inspection of the nematic director fields of all well-filled chambers on the chip. Figure 19 summarizes the pattern frequency as a function of d_o and d_i / d_o. We define the probability that a pattern P occurs in a given chamber geometry G as the number of observed instances of P given G divided by the total number of well-sealed chambers with geometry G (Fig. 20). A total of 243 chambers were analyzed: 80, 27, 26, 36, 43, and 31 chambers for d_i / d_o = 0, 0.1, 0.2, 0.3, 0.5, and 0.7 respectively; 77, 75, 55, 25, 9, and 2 chambers for d_o / μm = 10, 20, 30, 50, 70, and 100, respectively; 23, 113, 5, 21, 33, 32, and 16 chambers for patterns $U(1)$, C_2, C_3, N, S_1, S_2, and B, respectively.

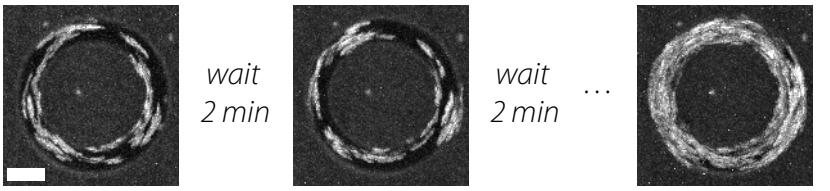

Figure 18. Optimal acquisition technique. **Left and center panels**: Maximum time projections of spinning-disk confocal data over 200 frames, corresponding to 20 s for each set of images. Each set exhibits elongates streaks of fluorescence owing to the anisotropy in rod diffusion in the nematic phase. **Right panel**: Maximum time projection over all sets of images, totaling 2000 frames. Over long enough time periods, viruses will have diffused across the entire chamber, resulting in virtually every pixel of the chamber having imaged at least one rod across all frames.

2.7 Image Analysis

We developed an algorithm where we quantify the orientation of the nematic director for each image pixel, given an image series (with N frames) of fluorescently labeled rods. In short, we determine rod orientation θ for each frame, and average over frames to get the mean orientation $<\theta>$ per pixel.

Step 1: Given an image of fluorescent rods (Fig. 21a), we compute their orientation θ (Fig. 21b) and the gradient energy, which quantifies the contrast between bright and dark pixels (Fig. 21c). This step is implemented using OrientationJ, which is a freely-available ImageJ plugin originally developed to track collagen and elastin fibers (Fonck et al., 2009; Rezakhaniha et al., 2012). This routine computes structure tensors constructed of the spatial gradients of fluorescence intensity around each pixel (x,y). Determining the eigenvectors of a structure tensor yields the characteristic orientation θ of the fluorescence intensity of a small region $(x\pm\sigma, y\pm\sigma)$ around each pixel (x,y). We set the parameter σ = 3 px, which corresponds to the typical length scale of a

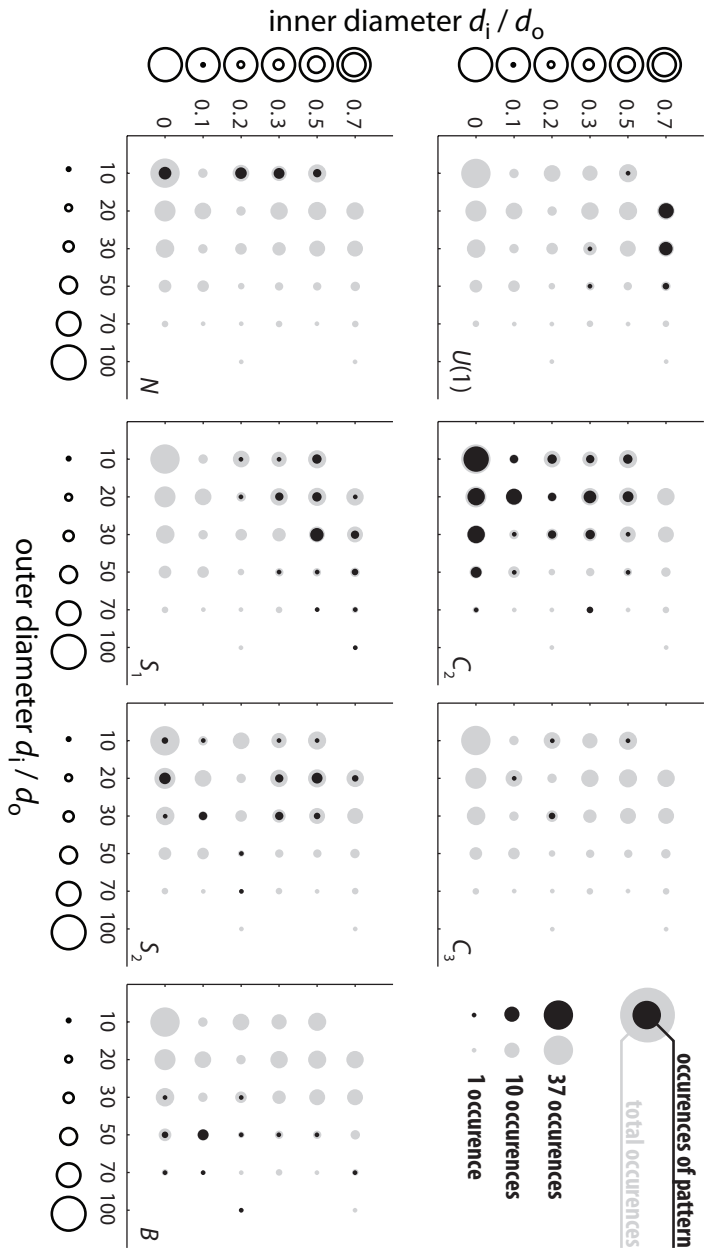

Figure 19. Frequency of occurrence over d_o-d_i phase space. Black circles denote number of occurrences of a given pattern. Gray circles denote total number of chambers analyzed. Circle area depicts frequency (legend, top-right).

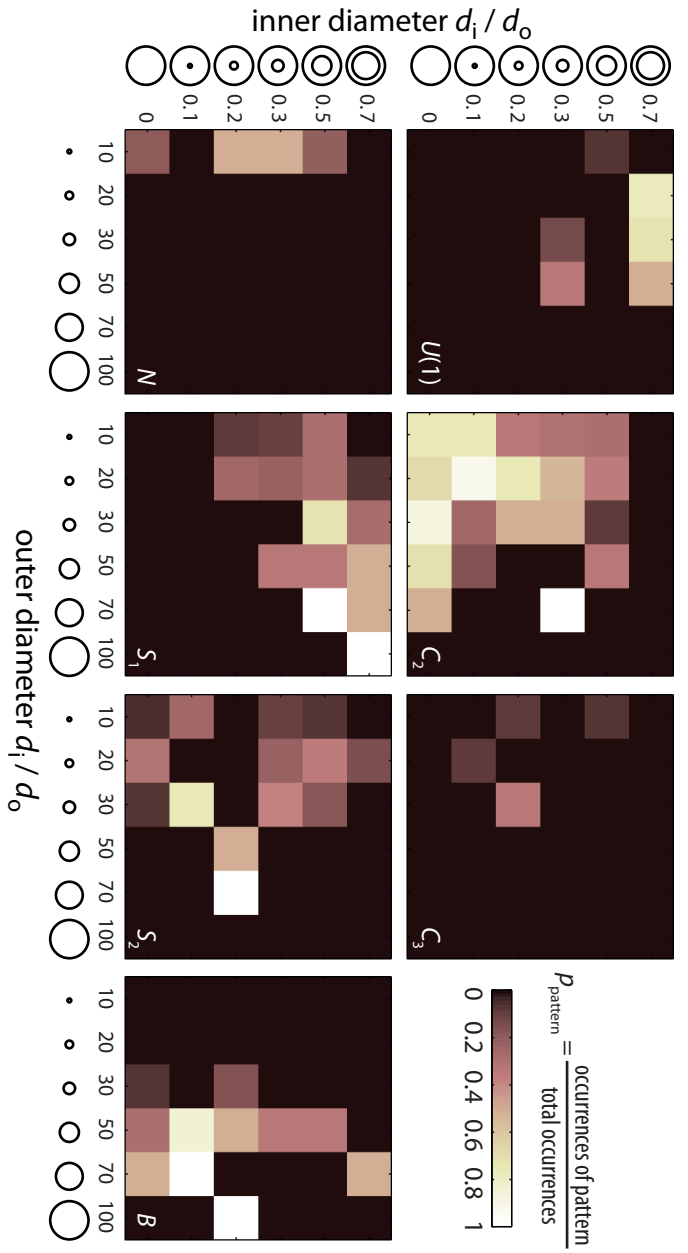

Figure 20. Probability of occurrence over d_o-d_i phase space. Color denotes probability (legend, top-right), defined by the number of occurrences observed divided by the total number of chambers analyzed.

rod. Furthermore, the trace of the structure tensor yields the gradient energy Note that this quantity should not be confused with a physical energy. Rather, it is related to the notion of signal energy (Mitra and Kaiser, 1993).

Step 2: The energy image from Step 1 is thresholded (Fig. 21d) using Otsu's method (Otsu, 1975). This yields a binary image comprising connected components of bright pixels (1) against a dark background (0). Bright pixels in this image correspond to points at or near a fluorescently labeled virus particle.

Step 3: The orientation image from Step 1 is masked using the threshold from Step 2 (Fig. 21e). The result is a set of orientation measurements θ only for pixels at or near a fluorescently labeled virus particle. We thus discard orientation measurements of background pixels.

Step 4: Steps 1–3 are repeated for the N frames of the dataset (Fig. 21f,g). The result is a series of N images produced by Step 3 (Fig. 21h,i).

Step 5: The average orientation $<\theta>$ per pixel is determined given the N images from Step 4 (Fig. 21j,k). Each pixel can have up to N orientation measurements, depending on how often it passes the

---

Figure 21. Algorithm for determining average orientation $<\theta>$ of the nematic director given many measurements of rod orientation θ *in each pixel*. **a**. First frame of original data. **b**. Orientation output of OrientationJ. Color corresponds to orientation θ around each pixel (calibration wheel, below). **c**. Energy output of OrientationJ. Note that energy is highest where changes in fluorescence intensity are largest. **d**. Otsu threshold of the energy image (c). **e**. Masking the orientation image (b) with the threshold image (d). Note that color corresponds to orientation of virus rods in original image (a). **f–i**. Looping over all frames of a set of images. f,g: original data for frames 200 and 2000. h,i: Masked orientation images for frames 200 and 2000. **j**: Maximum time projection of the original data for all frames. **k**: Average orientation of all rods, $<\theta>$, which gives the local direction of the nematic director in each image pixel.

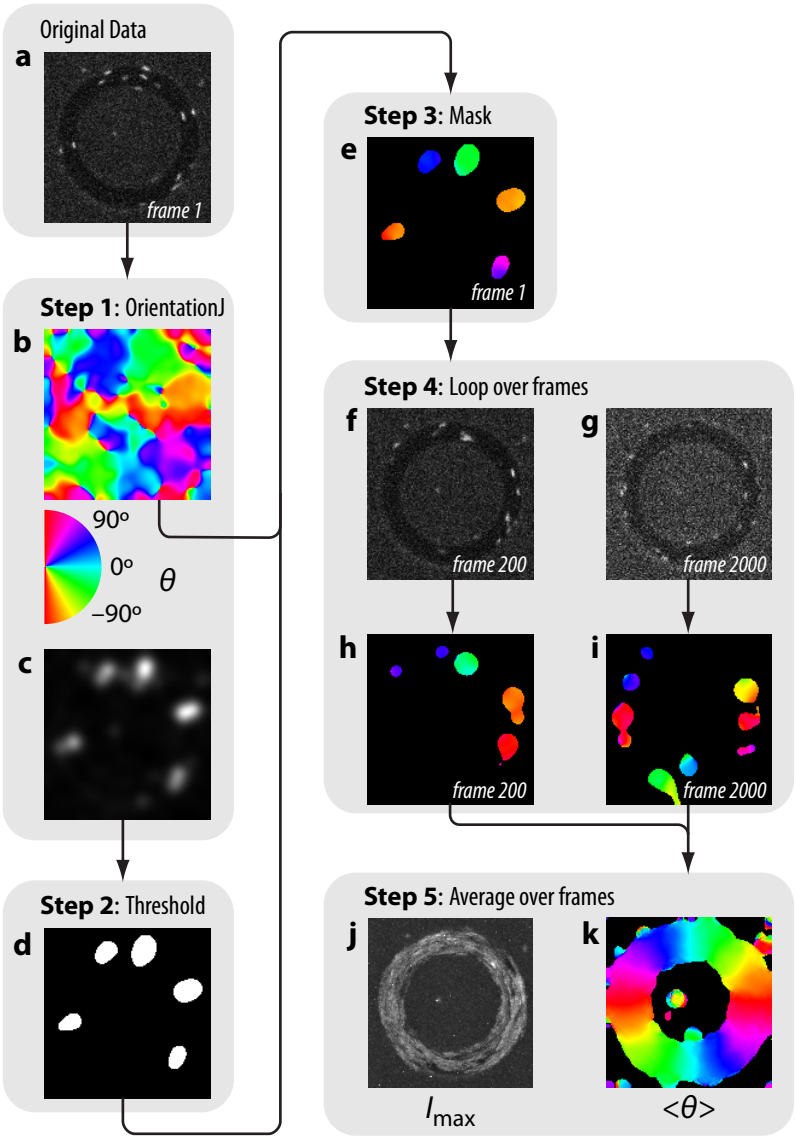
Original Data
a
frame 1
Step 1: OrientationJ
b
90°
0°
−90°
θ
c
Step 2: Threshold
d
Step 3: Mask
e
frame 1
Step 4: Loop over frames
f
frame 200
g
frame 2000
h
frame 200
i
frame 2000
Step 5: Average over frames
j
k
I_{max}
<θ>

Figure 21

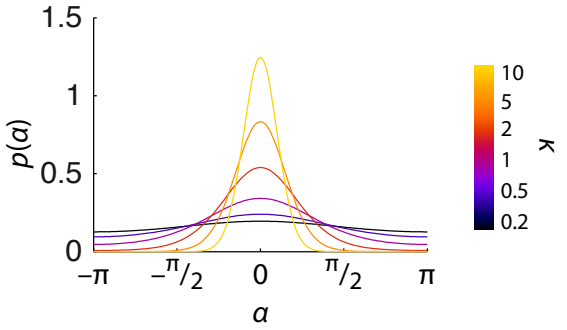

Figure 22. The von Mises distribution, defined over a closed, periodic support. All curves shown represent distributions with the same mean angle $<\alpha> = 0$ but varying values of the concentration κ (calibration bar, right).

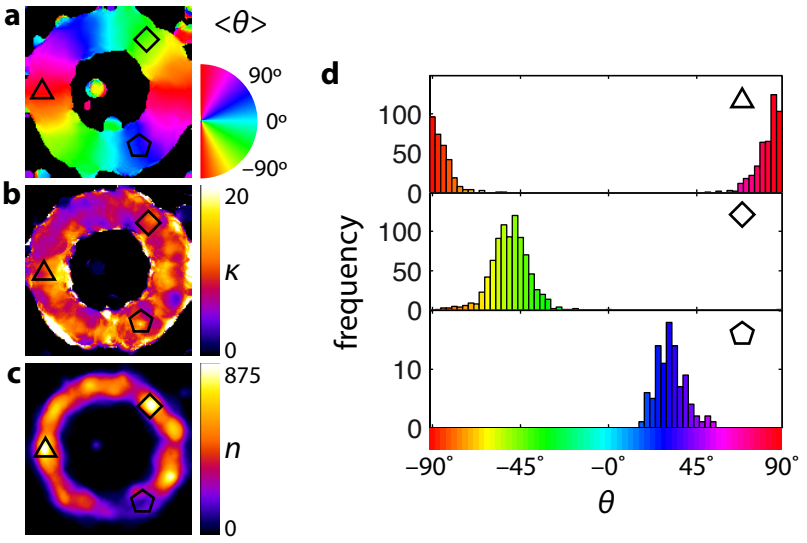

Figure 23. Determining mean orientation $<\theta>$ from distributions of individual measurements θ. **a**. Mean orientation $<\theta>$, as in Figure 21, panel k. **b**. Concentration κ for each pixel corresponding to panel a, where color corresponds to values of κ as indicated in the calibration bar on the right. **c**. Number of orientation measurements n per pixel, as determined by the number of frames that a given pixel passes the threshold in Step 2. **d**. Histogram of orientation measurements for three pixels indicated by triangles, diamonds, and pentagons in panels a–c.

threshold from Step 2. Usually, background pixels never pass the threshold from Step 2 and therefore do not have orientation measurements.

The von Mises distribution. Computing the arithmetic mean is not a suitable method to determine average orientation $\langle\theta\rangle$ since the orientation θ is a circular quantity, which takes on values over a finite range (between –90° and 90°) that is periodic (–90° = 90°). Computing the arithmetic mean can give incorrect average orientations: we should expect the two measurements –89° and 89° to average out to 90°, but the arithmetic mean yields 0°. In order to accurately determine average orientation $\langle\theta\rangle$, we first consider the von Mises distribution (a.k.a. circular normal distribution), which is the circular analog of the Gaussian distribution (Jammalamadaka and Sengupta, 2001) (Fig. 22):

$$p(\alpha) = \frac{e^{\kappa \cos(\alpha - \langle\alpha\rangle)}}{2\pi I_0(\kappa)},$$

where α is a circular quantity that varies in the range [-π, π) and usually corresponds to an angle or phase. The von Mises distribution is parametrized by two parameters: the expectation value $\langle\alpha\rangle$ and the concentration κ. These two parameters are analogous to the expectation value μ and the inverse of the standard deviation σ^{-1} of a Gaussian distribution. Note that orientation θ varies in the range $[-\pi/2, \pi/2)$, whereas angle α varies in the range [-π, π). Although most circular quantities are measured by an angle α (wind direction, phase of a wave), some physical quantities are rather measured by an orientation θ (polarization of light, orientation of apolar rods). In order to relate θ to the von Mises distribution, orientation measurements are multiplied by a factor of 2 to recover angles α. The average angle $\langle\alpha\rangle$ is computed, and then divided by a factor of 2 to recover the average orientation $\langle\theta\rangle$. The concentration κ remains unchanged when converting between orientation θ and angle α.

In Step 5, we use the "CircStat" MATLAB toolbox (Berens, 2009) to compute $\langle\theta\rangle$ for each pixel (Fig. 23a), which yields the orientation of the nematic director. We also compute the concentration κ of the distribution for each pixel (Fig. 23b). In principle, κ could act as a measure of the order parameter of the liquid crystal: higher values of κ indicate a more sharply peaked distribution. Finally, Fig. 23c shows

the number of orientation measurements per pixel. Most areas are well-sampled ($N \sim 10^2$), but a few restricted sites are under-represented.

Acknowledgements

Experimental results and data analysis were obtained in collaboration with Oliver Dammone (U Oxford), Pavlik Lettinga (FZ Jülich) and Dirk Aarts (U Oxford). Bacteriophage fd-virus was kindly provided by Pavlik Lettinga. Simulations and analytical theory were designed and executed by Pieter Mulder, Ioana Garlea, and Bela Mulder (AMOLF). We thank all of these collaborators for fruitful discussions. We furthermore thank Dimitry Lamers, Andries Lof, Gijs Vollenbroek, and Chris Rétif for assistance with microfabrication and electron microscopy. The OrientationJ plugin was written by Daniel Sage (EPFL, Lausanne).

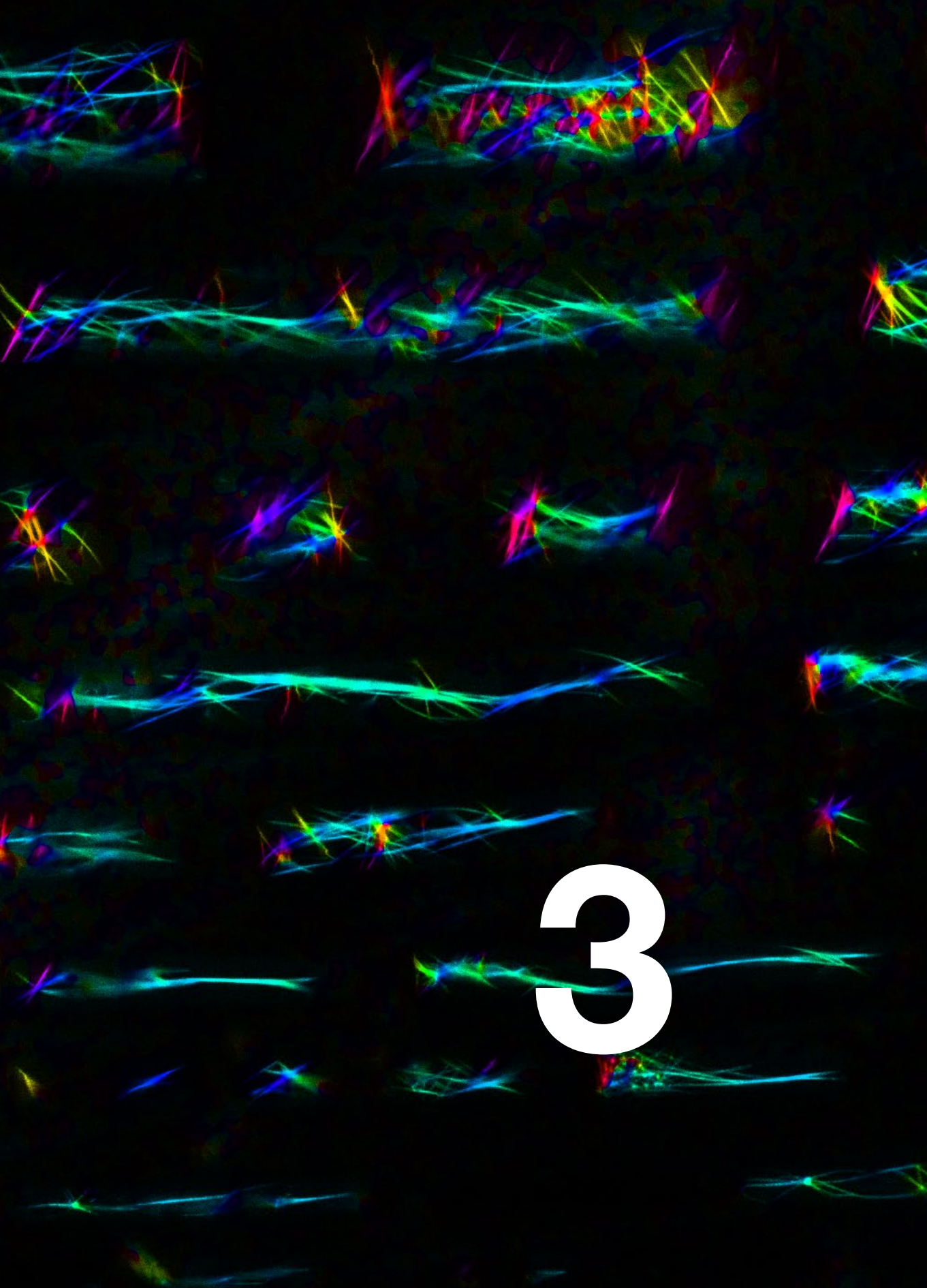
3

3. Alignment in confined semiflexible polymer networks

The finite size of cells poses a spatial constraint on the cytoskeleton. At the same time, the high packing density of cytoskeletal filaments poses mutual packing constraints. Here, we investigate the competition between bulk and surface packing constraints on the orientational ordering of confined networks of actin filaments in nematic and bundled phases. We fabricate shallow, rectangular microchambers of different sizes and aspect ratios, and grow networks of actin inside them. We determine the director field by fluorescence microscopy and custom-written image analysis software. We find that isotropic networks are insensitive to confinement, whereas nematic and bundled networks preferentially align along the diagonal axis of the chambers. The chapter ends with a section in which we present two additional image analysis techniques, one to determine the presence of bundles and one to determine the dependence of actin concentration on radial position inside microchambers. Our pixel-based methods have the advantage of being able to extract density and orientation information even when the length scales of the filamentous networks are below the diffraction limit. Our method could thus be applied also to images of the actin cytoskeleton in confined regions of cells such as the protrusive lamellipodium of migrating cells.

3.1 Introduction

The mechanical properties of eukaryotic cells are largely determined by the cytoskeleton, a meshwork of filamentous proteins with unique mechanical properties (Storm et al., 2005). Three cytoskeletal components are known to significantly contribute to cell stiffness, cell shape (Paluch and Heisenberg, 2009) and internal organization (Mullins, 2010).

The finite size of cells poses a spatial constraint on the cytoskeleton. In plants, the cytoplasm, and hence the cytoskeleton, is confined to thin layers pressed between the rigid cellulose cell wall and the vacuole, which occupies 90% of the cell volume (Gunning and Steer, 1996). In animal cells, large, three-dimensional cytoplasms prevail, though anchoring to the plasma membrane often results in a thin actin cytoskeletal cortex (Salbreux et al., 2012). The plasma membrane of animal cells is in principle soft and deformable, but still cell shape in many tissues is strongly constrained, either due to the anchoring of a rigid pericellular coat on the membrane exterior (Nijenhuis et al., 2009; Tanaka et al., 2005), or due to close packing of cells within epithelial layers (Fernandez-Gonzalez et al., 2009). Recent biophysical research has begun to address the effect of spatial confinement on intracellular organization by culturing individual cells or confluent cell monolayers on micropatterned substrates (Vedula et al., 2012; Vignaud et al., 2012). External confinement has been shown to strongly affect the spatial organization of the cytokinetic contractile ring (Théry et al., 2005), mitotic spindle (Fink et al., 2011), and nucleus (Versaevel et al., 2012), and thereby strongly affect cell fate (Chen et al., 1997). In addition to global cell shape confinement, a variety of thin cellular extensions locally constrain the cytoskeleton to confined geometries. On flat substrates and in some tissues, cells migrate using a protrusive flat sheet-like array of actively treadmilling actin filaments called the lamellipodium (Mogilner and Oster, 2003; Small et al., 1995; Verkhovsky et al., 2003). Cells also extend actin filaments and microtubules into linear protrusions, such as filopodia (Bryant, 1999; Davenport et al., 1993; Mogilner and Rubinstein, 2005; Svitkina et al., 2003), stereocilia (Manor and Kachar, 2008; Tilney et al., 1989; Zheng et al., 2000), flagella (Luck, 1984; Nicastro et al., 2006),

and neurite processes (Dehmelt and Halpain, 2003). A mechanistic understanding of the effect of geometrical confinement on the spatial organization of cytoskeletal networks remains elusive.

In-vitro experiments with reconstituted cytoskeletal polymer networks provide a convenient way to study the role of confinement in cytoskeletal organization in the absence of complicating factors such as active processes and biochemical regulation. In dilute suspensions of actin filaments and microtubules, confinement to small geometries with rigid boundaries forces filaments to align along the walls to minimize bending energy (Cosentino Lagomarsino et al., 2007). Narrow channels have been shown to elongate filaments of actin (Choi et al., 2005; Hirst et al., 2005; Köster et al., 2005) and DNA (Bonthuis et al., 2008; Tegenfeldt et al., 2004) by constraining thermal bending undulations. Specific geometries of actin or microtubule filament nucleation imposed by micropatterned substrates can result in bundle formation in the absence of crosslinks (Portran et al., 2013; Reymann et al., 2010).

But in addition to external confining geometries, mutual packing interactions between filaments at high packing densities can also affect the organization of polymer networks. At low densities, filaments form an isotropic phase which lacks a preferred orientation. Above a critical density, filaments spontaneously align to reduce their excluded volume and form a nematic liquid-crystalline phase. Initial theoretical work by Onsager showed that the critical density depends solely on the aspect ratio of filaments if the filaments interact exclusively by steric repulsion (Onsager, 1949). Both filament flexibility (Chen, 1993; Khokhlov, 1982; Odijk, 1986) and filament length polydispersity (Flory and Abe, 1978; Odijk, 1986) have been theoretically shown to increase the critical density compared to the Onsager transition. Onsager's theory and modifications thereof have been highly successful in predicting the phase behavior of rod-shaped filamentous viruses like tobacco mosaic virus (Bawden et al., 1936) and fd-virus (see Chapter 1) as well as actin filaments (Helfer et al., 2005; Käs et al., 1996). For instance, reducing actin filament length with the capping protein gelsolin has been shown to increase the critical density for nematic liquid crystalline ordering in close agreement with the Onsager theory (Coppin and Leavis, 1992; Furukawa et al., 1993; Oda et al., 1998; Suzuki et al., 1991; Viamontes and Tang, 2003).

The combination of packing constraints from mutual filament interactions and external confinement has been little explored. Isotropic actin networks in emulsion droplets and vesicles form peripheral shells to minimize bending energy (Claessens et al., 2006a; Limozin et al., 2003), similar to individual confined filaments. Confinement of actin networks in microchambers was shown to cause nematic alignment at densities below the bulk isotropic-nematic (Onsager) transition (Soares e Silva et al., 2011a).

In contrast to *in-vitro* systems, living cells do not appear to exhibit networks of cytoskeletal filaments in the nematic phase despite the rather high concentrations of actin in the cytoplasm (Koestler et al., 2009). Rather, cells actively regulate filament organization by orchestrating a wide array of accessory proteins which specifically interact with actin filaments to produce networks, bundles, and higher-order cytoskeletal structures (Chhabra and Higgs, 2007; Vignjevic et al., 2003). Bundling likely acts together with spatial confinement to form functional cell structures such as filopodia (Atilgan et al., 2006; Mogilner and Rubinstein, 2005). *In-vitro*, the combination of packing constraints from cross-linker-mediated interactions and external confinement has again been little explored. In reconstituted actin networks confined to microchambers or emulsion droplets, interesting organized patterns of bundles were observed when the solvent was allowed to slowly evaporate (Deshpande and Pfohl, 2012; Huber et al., 2012; Vonna et al., 2005). In narrow microchannels, actin bundles are efficiently aligned along the channel (Hirst et al., 2005).

In this chapter, we seek to quantify the effect of spatial confinement on the spatial organization of semiflexible polymer networks that form either isotropic, nematic, or bundled phases in bulk solution. We model external confining geometries by fabricating shallow, square microchambers with a systematically varied size and in-plane aspect ratio. Inside these chambers, we grow networks of actin filaments prepared in an isotropic or nematic phase, as well as networks of actin filaments bundled by various agents. We visualize these networks by fluorescence microscopy and quantify the spatial evolution of filament orientation using a pixel-based method related to previous methods which quantified filament orientation in the lamellipodium of migrating cells (Weichsel et al., 2009; 2012). We find that isotropic networks

remain isotropic in the microchambers, independent of chamber aspect ratio, whereas nematic liquid crystals of actin filaments adopt preferential alignment along the diagonal axis of the chambers. Further, we show that the spatial organization of bundle networks responds to the imposed confinement in a similar manner to nematic liquid crystals of actin filaments, preferentially aligning with the chamber's longest axis. The chapter ends with a section in which we present two additional image analysis techniques, one to determine the presence of bundles and one to determine the dependence of actin concentration on radial position inside microchambers.

3.2 Results

In order to quantify the effect of confinement on the spatial organization of semiflexible filament networks, we prepare microchambers with a well-controlled rectangular geometry (Fig. 1a; see Methods). Chambers were designed with lengths d_y in the range 3–100 μm and widths d_x such that the aspect ratio d_x / d_y varied in the range 1–10 (Fig. 1b). Chamber thickness d_z remains constant across all experiments at 3 μm. Inside these chambers, we grow networks of fluorescently labeled actin filaments under various conditions (Fig. 1c). We investigate the effect of chamber thickness on the spatial pattern of local orientations θ of actin filaments, based on anisotropy of fluorescence intensity (see Methods). From these orientation measurements, we determine the preferred orientation $<\theta>$ and the order-parameter S of the nematic director from the second-order tensor order-parameter $\mathbf{S}_2$ (see Methods).

Confined nematic liquid crystals of actin filaments. In order to investigate the effect of external geometry on the spatial organization of confined suspensions of semiflexible filaments in the nematic phase, we grow actin filaments at concentrations of 4 mg mL^{-1} in microchambers. At these high concentrations, actin filaments self-organize to form a nematic liquid crystal (Furukawa et al., 1993; Käs et al., 1996). We

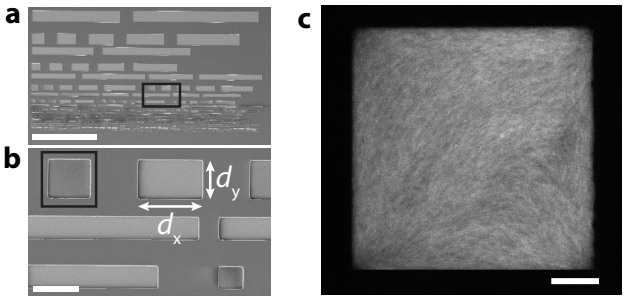

Figure 1. Experimental model system of actin filament networks confined to microchambers. **a**. Snapshot of chip patterned with microchambers, acquired by scanning electron microscopy. Scale bar 500 μm. **b**. Closeup of the area in the black box in panel a. Scale bar 50 μm. White arrows denote the chamber length d_y and width, d_x, from which we compute the chamber aspect ratio as d_x / d_y. The chamber height is 3 μm. **c**. Confocal fluorescence image of square microchamber (d_y = 50 μm, d_x / d_y = 1) filled with a suspension of fluorescently labeled actin filaments in the nematic phase ([actin] = 4 mg mL^{-1}). Scale bar 10 μm.

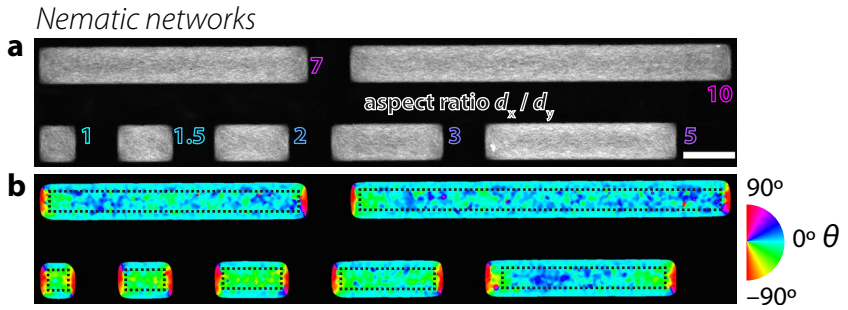

Figure 2. Nematic liquid crystals of actin filaments confined to microchambers. [actin] = 4 mg mL^{-1}, d_y = 15 μm. **a**. Snapshots of actin filaments in microchambers. Outlined text denotes chamber aspect ratios d_x / d_y from 1 (square) to 10 (long rectangle). Scale bar 20 μm. **b**. Maps of the orientations of fluorescence intensity in each pixel. Color corresponds to orientation θ of fluorescence intensity distribution (see calibration wheel, right). Dashed black boxes denote manually selected regions of interest. These regions were selected to avoid edge effects related to the sudden decrease in fluorescence intensity at the chamber boundaries.

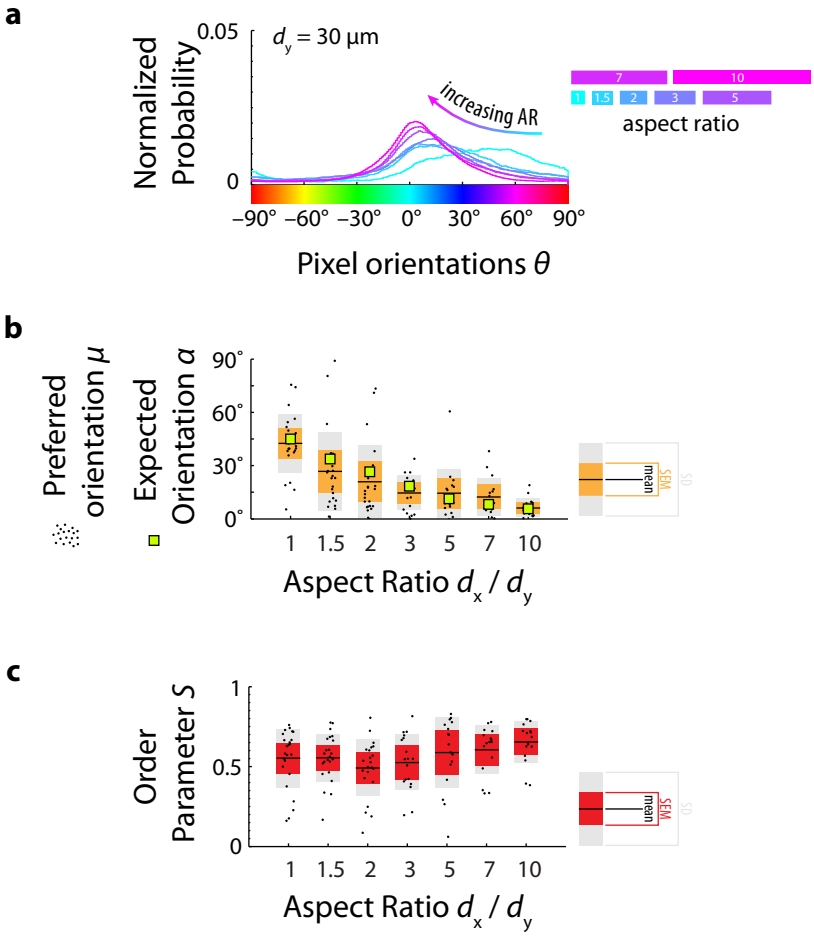

Figure 3. Quantitative analysis of confined nematic networks over multiple chambers with d_y = 30 µm. **a**. Probability distribution function of pixel orientations θ. Color corresponds to different aspect ratios (see legend, right; also see Figure 2a). Note that pixel orientations were multiplied by a factor of ±1 to account for the rectangular symmetry of the chambers (see Methods). **b**. Expected orientation α (green squares) and preferred orientation μ (black points) as a function of aspect ratio. Gray boxes denote standard deviation (SD) of values of μ across multiple chambers. Orange boxes denote standard error of the mean (SEM). Black lines denote arithmetic means. **c**. Order parameter S (black points) as a function of aspect ratio. Gray boxes denote SDs. Red boxes denote SEMs. Black lines denote arithmetic means. Two

visualize these confined networks by fluorescence microscopy, which reveals a fine aligned texture indicating nematic alignment (Fig. 2a). For all chamber sizes and aspect ratios, the networks appear rather homogeneous. However, due to the small mesh size (~ 150 nm) and small diameter of the filaments (~ 7 nm), we are unable to resolve and track individual actin filaments. Instead, we quantify the mean orientation of filaments per image pixel, which measures the local orientation θ of the nematic director (Fig. 2b, see Methods).

Initially, we would expect filaments to align along the long axis of the chamber, which is one of the two diagonals. This is the case for the chambers depicted in Figure 2b. For square geometries (aspect ratio d_x / d_y = 1), pixels in the center of the chamber report an orientation θ of approximately –45° along the diagonal of the chamber. This is evident in Fig. 2b (bottom-left), where green pixels correspond to –45°. As chamber aspect ratio increases to 10, the orientation θ of pixels shifts gradually to 0°. This is evident in a shift from green pixels to cyan pixels, which report orientations of 0°.

In order to quantify the effect of chamber geometry on the orientation of the nematic director, we plot histograms of orientation measurements for many identical chambers with chamber lengths d_y = 30 μm (Fig. 3a). Indeed, the distribution of orientations θ in square chambers (aspect ratio 1, light blue curve), is peaked around 45°. As aspect ratio increases, the peaks shift towards 0°. This gradual shift from 45° to 0° is also evident in Fig 3b. This panel shows the preferred orientation μ of several chambers (represented as black points) as well as the angle α of the chamber diagonal (represented as green squares), given by

$$\alpha = \arctan(d_y / d_x).$$

The mean preferred orientation $\langle\mu\rangle_{\text{chambers}}$ averaged across all chambers (represented as black horizontal lines) decreases towards 0° in a manner

---

distributions are statistically significantly different ($p \lesssim 0.01$) if their orange bars (SEM) do not overlap (Cumming et al., 2007). Number of chambers N = 24, 23, 22, 18, 17, 16, 16 for aspect ratio = 1, 1.5, 2, 3, 5, 7, and 10, respectively.

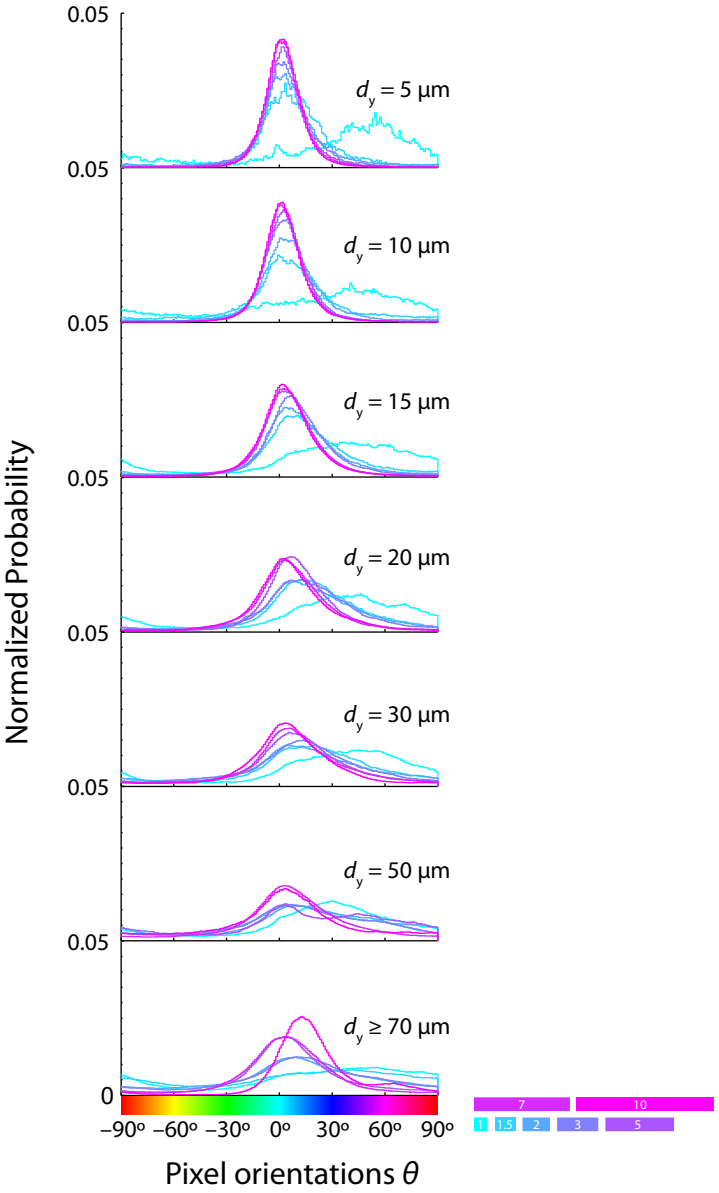

Figure 4. Quantitative analysis of confined nematic networks for chambers of all dimensions, as in Figure 3a. Plots show the probability distribution function of pixel orientations θ. Distributions are shown for different chamber lengths d_y (separate plots) and different aspect ratios d_x / d_y (color).

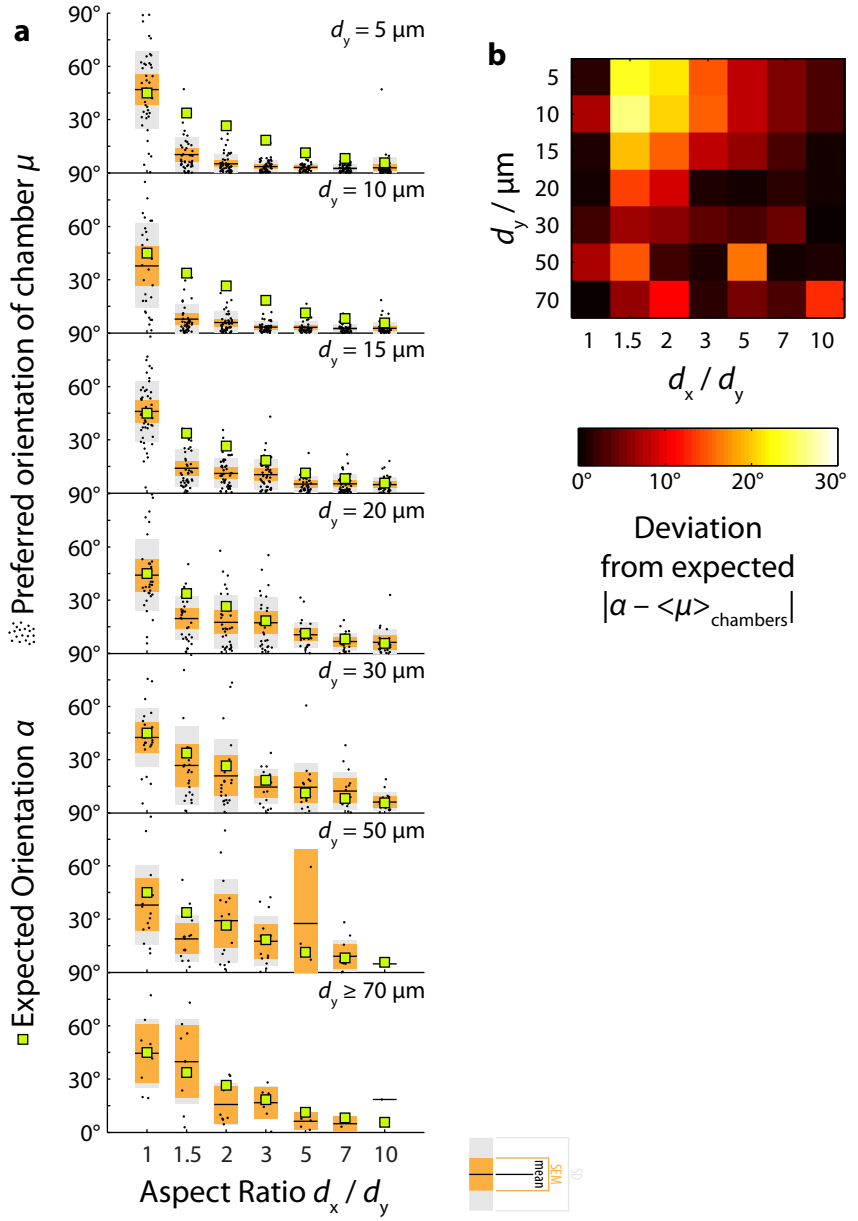

Figure 5. Quantitative analysis of confined nematic networks for chambers of all dimensions, as in Figure 3b. **a**. Expected orientation α (green squares) and preferred orientation μ (black points) for different chamber lengths d_y (separate plots) and different aspect ratios d_x / d_y

consistent with α. (Note that orientations are multiplied by a factor of ±1 to account for the rectangular symmetry of chambers, see Methods.) Furthermore, Figure 3c shows the order parameter S (represented as black points) of individual chambers. This quantity measures the dispersion of orientations θ across a single chamber (see Methods). The mean order parameter $\langle S \rangle_{\text{chambers}}$ averaged across all chambers slightly increases with increasing aspect ratio, although not in a statistically significant manner.

So far we have presented chambers where confined liquid crystals appear to closely follow the chamber diagonal. However, this is not satisfied for all chamber geometries. Many chambers appear to contain networks that rather align to the parallel edges of the chamber in the x-direction. This is shown in Figures 4 and 5. Figure 4 shows histograms of orientation measurements for all chamber geometries. Figure 5 shows the preferred orientation μ and the expected orientation α for all chamber geometries. We find that for small rectangular chambers ($d_y < 30$ μm, $d_x / d_y > 1$), networks prefer to orient along the x-axis ($\mu = 0°$) rather than the chamber diagonal ($\mu = \alpha$). This is evident in panel a, where $\langle \mu \rangle_{\text{chambers}}$ (represented as black horizontal lines) do not agree with the angle α of the chamber diagonal (represented as green squares). Many of these differences are statistically significant. (When orange bars do not overlap with green squares, $p \lesssim 0.01$.) Interestingly, networks in square chambers ($d_x / d_y = 1$) appear to align along the chamber diagonal for virtually all chamber lengths d_y. These results show that a slight anisotropy in chamber shape causes nematic networks to align along the longest parallel walls, rather than the chamber diagonal.

Apart from the preferred orientation μ, chamber dimensions strongly affect the mean order parameter $\langle S \rangle_{\text{chambers}}$ (represented as

---

(x-axis). **b**. Phase space of the deviation from expected angle, given by the difference between the expected orientation α and the mean preferred orientation $\langle \mu \rangle_{\text{chambers}}$ averaged over many chambers. The x-axis corresponds to chamber aspect ratio, y-axis to chamber length. Color corresponds to deviation (calibration bar, below). For number N of chambers, see Methods.

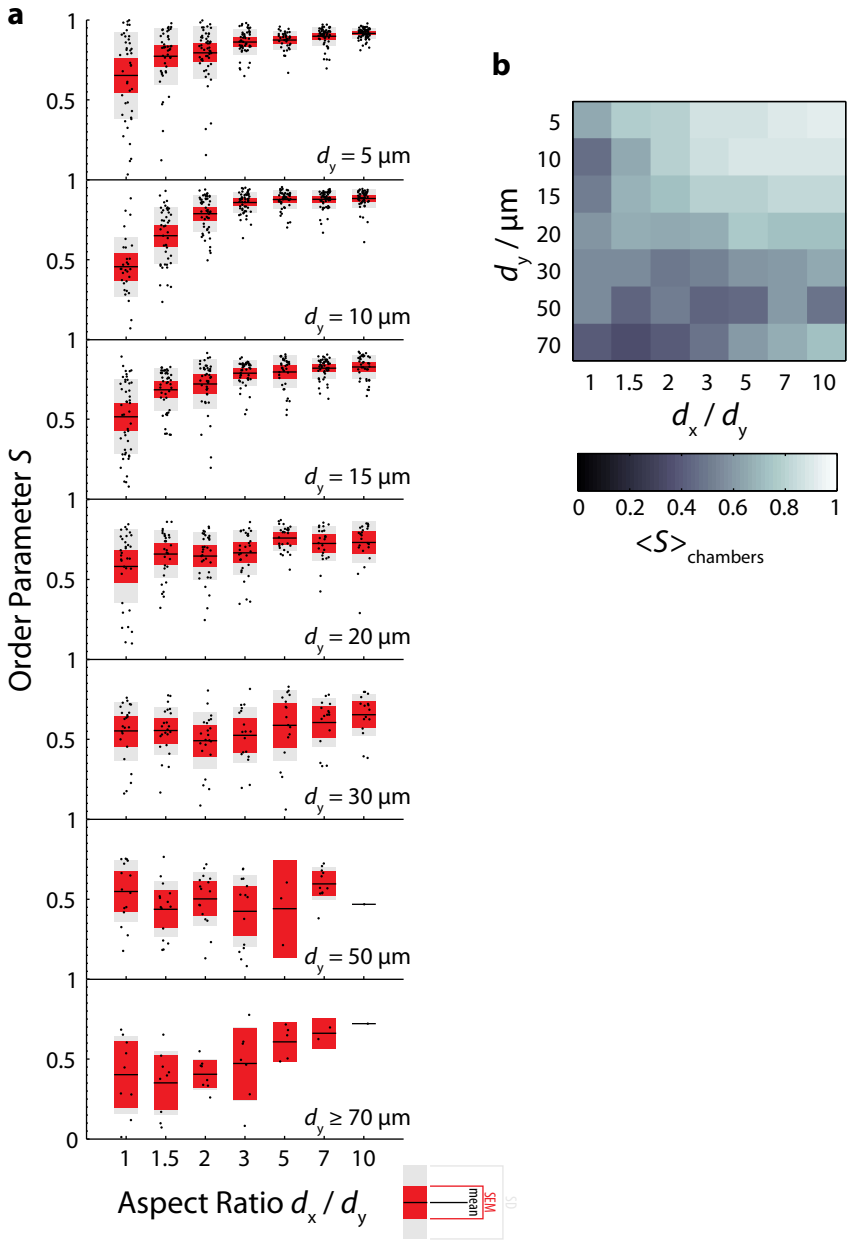

Figure 6. Quantitative analysis of confined nematic networks for chambers of all dimensions, as in Figure 3c. a. Order parameter (black points) for different chamber lengths d_y (separate plots) and different aspect ratios d_x / d_y (*x*-axis). b. Phase space of the mean order parameter

black horizontal lines, Fig. 6). Smaller chambers exhibit a higher order parameter. For $d_y < 20$, the order parameter increases with increasing aspect ratio. Many of these increases are statistically significant. However, for larger chambers, the order parameter is not significantly affected by the aspect ratio. These results show that nematic networks exhibit a more well-defined preferred direction as the confining geometry decreases in length scale and increases in anisotropy.

Interestingly, the networks appear to be rather homogeneous for all chamber sizes (down to 5 μm) and aspect ratios (cf. Figure 2). This result is surprising in light of prior studies of networks confined in spherical confinement (vesicles (Limozin et al., 2003) and emulsion droplets (Claessens et al., 2006a)), where networks formed peripheral shells below 10-15 μm, which coincided with the persistence length of actin filaments.

Confined networks of bundled actin filaments. So far we investigated the effect of an external confining geometry on entangled networks of actin filaments in the nematic phase. However, actin filaments in living systems are often assembled into bundles by a variety of actin-binding proteins. In order to investigate the combined effect of crosslink-induced organization and confinement-induced organization, we grow bundles of actin filaments in microchambers. We prepare bundles of actin using two different techniques.

We first prepared bundles of actin by polymerizing filaments at concentrations of 0.5 mg mL^{-1} in the presence of 20 mM magnesium chloride ($MgCl_2$). The positive, divalent magnesium ions accumulate around negatively-charged actin filaments to form a cloud of counterions; above a critical concentration of counterions, filaments share counterion clouds, which establishes attractive interactions between filaments and drives bundling (Tang et al., 1996) and raft formation (Wong et al.,

---

$\langle S \rangle_{\text{chambers}}$ averaged over many chambers. The *x*-axis corresponds to chamber aspect ratio, *y*-axis to chamber length. Color corresponds to mean order parameter (calibration bar, below). For number *N* of chambers, see Methods.

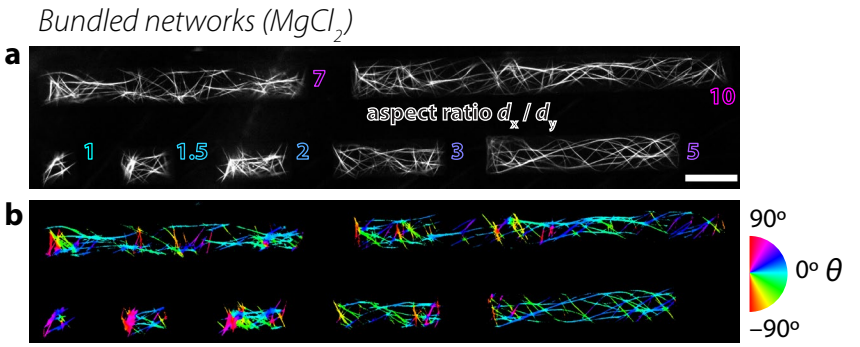

Figure 7. Networks of actin filaments bundled by counterion condensation and confined to microchambers: [actin] = 0.5 mg mL^{-1}, [$MgCl_2$] = 20 mM **a**. Snapshots of actin filaments in microchambers. Outlined text denotes chamber aspect ratios d_x / d_y from 1 (square) to 10 (long rectangle). Scale bar 20 μm. **b**. Maps of the orientations of fluorescence intensity in each pixel. Color corresponds to orientation θ of fluorescence intensity distribution (see calibration wheel, right). Orientation image was masked by an Otsu threshold of panel a.

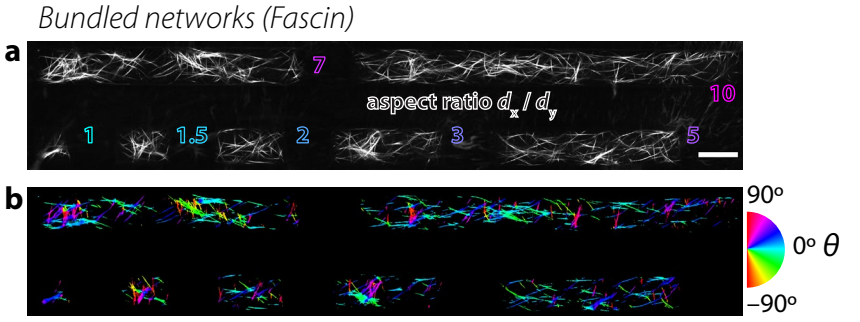

Figure 8. Networks of actin filaments bundled by fascin crosslinks and confined to microchambers: [actin] = 0.5 mg mL^{-1}, [fascin] = 1.2 μM **a**. Snapshots of actin filaments in microchambers. Outlined text denotes chamber aspect ratios d_x / d_y from 1 (square) to 10 (long rectangle). Scale bar 20 μm. **b**. Maps of the orientations of fluorescence intensity in each pixel. Color corresponds to orientation θ of fluorescence intensity distribution (see calibration wheel, right). Orientation image was masked by an Otsu threshold of panel a.

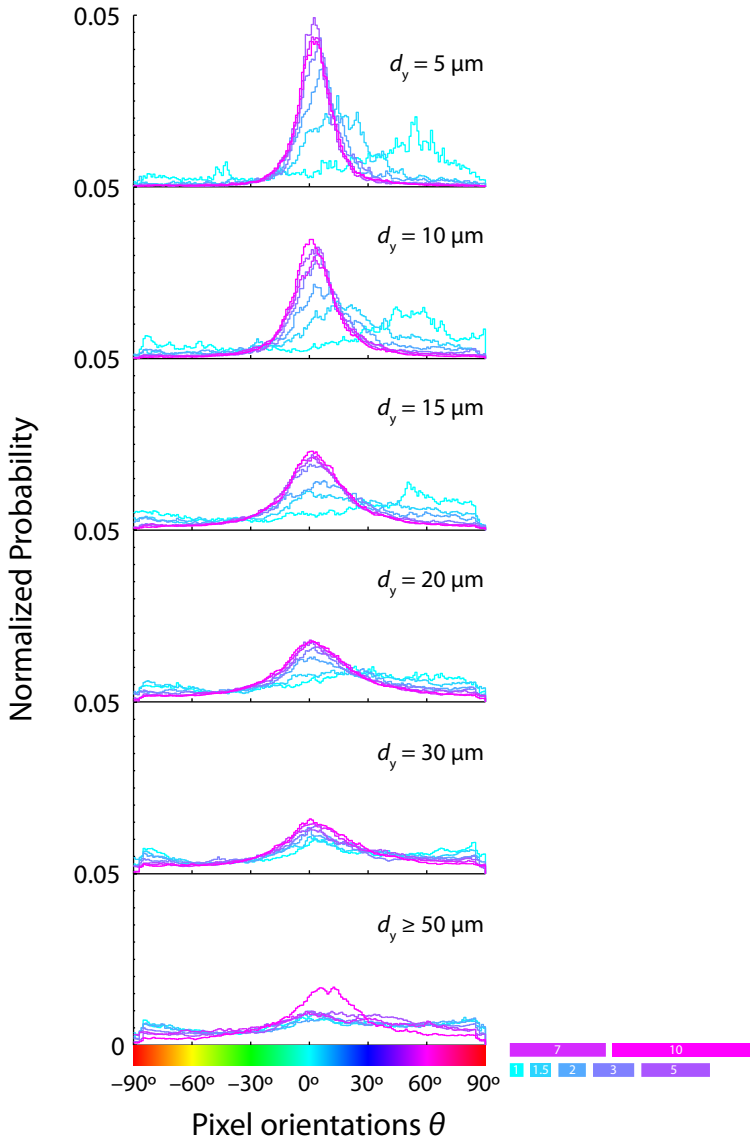

Figure 9. Quantitative analysis of confined bundled networks for chambers of all dimensions, as in Figure 3a. Plots show the probability distribution function of pixel orientations θ. Distributions are shown for different chamber lengths d_y (separate plots) and different aspect ratios d_x / d_y (color).

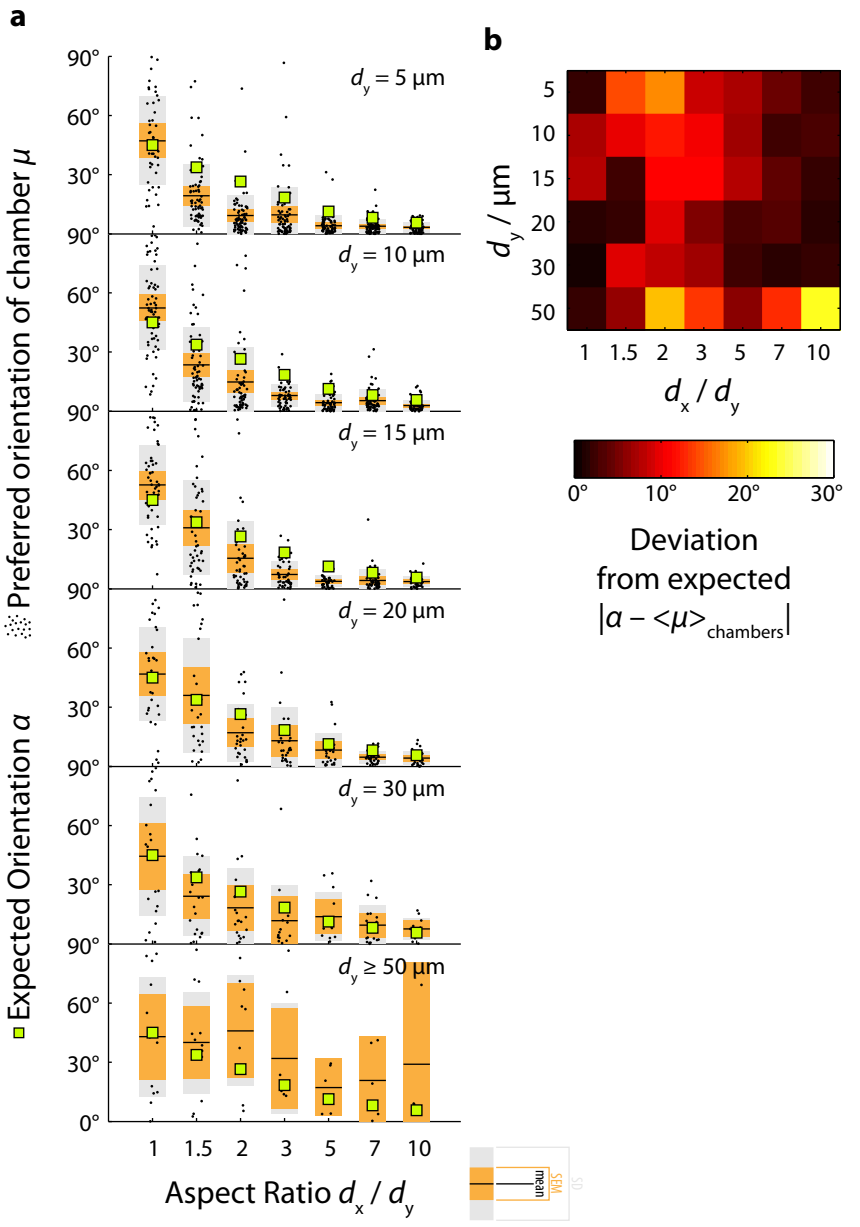

Figure 10. Quantitative analysis of confined bundled networks for chambers of all dimensions, as in Figure 3b. **a**. Expected orientation α (green squares) and preferred orientation μ (black points) for different chamber lengths d_y (separate plots) and different aspect ratios d_x / d_y

2003). Figure 7a depicts networks of actin bundled by $MgCl_2$ confined to microchambers. The bundle orientations are shown in Figure 7b.

We also formed bundles with the crosslink protein fascin. Fascin is enriched in cellular structures called *filopodia* (Svitkina et al., 2003): linear extensions that protrude the plasma membrane in migrating cells. Fascin proteins simultaneously bind two actin filaments via two actin-binding sites (Jansen et al., 2011), forming bundles with a well-controlled maximum number of 19 filaments (Claessens et al., 2008). We polymerize actin filaments at 0.5 mg mL^{-1} in the presence of 1.2 μM fascin crosslinks. We find that fascin bundles organize similarly to magnesium-chloride bundles (Fig. 8 a,b).

In order to quantify the effect of chamber geometry on the distribution of bundle orientation, we plot histograms of orientation measurements (Fig. 9), the preferred direction (Fig. 10), and the order parameter (Fig. 11). Bundled networks appear to more closely follow the chamber diagonal than nematic networks. Figure 10b shows that the mean preferred direction $\langle\mu\rangle_{chambers}$ does not deviate from α by more than ~10° (compared to up to ~30° for the nematic case), except for large chambers (d_y > 50 μm). These results show that bundled networks organize preferentially along the long axis of a rectangular confining geometry. These results are also consistent with a prior study of actin networks bundled in the presence of α-actinin and confined within long, narrow microchannels (Hirst et al., 2005).

The mean order parameter $\langle S\rangle_{chambers}$ attains values slightly lower than those for nematic networks (Fig. 11). The dependence of the order parameter on chamber aspect ratio is also less pronounced. These results show that bundled networks do not attain the same orientational state as nematic networks. The bundle patterns may represent equilibrium

---

(*x*-axis). **b**. Phase space of the deviation from expected angle, given by the difference between the expected orientation α and the mean preferred orientation $\langle\mu\rangle_{chambers}$ averaged over many chambers. The *x*-axis corresponds to chamber aspect ratio, *y*-axis to chamber length. Color corresponds to deviation (calibration bar, below). For number *N* of chambers, see Methods.

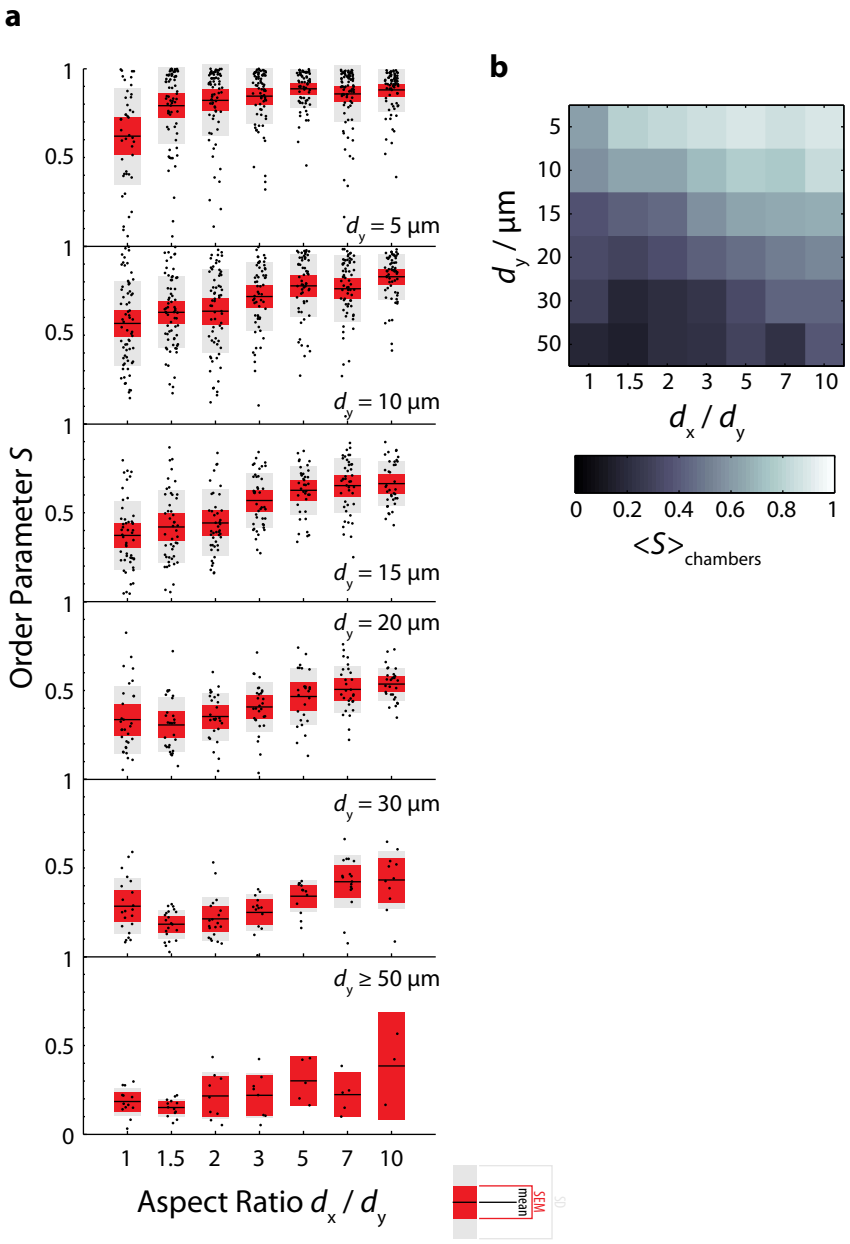

Figure 11. Quantitative analysis of confined bundled networks for chambers of all dimensions, as in Figure 3c. a. Order parameter (black points) for different chamber lengths d_y (separate plots) and different aspect ratios d_x / d_y (*x*-axis). b. Phase space of the mean order parameter

structures resulting from a balance of boundary effects and linker-assisted filament aggregation (Borukhov et al., 2005), but may also be influenced by kinetic trapping, depending on the balance of the kinetics of actin filament polymerization and bundling (Falzone et al., 2012; Huber et al., 2012; Kiemes et al., 2011; Schmoller et al., 2008).

3.3 Discussion

We have shown that an external geometry can strongly influence the spatial organization of semiflexible polymer networks. Actin filaments were found to align preferentially along the long axis of microchambers, provided the filaments were either in a nematic liquid crystalline network or bundled by counterion condensation or the physiological crosslink protein fascin. In contrast, filament orientations in isotropic networks were insensitive to confinement.

We measured an order parameters S of over 0.9 for confined nematic liquid crystals (cf. Fig. 3c). This value is higher than previously measured order parameters, which vary in the range 0.4–0.75, as measured by optical birefringence and x-ray scattering (Helfer et al., 2005) and single filament dynamics (Viamontes et al., 2006a). Similar values of the order parameter were measured for suspensions of tobacco-mosaic virus (Fraden et al., 1993), bacteriophage fd (Purdy et al., 2003), and microtubules (Bras et al., 1998). However, the order parameter we measured here is not equivalent to the order parameter measured by these techniques, which are sensitive to the differences

---

$\langle S \rangle_{\text{chambers}}$ averaged over many chambers. The x-axis corresponds to chamber aspect ratio, y-axis to chamber length. Color corresponds to mean order parameter (calibration bar, below). For number N of chambers, see Methods.

in filament orientation on microscopic length scales. In contrast, the orientation measurements θ reported here were determined by computing the average orientation of a window of 3 px radius around each pixel, corresponding to a window of approximately 1 μm in diameter. Therefore, our order parameter S does not directly report the microscopic arrangements of filaments. Rather, it measures the variance of measurements of θ across all pixels investigated. However, the order parameter thus determined does give at least a quantitative measure of the variation of orientation measurements across an entire chamber. Furthermore, our method allows for the quantitative measurement of the preferred orientation $<\theta>$ of the nematic director of liquid crystals. In particular, we were able to determine the effect of microchamber dimensions on the preferred orientation.

An important advantage of our technique is that it can be generally applied to confocal microscopy images of any filamentous network, including *in-vitro* cytoskeletal networks but also networks of synthetic fibers like carbon nanotubes (Islam et al., 2004; Puech et al., 2010). Thus, alignment and nematic ordering can be determined without a need for sophisticated techniques such as the PolScope (Gentry et al., 2009; Viamontes and Tang, 2003; Viamontes et al., 2006b) or polarized fluorescence (Coppin and Leavis, 1992), which may be especially difficult to combine with confinement in microchambers. Importantly, the technique is applicable to a broad range of different images, being able to extract orientation information even when the length scales of the filaments or the network mesh size are below the diffraction limit. Our method could be applied also to images of the cytoskeleton in cells. This would for instance be interesting in the context of the orientation distribution of actin filaments in the lamellipodium of migrating cells, which protrude by directed polymerization of a branched actin network (Mogilner and Oster, 2003; Quint and Schwarz, 2011; Schaus et al., 2007; Weichsel and Schwarz, 2010), where our analysis could provide information complementary to more labor-intensive filament reconstruction of electron tomography data (Maly and Borisy, 2001; Urban et al., 2010; Verkhovsky et al., 2003; Weichsel et al., 2012; Yang and Svitkina, 2011).

The effect of a confining boundary on the spatial organization of the actin cytoskeleton of living cells remains an open question. Based on

our *in-vitro* results, we expect the cell boundary to play a significant role. Although cells regulate actin-based structures via specific interactions with accessory proteins, more general physical mechanisms such as the effect of depletion (Marenduzzo et al., 2006) or confinement could assist such organization. Our results demonstrate the need for better physical models that so far cannot account for the effect of spatial confinement on entangled and nematic semiflexible polymer networks. A better theoretical understanding is necessary in determining the extent of physical forces in determining cytoskeletal organization.

3.4 Methods

Protein preparation. Lyophilized monomeric G-actin was purchased from Cytoskeleton (via Tebu-Bio). Resuspended G-actin was stored in G-buffer (2 mM Tris, 0.2 mM sodium adenosine-triphosphate, 0.2 mM calcium chloride, 0.2 mM dithiothreitol, pH 8.0), stored at 0 °C, and used within one week. Actin monomers were labeled with Alexa Fluor 594 (Invitrogen) and mixed with unlabeled monomers to yield a 10% molar ratio of dye to protein. Recombinant mouse fascin was prepared from T7 pGEX *E. coli*, as described elsewhere (Gentry et al., 2012). The fascin plasmid was a kind gift from Scott Hansen and R. Dyche Mullins (UC, San Francisco). Protein concentrations were determined by measuring the solution absorbance at 280 nm with a NanoDrop 2000 (ThermoScientific, Wilmington, DE, USA), using extinction coefficients, in M^{-1} cm^{-1}, of 26600 (actin (Pardee and Spudich, 1982)), and 66280 (fascin, computed from amino acid sequence (Artimo et al., 2012)).

Microchamber preparation. Microchambers were assembled using a standard photolithographic technique. In short, glass cover slips were spin-coated with a layer of photoresist and exposed to UV

light patterned by a customized mask. Before spin-coating, cover slips (thickness #1, Menzel Gläser) were cleaned with base piranha (water, 30% ammonium hydroxide, 30% hydrogen peroxide at a ratio of 5:1:1; 75 °C for 15 min), followed by rinsing with water and baking (200 °C, 5 min). Cover slips were coated (Delta 80 GYRSET, SUSS MicroTec; spin speed 3000 rpm) with a negative photoresist (SU-8 2005, MicroChem). Layer thickness was adjusted by diluting photoresist with cyclopentanone by approximately 10–20% and measured by a profilometer (Alpha-Step 500, KLA-Tencor). Coated cover slips were then baked (95 °C, 5 min) before exposure to ultraviolet light (only wavelengths above 365 nm, BG-12 bandpass filter, Schott) in a mask aligner (MJB, Karl Süss; typical dosage: 50–100 mJ cm^{-2}). Patterning was achieved through custom-designed mask of chromium features printed on soda-lime glass (DeltaMask). Mask design included square and rectangular geometries with various dimensions. Chamber lengths d_y were 3, 5, 10, 15, 20, 30, 50, 70, and 100 μm. For each length d_y, various aspect ratios d_x / d_y were designed, ranging from 1, 1.5, 2, 3, 5, 7, and 10. This results in 56 possible geometries. However, an upper bound of resolution of ~1–3 μm prevents the smallest and thinnest patterns from properly forming. Exposed cover slips were baked (95 °C, 5 min), developed (2-methoxy-1-methylethyl acetate, MicroChem; 1–2 min), rinsed with isopropanol, and ultimately hard-baked (150°C, 2h). This process results in a glass substrate with photoresist microchambers. Next, lids were created by coating microscope slides (Menzel Gläser) with a layer (~1 mm thick) of polydimethylsiloxane rubber (Sylgard 184, Dow Corning; 10:1 base:curing-agent w/w ratio; 120 °C, 5 min). Rubber-coated glass was rendered hydrophilic by corona discharge (BD-20V high-frequency generator, Electro-Technic Products) and soaked overnight in G-buffer + 0.1% amphiphilic block copolymer Pluronic F-127 (Sigma-Aldrich) to block nonspecific adsorption of actin filaments to the surface of the chambers. Saturation of the PDMS with buffer prevented drying of the sample.

Confinement Assay. To polymerize actin filaments, we added a solution containing salts and buffer to a tube containing monomeric G-actin (10% label-to-monomer molar ratio). Samples were mixed to yield a final buffer composition of 20 mM imidazole pH 7.4, 50 mM potassium chloride, 1 mM dithiothreitol, and 0.1 mM adenosine

triphosphate. In addition, 1 mM trolox, 2 mM protocatechuic acid, and 0.1 μM protocatechuate 3,4-dioxygenase were added to minimize photobleaching. Furthermore, actin filaments were stabilized with phalloidin in all cases. Freshly mixed samples were immediately mixed with phalloidin (in an amount equimolar to actin monomers) dried on a patterned glass slide, and pressed against the rubber-coated glass to form closed microchambers. After hermetically sealing glass edges with VALAP (equal parts vaseline, lanolin, and paraffin wax), samples were left to equilibrate for 30 mins and subsequently visualized by fluorescence microscopy. Only chambers that were well-sealed were considered, amounting to approximately 40% of all chambers. Chambers that were not well-sealed were evident by the presence of fluorescently labeled actin between chambers at the interface between patterned glass and rubber lid.

Fluorescence microscopy. Microchambers were visualized with a confocal point scanner (Nikon) on an inverted microscope (Ti, Nikon) with a photomultiplier tube detector (A1, Nikon). Labeled actin filaments were excited with 561 nm laser light (Coherent). Images were acquired over several fields of view which were automatically acquired and stitched (NIS Elements, Nikon). The orientations θ of all image pixels were determined by image analysis with the freely-available plugin OrientationJ (http://bigwww.epfl.ch/demo/orientation/), using a Gaussian window with radius σ = 3 px (see Image Analysis). The orientation distributions serve as input for calculating the order parameter and preferred orientation (see below).

Scalar order parameter. Given a collection of orientation measurements θ of pixels of a chamber in the range [-90°, 90°), we first compute the second-order tensor order-parameter $\mathbf{S}_2$ (Hess and Köhler, 1980):

$$\mathbf{S_2} = \begin{bmatrix} \langle \cos 2\theta \rangle & \langle \sin 2\theta \rangle \\ \langle \sin 2\theta \rangle & -\langle \cos 2\theta \rangle \end{bmatrix}.$$

Angle brackets <·> denote arithmetic means over all measurements. The tensor $\mathbf{S}_2$ is symmetric and traceless. Solving the eigenvalue problem for $\mathbf{S}_2$ yields two eigenvalues

$$\lambda_{\pm} = \pm\sqrt{\langle \cos 2\theta \rangle^2 + \langle \sin 2\theta \rangle^2} = \pm S,$$

which are equal to the scalar order-parameter S. This order parameter quantifies the width of the distribution of orientation measurements. It is zero for a uniform distribution of orientations, and approaches one for a sharply-peaked distribution. The eigenvector $\boldsymbol{\lambda}_+$ corresponding to the eigenvalue λ_+ points in the *preferred orientation*, which we denote by $\langle\theta\rangle_S$ and compute with the following formula:

$$\langle\theta\rangle_S = \arctan\left(\frac{\lambda_{+,x}}{\lambda_{+,y}}\right),$$

where $\lambda_{+,x}$ and $\lambda_{+,y}$ denote the x- and y-components of the eigenvector $\boldsymbol{\lambda}_+$. Angle brackets $\langle\cdot\rangle_S$ do not denote an arithmetic mean, but rather computation of the preferred direction given the tensor S_2. Note that this value does not make any assumptions about the distribution of measured values of θ.

Rectangular symmetry. Square and rectangular chambers exhibit two identical diagonals with angles $\pm\alpha$. This arises from the two-fold symmetry of rectangles. We therefore do not distinguish chambers with preferred orientations $\pm\langle\theta\rangle_S$. In order to account for this symmetry, we multiply all pixel orientation measurements θ of a chamber by a factor of $\mathrm{sgn}(\langle\theta\rangle_S) = \pm 1$. For this reason, the distributions shown in Figure 4 and Figure 9 are unimodal, centered around a positive angle, rather than bimodal. We use the symbol $\mu = \mathrm{abs}(\langle\theta\rangle_S)$ to refer to the preferred orientation of a chamber after accounting for the absolute value. Note that μ only varies in the range (0°, 90°], rather than (-90°, 90°] for $\langle\theta\rangle_S$.

Chamber-ensemble averages. In order to quantify the preferred direction given a chamber geometry, we compute the arithmetic mean of values of μ across identical chambers. Similarly, we quantify the average order parameter of a chamber geometry by computing the arithmetic mean of values of S across identical chambers. We denote these ensemble averages with angle brackets $\langle\cdot\rangle_{\mathrm{chambers}}$.

Number of chambers analyzed. A total of 3075 chambers were analyzed: 1470 nematic chambers, and 1605 bundled chambers (800 fascin, 805 $MgCl_2$). Number of chambers N for aspect ratios d_x / d_y = [1, 1.5, 2, 3, 5, 7, 10] are as follows. Isotropic: $d_y = 5$: [53, 46, 55, 55, 39, 58, 71]. $d_y = 10$: [30, 44, 51, 53, 48, 53, 54]. $d_y = 15$: [47, 45, 45, 43, 37, 48, 39]. $d_y = 20$: [33, 31, 33, 32, 28, 24, 23]. $d_y = 30$: [24, 23, 22, 18, 17, 16, 16]. $d_y = 50$: [15, 15, 16, 14, 3, 11, 1]. $d_y \geq 70$: [9, 9, 8, 7, 5, 2, 1]. Bundled:

d_y = 5: [43, 67, 74, 75, 68, 86, 75]. d_y = 10: [66, 67, 65, 59, 58, 66, 60]. d_y = 15: [50, 47, 45, 43, 38, 43, 37]. d_y = 20: [31, 28, 27, 30, 26, 29, 29]. d_y = 30: [21, 21, 20, 14, 13, 17, 11]. $d_y \geq 50$: [13, 13, 9, 8, 5, 5, 3].

3.5 Image Analysis

The confined actin networks studied so far are homogeneous. These results were all obtained with gel-filtered actin. In earlier experiments in collaboration with Marina Soares e Silva and Jeanette Nguyen, we studied networks of non-gel-filtered actin in microchambers and observed besides alignment also confinement-induced bundling (Soares e Silva, 2011; Soares e Silva et al., 2011a). A typical example is shown in Fig. 12a. Actin filaments prepared from non-gel-filtered actin are shorter than filaments prepared from gel-filtered actin, since gel-filtration removes oligomers, which may act as seeds, and capping proteins. Potentially, depletion attractions promoted by short actin filaments in combination with quasi-2D confinement may bundle the longest filaments in the polydisperse distribution of filament lengths (Soares e Silva, 2011; Soares e Silva et al., 2011a). In addition, gel filtration may remove residual crosslinker proteins such as α-actinin, which may potentially also account for the bundling seen for non-gel-filtered actin. However, we note that bundling was only observed in confinement.

To quantify the degree of filament bundling, we developed an extension of the orientation analysis, which we will outline in this section. We constructed a bundling parameter B, where $B = 0$ corresponds to unbundled networks and $B = 1$ corresponds to purely bundled networks. We also developed a technique for determining the radial distribution of actin filaments in microchambers. These techniques use a combination of MATLAB and ImageJ commands, including the plugin OrientationJ. First, we shall introduce OrientationJ and briefly describe its outputs before describing our analysis techniques.

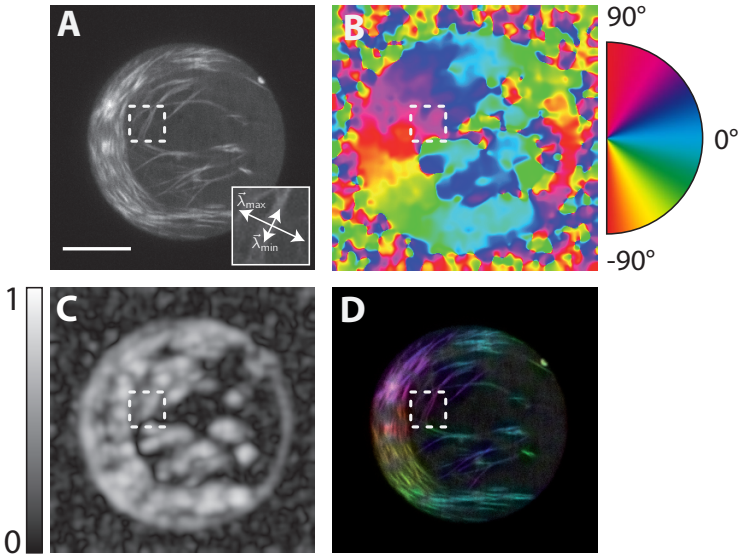

Figure 12. OrientationJ. **a**: Example input image $I(x,y)$ of a fluorescently labeled actin network confined to a circular microchamber, [actin] = 5 mg mL^{-1}, [gelsolin] / [actin] = $^{1}/_{370}$, chamber diameter = 40 µm and depth = 5 µm. Scale bar 10 µm. Inset: Close-up of dashed box, with the eigenvectors $\boldsymbol{\lambda}_{\mathbf{min}}$ and $\boldsymbol{\lambda}_{\mathbf{max}}$ of the center pixel's structure tensor **J**. Note that $\boldsymbol{\lambda}_{\mathbf{min}}$ points in the direction of the bundle. **b**: Orientation $\theta(x,y)$ of panel a. Pixel hues correspond to θ according to the legend (right). Dashed box denotes same area as in panel a. Note that it encloses magenta pixels, which correspond to approximately 60°. **c**: Coherency $c(x,y)$ of panel a. Pixel intensities correspond to c according to the calibration bar, left. Dashed box same as panel a. Note that it encloses higher coherency values than the low-coherency, isotropic region right. **d**: Color survey of panel a. Dashed box same as panel a. Note that hue matches that of panel b and grey (low-saturation) values match locally isotropic areas.

OrientationJ. This plugin was written by Daniel Sage at the Biomedical Imaging Group, EPFL, Switzerland and originally designed to quantify the orientation of elastin (Fonck et al., 2009) and collagen (Rezakhaniha et al., 2012) fibers. OrientationJ quantifies the anisotropy of features found in an image of pixel intensities $I(x,y)$ (Fig. 12a). Among

its several outputs, we use the coherency $c(x,y)$ and orientation $\theta(x,y)$ for our analysis. These quantities derive from the structure tensor $\mathbf{J}(x,y)$, defined by the spatial gradients of $I(x,y)$:

$$\mathbf{J}(x,y) = \begin{bmatrix} \int_{\mathrm{ROI}} dx\, dy\, \nabla_x I(x,y) \cdot \nabla_x I(x,y) & \int_{\mathrm{ROI}} dx\, dy\, \nabla_x I(x,y) \cdot \nabla_y I(x,y) \\ \int_{\mathrm{ROI}} dx\, dy\, \nabla_x I(x,y) \cdot \nabla_y I(x,y) & \int_{\mathrm{ROI}} dx\, dy\, \nabla_y I(x,y) \cdot \nabla_y I(x,y) \end{bmatrix}.$$

The region of interest (ROI) around each pixel (x,y) is a Gaussian window with a user-defined width σ. This is the only freely-variable input parameter, which should match the desired feature size.

Diagonalizing the structure tensor $\mathbf{J}$ yields two eigenvalues λ_{min} and λ_{max} whose eigenvectors $\boldsymbol{\lambda}_{\mathbf{min}}$ and $\boldsymbol{\lambda}_{\mathbf{max}}$ point in the direction of the minimum and maximum changes in pixel intensity, respectively (Fig. 12a, inset). The dominant orientation θ of a region is given by the direction of $\boldsymbol{\lambda}_{\mathbf{min}}$ (Fig. 12b). The relative difference between λ_{min} and λ_{max}, called the coherency c, serves as a measure of a region's anisotropy (Fig. 12c):

$$c = \frac{\lambda_{\mathrm{max}} - \lambda_{\mathrm{min}}}{\lambda_{\mathrm{max}} + \lambda_{\mathrm{min}}}.$$

We rely on the coherency to quantify the presence of bundles. OrientationJ furthermore produces a so-called "color survey" (Fig. 12d): an RGB image where the orientation $\theta(x,y)$ determines its hue, the coherency $c(x,y)$ determines its saturation, and the original image $I(x,y)$ determines its brightness.

Bundle Parameter. Fluorescence microscopy is well suited to detect the presence of bundles in a labeled filamentous network. Bundles are detectable because (i) they are brighter than the surrounding unbundled network, owing to the spatial condensation of filaments and (ii) they are long and thin, owing to the linear structure of the component filaments. In order to automatically detect the presence of bundles in an image, we developed an algorithm based on these two properties. For a pixel to belong to a bundle, we require that (i) it is brighter than background pixels and (ii) neighboring pixels' intensities vary slowly along the direction of the bundle but quickly in the orthogonal direction. Standard thresholds satisfy requirement (i), and the coherency output from OrientationJ satisfies requirement (ii). We combine these methods in a six-step process (Fig. 13) comprising ImageJ and MATLAB scripts. By processing images of many different chambers, we produce an

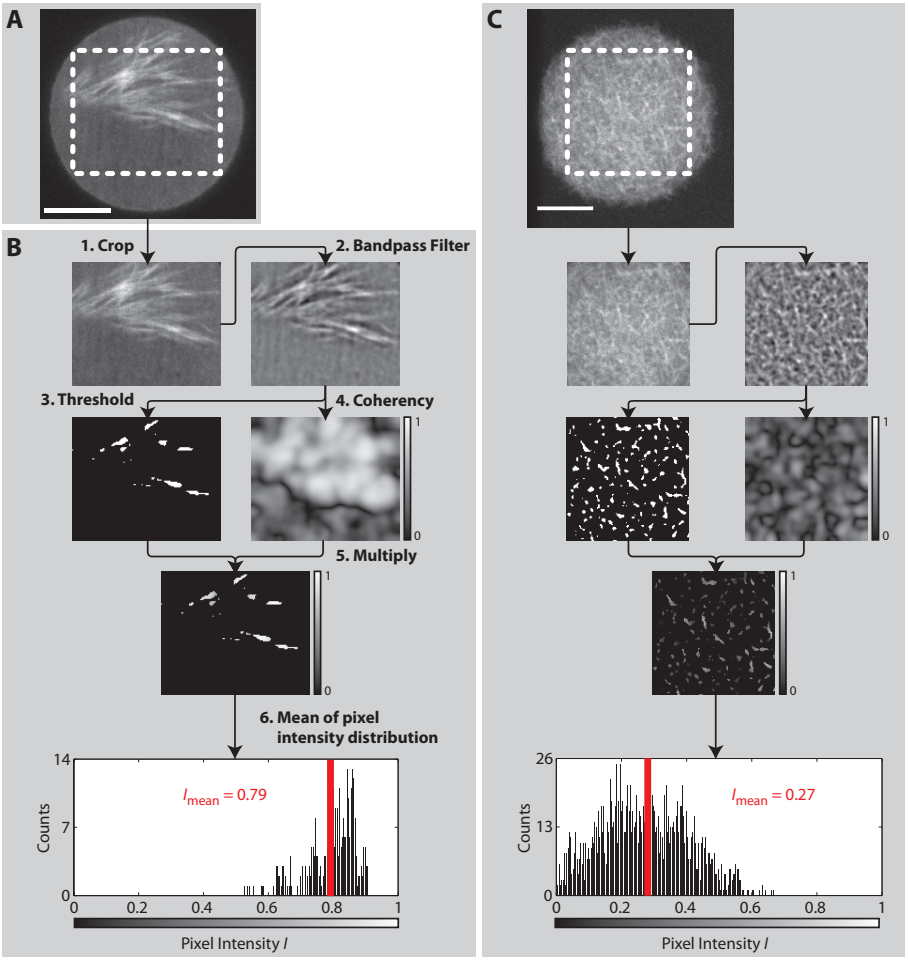

Figure 13. Bundle parameter. **a**: Example input image, [actin] = 5 mg mL^{-1}, [gelsolin] / [actin] = $^{1}/_{370}$, chamber diameter = 30 μm, chamber depth = 5 μm. Scale bar 10 μm. **b**: Six-step algorithm for processing images. **Step 1**: crop to the largest rectangle fitting the chamber (panel a, dashed box). **Step 2**: bandpass filter. **Step 3**: threshold with Kapur's method. **Step 4**: coherency of cropped image from Step 1. Pixel intensities vary with calibration bar, left. **Step 5**: multiply images from Steps 3 & 4. Pixel intensities vary with calibration bar, left. **Step 6**: mean of intensity distribution of nonzero pixels from Step 5. Red bar denotes mean intensity, which determines the bundle parameter *B*. For the image in panel a, the bundle parameter is 0.79. Calibration bar, below, corresponds to Step 5. **c**: Determining the bundle parameter for

ensemble-averaged bundle parameter *B* for every chamber geometry and biochemical condition investigated.

Briefly, we threshold images to find the brightest pixels, and use this to mask the coherency image. Bright pixels in this masked image satisfy both requirements for bundling. We now present each step, followed by a discussion of the parameter choices.

Step 1: Crop. We manually crop each image (Fig. 13a) to the largest rectangle fitting inside the chamber (Fig. 13b.1). This step avoids artifactual coherencies arising at the chamber edges (cf. Fig. 12c).

Step 2: Bandpass Filter. We apply the ImageJ "FFT Bandpass Filter" routine (Fig. 13b.2). This step introduces two freely variable parameters that determine which spatial frequencies to preserve. We choose to remove features below 2px (camera noise) and above 30px (uneven illumination, blooming). Because bundles are typically ~5px thick, their structure is preserved in the filter. The choice of 30px is discussed below.

Step 3: Threshold. We apply Kapur's threshold method (Fig. 13b.3), known in ImageJ as "Maximum Entropy", discussed below.

Step 4: Coherency. We apply OrientationJ to the cropped image from the first step and extract the coherency image (Fig. 13b.4). This step introduces another variable input parameter which determines the width of the ROI around each pixel. We choose the typical bundle thickness of 5px for this value.

Step 5: Multiply. We multiply the images from the second and fourth steps, effectively masking the coherency image with the thresholded image (Fig. 13b.5).

Step 6: Average. We calculate the mean pixel intensity, averaged over nonzero pixels (Fig. 13b.6). This mean defines the bundle parameter *B*.

If we eliminate the high-pass cutoff of 30 px in step 2 or make it too high, the resulting thresholds become inaccurate, passing more

---

a chamber lacking bundles. [actin] = 1 mg mL^{-1}. Note that the bundle parameter decreases to 0.27 due to the lack of bundles in the original image.

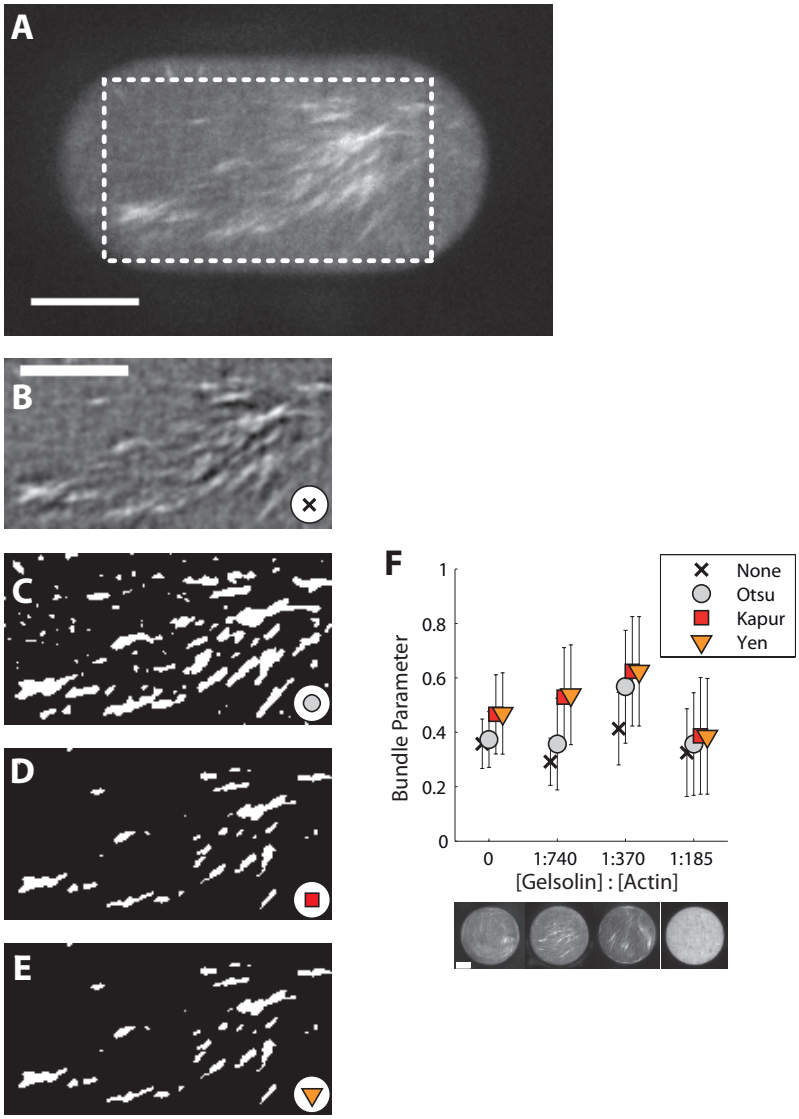

Figure 14. Dependence of the bundle parameter on threshold. **a**: A sample input image, [actin] = 5 mg mL^{-1}, [gelsolin] / [actin] = $^{1}/_{740}$, pill-shaped chamber with *xy*-dimensions = 60 µm x 30 µm and depth = 5 µm. **b**: Cropped version of panel a along dashed box. **c**-**e**: Threshold of panel b after bandpass filter, according to the method of Otsu (c), Kapur (d), and Yen (e). **f**: Dependence of threshold on bundle parameter for four conditions of constant actin concentration (5 mg mL^{-1}) and of increasing

background pixels next to regions with many bundles that appear brighter due to blooming. Setting the high-pass cutoff too low results in thresholds that may more closely resemble bundles, but include too many dark pixels of the original image, contrary to requirement (i). The choice of 30px represents a trade-off between these two limits, though this value does not significantly affect the bundle parameter.

The threshold in the third step has no variable input parameters, but the choice in algorithm requires discussion. Figure 14a,b show an extreme example of a chamber where the bundle parameter is very sensitive to the choice in threshold algorithm. In this image, the boundary between bundle and background is unclear. Here, a permissive threshold allows more low-coherency background pixels to pass (Fig. 14c). A more restrictive threshold allows only the brightest pixels to pass (Fig. 14d,e), producing a more accurate mask in accordance with requirement (i).

By comparing different threshold methods on different types of images, we found that Otsu's method, a widely-used threshold algorithm, is fairly permissive and allows many background pixels to pass (Fig. 14c). More recent methods based on information theory seem to more accurately separate bundles from their background. Kapur's method (Fig. 14d), known as "Maximum Entropy" in ImageJ, maximizes the combined entropy of the pixel intensity distributions of the foreground and background, defined as (Kapur et al., 1985)

$$S = -\sum_{I=0}^{1} p(I) \log_2 p(I)$$

---

gelsolin concentration. Black crosses denote no threshold, gray circles Otsu's method, red squares Kapur's method, yellow triangles Yen's method. Error bars indicate standard deviations of ensemble averages over N = 177, 43, 70, and 48 chambers for [gelsolin] / [actin] = 0, $1/740$, $1/370$, and $1/185$, respectively. **Below**: unprocessed representative images of each condition. Every chamber has diameter = 40 μm and depth = 5 μm. Scale bar 10 μm.

Yen's method (Fig. 14e) minimizes a cost function that considers the discrepancy between thresholded and original images along with the number of bits needed to represent the original image (Yen et al., 1995).

Fig. 14f shows how these thresholding algorithms affect the bundle parameter. In the absence of a threshold (black crosses), the bundle parameter does not change with gelsolin concentration, even though bundles are clearly visible in the original images (Fig. 14f, below). Otsu's method (gray circles) yields an increase in the bundle parameter but, because it averages over more background pixels and hence over more low-coherency pixels, yields a lower bundle parameter than Kapur's (red squares) and Yen's (yellow triangles) methods, especially for [gelsolin] : [actin] = 1:740, which produce more accurate thresholds.

The need for an accurate threshold reflects a conscious design principle behind the bundle parameter: we consider only the coherency of pixels that pass the threshold, but do not normalize against chamber volume. Rather than characterizing volume fractions of bundles, we only seek to quantify the degree of bundling, reflected in requirements (i) and (ii) given above.

Edge Accumulation. Besides bundling, we also observed inhomogeneous distributions of non-gel-filtered actin in microchambers. Prior studies of actin networks in spherical confinement (vesicles and emulsion droplets) showed that actin filaments tend to adopt a peripheral localization in order to minimize filament bending. To test whether such edge accumulation also occurs in microchambers, we developed an image analysis routine to quantify the dependence of fluorescence intensity in each chamber as a function of the radial distance from the chamber center. To this end, we developed a five-step process comprising a MATLAB script (the "onion peel" algorithm).

Briefly, we threshold the complete image of a chamber to find its boundary and then "peel" away layers from this threshold. Pixels of the same peel are equidistant from the chamber boundary/center. We then separate the original image into a series of peels and plot the mean intensity of each peel against the distance from the chamber center. We now present each step in more detail:

Step 1: Median filter. We median filter the original image (Fig. 15a) with a circular kernel of radius 10px (Fig. 15b.i). We choose

this filter because it smoothes the image but preserves edges. This is necessary to accurately detect chamber boundaries.

Step 2: Threshold. We apply Otsu's threshold method, which in this case accurately captures chamber boundaries (Fig. 15b.ii). Kapur's and Yen's methods (Fig. 15b.iii and iv, respectively), being more restrictive as discussed previously, capture details inside the chamber but not its boundary. Applying Otsu's method to the original image, without median-filtering, also results in an inaccurate threshold (Fig. 15b.v).

Step 3: "Peel-the-onion: loop". We erode the threshold by one pixel and subtract the result to recover a ring of pixels corresponding to the chamber's boundary (Fig. 15b.vi, "onion skin"). We loop this process, where each iteration j yields a series of images (Fig. 15b.vii,viii, "peels") and continues until the final iteration which corresponds to the center of the chamber (Fig. 15b.ix, "onion core"). Eroding this image would yield a dark image with no white pixels. We furthermore convert loop iteration j into a unitless distance from boundary by dividing j by the total number of iterations j_{tot} (58 total iterations for Fig. 15). Transforming by $x \rightarrow 1\text{-}x$ yields a unitless distance from center r / r_c, where r is a distance, normalized by the chamber's "radius" r_c. Note that r and r_c correspond to real radii for circular chambers, though for pill-shaped chambers, r corresponds to a minimum distance from the "onion core" (Fig. 15b.ix).

Step 4: Multiply. We multiply each peel with the original image. This yields a series of images (Fig. 15b.x-xiii) which chop the original image into component peels. Because each pixel corresponds to one and only one onion peel, the original image is faithfully decomposed according to equivalence classes based on distance from boundary.

Step 5. Mean. We compute the mean I of the intensity distribution of every peel (Fig. 15b.xiv-xvii), averaged over nonzero pixels, as in Fig. 15b.1. Because most peels comprise hundreds of pixels (see caption, Fig. 15b.xiv-xvii), we do not require spatial filtering to become insensitive to camera noise. However, because inner peels comprise fewer pixels, noise increases as r approaches 0.

We furthermore compute the chamber median I_m, defined as the median of the product image between the original image (Fig. 15a) and the threshold (Fig. 15b,ii), and normalize I by I_m. We choose to normalize against the median as opposed to the mean because of a

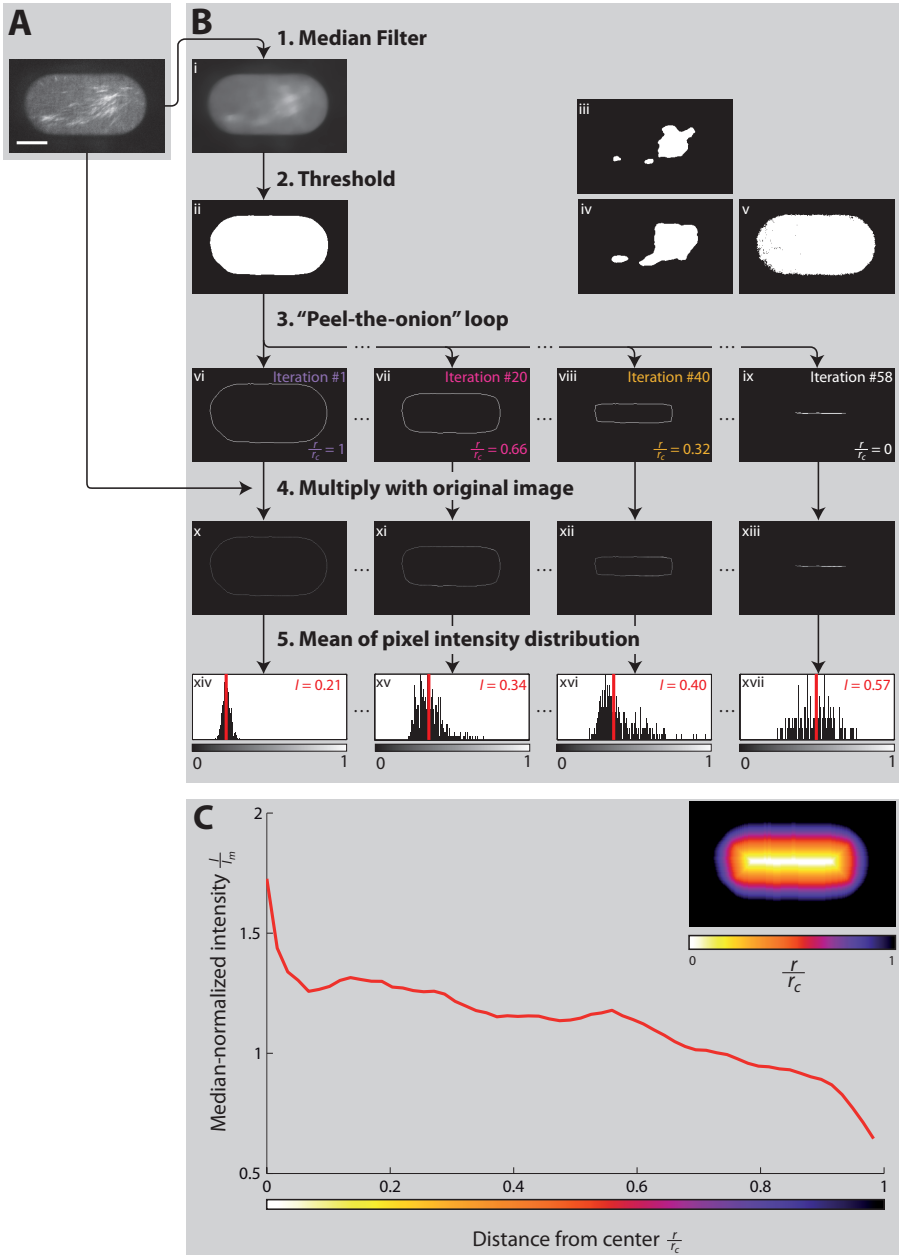

Figure 15. Edge accumulation analysis ("onion peel algorithm"). **a**: Example input image, [actin] = 5 mg mL^{-1}, [gelsolin] / [actin] = $^{1}/_{740}$, pull-shaped chamber with *xy*-dimensions = 60 µm x 30 µm and depth = 5 µm. Scale bar 10 µm. **b**: Five-step algorithm for processing images. **i**: Step

systematic decrease in intensity as r / r_c approaches 1. This decrease corresponds to a diffuse, diffraction-limited boundary between chamber and background. The median is insensitive to this systematic decrease. We then plot I / I_m as a function of r / r_c, yielding the desired fluorescence intensity as a function of distance from center (Fig. 15c). In the example shown, there is no obvious radial dependence of the fluorescence intensity.

Acknowledgements

A part of this work was performed in collaboration with Marina Soares e Silva, Jeanette Nguyen, Nefeli Georgoulia, and Bela Mulder. We thank them for insightful discussions. We furthermore thank Dimitry Lamers, Andries Lof, Gijs Vollenbroek, and Chris Rétif for assistance with

---

1: median filter. **ii-iv**: Step 2: threshold with the method of Otsu (ii), Kapur (iii), and Yen (iv). **v**: Otsu threshold of the original image (panel a). **vi-ix**: Step 3: "onion peels" corresponding to loop iteration j=1 (vi, "onion skin"), 20 (vii), 40 (viii), and 58 (ix, "onion core"). **x-xiii**: Step 4: multiply with original image (panel a). **xiv-xvii**: Step 5: normalized intensity distribution of nonzero pixels of (x-xiii). x-axes denote pixel intensity. Calibration bars correspond to (x-xiii). Ordinates denote normalized frequency with maximum frequencies 44, 17 , 12, and 6 (xiv-xvii, respectively). Red bars denote mean intensity I, ensemble-averaged over total number of pixels 551, 467, 356, 162 (xiv-xvii, respectively). **c**: Plot of I / I_m versus r / r_c. Calibration bar at x-axis roughly corresponds to label color in (b.vi-ix). Sampling frequency of x-axis is 58^{-1} = 0.017. Inset: combining all 58 images from step 3 and shading according to iteration j yields a level set. Pixel color map corresponds to calibration bar, below, and to x-axis in main panel.

microfabrication and electron microscopy. We thank Marjolein-Kuit Vinkenoog for assistance with purifications. We thank Scott Hansen and Dyche Mullins (UC San Francisco) for providing us with fascin plasmid. The OrientationJ plugin was written by Daniel Sage (EPFL, Lausanne).

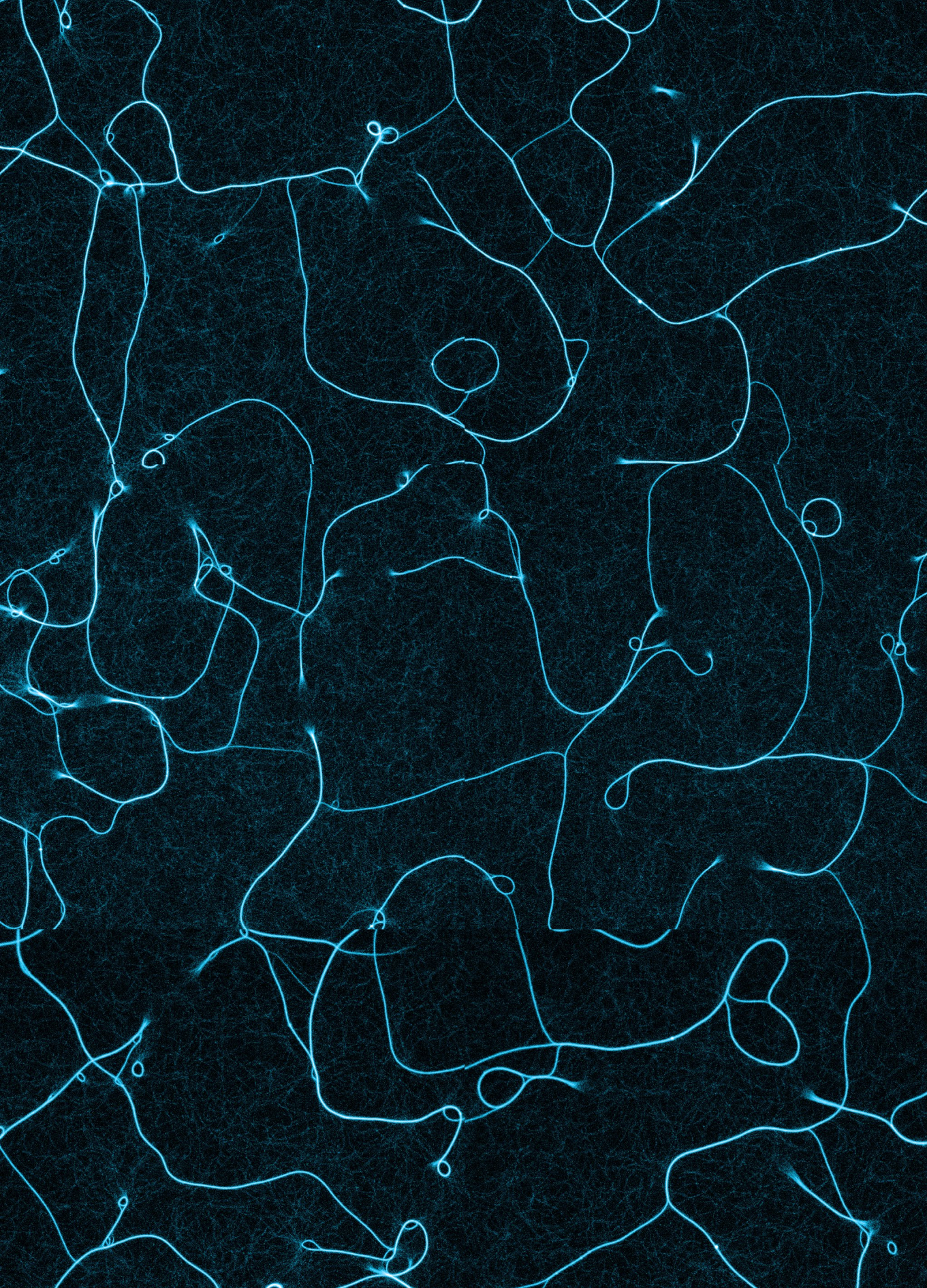

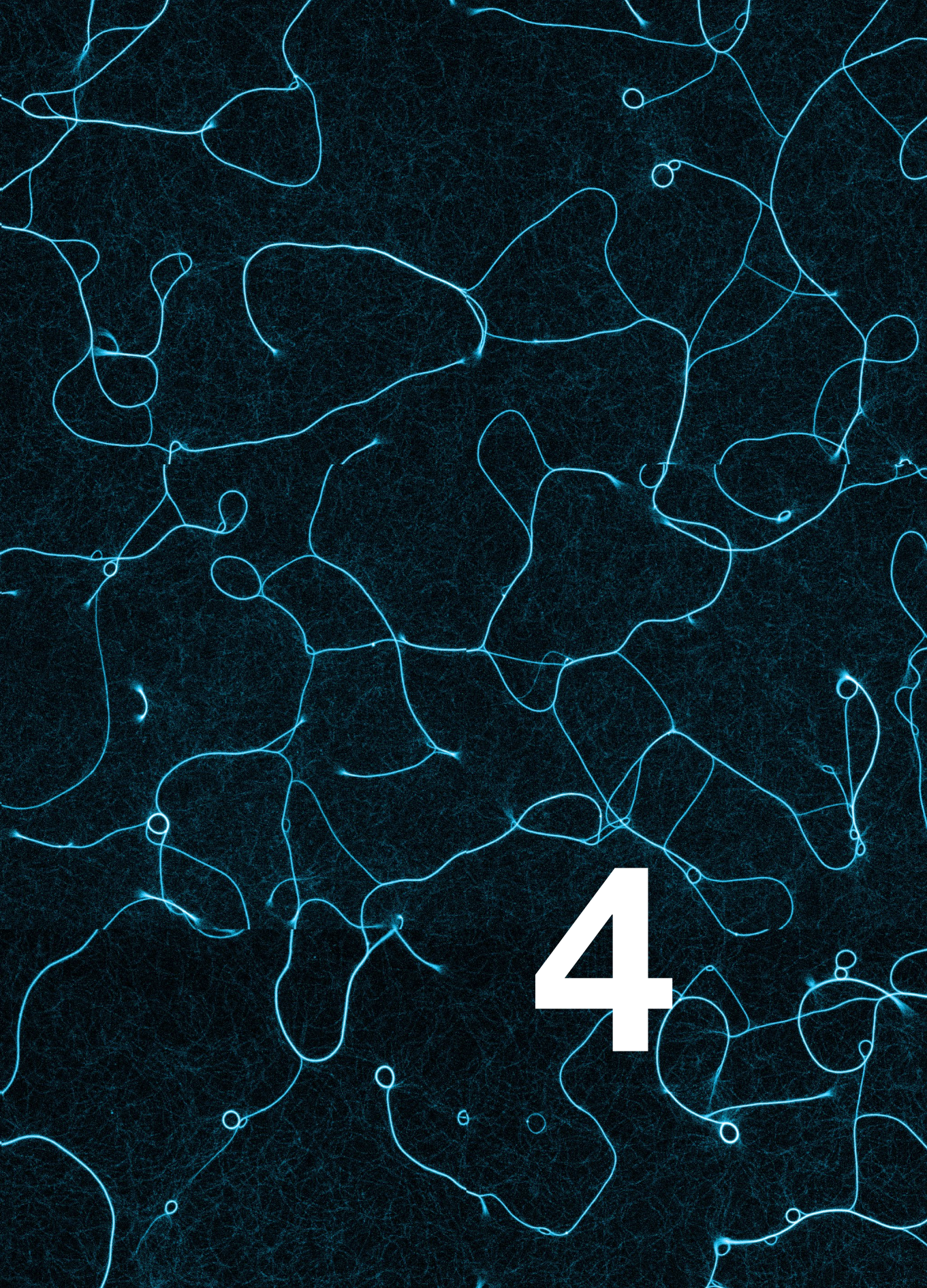
4

4. Septins bundle and curve actin filaments

Actin filaments and myosin motors form a contractile ring during cytokinesis, which physically divides the cytoplasm of mitotic cells into two daughter cells. Despite the essential role played by actin and myosin in this process, the molecular mechanisms that determine their organization into a contractile ring remain poorly understood. Here we investigate the actin-organizing capabilities of septins, a conserved and essential component of the cytokinetic ring. A close interplay between septins and the actin cytoskeleton has been previously suggested, but the nature of this interaction has remained unclear. In order to investigate this interaction, we performed fluorescence microscopy experiments on an *in-vitro* model system of actin filaments crosslinked by fly or human septin hexamers. We find that septins directly bind and bundle actin filaments. Surprisingly, we also find rings of actin bundles. We implement a novel image analysis algorithm to analyze in detail the curvature of these rings and correlate this to actin bundle thickness and septin binding. We find the same bundling and curving activity for fly and human septins, suggesting a conserved function. Our observations demonstrate that septins alone are sufficient for actin ring formation, which may explain recent *in-vivo* experiments showing that septins are necessary for proper contractile ring formation in *Drosophila* embryos undergoing cellularization.

4.1 Introduction

Multicellular organisms typically grow by increasing cell number rather than cell size. To establish this kind of growth, cells can divide into two daughter cells in a process called cytokinesis (Alberts, 2008). During cytokinesis, a contractile ring forms at the cell equator, which constricts the plasma membrane and ultimately divides the cytoplasm. Despite the fundamental importance of cytokinesis in cell proliferation, tissue growth, and differentiation, the mechanisms that allow the contractile ring to constrict the membrane remain poorly understood (Eggert et al., 2006). A core set of approximately 20 conserved proteins is known to be needed for cytokinesis, yet their functions in enabling constriction remain unclear (Glotzer, 2005).

Septins are among the set of conserved core proteins that are necessary for cytokinesis. Septins were originally identified as genes that control cytokinesis in the budding yeast *Saccharomyces cerevisiae* (Hartwell, 1971), where septins form a ring of filaments at the bud neck (Byers, 1976) and compartmentalize the plasma membrane by acting as diffusion barriers (Dobbelaere and Barral, 2004; Takizawa et al., 2000). Later, septins were also found to localize at the contractile ring in higher eukaryotes (Kinoshita and Noda, 2001). Perturbations in septin expression are known to lead to defects in cytokinesis, which result in aneuploidy and various pathological disorders (Hall and Russell, 2004; Lacroix and Maddox, 2011). Yet although septins are known to play an essential role in cell division, a molecular understanding of how septins contribute to the organization of the contractile ring remains elusive.

Septins are evolutionarily conserved across a wide variety of species from yeast to humans (Nishihama et al., 2011; Pan et al., 2007). Septin isoforms share several conserved domains: a polybasic domain that binds phospholipids on the plasma membrane, a GTP-binding domain, an evolutionarily conserved domain of unknown function called the septin unique element (Mostowy and Cossart, 2012) (Fig. 1a). Additional, less conserved domains also occur. Near the N-terminus, some septin isoforms exhibit proline-rich stretches. Near the C-terminus, many septin isoforms exhibit coiled-coil domains. Many different septin genes and splice variants are known to exist. The number of septin isoforms

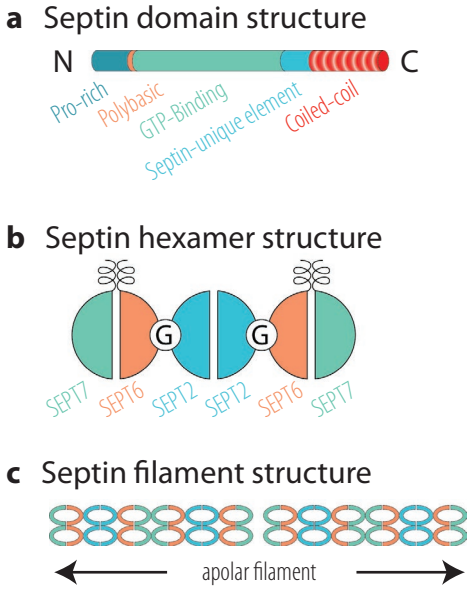

Figure 1. Schematic of septin architecture. **a**. Domain structure of septin proteins. **b**. Human septin hexamer structure. Color denotes septin isoform. Labels refer to nomenclature from human septins. Black spirals represent coiled-coil domains. Circles labeled "G" denote GTPase domains located at the interface between septin subunits. **c**. Septin filament structure, which is axially apolar but has a top-down asymmetry with membrane-binding domains on one side and coiled-coil domains on the other side.

per organism depends on species: the green alga *Chlamydomonas reinhardtii* encodes 1 septin, *Caenorhabditis elegans* and *Xenopus laevis* have 2 septins each, *Drosophila melanogaster* has 5, *Saccharomyces cerevisiae* has 7 septins and *Homo sapiens* has 13 (Beise and Trimble, 2011; Weirich et al., 2008). Animal septin genes can be classified into four groups—commonly denoted as 2, 3, 6, and 7—based on sequence homology (Nishihama et al., 2011; Pan et al., 2007). Endogenous septins commonly exist as hetero-oligomeric complexes comprising different septins. Human septins assemble in hexamers of groups 7-6-2-2-6-7, or in octamers which also include septins from group 3 (Sellin et al., 2011) (Fig. 1b). Hexamer formation is mediated by the GTP-binding domain

and the N- and C-terminal regions between monomers (Sirajuddin et al., 2007). Septin hexamers can further assemble end-to-end into filaments, which are symmetric along the filament axis (Bertin et al., 2008; Sirajuddin et al., 2007) (Fig. 1c). Septin filaments, in turn, can further associate to form higher-order structures, such as laterally-associated bundles which are likely mediated by interactions between coiled-coil domains (Bertin et al., 2008). Septin bundles can form ring-like assemblies or flat, gauze-like structures (Bertin et al., 2010; Garcia et al., 2011). Given that septins readily assemble to form a rich variety of filamentous structures, septins are gaining recognition as a component of the cytoskeleton distinct from actin filaments, microtubules, and intermediate filaments (Mostowy and Cossart, 2012).

Previous studies have established a number of interactions between septins and various molecular partners. Septins bind cell membranes through specific recognition of acidic phospholipids (Bertin et al., 2010; Casamayor and Snyder, 2003; Tanaka-Takiguchi et al., 2009; Zhang et al., 1999) and stiffen the plasma membrane to facilitate bleb retraction in T-cells (Gilden et al., 2012; Tooley et al., 2009). Septins have also been shown to significantly contribute to the cortical rigidity of interphase human carcinoma cells (Mostowy et al., 2011). Septins furthermore bind the actin-binding protein anillin (D'Avino et al., 2008; Field, 2005; Kinoshita et al., 2002; Oegema et al., 2000; Silverman-Gavrila et al., 2008) as well as non-muscle myosin II motors (Joo et al., 2007; Mostowy et al., 2010). Septins have also been shown to regulate the contractility of the actomyosin ring during cytokinesis in developing *Drosophila* epithelia (Founounou et al., 2013; Guillot and Lecuit, 2013). A close interplay between septins, the plasma membrane, and the actomyosin network is likely essential for many cortical biological processes including cytokinesis (Gilden and Krummel, 2010). But understanding how these interactions allow septins to organize the contractile ring remains elusive.

In this chapter, we present results that show that *Drosophila* and human septins alone are sufficient to organize actin filaments into bundles and bundle rings, which may be necessary for proper contractile ring assembly. In Section 2, we briefly introduce *in-vivo* experiments, performed by Manos Mavrakis, which demonstrate that septins are necessary for proper actomyosin ring formation in *Drosophila* embryos

undergoing cellularization, a process driven by constriction of an actomyosin ring in a process resembling cytokinesis. In Section 3, we report fluorescence microscopy experiments on an *in-vitro* model system of actin filaments crosslinked by *Drosophila* septin hexamers. We find that septins directly bind and bundle actin filaments. Surprisingly, we also find rings of actin bundles, which have a characteristic radius of curvature of ~1 μm. This observation shows that septins are sufficient for proper actin bundle and bundle ring formation. We find the same bundling and curving activity for human septin hexamers, suggesting a conserved function. We implement a novel image analysis algorithm to analyze the curvature of actin rings and bundles and correlate this to actin bundle thickness and septin binding. In Section 4, we discuss the mechanisms that may be responsible for the ability of septins to readily form curved bundles and rings. This property makes septins unique among the actin-binding proteins currently known.

4.2 Motivation

In order to investigate the role of septins in organizing the actin cytoskeleton, we consider *Drosophila melanogaster* (fruit fly) embryos undergoing cellularization. We briefly introduce the main findings of experiments performed by our collaborator Manos Mavrakis (CNRS/ Aix-Marseille U) that elucidate the physiological role of septins, which have been found necessary to organize the actomyosin contractile ring during cellularization.

At 2h 10min after fertilization, *Drosophila* embryos undergo a process called *cellularization* (Fig. 2a). During this phase of development, the syncytial embryo, which consists of a single cell (~500 μm in length) with thousands of nuclei, undergoes a drastic morphogenetic change. The plasma membrane invaginates to separate each nucleus and eventually form a closed epithelium of individual cells in roughly two steps. During the first step a membrane front called the furrow canal

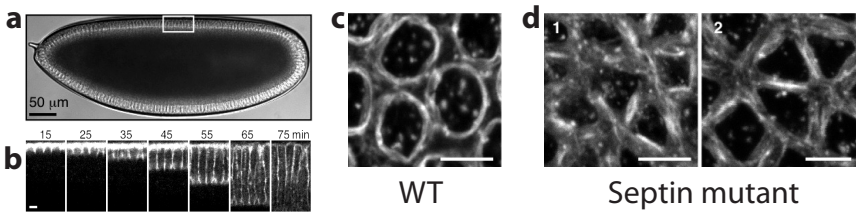

Figure 2. *Drosophila* embryos lacking septins fail to form circular contractile rings. **a**. A wild-type embryo during cellularization. Scale bar 50 µm. **b**. Closeup of a, acquired by two-photon fluorescence microscopy. Fluorescence signal corresponds to the location of myosin at the membrane front, which migrates away from the apical surface. **c**. Top view of actin signal at the membrane front during the slow phase. Actin forms uniform rings. **d**. Top view of actin signal at the membrane front during the slow phase for embryos lacking septins. Note that actin filaments arrange in linear bundles which form disconnected polygonal arrays. Scale bars 5 µm.

invaginates from the apical side (Fig. 2b). During invagination, proteins at the furrow canal assemble into circular contractile rings (Fig. 2c). In the second step, the contractile rings constrict (from a diameter of ca. 5 µm to 2 µm) to form thousands of distinct, polarized epithelial cells. The constriction of the furrow canal is reminiscent of cytokinesis (Lecuit, 2004). The contractile ring at the furrow canal contains actin filaments, non-muscle myosin-II motors, anillin, and septins (Pnut/hSep7, DSep1, and DSep2). This cytoskeletal structure is thought to stabilize the tips of invaginating membranes and drive constriction (Field, 2005).

When septins are absent, cellularization and the associated cytoskeletal structures are markedly changed, as demonstrated by live cell imaging of fly knock-out mutants lacking Pnut/hSep7 and DSep1. During the first step of cellularization, the membrane front invaginated more slowly and accumulated less myosin and actin compared to wild type embryos (data not shown). During the second step, the furrow canal failed to form circular rings. Rather, actin accumulated in linear structures along polygonal segments (Fig. 2d). Polygon vertices were largely devoid of actin. Myosin foci were unevenly distributed in polygonal arrays (data not shown). Furrow canals showed defects in

constriction: some constricted poorly, some constricted prematurely, and some constricted normally.

During both invagination and constriction, anillin was present at the furrow canal, consistent with previous findings (Adam et al., 2000). In septin knock-outs, anillin co-localized with actin and myosin at polygonal arrays. This result suggests that anillin is not necessary to form ring-like structures. Indeed, anillin point mutations that interfere with septin binding to the furrow canal result in the same phenotypes as observed for the septin knock-outs (Field, 2005). Together, this evidence shows that septins are necessary for the proper assembly of the contractile ring during cellularization in *Drosophila* embryos. Furthermore, this evidence suggests that septins directly interact with the actin cytoskeleton.

However, septins are commonly believed to not interact directly with actin. A previous *in-vitro* study showed that human septins (Sep2-Sep6-Sep7 hexamers) do not interact directly with actin filaments, but instead interact indirectly through the protein anillin (Kinoshita et al., 2002). Yet this study is difficult to reconcile with growing *in-vivo* evidence suggesting a strong interplay between septins and the actin cytoskeleton. Septins decorate interphase stress fibers (Surka et al., 2002), and septin-depleted fibroblasts lack stress fibers (Kinoshita et al., 2002). Septin depletion in human carcinoma cells decreases cortical stiffness in a manner consistent with actin disruption (Mostowy et al., 2011). Since anillin is sequestered within the nucleus during interphase (Field and Alberts, 1995; Oegema et al., 2000), this stiffness modulation is independent of anillin. We therefore set out to test whether septins and actin can directly interact by systematically combining purified proteins at a range of different protein concentrations.

4.3 Results

In order to investigate whether septins can organize the cytoskeleton into higher-order structures, we perform experiments with a minimal *in-vitro* model system of fluorescently labeled, reconstituted proteins imaged by TIRF microscopy (see Methods). We polymerize purified rabbit skeletal muscle actin at low concentration (1 μM), where filaments are largely non-overlapping, in the presence of recombinant *Drosophila melanogaster* (fly) septin complexes (DSep1-DSep2-Pnut).

Morphology of septin-actin structures. Polymerizing actin filaments in the presence of septin hexamers yields a variety of bundled structures, as depicted in Figure 3. The septin concentration sensitively determines bundle morphology. For low concentrations of septins (up to 0.02 μM), we find single actin filaments that do not appear to interact. Increasing the septin concentration to 0.05 μM results in long, thick bundles. Bundles also exhibit a frayed brush of single actin filaments, both at bundle ends as well as along the bundle contour (see insets, black arrows). Single filaments are visible adjacent to these bundles. Increasing the septin concentration further to 0.1 μM again results in long, thick bundles. These bundles interconnect to form a sparse bundle network. Bundles sometimes form curved, looped structures. Increasing the septin concentration to 0.2 or 0.3 μM results in a drastic change: rather than straight bundles, actin filaments form highly curved structures. The most common structures found are closed rings. Straight bundles also occur. Rather than a frayed brush, bundle ends often exhibit lasso shapes. Further increasing the septin concentration to 0.5 and 1 μM similarly results in closed rings, but with a lower probability. Straight bundles and lassos occur more commonly than rings. Further increasing the septin concentration to 2 and 3.8 μM results in fewer rings and lassos, and a prevalence of thick, straight bundles. Strikingly, bundles exhibit sharp kinks and zigzags. These results show that bundle morphology is sensitively controlled by septin concentration.

In order to determine septin localization on actin structures, we polymerize actin filaments in the presence of fluorescently labeled Alexa-Fluor-488 fly septins. Figure 4 shows that fluorescently labeled septins are also capable of promoting the formation of actin filament rings,

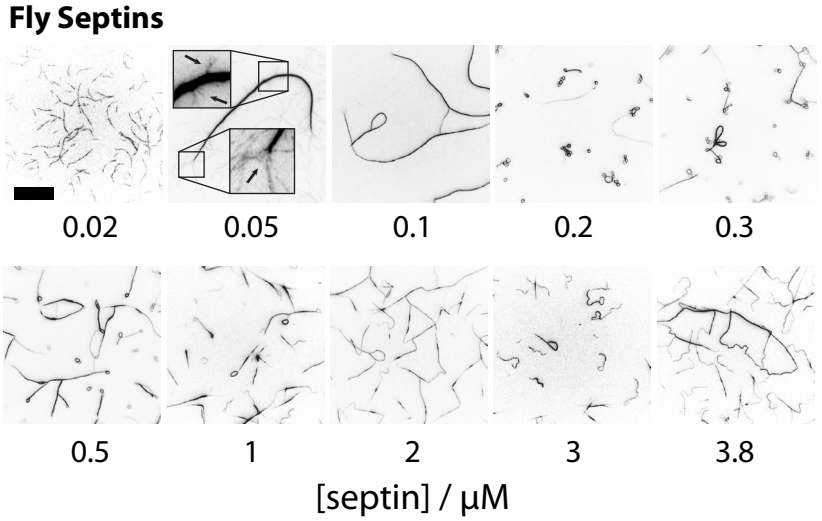

Figure 3. Dependence of F-actin bundle morphology on fly septin concentration. Snapshots are represented with an inverted lookup table. [actin] = 1 μM. Scale bar 20 μm.

consistent with the activity of unlabeled septins. For low concentrations (0.1 μM), bright septin puncta decorate long actin bundles. Increasing the septin concentration to 0.2 μM produces actin rings with septins still binding often as isolated puncta, though septins can also accumulate along the entire circumference of some rings. Increasing septins to 0.5 μM yields rings as well as linear bundles. The strongest septin signals occur on thick, straight segments, indicating strong bundling.

So far we have shown that *Drosophila* septins organize actin filaments into straight and curved bundle structures. In order to test if this ability is not restricted to a single set of species-specific septins, we repeat the above assays with recombinant human septins. Polymerizing actin filaments in the presence of human septin hexamers (hSep2-hSep6-hSep7) indeed yields similar behavior to fly septins (Fig. 5). Single actin filaments prevail up to 0.02 μM; thick bundles prevail at 0.05 μM; thick bundles and occasional rings prevail at 0.1 μM; loops and lassos prevail at 0.2, 0.3, and 0.5 μM; and finally straight and kinked bundles prevail at 1 μM and above. The morphologies of bundles formed with human septins do differ slightly from those of the fly-septin structures.

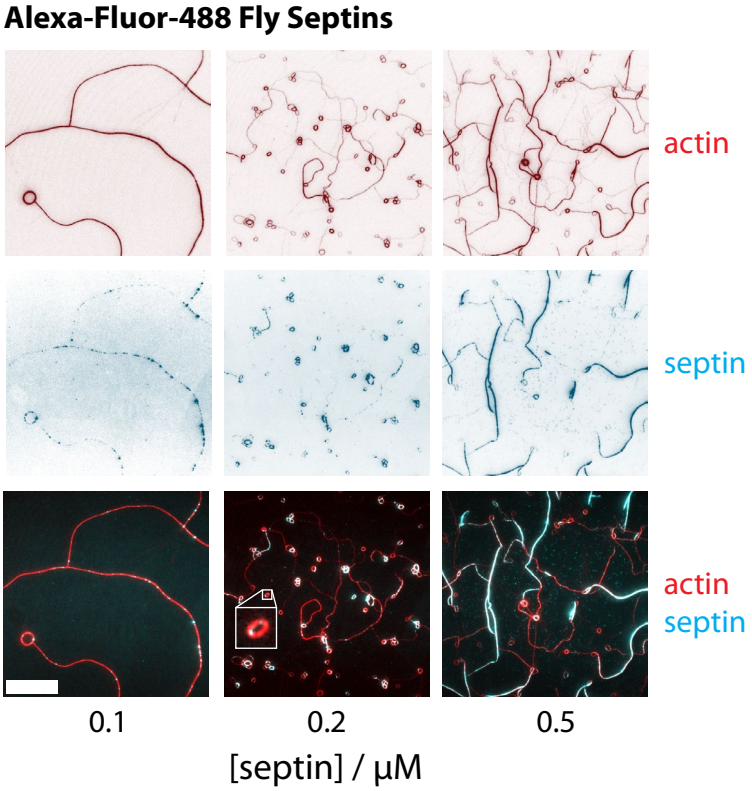

Figure 4. Localization of fly septins on F-actin bundles for different septin concentrations. **Top row**: snapshots of fluorescently labeled actin filaments, represented with an inverted lookup table. **Middle row**. snapshots of fluorescently labeled septins, represented with an inverted lookup table. **Bottom row**. merge of images from top and middle rows. Actin is shown in red, and septins are shown in cyan, both with linear lookup tables. [actin] = 1 μM. Scale bar 20 μm.

In particular, closed rings appear less frequently at 0.2–0.3 μM, though lassos remain common. Yet the concentrations of human septins that determine the onset of these different bundle morphologies agree well with fly septins. These results show that human septins organize actin similarly to fly septins, suggesting that the actin-organizing capabilities of septin complexes are evolutionarily conserved.

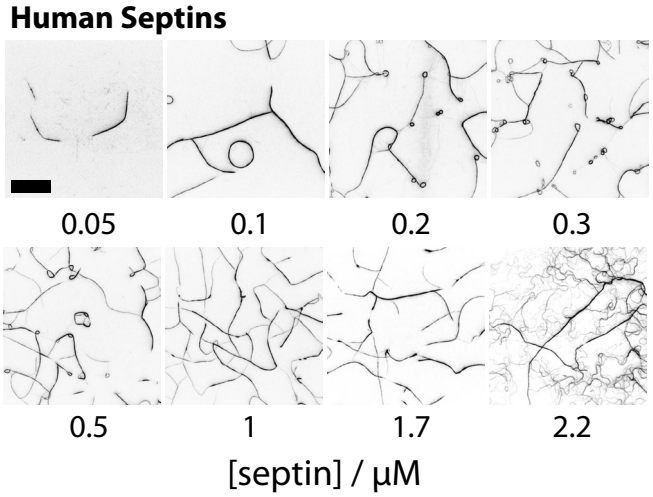

Figure 5. Dependence of F-actin bundle morphology on human septin concentration. Snapshots are represented with an inverted lookup table. [actin] = 1 μM. Scale bar 20 μm.

Curving actin bundles into rings and lassos entails a high energy penalty associated with bending of the semiflexible actin filaments. Bundle curvature should reflect a balance between adhesion energy provided by septins and bending energy associated with the actin filaments (Cēbers et al., 2006; Tang et al., 2001). To test this hypothesis, we repeated the TIRF experiments in the presence of the actin-binding drug phalloidin, which increases the persistence length of actin filaments from 9 to 18 μm (Isambert et al., 1995). Qualitatively, we find similar phase behavior of bundling for both fly septins (Fig. 6) and human septins (Fig. 7). However, the range of septin concentrations where rings and lassos form narrows slightly: for fly septins the concentration range is 0.2–1 μM with phalloidin versus 0.1–3 μM without phalloidin, and for human septins the concentration range is 0.3–0.5 μM with phalloidin versus 0.1–0.5 μM without phalloidin. Thus, loops and lassos appear qualitatively less frequently when phalloidin is present. This is particularly apparent at 0.2–0.5 μM, where long, straight bundles prevail instead of rings and lassos. These results indicate that phalloidin-induced filament stiffening partially inhibits ring and lasso formation.

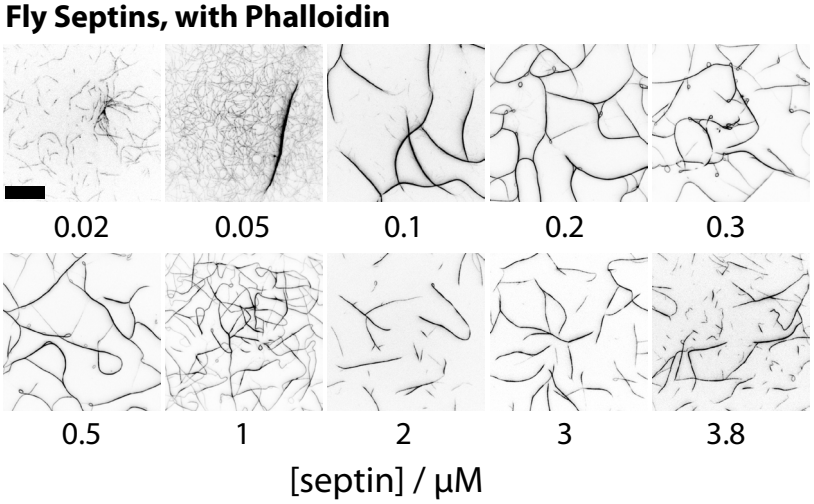

Figure 6. Effect of phalloidin on fly-septin-mediated F-actin bundling. Snapshots are represented with an inverted lookup table. [actin] = 1 µM, [phalloidin] = 1 µM. Scale bar 20 µm.

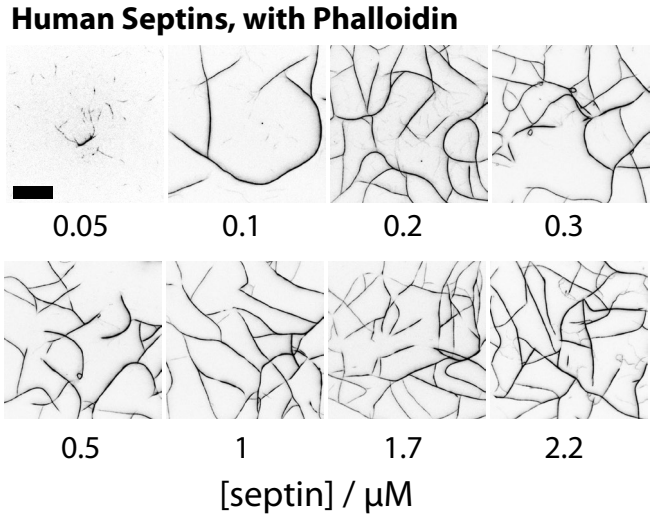

Figure 7. Effect of phalloidin on human-septin-mediated F-actin bundling. Snapshots are represented with an inverted lookup table. [actin] = 1 µM, [phalloidin] = 1 µM. Scale bar 20 µm.

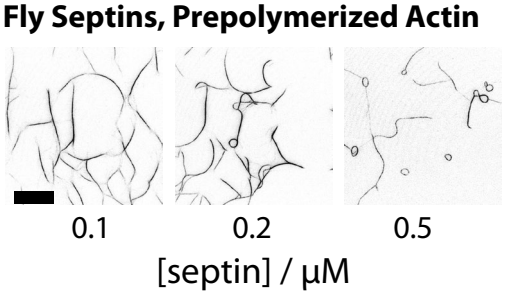

Figure 8. Effect of pre-polymerized actin filaments on fly-septin-mediated bundling. Snapshots are represented with an inverted lookup table. [actin] = 1 μM. Scale bar 20 μm.

So far we have presented results of actin filaments that co-polymerize in the presence of septins. For co-polymerization experiments, the morphology of bundled structures may strongly depend on the kinetics of actin filament assembly (Falzone et al., 2012). In some cases, kinetic trapping has been shown to induce residual stresses evident from increased bundle curvature (Schmoller et al., 2008). In order to determine the effect of assembly kinetics on septin-mediated actin bundle formation, we perform two experiments. First, we pre-polymerize actin in the absence of septins, and then add septins (Fig. 8). For 0.1 μM septins, straight or curved bundles prevail. Rings and lassos only occur after increasing the septin concentration to 0.2 and 0.5 μM. Rings and lassos do occur less frequently compared to co-polymerization experiments. However, their appearance depends on septin concentration in a manner consistent with co-polymerization experiments. This result indicates that kinetic effects alone cannot fully account for ring and lasso formation. Second, we ablate septin bundles using a pulsed infrared laser (see Methods). By recording images of septin bundles before and after ablation, we can determine whether relaxation occurred. Many ablation experiments appear to result in no relaxation (Fig. 9a, top row), likely because illumination caused photobleaching but not severing. However, we were able to clearly identify seven severing and relaxation events (Fig. 9a, bottom row;

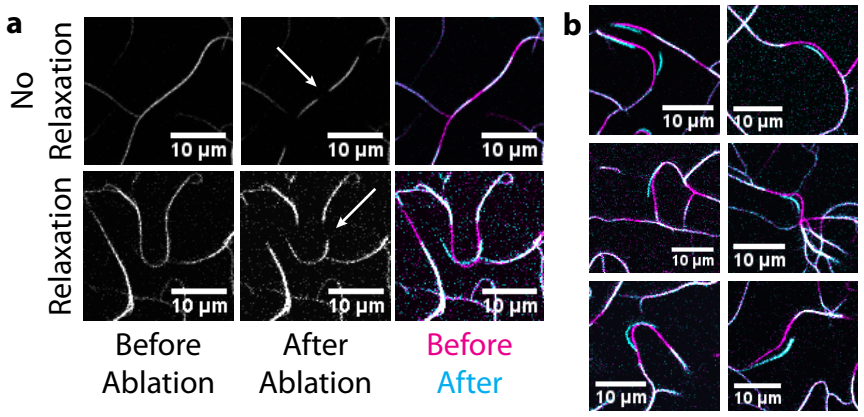

Figure 9. Cutting actin-fly septin bundles by localized laser ablation results in relaxation of bundle shape. [actin] = 1 μM, [septin] = 0.5 μM. Snapshots are represented with a linear lookup table. a. **Left column**. Snapshot of fluorescently labeled actin bundles before ablation. **Middle column**. After ablation. **Right column**. Merge of before (magenta) and after (cyan) images. **Top row**. Attempted laser ablation does not result in a significant reorganization of bundles, probably because bundles are not successfully severed. **Bottom row**. Bundles clearly relax after a successful laser ablation attempt. Arrows indicate location of ablation attempt. **b**. Merged snapshots of six successful ablation attempts. Scale bars 10 μm.

Fig. 9b). In these events, bundles became slightly straighter, indicating relaxation of internal stresses likely caused by kinetic effects.

Quantification of bundle curvature. The TIRF images shown so far present qualitative evidence that actin-septin bundles can exhibit a wide range of curved morphologies. In order to quantify these morphologies, we developed an algorithm to measure the curvature $C(s)$ of a point s on a bundle (see Image Analysis). Higher values of $C(s)$ denote regions that are more highly curved. Because samples yield a variety of different structures, here we restrict our analysis to over 4000 manually identified rings and lassos (see Methods). Figure 10a depicts representative examples of rings and lassos of various sizes, as well as the measured curvature along bundle contours. We represent an individual ring or lasso by the distribution of measurements $C(s)$ over

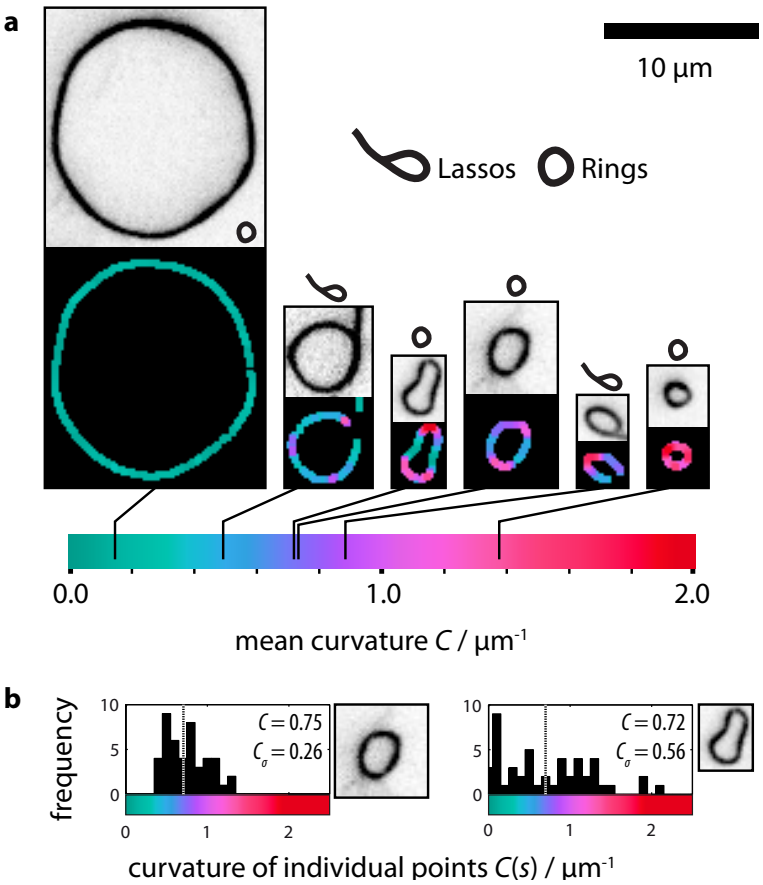

Figure 10. Representative images of manually selected rings and lassos, together with their measured curvatures. **a**. **Top**. Snapshots of fluorescently labeled actin filaments bundled by fly septins. **Bottom**. Result of curvature algorithm. Pixel color corresponds to the local curvature (calibration bar, below). Note that color changes from blue-green to red at positions along the bundle contour which are more highly curved. Actual features in curvature images are 1-px-thick. A maximum filter (1 px radius) was applied to make features thicker and more readily visible. Black lines pointing to calibration bar represent mean curvature, averaged over all pixels in the curvature image. **b**. Histogram of curvature measurements for the two loops pictured. Distribution is represented by the mean C (dashed black line) and standard deviation C_σ. Note that the kinked ring (right) exhibits a wider distribution of curvatures than the convex ring (left). [actin] = 1 µM.

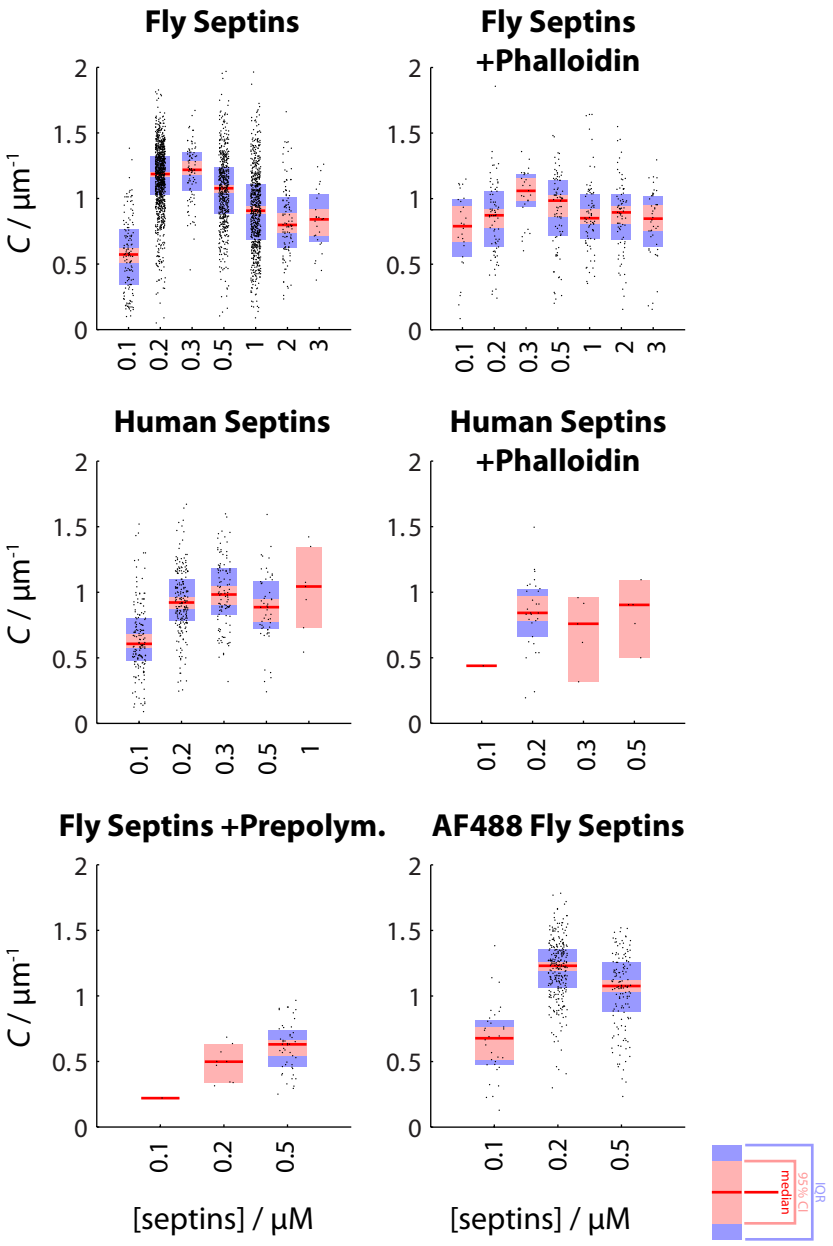

Figure 11. Effect of septin concentration on the curvature of rings and lassos for the different conditions as denoted in the graph titles. Box plots depict the distribution of mean curvatures *C*. Blue boxes denote interquartile ranges (IQR). Pink boxes denote 95% confidence intervals

all points s along its contour, and extract the mean curvature C and the standard deviation C_σ (Fig. 10b). Rings and loops can be approximated by a circle with radius $r_C = C^{-1}$. The value C_σ measures the deviation from a perfectly circular shape: circular rings yield relatively low values (Fig. 10b, left), while kinked and irregularly-shaped rings yield higher values (Fig. 10b, right).

We now quantify the effect of septin concentration on the curvature C. For example, Figure 11 represents the curvature C of individual loops and lassos, separated across different sample conditions. We characterize distributions with their medians (red lines), 95% confidence intervals (pink bars), and interquartile ranges (blue bars). We find that the septin concentration strongly affects curvature of rings and loops, C being always roughly maximized in the range of 0.2–0.5 μM septin. Lower and higher concentrations of septins tend to result in lower curvatures. However, the absolute value of C in this septin concentration range is dependent on the sample conditions. For fly septins, we find median values of curvature C / μm^{-1} = [1.19, 1.22, 1.08] for [0.2, 0.3, 0.5] μM septins, respectively. These values decrease by a factor of 1.1–1.4× to [0.87, 1.06, 0.98] μm^{-1} in the presence of phalloidin. For human septins, the values of C are lower than for fly septins: In the absence of phalloidin, C / μm^{-1} = [0.92, 0.98, 0.88] for [0.2, 0.3, 0.5] μM septins, respectively. Adding phalloidin further decreases curvature by a factor of 1.0–1.3× to C / μm^{-1} = [0.84, 0.75, 0.90]. For pre-polymerization experiments, we observe drastically smaller median curvature values, where C / μm^{-1} = [0.50, 0.63] for [0.2, 0.5] μM septins, respectively.

(CI), computed using the bootstrap method (see Methods). Red lines denote sample medians. Two datasets are statistically significantly different from each other ($p \lesssim 0.01$) if their CIs do not overlap. Number N of data points (each representing an individual ring or lasso) for the different distributions, from left to right: Fly Septins: 134, 1042, 88, 570, 717, 108, 27. Fly Septins +Phalloidin: 26, 78, 27, 85, 75, 77, 44. Human Septins: 156, 198, 108, 53, 7. Human Septins +Phalloidin: 1, 30, 5, 5. Fly Septins +Pre-polymerization: 1, 9, 47. Alexa-Fluor-488 Fly Septins: 32, 273, 139. [actin] = 1 μM.

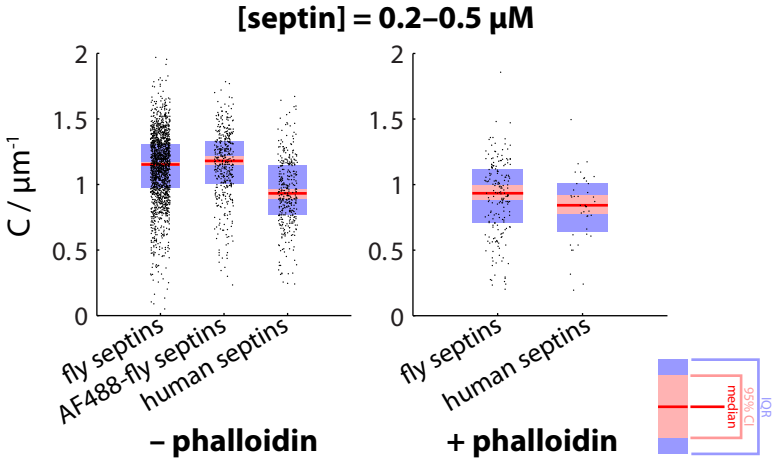

Figure 12. Effect of septin type as well as phalloidin on the curvature of rings and lassos in samples prepared at septin concentrations between 0.2 and 0.5 µM. Box plots depict the distribution of mean curvatures *C*, as in Figure 11. Number *N* of data points for the different distributions, from left to right: 1700, 412, 359; 190, 40. [actin] = 1 µM.

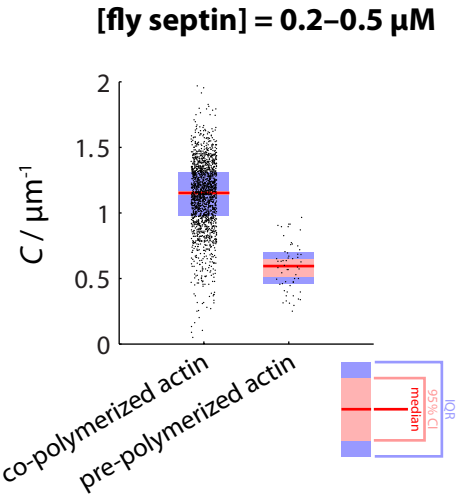

Figure 13. Effect of pre-polymerized actin on the curvature of rings and lassos for samples prepared at fly-septin concentrations between 0.2 and 0.5 µM in the absence of phalloidin. Box plots depict the distribution of mean curvatures *C*, as in Figure 11. Number *N* of data points for the different distributions, from left to right: 1700, 56. [actin] = 1 µM.

However, Alexa-Fluor-488-labeled fly septins show strikingly similar maximum values of C as unlabeled fly septins: [1.23, 1.08] μm^{-1} for [0.2, 0.5] μM septins, respectively.

In order to directly compare how different sample conditions affect the curvature C, we now restrict our attention to samples prepared with septin concentrations in the range 0.2–0.5 μM. Figure 12, left panel shows that fly septins yield significantly higher C than human septins (C / μm^{-1} = 1.15 vs. 0.93), while fluorescently labeled fly septins yield curvatures that are comparable to unlabeled fly septins (C / μm^{-1} = 1.18 vs. 1.15). This result indicates that labeling by Alexa-Fluor-488 does not interfere with ring formation. Meanwhile, the right panel shows that phalloidin reduces curvature of rings and lassos for both fly and human septins by factors of 1.2 and 1.1x to C / μm^{-1} = 0.93 and 0.84. This decrease of curvature indicates that phalloidin-treated actin filaments incur a higher energetic penalty due to bending. Figure 13 shows that curvature is drastically reduced by a factor of 1.9x in pre-polymerization experiments compared to co-polymerization assays (C / μm^{-1} = 0.59 vs. 1.15). This result indicates that assembly kinetics play a non-negligible role in filament formation. In Figure 14, we separately show the curvature of rings and lassos, for the pooled data (left panel) and separated by sample conditions (right panels). Lassos have lower curvatures than rings when pooling all data (C / μm^{-1} = 1.19 vs. 1.00), as well as individually for most sample conditions. These lower average curvatures stem from the mostly straight segments close to the lasso neck.

We hypothesized that bundle curvature arises from a balance between septin binding and actin-filament bending. So far, we have tested this hypothesis by varying actin filament stiffness with phalloidin. But in addition, we can estimate the number of bound septin hexamers per ring by averaging the fluorescence intensity of Alexa-Fluor-488 septins along bundle contours (see Methods). Figure 15 (left panel) shows the distributions of mean septin fluorescence on rings and lassos (pooled) as a function of the septin concentration. The fluorescence intensity of bound septins does not depend significantly on the concentration of septins in solution. Despite a five-fold increase in total septin concentration in solution, rings and lassos appear to exhibit roughly the same number of bound septins. Furthermore, rings that have more

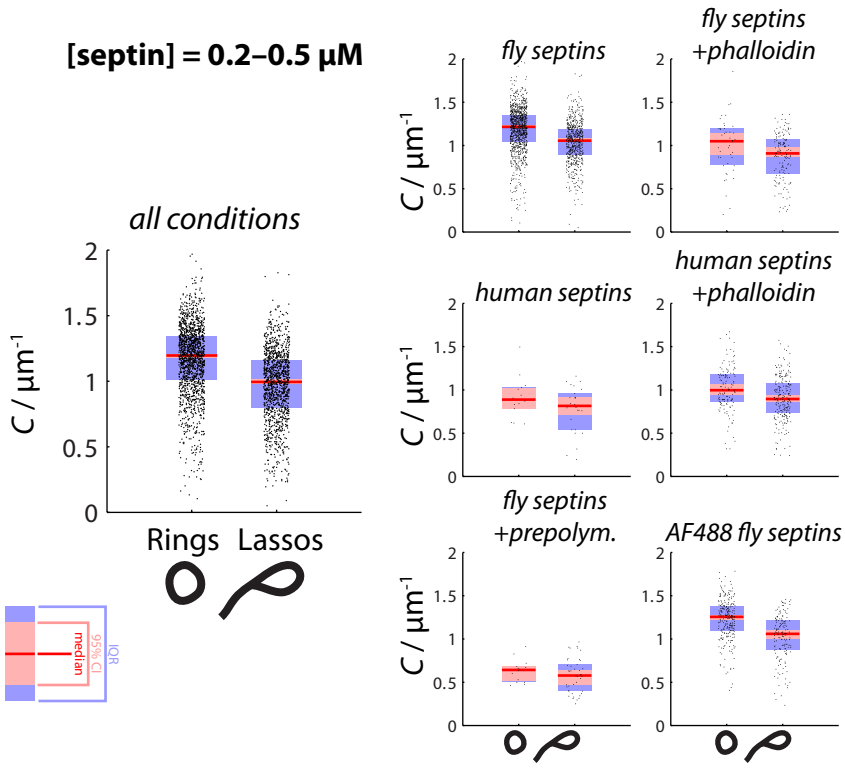

Figure 14. Differences between rings and lassos in samples prepared at septin concentrations between 0.2 and 0.5 µM, across all conditions (left panel) and broken down by condition (right panels). Box plots depict the distribution of mean curvatures *C*, as in Figure 11. Number *N* of data points for the different distributions, from left to right: All conditions: 1526, 1231. Fly septins: 1062, 638. Fly septins +phalloidin: 43, 147. Human septins: 133, 226. Human septins +phalloidin: 14, 26. Fly septins +pre-polymerization: 14, 42. Alexa-Fluor-488 fly septins: 260, 152. [actin] = 1 µM.

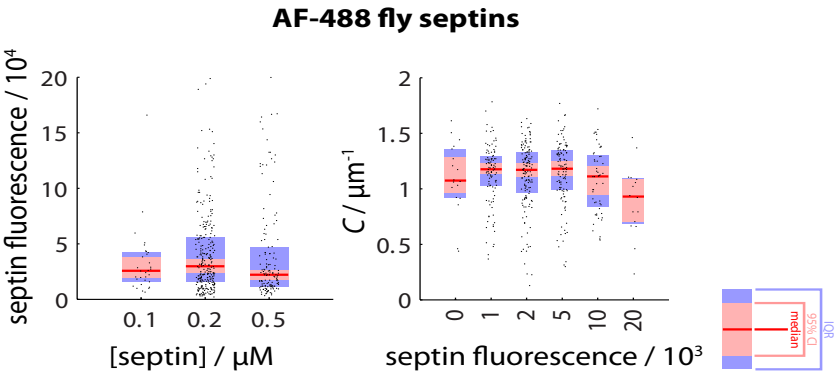

Figure 15. Rings and lassos with more septins exhibit lower curvatures. **Left**. Mean fluorescence intensity of Alexa-Fluor-488-labeled septins in rings and lassos. **Right**. Mean curvature *C* as a function of mean septin fluorescence. Mean septin fluorescence was assigned to different bins (0, 1, 2, 5, 10, or 20) by linear interpolation. Septin fluorescence is given in units of 10^4 pixel intensity values. Box plots as in Figure 11. Number *N* of data points for the different distributions, from left to right: 32, 273, 139; 18, 102 144, 112, 52, 16. [actin] = 1 µM.

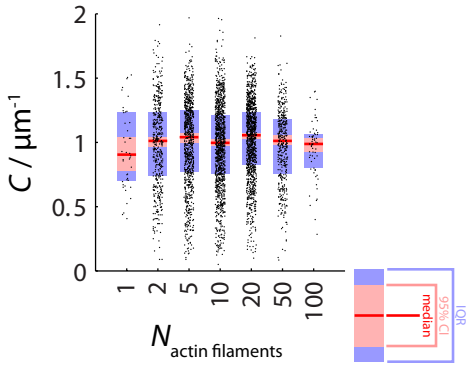

Figure 16. Curvature remains roughly constant over two orders of magnitude in actin fluorescence intensity. Mean curvature *C* as a function of the mean number of actin filaments in rings and lassos, determined by actin fluorescence signal (see Methods). Mean actin filament number was assigned to different bins (1, 2, 5, 10, 20, 50, or 100) by linear interpolation. Box plots as in Figure 11. Number *N* of data points for the different distributions, from left to right: 44, 457, 851, 1146, 1161, 414, 62. [actin] = 1 µM.

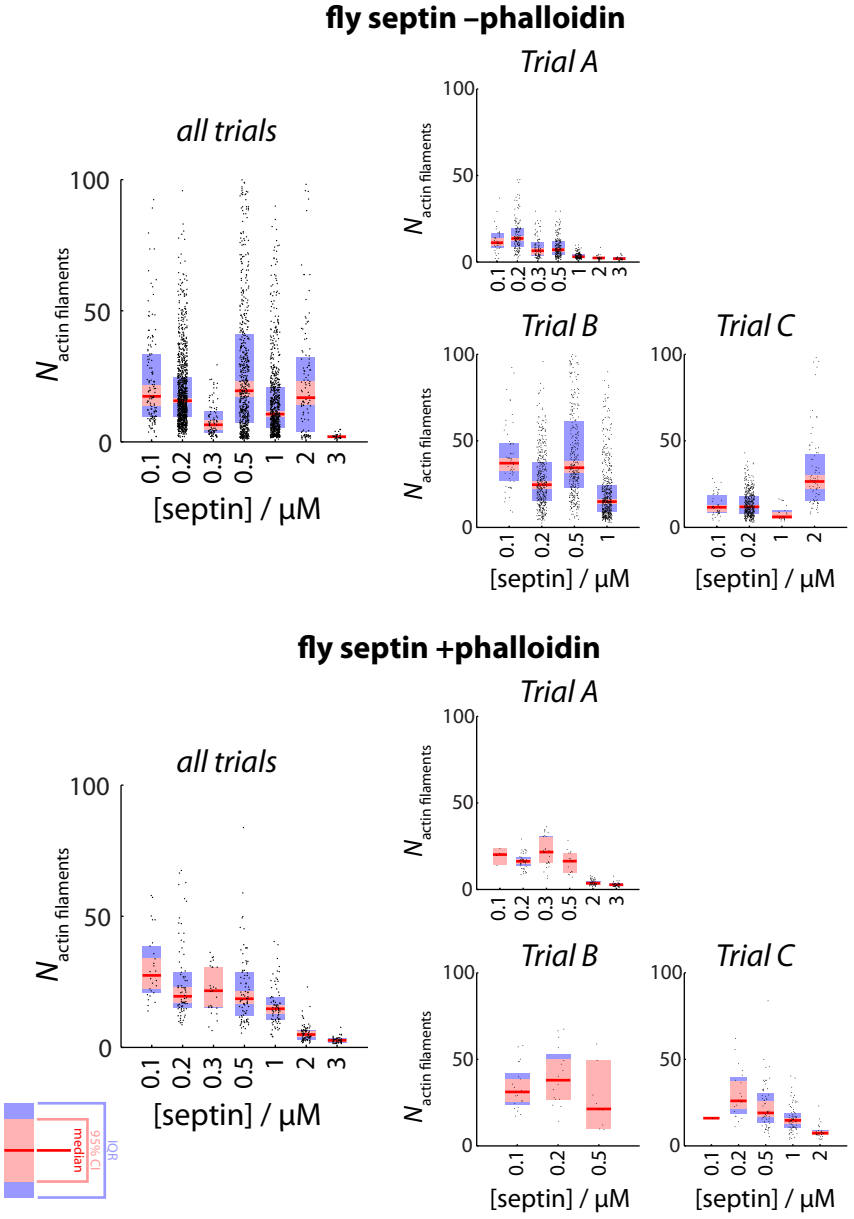

Figure 17. Number of actin filaments in rings and lassos depends strongly on experimental trial. **Top row**. Number of actin filaments plotted against the concentration of fly septin in the absence of phalloidin. **Bottom row**. In the presence of phalloidin. **Left panels**. Pooled data across all experimental trials. **Right panels**. Data broken

bound septins tend to exhibit slightly *lower* curvatures (Fig. 15, right). This result is surprising. According to our hypothesis, we should expect *higher* curvatures.

In order to further investigate the interplay between septin binding and filament bending, we estimate the number of actin filaments in rings and lassos by averaging the actin fluorescence intensity along bundle contours (see Methods). Across all samples, curvature does not depend significantly on the number of actin filaments per ring or lasso (Fig. 16, pooled data). This result indicates that bundle curvature remains constant for bundles of varying thickness. However, the number of actin filaments in a ring or lasso does depend on septin concentration. Surprisingly, at higher septin concentrations, rings and lassos contain fewer actin filaments. This trend is not always visible when plotting all experimental trials together (Fig. 17, left panels). But comparing data within individual trials shows that the number of actin filaments tends to decrease for septin concentrations at or above 1 μM (right panels of Fig. 17). Indeed, the number of actin filaments between trials can vary considerably (Fig. 18, left column). Meanwhile, curvature does not vary among different trials as strongly (Fig. 18, right column). The large variation of the number of actin filaments between samples could indicate sensitivity to kinetic effects. However, the number of actin filaments in a ring or lasso does not appear to significantly affect bundle curvature.

We found kinked bundles and zigzags at higher septin concentrations (cf. Figs 3, 5–7). In order to quantify this finding, we plot the standard deviation of curvatures C_σ, normalized by curvature C, as a function of septin concentration (Fig. 19). This dimensionless quantity attains maximal values for septin concentrations above 1 μM, both

---

down by experimental trial. Box plots as in Figure 11. Number N of data points for the different distributions, from left to right: Top row: All trials: 135, 1051, 88, 617 717, 108, 27. Trial A: 33, 142, 88, 200, 151, 32, 27. Trial B: 54, 422, 370, 544. Trial C: 47, 478, 22, 76. Bottom row: All trials: 26, 78, 27, 85, 75, 77, 44. Trial A: 4, 42, 27, 16, 50, 44. Trial B: 21, 16, 9. Trial C: 1, 20, 60, 75, 27. [actin] = 1 μM.

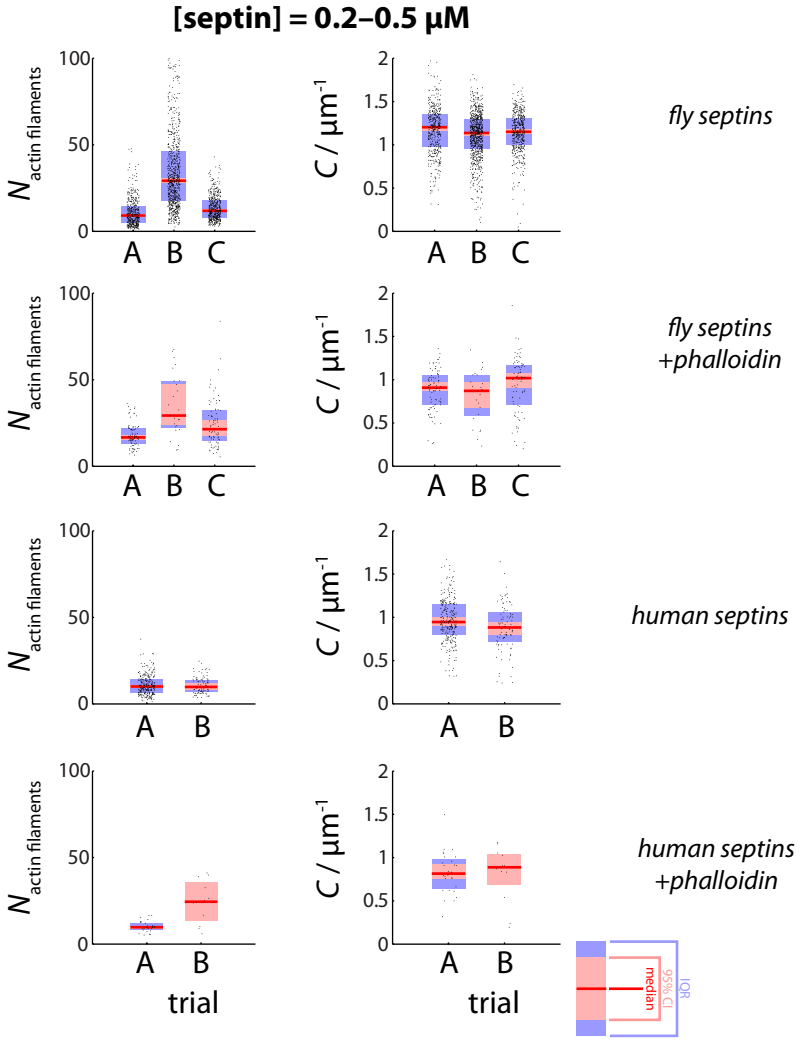

Figure 18. Number of actin filaments, but not curvature, depends strongly on experimental trial. **Left column**. Number of actin filaments plotted against experimental trial. **Right column**. Mean curvature *C* plotted against experimental trial. Different rows correspond to different conditions (see labels, right). Box plots as in Figure 11. Number *N* of data points for the different distributions, from left to right: Top row: 430, 792, 478; 430, 792, 478. Second row: 85, 25, 80; 85, 25, 80. Third row: 269, 90; 269, 90. Bottom row: 28, 12; 28, 12. [actin] = 1 µM.

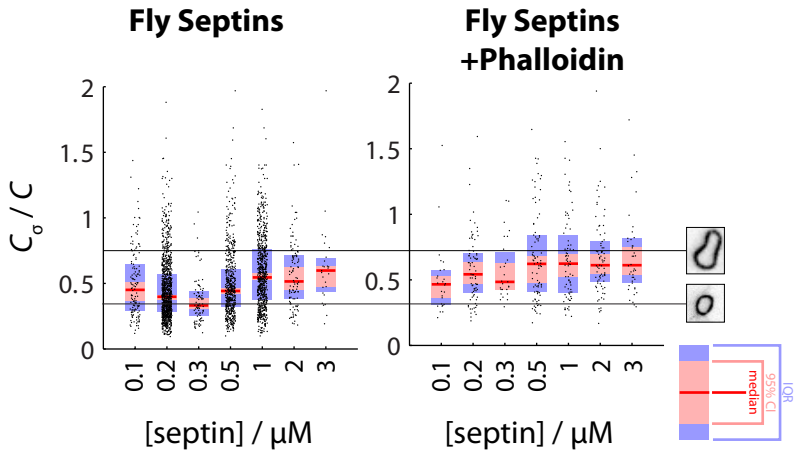

Figure 19. The dispersion of the distribution of curvatures of loops and lassos for samples is smaller for samples prepared with fly septin concentrations of 0.2–0.5 μM in the absence of phalloidin. Coefficient of variation (standard deviation C_σ of curvature measurements, normalized by mean curvature *C)*, as a function of septin concentration. For reference, values of C_σ / *C* of the two rings from Figure 10, panel b are shown in thin black horizontal lines. Box plots as in Figure 11. Number *N* of data points for the different distributions, from left to right: 134, 1042, 88, 570, 717, 108, 27; 26, 78, 27, 85, 75, 77, 44. [actin] = 1 μM.

in the absence (left) and presence (right) of phalloidin. Kinked rings have higher values of C_σ / *C* (cf. Fig. 10) and the increase of C_σ / *C* with increasing septin concentration agrees with the emergence of kinked rings at high septin concentrations (cf. Fig. 3).

Septins organize entangled actin solutions into networks of curved bundles. So far we have investigated the effect of septins at low actin concentrations (1 μM). We found that septins organize dilute suspensions of actin filaments into straight, as well as ring- and lasso-shaped bundles. At higher actin concentrations, actin filaments form entangled networks. Adding crosslinks to such entangled networks results in networks of bundles which may or may not coexist with a random meshwork of crosslinked filaments. Under these conditions, crosslinks strongly affect the mechanical properties of actin networks, which is evident in an increased storage modulus *G*' (Lieleg et al., 2010).

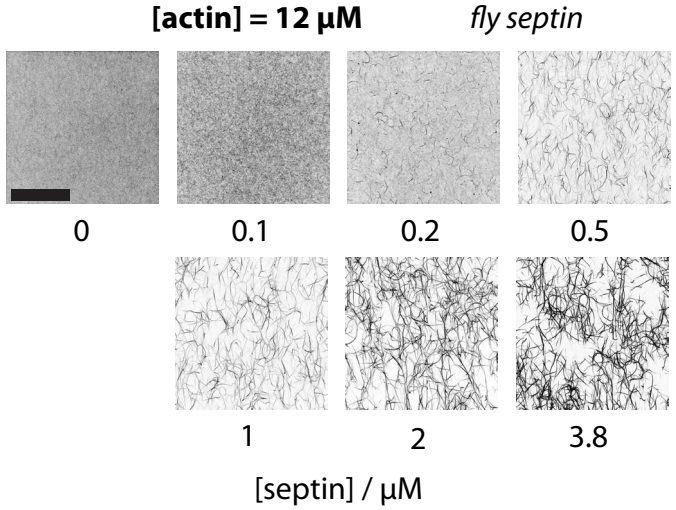

Figure 20. Effect of fly septins on entangled networks of actin filaments. [actin] = 12 µM. Snapshots depict maximum-z-projections over 10 µm. Snapshots are represented with an inverted lookup table. Scale bar 20 µm.

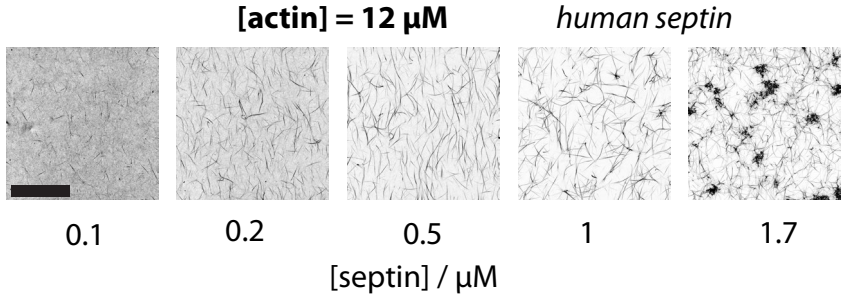

Figure 21. Effect of human septins on entangled networks of actin filaments. [actin] = 12 µM. Snapshots depict maximum-z-projections over 10 µm. Snapshots are represented with an inverted lookup table. Scale bar 20 µm.

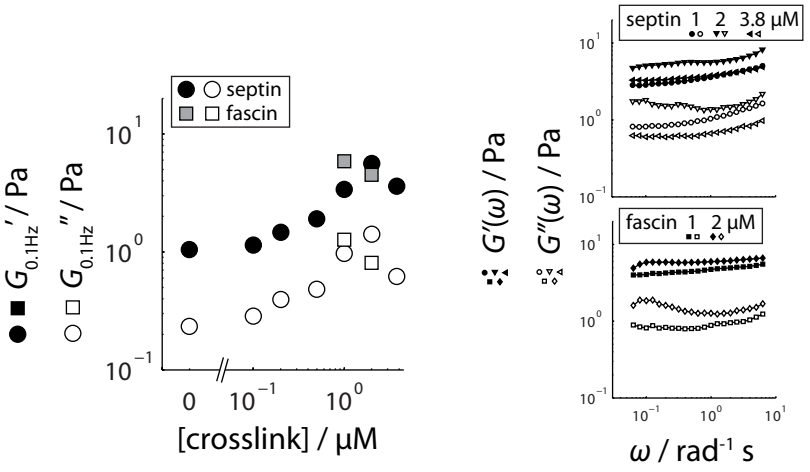

Figure 22. Fly septins stiffen entangled actin networks. [actin] = 12 μM. **Left panel**. Storage modulus *G*' (closed symbols) and loss modulus *G*" (open symbols) as a function of fly-septin (circle) and fascin (square) concentrations. **Right panels**. Frequency-dependence of *G*' and *G*". Symbol shape denotes septin concentration (see legend, top).

In order to determine how septins contribute to the morphology of entangled actin networks, we polymerize higher concentrations of actin (12 μM) in the presence of varying amounts of fly and human septins as well as phalloidin. We acquire snapshots of these networks by confocal microscopy (see Methods) and represent them by maximum-intensity projections along the *z*-direction. Figure 20 shows that for low concentrations of fly septins (up to 0.1 μM), actin networks form a fine meshwork with a homogeneous fluorescence signal across the field of view. Increasing the septin concentration to 0.2 μM produces short bundles surrounded by a fine meshwork of actin filaments. Further increasing the septin concentration results in longer, thicker bundles, while the surrounding actin meshwork decreases in fluorescence intensity. Human septins show similar behavior as fly septins, as shown in Figure 21.

In order to quantify the effect of septin bundling on the mechanical properties of these entangled networks, we measure the storage modulus *G*' and loss modulus *G*" of networks of actin filaments

polymerized in the presence of fly septins in a cone-plate rheometer (see Methods). For comparison, we also perform experiments with networks bundled by fascin, a well-characterized bundling protein that is known to increase the stiffness of actin networks (Lieleg et al., 2007). The storage modulus *G'* is a measure of a material's stiffness (solid-like component), whereas the loss modulus *G"* is a measure of a material's viscosity (fluid-like component) (Macosko, 1994). Figure 22 (left panel) shows the effect of septin concentration on *G'* and *G"*. For actin-only networks ([septin] = 0 μM), we find $G' \approx 1$ Pa, while *G"* is about 4-fold lower. The proportion of *G'* to *G"* remains essentially unchanged when adding septins to 1 μM. But increasing septin concentration results in stiffer networks, as evidenced by an increase in *G'*. At 2 μM septins, we find that stiffness increases to a maximal value of $G' \approx 4$ Pa. The network stiffness is comparable to the stiffness of actin networks bundled with fascin (square symbols). These results indicate that septins can stiffen entangled actin networks in a manner consistent with other crosslink proteins.

4.4 Discussion

We performed experiments characterizing the ability of septins to bind, bundle, and curve actin filaments. The ability of septins to bind and bundle actin filaments overthrows previous assumptions that septins do not directly interact with actin filaments. These assumptions were based on previous *in-vitro* experiments with recombinant septins (Kinoshita et al., 2002). In these experiments, septin complexes were assembled from human Sept6-Sept7 and mouse Sept2 (which is 99% identical to human Sept2) purified from Sf9 cells (as opposed to our bacteria-purified septins). These septin complexes only bound to actin bundles when anillin was present. Here we expressed septin complexes of human Sept2-Sept6-Sept7, as well as fly Pnut-DSep2-DSep1 and found that both septin complexes bundle actin in the absence of anillin. Furthermore,

we were able to investigate a wide range of septin concentrations, up to the micromolar range. In Kinoshita et al. (2002), the concentration of septin complex assayed was 0.3 μM. Our results indicate that human septins only cause bundling at concentrations above ~0.1 μM. The discrepancy between our results and those in Kinoshita et al. may arise from variability in the minimum concentration of septins needed to organize actin filaments into rings. Additionally, all our experiments were performed at 50 mM potassium chloride (KCl). When increasing KCl to 200 mM, septin-induced bundles disappeared (Tsai, 2013). The final KCl concentration used in Kinoshita et al. was likely above 100 mM.

The ring and lasso morphologies formed with septin are strikingly different from the straighter bundle morphologies observed with well-known actin bundlers, such as fimbrin (Glenney et al., 1981), fascin (Claessens et al., 2008; Edwards et al., 1995; Lieleg et al., 2007), α-actinin (Meyer and Aebi, 1990; Wachsstock et al., 1993), and filamin (Schmoller et al., 2009; Stossel et al., 2001). However, rings and lassos have been observed under non-physiological conditions, when actin was bundled by polyvalent cations (such as magnesium (Cēbers et al., 2006; Tang et al., 2001) or copper (Kaur et al., 2011)), depletion interactions (Cēbers et al., 2006; Lau et al., 2009; Sanchez et al., 2010), or biotin-streptavidin (Tang et al., 2001). Here it was proposed that actin curvature arises from a balance between adhesion energy provided by the attractive interaction between filaments and the energy penalty associated with bending the actin filaments (Cēbers et al., 2006). Typical ring diameters varied in the range of 3–10 μm for counterion-induced rings, while biotin-streptavidin crosslinks formed rings of 2–3 μm diameters. Smooth contours have been reported for depletion-induced rings (Cēbers et al., 2006), while kinked contours occur for counterion-induced and streptavidin-mediated rings (Cēbers et al., 2006; Kaur et al., 2011; Tang et al., 2001). Notably, the likelihood of encountering actin rings was not directly addressed in prior reports. Thus, ring formation in those reports may have been a rare event, perhaps occurring alongside more common linear bundles.

We showed that septins readily form actin rings and lasso structures. This surprising property of septins allowed us to quantify the effect of various conditions on the curvature C of over 4000 manually

identified rings and lassos. Median curvatures ranged from 0.5–1.3 μm^{-1}, which corresponds to ring diameters of 1.4–4 μm. These diameters are comparable to the diameters of rings formed by biotin-streptavidin links, and smaller than the rings formed by counterions and depletion agents. The ability of biotin-streptavidin crosslinks to promote smaller rings (higher curvature) than counterions and depletion agents was rationalized in terms of its extremely high binding affinity, with a dissociation constant K_d on the order of 10^{-14} M (Green, 1990). The binding affinity of septins for actin is orders of magnitude less, with values of K_d for *Drosophila* septins on the order of 10^{-6} M, as measured by co-sedimentation assays (Tsai, 2013). This affinity is comparable to that of other actin-binding proteins (Chen et al., 1999; Goldmann and Isenberg, 1993; Meyer and Aebi, 1990; Ono et al., 1997; Skau et al., 2011; Wachsstock et al., 1993; Yamakita et al., 1996). Surprisingly, we found that the number of actin filaments does not seem to strongly correlate with curvature (cf. Fig. 16). This is in strong contrast to previous qualitative observations that straight segments have a larger actin fluorescence intensity than kinks, suggesting an inverse relationship between bundle thickness and curvature (Tang et al., 2001).

The surprisingly high curvature of the rings and the lack of correlation with actin bundle thickness are inconsistent with a simple equilibrium model based on the balance of the two energetic contributions of actin filament bending (which depends on the number of filaments in the ring) and septin binding. One alternative scenario is that once a "nucleating" actin ring is formed by the complete bending of a single filament, subsequent filament growth and/or annealing of neighboring filaments can wrap around this initial ring, mediated by the addition of more septins. In this scenario, septins act as molecular "stickers", which have enough binding energy to pin actin filaments into curved geometries. Assuming such a scenario, we estimate the number n of septin crosslinks needed to bend a single actin filament into a ring. We consider the following formula, which was originally derived to estimate n for biotin-streptavidin crosslinks (Tang et al., 2001):

$$n = \frac{4\pi \ell_p}{R \ln K_a},$$

where l_p is the persistence length of F-actin, R is the radius of the ring, and K_a is the association constant of the linker bond. For biotin-streptavidin links, Tang et al. (Tang et al., 2001) measured $n = 5.8$, given $l_p = 17$ μm for phalloidin stabilized actin filaments, $R = 1.2$ μm, and 2.5×10^{15} M^{-1} for the association constant of biotin-streptavidin crosslinks. Replacing the above value of K_a with the value of 10^6 M^{-1} for septins results in a value of $n = 12.9$, which could represent a plausible value. Yet, several observations argue against the molecular sticker hypothesis. First, n is expected to depend linearly on persistence length l_p. However, when we added phalloidin, which increases the persistence length by a factor of two, the median curvature only changed modestly, by factors of 1.0–1.4x. Second, based on the above formula, we expect higher curvatures when more septins are bound. In contrast, we observed that rings which contained more septins exhibited *lower* curvatures (cf. Fig. 15). Based on these observations, we rule out the molecular sticker hypothesis.

Another alternative hypothesis is that septin binding decreases the persistence length of actin filaments. Such behavior has been reported for some other actin-binding proteins, most notably cofilin (Fan et al., 2013). Cofilin stabilizes a polymorphic form of actin that has a lower bending rigidity than the canonical form (Galkin et al., 2011; Pfaendtner et al., 2010). This hypothesis may be tested by measuring the bending rigidity of septin-decorated single filaments by video microscopy or optical tweezers (Brangwynne et al., 2008; Schnurr et al., 1997; van Mameren et al., 2009). However, this hypothesis is difficult to reconcile with our observations. We found that the number of fluorescent septins bound to rings did not vary significantly with the total concentration of septins in solution (cf. Fig. 15). However, the probability of ring formation did depend strongly on septin concentration, with rings forming in an optimum window of septin concentrations (cf. Fig. 3). When the total concentration of labeled septins was higher than this optimum window, we found a strong accumulation of labeled septins on straight bundles (cf. Fig. 4, right column). Furthermore, we found two other interesting changes in bundle morphology for high septin concentrations. First, kinked rings and zigzags occurred above 1 μM fly septins (cf. Figs 3 & 19). Second, the number of actin filaments in rings and lassos decreased with increasing septin concentration (despite variations between

experimental trials) (cf. Fig. 17). These results demonstrate that an abundance of septins frustrate proper ring formation.

Another possible hypothesis is that septin binding could induce a spontaneous curvature of actin filaments. Such a mechanism would be reminiscent of proteins which curve lipid bilayer membranes upon binding (Zimmerberg and Kozlov, 2005). In fact, fractions of brain-tissue extracts which contain septins can curve membranes when added to giant unilamellar vesicles (Tanaka-Takiguchi et al., 2009). Such curvature control could originate from the regulation of actin filament twist. Experiments on colloidal membranes composed of fd-virus rods have found that the interplay between frustrated molecular chirality and interfacial tension can manifest itself on larger length scales, leading to multiple conformational states (Gibaud et al., 2012). In the case of actin, fascin crosslinks have been shown to over-twist actin filaments, resulting in tight bundles with a well-defined composition (Claessens et al., 2008). This hypothesis could be readily tested by X-ray scattering experiments on actin-septin bundles.

Kinetic effects likely play a role in ring formation. Kinetic effects have been found to significantly affect the morphology of actin bundles in simulations (Nguyen et al., 2009), as well as experiments of actin networks bundled by filamin (Schmoller et al., 2008) and α-actinin (Falzone et al., 2012). We observed that rings have a nearly 2-fold lower curvature when septins interact with pre-polymerized actin filaments compared to co-polymerization (cf. Fig. 13). Curved septin bundles also relaxed their shape when ablated (cf. Fig. 9). However, kinetic effects alone cannot account for ring and lasso formation. In pre-polymerization experiments, rings only appeared when septins were present.

Our results raise several interesting questions. The first key question is which domain of septin hexamers binds to actin filaments. Elucidating the actin-septin binding mechanism should lead to a better understanding of how septins differ from other actin-binding proteins. The second key question is whether this actin-binding still occurs when septin is immobilized on a lipid membrane or bound to myosin, or if it competes with membrane and/or myosin interactions. If this is the case, then septin is likely to play a direct role in stabilizing a curved actin-myosin ring underneath the membrane during cytokinesis and fly cellularization. The fact that we found similar behavior for fly and human

septins suggests that septin's unique property of promoting bundling and, in particular, bundle ring formation could be evolutionarily conserved.

4.5 Methods

Protein purification. Monomeric G-actin was purified from rabbit psoas skeletal muscle (Soares e Silva et al., 2011b). G-actin was purified with a Superdex 200 column (GE Healthcare, Waukesha, WI, USA). Aliquots were stored at −80 °C in G-buffer (2 mM tris-hydrochloride pH 8.0, 0.2 mM disodium adenosine triphosphate, 0.2 mM calcium chloride, 0.2 mM dithiothreitol). Freshly thawed aliquots were treated with 5 mM dithiothreitol, centrifuged at 30 psi (120,000 g) for 30 min in a Beckman airfuge, and sonicated for 5 min to remove actin dimers. G-actin was labeled with either Alexa-Fluor-488 or Alexa-Fluor-594 carboxylic acid, succinimidyl ester (Soares e Silva et al., 2011b). Recombinant *Drosophila* and human septin hexamers were provided by Manos Mavrakis. Protein concentrations were determined by measuring absorbance at 280 nm with a NanoDrop 2000 (ThermoScientific) and using extinction coefficients, in M^{-1} cm^{-1}, of 26600 (actin (Pardee and Spudich, 1982)), 249000 (myosin (Margossian and Lowey, 1982)), 167320 (*Drosophila* septin hexamer, predicted from amino acid sequence (Artimo et al., 2012)), and 161360 (human septin hexamer, predicted from amino acid sequence (Artimo et al., 2012)).

Flow cell preparation. Microscope slides and cover slips were cleaned for 30 min in base-piranha solution (5% hydrogen peroxide, 5% ammonium hydroxide, heated to 70°C) and stored in 100% isopropanol. Flow cells were assembled by sandwiching strips of Parafilm between clean glass substrates and melting at 120°C. Resulting cavities were then passivated by incubating for 5 min with 1 M potassium hydroxide, rinsing with Milli-Q water, blow-drying with nitrogen gas, incubating for 30 min with 0.2 mg/mL poly-L-lysine-polyethylene-glycol (Surface

Solutions), rinsing with Milli-Q water, and blow-drying with nitrogen gas. Passivated flow cells were then used immediately. Actin solutions were loaded into flow cells and hermetically sealed with VALAP (equal parts petrolium jelly, lanolin, and paraffin wax).

Sample preparation. Samples were mixed to yield a final buffer composition of 20 mM imidazole pH 7.4, 50 mM potassium chloride, 1 mM dithiothreitol, and 0.1 mM magnesium-adenosine triphosphate. Furthermore, 1 mM trolox, 2 mM protocatechuic acid, and 0.1 μM protocatechuate 3,4-dioxygenase were added to minimize photobleaching. TIRF microscopy samples additionally contained 0.1 % (w/v) methylcellulose. For phalloidin-treated samples, a drop of phalloidin (in equimolar amounts to actin) was left to evaporate in a separate tube; freshly mixed samples were pipetted in the phalloidin-containing tube before loading into flowcells. For pre-polymerization samples, a stock of actin filaments (10 μM) was prepared and mixed with septins at least 45 min after initiating polymerization. Fluorescently labeled G-actin monomers were mixed with unlabeled monomers to yield a 10% molar ratio of dye to protein.

Fluorescence microscopy. For TIRF experiments, samples were imaged with a Nikon Apo TIRF 100x/1.49 NA oil objective mounted on an Eclipse Ti microscope (Nikon) using 491 nm and 561 nm laser lines and imaged with a QuantEM 512SC EMCCD camera (Photometrics). For confocal experiments, samples were imaged with a Nikon Apo TIRF 100x/1.49 NA oil objective mounted on an Eclipse Ti microscope (Nikon) using 488 nm and 561 nm laser lines and imaged with an A1 PMT detector unit (Nikon). All TIRF images were acquired under the same illumination and detection settings.

Ablations. For ablation experiments, samples were prepared as described above and imaged with an A1 R-MP confocal point scanner (Nikon) on an inverted microscope (Eclipse Ti, Nikon) with a photomultiplier tube detector (A1, Nikon). Samples were imaged and ablated with a pulsed infrared laser (Mai Tai DeepSee, SpectraPhysics) tuned to 760 nm. Ablations were performed by scanning a line perpendicular to the bundle long axis for a total exposure of 45 s.

Rheology. Networks were sheared by a stress-controlled rheometer (Physica MCR 501, Anton Paar). Samples were polymerized at room temperature between a top cone plate (CP-20-1) and a bottom planar

plate. A wet tissue was placed around the sample and a surrounding hood was lowered to maintain humidity. Network evolution was monitored by probing samples at low strains (0.5 %, 0.5 Hz) for 5 min, followed by a idle period of 25 min, repeated over the course of 1.5 h. Next, network mechanical properties were probed by a frequency sweep (frequencies 1–0.01 Hz) using a small strain amplitude of 5%, which was still within the linear viscoelastic regime.

Rings and lassos. A total of 2097 rings and 2065 lassos were manually identified across 1770 images. Rings are defined as bright structures that form a closed loop and do not contact other structures of comparable brightness. Lassos are defined as bright structures that either (i) form a closed loop which contact the end of a single bundle of comparable brightness or (ii) double over to form a closed loop. Rings and lassos were analyzed using a custom-built algorithm for detecting curvature.

Statistics. Curvature, actin fluorescence, and septin fluorescence distributions were characterized by sample medians and the 95% confidence intervals (CI) of the median. CIs were computed from 10^5 bootstrap samples (Davison and Hinkley, 1997) with the MATLAB function "bootci", using the bias corrected and accelerated percentile method (Efron, 1987).

4.6 Image Analysis

We developed an algorithm to compute the curvature $C(s)$ of a point s from images of fluorescently labeled actin-septin bundles. In short, this method determines bundle contours and computes the change in angle θ along these contours.

Step 1: The original image (Fig. 23a) is bandpass filtered to accentuate bundle contours (Fig. 23b). Bandpass filters remove spatial frequencies below ν_{low} (usually detection noise) and above ν_{high} (usually uneven illumination). Bandpass filtering was performed with ImageJ,

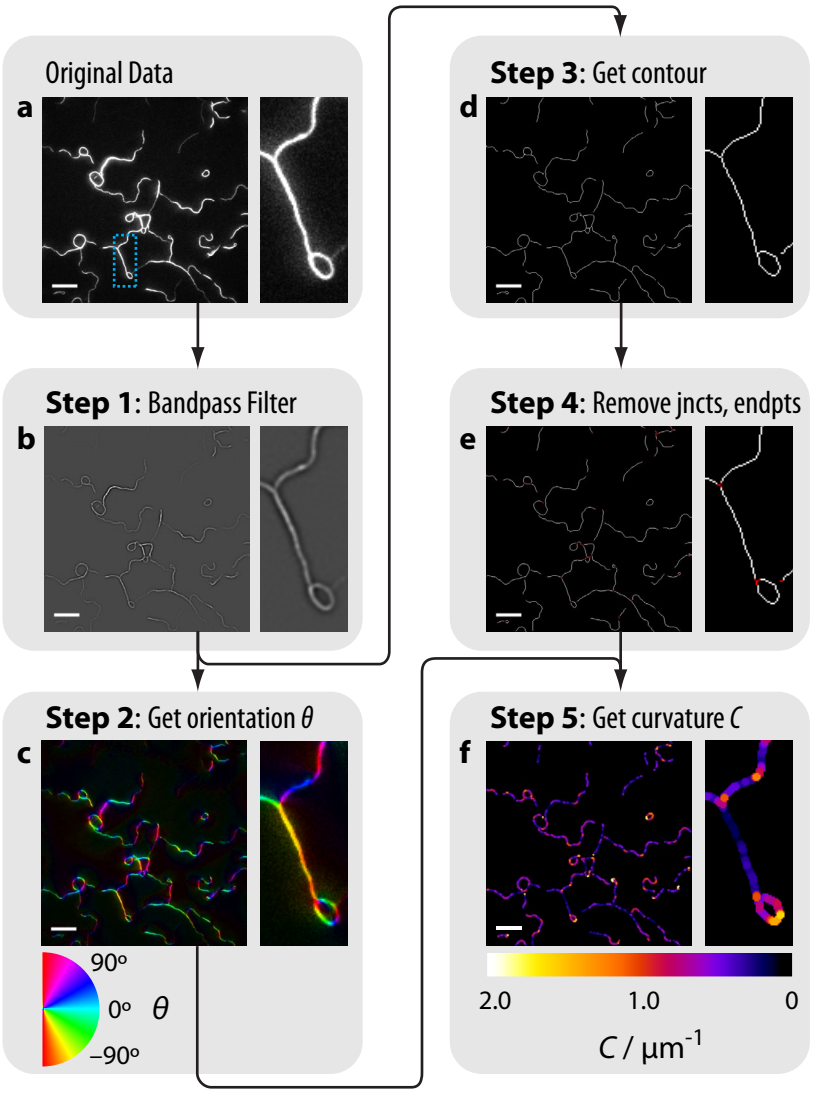

Figure 23. Algorithm to compute curvature C from images of fluorescently labeled actin-septin bundles. **a**. Original image of fluorescently labeled actin (1 μM) in the presence of fly septins (1 μM) obtained by TIRF microscopy. Right: 4x magnified closeup (blue dashed box) **b**. Bandpass-filtered image. **c**. Bundle orientation θ, resulting from OrientationJ analysis. Image hue denotes θ (calibration wheel, bottom), image brightness is given by the original image (panel a). **d**. Bundle contour. **e**. Interior of bundle contour, which consists of

which calculates ν_{low} and ν_{high} in the frequency domain given input values in the spatial domain. Here, values of 2 px (corresponding to ν_{high}) and 4 px (corresponding to ν_{low}) were chosen. The result is a modified image where structures of 3 px, which corresponds to the typical width of a bundle, are accentuated.

Step 2: The filtered image from Step 1 is used to determine the local orientation θ of intensity around each pixel (Fig. 23c). This step implements OrientationJ, a freely-available ImageJ plugin that was developed to track collagen and elastin fibers (Fonck et al., 2009; Rezakhaniha et al., 2012). This routine computes the eigenvectors of a structure tensor constructed of the spatial gradients of fluorescence intensity around each pixel. The result is an image where each pixel (x,y) reports the orientation θ of the eigenvectors corresponding to a small region $(x\pm\sigma, y\pm\sigma)$ in the original image. The parameter σ, in pixels, should match the typical length scale of the desired features.

Step 3: The filtered image from Step 1 is used to determine bundle contours (Fig. 23d). First, the image is thresholded using Otsu's method (Otsu, 1975). This yields a binary image comprising connected components of bright pixels (1) against a dark background (0). Next, the thresholded image is skeletonized. This converts connected components to lines that are one pixel thick. These lines define the contour of the bundle. Finally, contours that are smaller than ten pixels are removed. This removes short contours that correspond to stray fluorescence intensity fluctuations of the background. The result is a binary image with connected components that are one pixel thick which correspond to bundle contours.

Step 4: Bright pixels from Step 3 that correspond to junctions or endpoints are removed (Fig. 23e). At junction points, curvature is ill-

---

bright pixels with exactly two neighboring bright pixels (white). Pixels at endpoints or at junctions (red) are discarded. **f**. Curvature C of the pixels corresponding to bundle interiors (panel e). A maximum filter of 1 px was applied to the image for clarity. Dark blues and purples denote areas of low curvature; light yellows and whites denote areas of high curvature (calibration bar, below). Scale bars 10 μm.

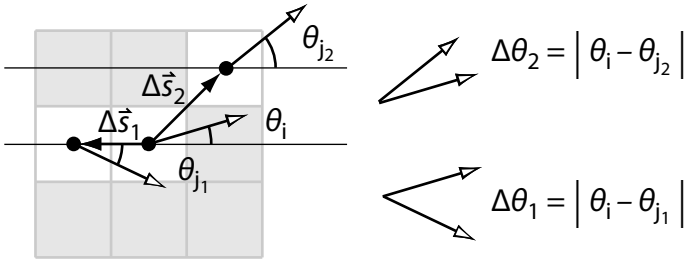

Figure 24. Determining curvature by computing changes in orientation $\Delta\theta$ (white arrowheads) along bundle contour, given a bright pixel i and neighboring bright pixels j_1 and j_2 separated by distances Δs_1 and Δs_2 (black arrowheads), respectively.

defined. At endpoints, orientation measurements are noisy, particularly for lower values of σ. To remove these points, the image of bundle contours is first filtered with a kernel of [1, 1, 1; 1, 0, 1; 1, 1, 1]. This yields an image where each pixel value corresponds to the number of neighboring bright pixels. Endpoints yield 1, pixels along a bundle contour yield 2, and junctions yield 3 or more. Next, pixels with a value of 2 were then selected. Finally, the resulting image was masked with the contour image from Step 3 with a bitwise AND operation. Repeating this step iteratively increases the number of pixels removed. Here we perform $N = 2\sigma$ iterations. Given a skeletonized binary image I, the following line of code implements an iteration of Step 4:

imfilter(I, [1 1 1;1 0 1;1 1 1]) == 2 & I)

Step 5: Curvature is calculated for each bright pixel from Step 4 (Fig. 23f). First, the orientation image from Step 2 is masked with the result of Step 4. Second, for each pixel i, the change in orientation is computed by considering the orientations of neighboring pixels j_1 and j_2. The change in orientation is given by $\Delta\theta_k = \left|\theta_i - \theta_{j_k}\right|$ (Fig. 24a), where k = 1,2. Dividing this by the distance $\Delta s_k = \left|\vec{r}_i - \vec{r}_{j_k}\right|$ between neighboring pixels (which can equal either 1 or $\sqrt{2}$) yields the curvature $C(s)$ (henceforth denoted by C in the remainder of this section). Curvature C is defined as the derivative of orientation along the bundle contour:

$$C = \frac{d\theta}{ds} = \lim_{\Delta s \to 0} \frac{\Delta\theta}{\Delta s} = \frac{1}{2}\left(\frac{\Delta\theta_1}{\Delta s_1} + \frac{\Delta\theta_2}{\Delta s_2}\right).$$

Finally, we recover the radius of curvature r_C by inverting:

$$r_C = \frac{1}{C}.$$

Both curvature C and radius of curvature r_C are appropriate measures of contour curvature. r_C corresponds to the radius of the circle that best fits a point s along a contour (Spiegel, 1968). But because low r_C denotes highly curved regions, C is sometimes a more intuitive measure: higher C denotes more highly curved contour sections, and the curvature C scales linearly with bending energy (Landau et al., 1986).

Validation against synthetic data. We validate this algorithm by producing test images of circles with a known radius of curvature r_C. 16-bit test images were produced in Adobe Photoshop CS4 by drawing 1-px wide, anti-aliased, circular white strokes on a black background. The images were then Gaussian blurred by 1 px, and noise was introduced with the ImageJ "Add specified noise" plugin (standard deviation = 2000). These values were chosen to produce test images that mimic our microscopy data. Separate test images were created for r_C / px = 3, 5, 10, 20, 50, 100, 200, and 500 (r_C = 20 px is shown in Fig. 25a,b). Each test image was processed using the algorithm described above (Fig. 25c). Computed radii of curvature (Fig. 25d) were averaged across the entire image. Accuracy of the algorithm can be demonstrated by plotting measured r_C resulting from image analysis versus the known values of r_C (Fig. 25e). Accurate results fall on the $r_{C,known} = r_{C,measured}$ line. For a local window of size σ = 1, the analysis has an accuracy range of $r_{C,known}$ = 3–20 px. (For our microscopy setup, this corresponds to $r_{C,known}$ = 0.5–3.2 μm). Above 20 px, the algorithm underestimates radii of curvature: for straight features with low curvature (high r_C), the change in angle between neighboring pixels is too small to detect. This can be overcome by increasing σ to higher values. For instance, for sigma = 5 px, large radii of curvature are accurately detected, yielding an accuracy range of $r_{C,known}$ = 20–500 px (Fig. 25f). (For our microscopy setup, this corresponds to $r_{C,known}$ = 3.2–79 μm). Below 10 px, the algorithm overestimates radii of curvature: OrientationJ (Step 2) is insensitive to image features smaller than σ, so loops with a radius of curvature approaching σ or smaller are not resolved. The choice of σ therefore determines the curvatures that can be accurately detected (Fig. 25g).

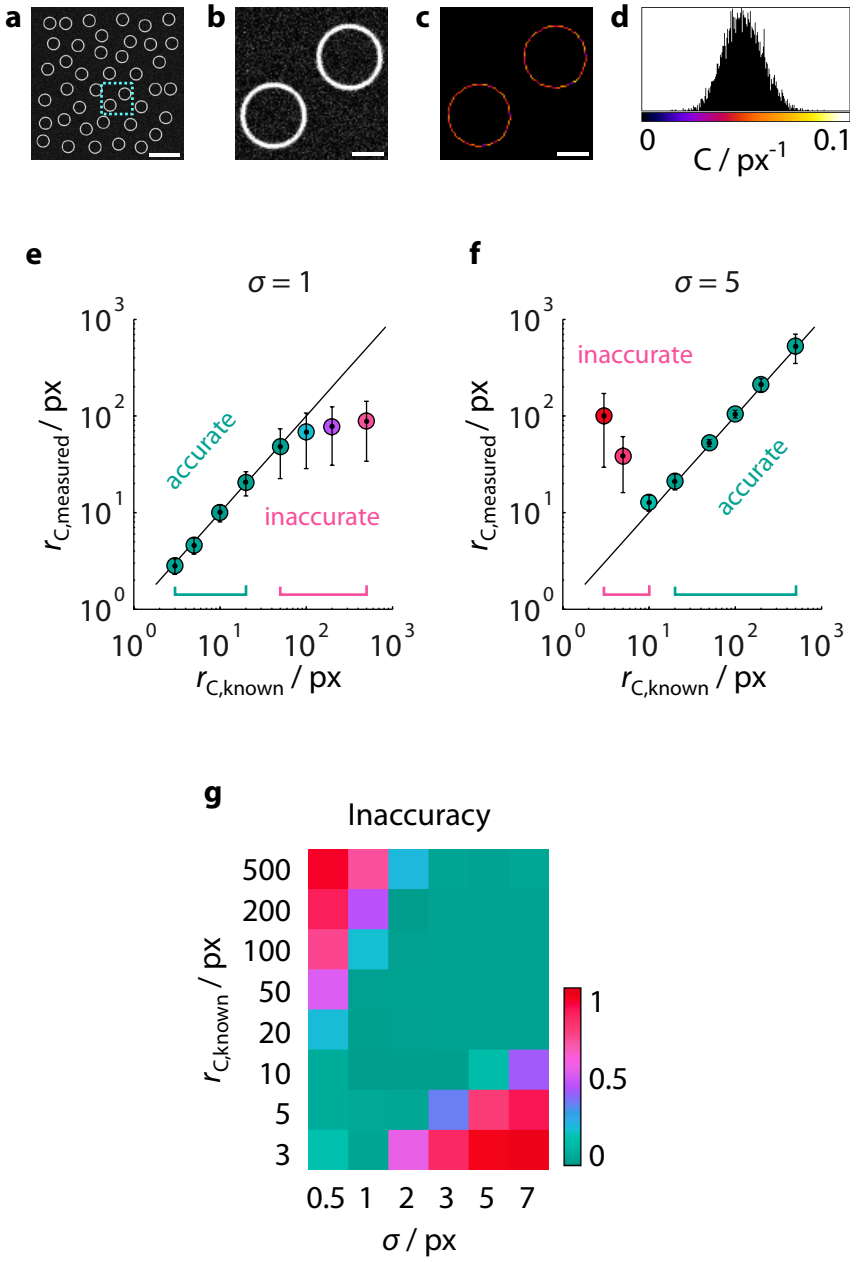

Figure 25. Validation of algorithm to circles of known curvature. **a**. Synthetic data generated by circles with a radius of 20 px. Scale bar 100 px. **b**. Close-up of panel a, dashed box. Scale bar 20 px. **c**. Curvature

Estimating true r_C given $r_{C,measured}$. For actual microscopy data where r_C is not known *a priori*, estimating the true r_C given $r_{C,measured}$ is not immediately straightforward. Results from analyzing images of synthetically generated circles reveal that $r_{C,known}$ and $r_{C,measured}$ are not always related by a one-to-one mapping. This is shown in the accuracy plots depicted in Fig. 26. For example, the accuracy plot for $\sigma = 5$ shows that $r_{C,measured} = 1000$ px could correspond to either $r_C = 3$ px or $r_C = 1000$ px. This one-to-many mapping introduces substantial error in estimating r_C given $r_{C,measured}$. In order to minimize these errors, we consider only values of $r_{C,measured}$ which are related to $r_{C,known}$ by a one-to-one mapping. Such values of $r_{C,measured}$ appear as striped regions in Fig. 26. Often, these regions are narrow in $r_{C,measured}$, which limits the range of r_C we can reliably estimate. However, as σ increases, the range of precision of $r_{C,measured}$ shifts to higher values. We exploit this upward shift to extend the range of precision. We iterate the algorithm four times using different values of σ (1, 2, 3, and 5). For each iteration, we only record values of $r_{C,measured}$ which fall within the range specified by Figure 26.

---

map, as measured by analysis ($\sigma = 1$ px). Brighter colors indicate higher measured curvature (calibration bar, panel d). Scale bar 20 px. **d**. Histogram of measured curvature for the entire image (panel a). The average curvature, $\langle C \rangle$ / px^{-1} = 0.049 ± 0.009, corresponds to an average radius of curvature of $\langle r_C \rangle$ / px = 20.5 ± 4.0 and agrees well with the known value of 20 px. (Uncertainty bounds for measured $\langle C \rangle$ denote standard deviation; for $\langle r_C \rangle$, propagated uncertainty). **e**. Accuracy plot. Measured curvatures are plotted against known curvatures. Note that performing the analysis with $\sigma = 1$ produces accurate measured values of r_C only for lower values of $r_{C,known}$. Color denotes inaccuracy (calibration bar, panel g). **f**. Accuracy plot, as in panel e, for $\sigma = 5$. Note that the range of accuracy (green symbols) shifts towards higher values of $r_{C,known}$. **g**. Map of inaccuracy of $r_{C,measured}$, given by

$$|r_{C,measured} - r_{C,known}| / (r_{C,measured} + r_{C,known}),$$

and plotted as a function of σ and $r_{C,known}$. Note that the range of accuracy (green zones) shifts towards higher values of $r_{C,known}$ as σ increases.

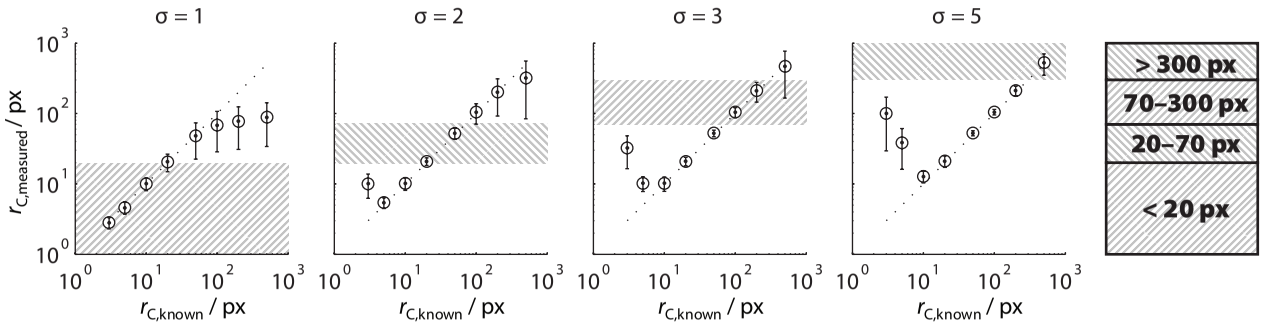

Figure 26. Accuracy plots for σ = 1, 2, 3, and 5. Striped regions denote values of $r_{C,measured}$ which can be mapped one-to-one to values of $r_{C,known}$. Note that striped regions shift to higher values of $r_{C,measured}$ as σ increases.

Validation against microscopy data. We test the above modification by considering a microscopy image of actin-septin bundles and rings (Fig. 27a). We visually inspect the resulting curvatures produced by the algorithm (Fig. 27b). Reported curvatures should produce circles with radii that visibly fit the bundle contour. This is shown in Fig. 27c–f.

Discussion. Several methods have been proposed in the biophysical literature to determine the curvature of linear contours. For example, the curvature of crawling *Dictyostelium discoideum* cell boundaries was determined by fitting circles to boundary points along the cell exterior (Driscoll et al., 2012). The technique for determining cell boundary was based on the minimization of an energy computed from pixel intensities (Xu and Prince, 1998), which has also been adapted to track cytoskeletal structures (Smith et al., 2010). These methods track linear contours to subpixel precision. However, attaining reliable contours requires tuning various parameters and supervising results. A different method for quantifying the curvature of cell boundaries (for mouse melanoma and buffalo rat liver cells) uses least-squares fitting of circular arcs between pairs of points (Bischofs et al., 2008). However, this method requires the user to select pairs of points between which the boundary exhibits a constant curvature. Here, we instead determine curvature without knowledge of bundle contours, without fitting circles, and without manual user input. We use the plugin OrientationJ to compute orientation θ to floating-point precision. Because OrientationJ requires only one parameter, σ, the algorithm described here requires less supervision and can thus be easily automated.

Determination of the number of filaments. The number of actin filaments was estimated based on the fluorescence intensity of the actin signal (Fig. 28a). The fluorescence intensity of a single filament was estimated by acquiring a series of 600 images (Fig. 28b) and determining the filament contour for each image (Fig. 28c). The mean fluorescence of filament contours was found to be 296 ± 109 pixel intensity units.

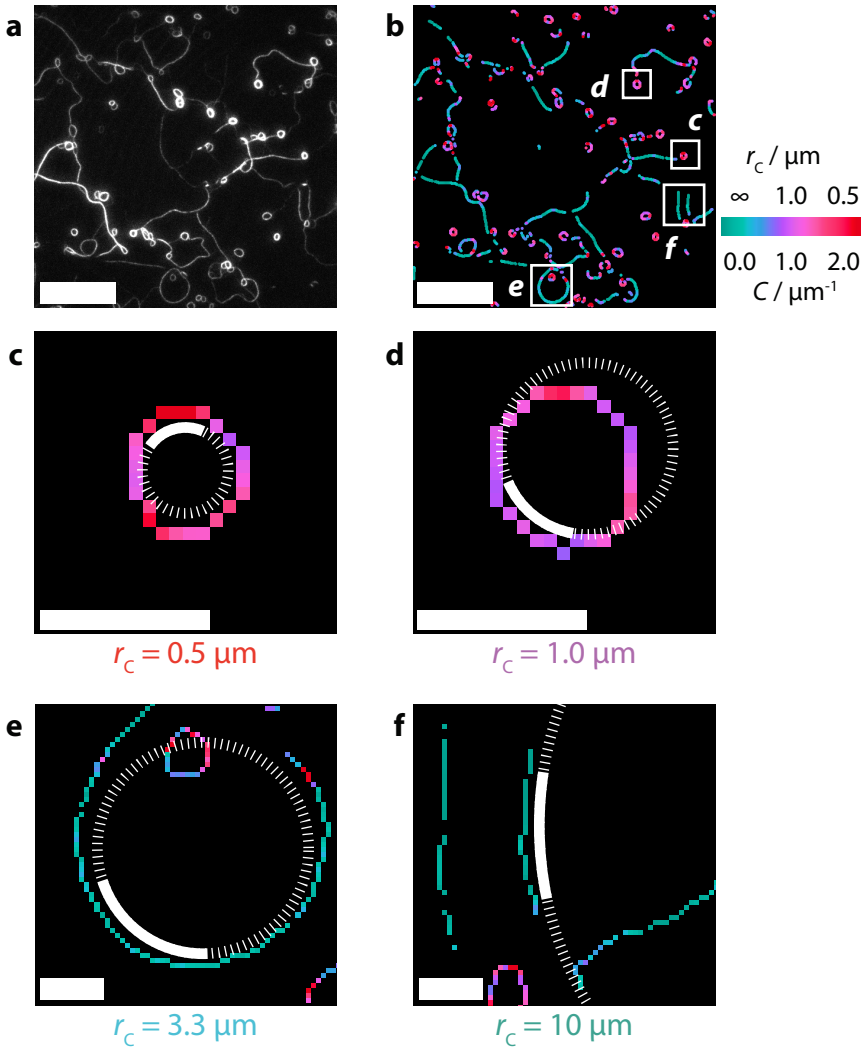

Figure 27. Validation of algorithm to experimental data. **a**. Image of fluorescently labeled actin filaments (1 µM) bundled by fly septins (0.2 µM). Small rings (high curvature) and long bundles (low curvature) are visible. Scale bar 20 µm. **b**. Result of curvature analysis. Color corresponds to curvature C, or equivalently, radius of curvature r_C (see calibration bar, right). A maximum filter (1 px radius) was applied to thicken bundle contours (nominally 1 px thin). Scale bar 20 µm. **c**. Closeup of small ring (panel b). Note that red pixels report $r_C \sim 0.5$ µm, which agrees with the bold section of the dashed, white circle (r_C =

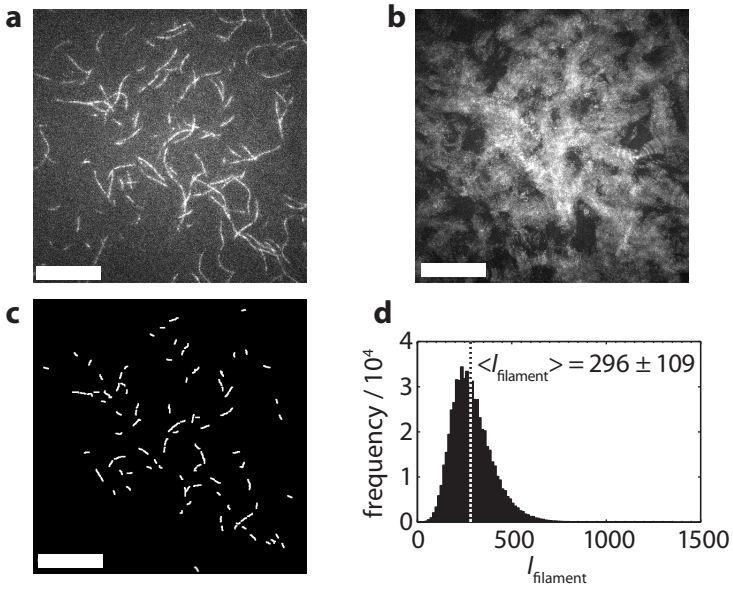

Figure 28. Determining the intensity of a single-actin filament. **a**. TIRF image of single actin filaments. **b**. Maximum time projection over 600 frames. Cloudy white regions correspond to the areas occupied by single filaments as they fluctuate over time. **c**. Filament contours. A maximum filter (radius 1 px) was applied to make 1-px-thick contours visible. **d**. Histogram of background-subtracted fluorescence intensities of filament contours. The average filament intensity $\langle I_{\text{filament}} \rangle$ is 296 ± 109 (uncertainty denotes standard deviation). Scale bars 20 μm.

0.5 μm). Scale bar 2 μm. **d**. Closeup of larger ring (panel b). Note that magenta pixels report $r_C \sim 1.0$ μm, which agrees with the bold section of the dashed, white circle ($r_C = 1.0$ μm). Scale bar 2 μm. **e**. Closeup of large loop (panel b). Note that cyan pixels report $r_C \sim 3.3$ μm, which agrees with the bold section of the dashed, white circle ($r_C = 3.3$ μm). Scale bar 2 μm. **f**. Closeup of curved bundle (panel b). Note that green pixels report $r_C \sim 10$ μm, which agrees with the bold section of the dashed, white circle ($r_C = 10$ μm). Scale bar 2 μm.

Acknowledgements

Experiments were performed in collaboration with Feng-Ching Tsai (AMOLF, Amsterdam), Manos Mavrakis (CNRS/Aix-Marseille U), and Aurelie Bertin (Institut Curie, Paris). We thank Dirk-Jan Spaanderman (AMOLF) for designing Figure 1, Roland Dries (AMOLF) for help with microscopy and laser ablations, François Iv (Aix-Marseille U) and Marjolein Kuit-Vinkenoog (AMOLF) for purifications, and Magdalena Preciado–López (AMOLF) for insightful discussions.

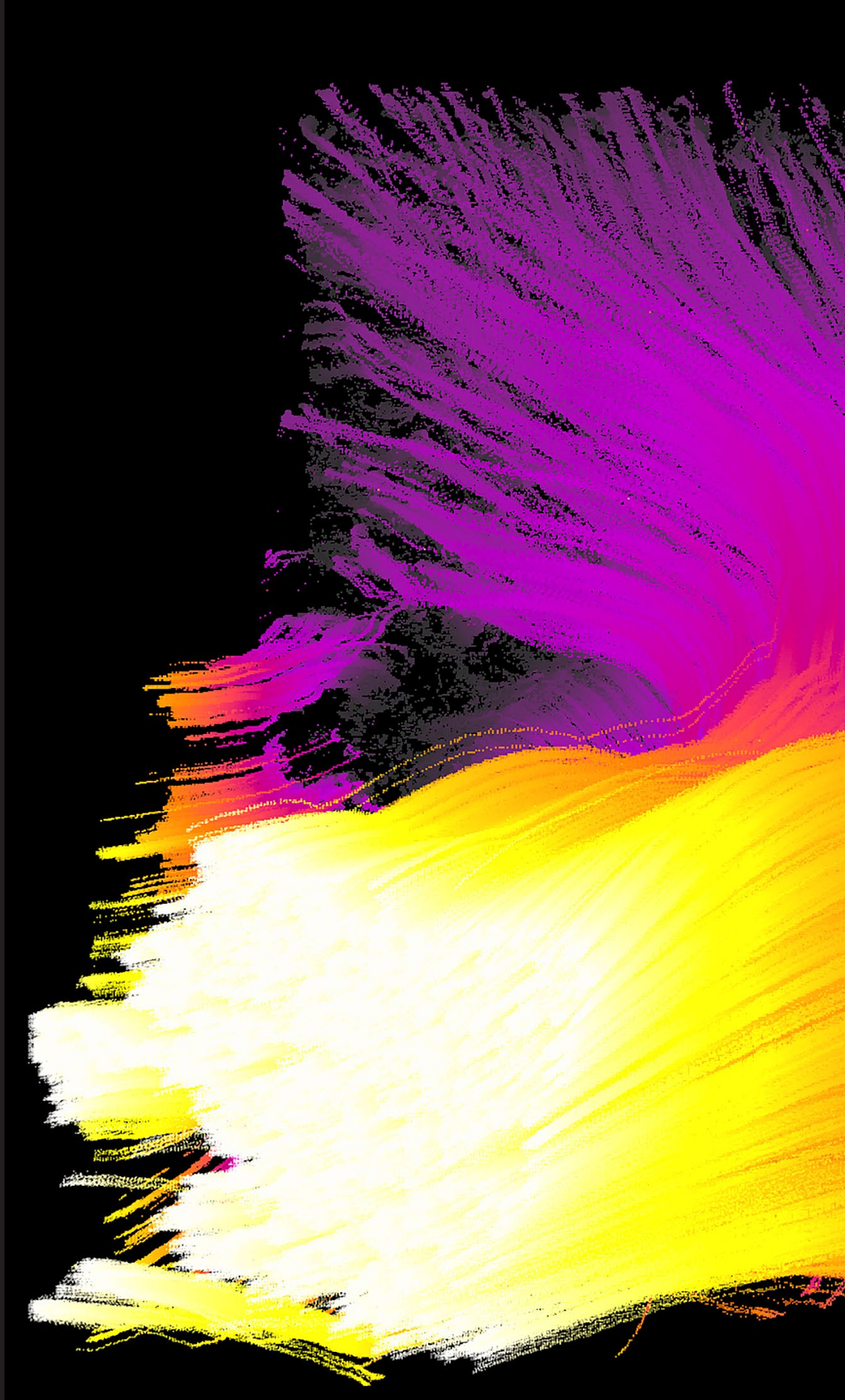

5

5. Molecular motors robustly drive active gels to a critically connected state

Living systems often exhibit *internal driving*: active, molecular processes drive nonequilibrium phenomena such as metabolism or migration. Active gels constitute a fascinating class of internally driven matter, where molecular motors exert localized stresses inside polymer networks. There is evidence that network crosslinking is required to allow motors to induce macroscopic contraction. Yet a quantitative understanding of how network connectivity enables contraction is lacking. Here we show experimentally that myosin motors contract crosslinked actin polymer networks to clusters with a scale-free size distribution. This critical behavior occurs over an unexpectedly broad range of crosslink concentrations. To understand this robustness, we develop a quantitative model of contractile networks that takes into account network restructuring: motors reduce connectivity by forcing crosslinks to unbind. Paradoxically, to coordinate global contractions, motor activity should be low. Otherwise, motors drive initially well-connected networks to a critical state where ruptures form across the entire network.

5.1 Introduction

One of the defining qualities of soft matter is that it is readily driven far from thermodynamic equilibrium by external stress. Driving forces such as those due to an electric field or shear can drive colloidal suspensions and polymer networks into fascinating non-equilibrium patterns, including banded (Fielding et al., 2009; Vissers et al., 2011), jammed (Weeks et al., 2000), and randomized steady states (Corté et al., 2008). Much progress has been made in understanding such *externally* driven systems (van Hecke, 2009). By contrast, living soft matter systems such as cells and tissues naturally exhibit a unique form of *internal* driving in the form of mechanochemical activity (Jülicher et al., 2007; Zemel et al., 2011). A prominent example is the *cytoskeleton*, a meshwork of protein polymers and force-generating motor proteins that constitutes the scaffold of cells. In solutions of purified cytoskeletal filaments and motors, remarkable self-organized patterns have been observed (Nédélec et al., 1997; Sanchez et al., 2012), inspiring theoretical work of these so-called active gels (Marchetti et al., 2012).

More recently, attention has shifted to the important role of network connectivity in active gels, which can be controlled by the number of crosslinks between filaments. In weakly connected systems, motors slide filaments to form static or dynamic clusters (Backouche et al., 2006; Köhler et al., 2011a; Smith et al., 2007; Soares e Silva et al., 2011b). In the opposite limit of a well-connected, elastic network, motors generate contractile stresses as they pull against crosslinks, which can dramatically change the elastic properties of the network (Koenderink et al., 2009; Mizuno et al., 2007) or lead to contraction (Bendix et al., 2008; Köhler et al., 2012). The existence of a threshold connectivity that separates these two behaviors has been proposed, since macroscopic contractions are known to occur above certain minimum values of crosslink or actin concentration (Bendix et al., 2008; Köhler et al., 2011a; Wang and Wolynes, 2012a; 2012b). We should expect remarkable critical behavior at the threshold of contraction. Recent theoretical models predict diverging correlation length-scales and a strong response to external fields (Broedersz et al., 2011; Sheinman et al., 2012a; 2012b; Wyart et al., 2008) at the threshold of rigidity. In

suspensions of self-propelled patches, critical slowing was predicted at the threshold of alignment (Weber et al., 2012). Yet the threshold of contraction still remains poorly understood, and experimental evidence of criticality in active gels remains lacking.

Here, we experimentally study model cytoskeletal systems composed of actin filaments and myosin motors. We vary network connectivity over a broad range by adding controlled amounts of crosslink protein. We show that the motors can actively contract the networks into disjoint clusters that exhibit a power-law size distribution. This behavior is reminiscent of classical conductivity percolation (Stauffer and Aharony, 1994), for which a power-law size distribution of clusters occurs close to a critical point. However, in sharp contrast to this equilibrium phenomenon, we observe critical behavior over a wide range of initial network connectivities. To understand this robustness, we develop a general theoretical model of contractile gels that can quantitatively account for our observations. In this model, motors not only contract the network, but also reduce the connectivity of initially stable networks down to a marginal structure by promoting crosslink unbinding. Below this marginal connectivity, the network no longer supports stress and the system rapidly devolves to disjoint clusters which reflect the critical behavior of the marginal structure. Our model predicts cluster size distributions that agree well with experiment. Moreover, it predicts an inverse relationship between cluster size and motor activity, which we also confirm experimentally.

5.2 Experiments

In order to resolve the interplay between motor activity and network connectivity in active cytoskeletal networks, we develop a biomimetic model system with a well-controlled composition (Fig. 1a). Networks are formed by initiating actin filament polymerization, which results in a semiflexible polymer meshwork with a pore size of ~0.3 μm. We

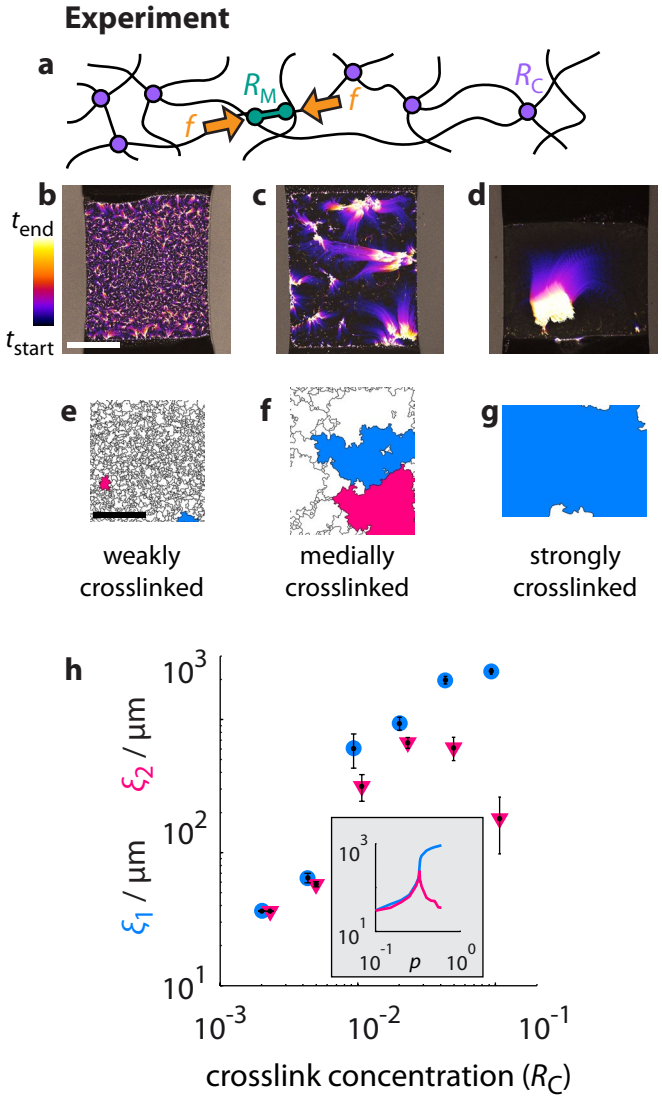

Figure 1: Experiments with motor-driven networks show that initial connectivity controls the length scale of contraction. **a**: Schematic representation of the experiment. Actin filaments (black lines) are connected by crosslinks (purple circles), and myosin motors (green dumbbells) exert force dipoles (orange arrows) on actin filaments. **b–d**: Temporal evolution of three networks with varying amounts of fascin crosslinks (a. $R_C = 0.01$; b. $R_C = 0.05$; c. $R_C = 0.1$). Actin and

control the motor activity by adding different amounts of myosin motors, expressed in terms of the myosin-to-actin molar ratio, R_M = [myosin] / [actin]. We control the network connectivity by adding different amounts of the crosslink fascin, which can simultaneously bind to two neighboring actin filaments (see Methods). We express the crosslink density in terms of the fascin-to-actin molar ratio, R_C = [fascin] / [actin]. To ensure that we can observe motor-driven contraction on all scales, from microscopic to macroscopic, we prepare networks in customized flow-cells, which fit entirely in the field-of-view of the 4× objective of a confocal microscope (see Methods). To track the temporal evolution of the networks, we acquire time-lapse movies starting from 1 minute after the initiation of actin polymerization, where the solution is still homogeneous, until 2 hours afterwards.

To resolve the influence of network connectivity, we first prepare a series of networks with constant myosin activity (R_M = 0.01) and gradually increasing crosslink density (R_C). Even at low R_C, the motors can contract actin networks. However, contraction occurs only on a small length scale, as seen in the time projection image in Fig. 1b. However, when we increase R_C, contraction occurs on a larger length scale (Fig. 1c). The motors break the network up into multiple disjoint

---

motor concentrations are constant: [actin] = 12 μM; R_M = 0.01. Color corresponds to time according to calibration bar (b, left). Times (t_{start}, t_{end}) in minutes after initiation of actin polymerization: b. (2, 20); c. (2,120); d. (1,5). Scale bar 1 mm. **e–g**: Decomposition into clusters, delimited by black lines. Color indicates the largest (blue) and the second-largest (pink) cluster, whose sizes correspond to ξ_1 and ξ_2 respectively. Note that (g) does not have a second-largest cluster because we exclude long edge domains from our analysis (see Figure A6 in Appendix). **h**: Dependence of ξ_1 (blue circles) and ξ_2 (pink triangles) on crosslink concentration (R_C). Error bars denote standard errors of the mean for repeat experiments: 1, 6, 13, 14, 9, and 5 experiments for R_C = 0.002, 0.005, 0.01, 0.02, 0.05, and 0.1, respectively. *Inset*: Predicted dependence of ξ_1 and ξ_2 on connection probability p according to percolation theory, given experimental parameters (see Appendix).

clusters. At still higher R_C, motor activity contracts the entire network into a single dense cluster which often retains the square shape of the assay chamber (Fig. 1d).

To quantify the effect of connectivity on the length scale of network contraction, we developed an image processing algorithm which identifies the clusters in the final image and traces their origin back in time. As shown in Fig. 1, the initial areas of each cluster are small in weakly crosslinked networks (panel d). The smallest clusters are ~30 μm in size, which corresponds to the typical distance between myosin motor clusters in the absence of cross-links (Figure A1 in Appendix). However, the clusters increase in size when the crosslink density is increased (panel f). In strongly crosslinked networks, the entire network forms one cluster (panel g).

Qualitatively, the transition from local to macroscopic contraction is reminiscent of a classical conductivity percolation transition. Below this transition, a system is only locally correlated and cannot establish connections over long distances. Only above a certain critical connectivity can the system establish global correlations. In order to determine the extent of agreement between our experimental results and percolation theory, we investigate three key predictions (Stauffer and Aharony, 1994).

First, conductivity percolation theory predicts how connectivity determines the size of the largest and second-largest connected clusters. Connectivity is quantified by the probability p of creating a connection. The largest cluster (of size ξ_1) is predicted to increase monotonically with p, while the second-largest cluster (of size ξ_2) should exhibit a peak right at the conductivity percolation threshold, where ξ_1 and ξ_2 both approach the system size, L (Fig. 1h, inset). Our experiments agree with this prediction: the measured cluster sizes, ξ_1 and ξ_2, are both small at low crosslink density and increase monotonically with increasing crosslink concentration until they approach the system size, $L \approx 2.5$ mm, around $R_C \sim 0.01$ (Fig. 1h). Above this threshold connectivity, ξ_1 remains close to L whereas ξ_2 decreases towards zero as the entire network contracts to one large cluster.

Second, percolation theory predicts how cluster sizes are distributed: around the critical point, we should find a power law with an exponent of −2. To test this prediction, we begin by looking for networks

which satisfy $\xi_1 \sim \xi_2 \sim L$. We replot all measurements separately in ξ_1-ξ_2-space (Fig. 2a). Because $\xi_2 < \xi_1$ by definition, all samples are located within a triangle in ξ_1-ξ_2-space. We can clearly identify the samples at the triangle's peak, where $\xi_1 \sim \xi_2 \sim L$. We denote this peak as the *critically connected regime*. To the left of the peak are samples with low R_C, which we denote the *local contraction regime*. To the right of the peak are samples with high R_C, the *global contraction regime*.

Do the samples in the critically connected regime really exhibit critical behavior? To test this more rigorously, we plot the entire distribution of cluster sizes (Fig. 2b). We represent the observed distribution as a histogram (open circles), where power-law distributions appear as straight lines on a log-log plot. We additionally plot complementary cumulative probability distributions (solid lines), whose visual form does not depend on bin size. We find that our experiments are again consistent with percolation theory: the critically-connected regime indeed exhibits a cluster-size distribution that is statistically consistent with a power-law across more than two orders of magnitude in measured area (Clauset et al., 2009). The power-law exponent is −1.9, close to the exponent of −2 predicted by percolation theory. The distributions of the other two regimes furthermore agree with percolation theory. The local contraction regime exhibits a short-tail distribution with a sharp cut-off. The global contraction regime exhibits a bimodal distribution with two well-separated length scales: the percolating cluster with size $\xi_1 \sim L$ and other small disjointed clusters with a typical size of $\xi_2 << L$.

Third, percolation theory predicts that only systems that are close to the critical point should exhibit a power law. But this prediction is difficult to reconcile with our data: the critically connected regime in ξ_1-ξ_2-space (Fig. 2a) is populated by samples which span a wide range of cross-link densities (from $R_C = 0.01$ to $R_C = 0.1$). This is also reflected in Fig. 1h, which shows a broad ξ_2-peak that is over half an order of magnitude wide in R_C, in sharp contrast with the narrow ξ_2-peak expected from percolation theory (inset of Fig. 1h). We can therefore conclude that classical conductivity percolation theory cannot provide a complete description of the physics of active, contractile networks.

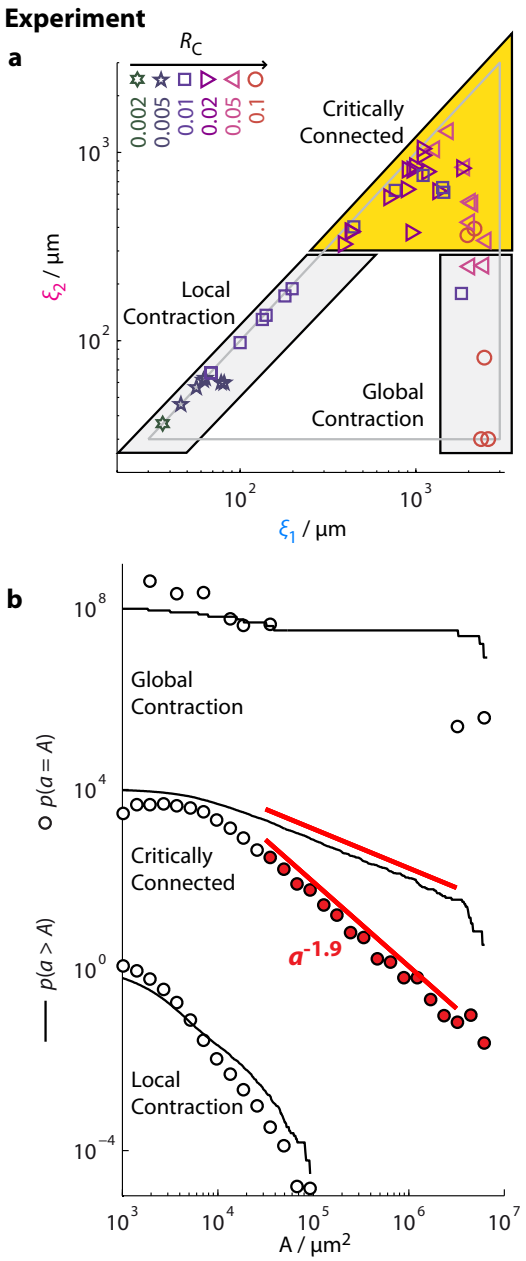

Figure 2: Cluster size distributions depend on network connectivity, exhibiting power-law distributions when $\xi_1 \sim \xi_2 \sim L$. **a**. Scatter plot of 48 samples with different R_C in ξ_1-ξ_2-space (see legend, top left). Boxes delimit different regimes: local contraction ($\xi_1 < 300$ µm), critically

5.3 Simulations

Percolation theory describes a network with a fixed connectivity. This can be appropriate for equilibrium fiber networks without internal driving. However, in motor-driven networks, the total connectivity can change significantly (Haviv et al., 2008; Murrell and Gardel, 2012; Vogel et al., 2013). When we image our networks at high resolution, we found that motors actively pull on network strands and disconnect them, thereby reducing connectivity (Alvarado et al., 2013). Crosslinks bind only transiently (~10 s in case of fascin (Courson and Rock, 2010)), and their binding kinetics are typically stress-dependent (Evans and Ritchie, 1997). There is strong evidence that unbinding of fascin crosslinks is promoted under stress. For instance, in gliding assays where actin-fascin bundles move over immobilized myosin motors, the motors actively zipped open the bundles (Ishikawa et al., 2003). We hypothesize that such stress-dependent binding kinetics allow motor activity to drive initially well-connected networks down towards a critically connected state.

To test this hypothesis, we develop a computational model of contractile actin-myosin networks using molecular dynamics. We model actin filaments with a planar triangular lattice of nodes

---

connected ($\xi_1 \geq 300$ μm and $\xi_2 \geq 300$ μm), and global contraction ($\xi_1 \geq 1500$ μm and $\xi_2 < 300$ μm). Two data points with $\xi_2 = 0$ are depicted here with $\xi_2 = 30$ μm. **b**: Histogram (circles) and complementary cumulative probability distribution (solid lines) of cluster areas, a / μm^2, for the three regimes. For the critically connected regime, data across more than two orders of magnitude (red circles) are statistically consistent with a power-law distribution (solid red lines) with an exponent of -1.91 ± 0.06, $p = 0.52$, where $p > 0.1$ indicates plausible agreement with a power law (see Appendix). Note that the slope of the complementary cumulative probability distribution is equal to one plus the slope of the histogram because the histogram is the absolute value of the derivative of the complementary cumulative probability distribution.

Figure 3: Simulations show that motors can drive initially well-connected networks to a critical state. **a**: Schematic representation of the simulation. A triangular lattice of nodes, connected by line segments (black lines), contains an average of N crosslinks per node (purple circles). During the course of the simulation, pairs of nodes experience contractile forces (orange arrows) and move in response to these forces. **b**: Temporal evolution of a representative network in the absence of remodeling. **c**: Motors cause network restructuring by generating tension T on crosslinks that increases the off-rate k_{off}. **d-j**: Simulated networks exhibit behavior consistent with experiment. **d,f,g**: Temporal evolution of three networks differing in initial connectivity: a. $c = 0.025$; b. $c = 3$; c. $c = 10000$. Force is constant: $f / k = 50$. Color corresponds to simulation time according to calibration bar (d, left). Box size L is 100 times longer than the initial lattice size l_0. **e,g,i**: Decomposition into clusters, shaded by pastel colors. Bold color indicates the largest (blue) and the second-largest (pink) clusters, whose sizes correspond to ξ_1 and ξ_2 respectively. **j**: Dependence of ξ_1 (blue circles) and ξ_2 (pink triangles) on crosslink concentration c across repeat simulations. Open symbols indicate values at $t = 0$, which corresponds to passive networks described by classical percolation theory. Closed symbols indicate values at the end of the simulation, after the network has broken up into clusters. Yellow regions correspond to values of c for which $\xi_2 > L / 10$ and the cluster size distribution exhibits a power-law. Note that this region is narrow for classical percolation theory (diagonal yellow stripes) but broadens substantially in response to active internal driving (solid yellow box).

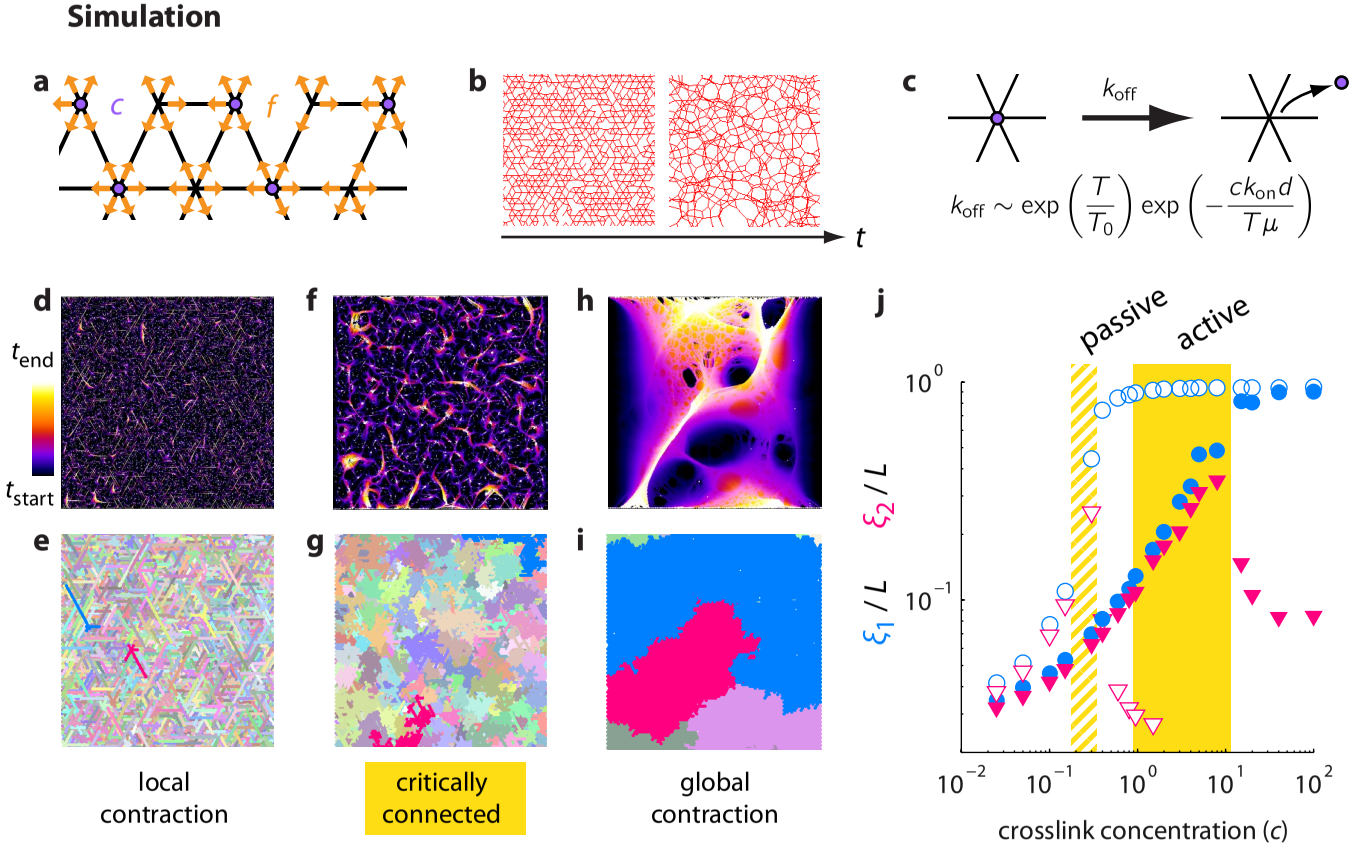
Simulation
a
c
f
b
t
c
k_{off}
$k_{off} \sim \exp\left(\frac{T}{T_0}\right) \exp\left(-\frac{ck_{on}d}{T\mu}\right)$
d
t_{end}
t_{start}
f
h
e
g
i
local contraction
critically connected
global contraction
j
passive
active
ξ_2 / L
ξ_1 / L
10^0
10^{-1}
10^{-2}
10^{-1}
10^0
10^1
10^2
crosslink concentration (c)

connected by line segments of length l_0 (Fig. 3a). Filaments possess stretching modulus k and can strain-stiffen (Storm et al., 2005) and buckle (Chaudhuri et al., 2007). We set the average number z of line segments connected to a node (i.e. coordination number) to 4.0. Point-like crosslinks are randomly placed on nodes with probability p, which depends on crosslink concentration c. We assume first-order kinetics of crosslink (un)binding, which yields $p = c/(1+c)$. We model the crosslinks by freely-hinged constraints, which prevent relative sliding of connected filaments. Motor activity results in contractile stresses (Lenz et al., 2012b; Mizuno et al., 2008; Soares e Silva et al., 2011b), which we model by pairs of forces f between nodes. Every node has mobility μ and experiences an effective, free-draining viscosity, η. The network evolves over time to achieve force balance at the nodes (Fig. 3b). For fixed crosslinks, network connectivity remains unchanged and ξ_1 and ξ_2 remain constant. We now introduce into the model the important ingredient of *network restructuring*: connectivity can change via crosslink unbinding and rebinding. The unbinding rate of a crosslink k_{off} increases exponentially with the tension T according to Bell's law (Evans and Ritchie, 1997): $k_{off} = k_{off,0} \exp(T / T_0)$, where $k_{off,0}$ denotes the off-rate in the absence of tension, and T_0 a characteristic tension (Fig. 3c). To account for rebinding, we consider the probability that an unbinding event is followed by a rebinding event at the same location before filaments are separated, which is given by $\exp(-c\, k_{on}\, d\, /\, T\, \mu)$, where d is an effective distance on the order of the mesh size over which filaments can move with velocity equal to $T\,\mu$ and k_{on} is the binding rate of a crosslink. The effective unbinding rate is thus given by

$$k_{off} = k_{off,0} \exp(T / T_0) \exp(-c\, k_{on}\, d/\, T\, \mu).$$

By varying c across many simulations (keeping f constant), we recover the three regimes found in experiment: the local contraction (Fig. 3d,e), critically connected (Fig. 3f,g), and global contraction regimes (Fig. 3h,i). The crosslink-dependence of ξ_1 and ξ_2 versus c (Fig. 3j) as well as the cluster size distributions (Figure A2 in Appendix) are fully consistent with experiment. The model clearly reveals that motor activity broadens the ξ_2-peak: in the absence of active network restructuring (panel j, open symbols), only a narrow region (yellow stripes) around the critical point exhibits critical behavior. In the presence of network restructuring (panel j, closed symbols), this region

broadens (solid yellow box). Motor-driven network restructuring can therefore account for the surprising robustness of critical behavior we found in experiment.

5.4 Motors promote network restructuring

So far we have investigated the effect of connectivity in experiment and simulation (R_C and N), but kept motor activity constant (R_M and f). Network restructuring breaks networks into clusters because motor stresses unbind crosslinks. Increased motor activity should therefore increase tension on crosslinks, enhance their unbinding, and lead to smaller clusters. To test this hypothesis, we simulate well-connected networks with constant c but varying motor activity (modeled through changes in the force f). Increased force indeed leads to smaller clusters (Fig. 4a-d). At low force ($f/k < 0.1$), the networks contract macroscopically ($\xi_1 >> \xi_2$), while at higher force levels ξ_1 sharply decreases as f increases (Fig. 4e). Increasing f allows networks that would otherwise contract globally to exhibit clusters with a power-law size distribution.

In order to validate these predictions, we perform experiments in well-connected networks (R_C = 0.02) where we change motor activity by varying the myosin-to-actin molar ratio R_M. In agreement with the model's prediction, the length scale of contraction strongly depends on myosin concentration. For low motor concentrations up to R_M = 0.002, the networks appear stationary for the entire duration of the experiment. Large-scale collective breathing fluctuations are visible, indicative of a strongly connected network, but the motors exert insufficient force to contract the network (Alvarado et al., 2013). Increasing the motor concentration to R_M = 0.005 results in a drastic change: the entire network collapses into one large cluster mediated by a uniform global contraction (Fig. 4f,h). However, a further increase of R_M results in smaller clusters (Fig. 4g,i). At high motor densities, ξ_1 decreases in a

Figure 4: Simulation and experiment both show that increased motor force reduces cluster size. **a,b**: Temporal evolution of two simulated networks with constant network connectivity (c = 3) but with either (a) low force, $f / k = 3$; or (b) high force, $f / k = 150$. Color corresponds to simulation time. **c,d**: Decomposition into clusters. **e**: Dependence of ξ_1 (blue circles) and ξ_2 (pink triangles) on force f. **f,g**: Temporal evolution of two experimentally prepared networks with (f) low myosin concentration, R_M = 0.005; or (g) high myosin concentration, R_M = 0.02. Color corresponds to time. Times (t_{start}, t_{end}) in minutes after initiation of actin polymerization: a. (2, 43); b. (2,14). The network connectivity is the same in both cases ([actin] = 12 μM, R_C = 0.02). **h,i**: Decomposition into clusters. **j**: Dependence of ξ_1 (blue circles) and ξ_2 (pink triangles) on myosin concentration, given by R_M. Scale bars 1 mm. Error bars denote standard errors of the mean for repeat experiments: 5, 14, and 5 experiments for R_M = 0.005, 0.01, and 0.02, respectively. Dashed lines depict f^{-1} (panel e) and R_M^{-1} (panel j).

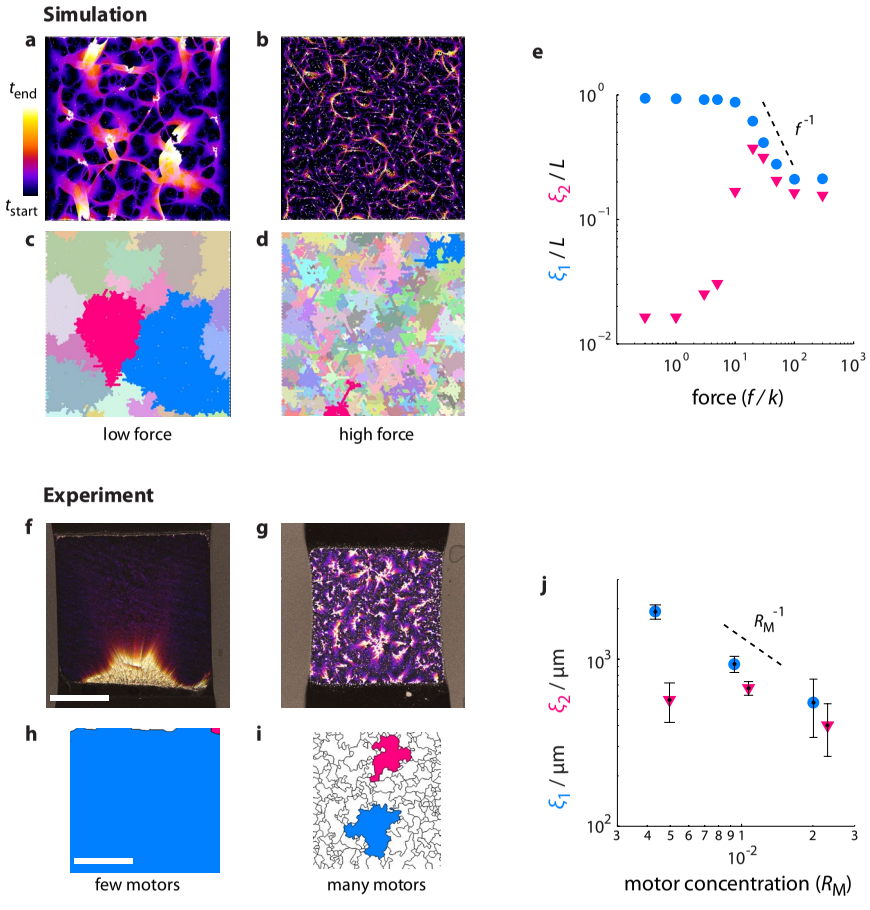
Simulation
a
b
t_{end}
t_{start}
c
d
low force
high force
e
10^0
10^{-1}
10^{-2}
ξ_2 / L
ξ_1 / L
f^{-1}
10^0 10^1 10^2 10^3
force (f / k)
Experiment
f
g
h
i
few motors
many motors
j
10^3
10^2
ξ_2 / µm
ξ_1 / µm
R_M^{-1}
3 4 5 6 7 8 9 1 2 3
10^{-2}
motor concentration (R_M)

manner consistent with the model's prediction (Fig. 4j) and we again recover scale-free cluster size distributions (Figure A3 in Appendix.)

These results lead to a counterintuitive consequence: in order to coordinate contractions over macroscopic length scales, *less* motor activity is needed. Increasing motor activity only yields small clusters.

5.5 Motors nucleate concurrent ruptures

In order to better understand the effect of force on cluster size, we consider the opposing limits of local and global contraction in our simulations. These two regimes are clearly separated by the critically connected regime, as evident in the schematic phase space diagram in Fig. 5. The global contraction regime is located at the bottom-right corner, where motor forces are low and network connectivity is high. In this limit, networks are rigid, filaments remain straight, and the network deforms affinely (Broedersz et al., 2011). On the opposite corner of the phase diagram, where connectivity is low and force is high, we find the local contraction regime. Such weakly connected, loose networks deform nonaffinely, and filaments are significantly bent.

We can interpret these limits by considering two relevant timescales, τ_{off} and τ_{relax}. The first timescale is the characteristic crosslink unbinding time $\tau_{off} = k_{off}^{-1}$. The tension T experienced by a crosslink depends on both the motor force f and the network configuration, which can change over time. Although the full dependence of crosslink tension on motor force is complex, the qualitative behavior is clear: when filaments are straight, motor stress does not greatly induce crosslink tension; when filaments are bent, crosslinks experience tension (Figure A4 in Appendix).

The second timescale, τ_{relax}, is the time it takes for filaments in the network to relax in response to a crosslink unbinding event. We estimate the values of τ_{off} and τ_{relax} from previous work (Courson and Rock, 2010; Gisler and Weitz, 1999):

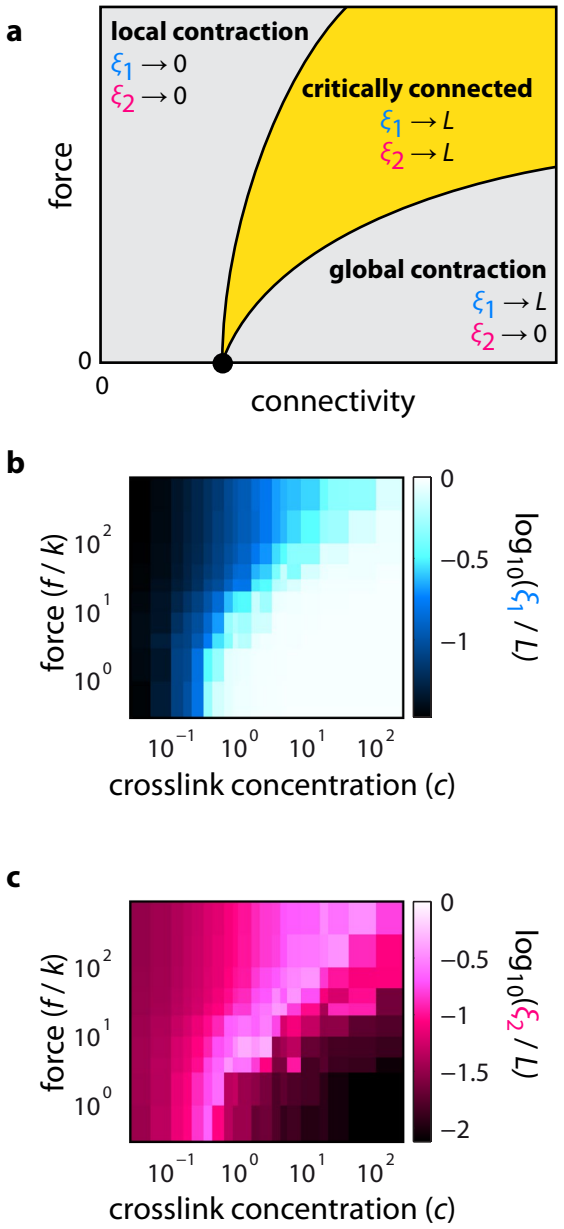

Figure 5: The critically connected regime broadens with increasing force. **a**: Schematic of proposed phase diagram in force-connectivity space, where the critically connected regime separates the local contraction and global contraction regimes. **b, c**: Dependence of ξ_1 (b) and ξ_2 (c) simulated over a broad range of force and connectivity.

$\tau_{off,0} \sim 1–10s$ $\tau_{relax} \sim 0.1–1s.$

The above value for τ_{relax} is set by the thermal equilibration of individual filaments. It acts as an upper bound: forces can cause faster relaxation. Therefore in the absence of tension, $\tau_{off} > \tau_{relax}$.

We now consider how these timescales respond to the two limits of local and global contraction. In the global contraction limit, f and T are small, and $\tau_{off} > \tau_{relax}$ holds: once a crosslink unbinds, the network fully relaxes before the next crosslink unbinds. This well-known limit corresponds to a quasistatic process (Heussinger, 2012). Boundary conditions determine how the network evolves in this limit: networks fixed at rigid boundaries build up stress and rupture via the nucleation of a large crack at a microscopic flaw, reminiscent of Griffith's criterion (Griffith, 1921). Unanchored networks contract affinely, or drive shape changes when coupled to deformable boundaries (Martin et al., 2009).

In the opposite limit of local contraction, f and T are large, and the network satisfies $\tau_{off} < \tau_{relax}$: strong internal driving causes crosslinks to unbind quickly. Many cracks that rupture the network into clusters form across the whole network, rather than nucleating at a single flaw. The presence of a finite viscosity in our model is essential for this behavior. Neglecting viscosity leads to $\tau_{relax} = 0$, and networks fail only via quasistatic crack propagation (Heussinger, 2012).

In between the two limits of global and local contractions, we find critically connected networks with a scale-free distribution of clusters. For zero force, this regime is narrow and centered around the critical point. As forces increase, this regime broadens and shifts to higher connectivities. This rightward shift reflects an asymmetry where motor activity reduces connectivity, rather than increasing it. The broadening shows that increased motor activity drives networks more robustly to a critical state.

Intriguingly, robust critical behavior has been demonstrated in many biological systems (Bialek et al., 2012; Camalet et al., 2000; Mora and Bialek, 2011; Veatch et al., 2008; Zhang et al., 2010). Internal driving could underlie robust criticality (Furusawa and Kaneko, 2012), but so could other mechanisms, including natural selection (Halley and Winkler, 2008; Torres-Sosa et al., 2012). Disentangling these mechanisms cannot be addressed by studying living systems alone. Here we report robust criticality in a minimal model system and show that

internal driving is directly responsible. These results may help explain criticality in other biological contexts and may prove useful in designing the physical properties of synthetic active materials, which have recently become available (Bertrand et al., 2012).

Our framework offers a minimal microscopic mechanism that should help in modeling contractile systems in biology. Recent studies in live cells suggest that motor myosin-driven cytoskeletal ruptures play an important functional role in cell division, (Sedzinski et al., 2011), whereas they contribute to developmental defects in developing embryos (Martin et al., 2010). Consistent with our findings, decreased connectivity caused dramatic rupture of the ventral furrow into clusters of cells in developing fly embryos. We anticipate that our framework applies more generally to tissues of interconnected cells (Schwarz and Safran, 2002; Schwarz and Gardel, 2012), where a supracellular actomyosin network transmits forces over tissue length scales.

5.6 Appendix

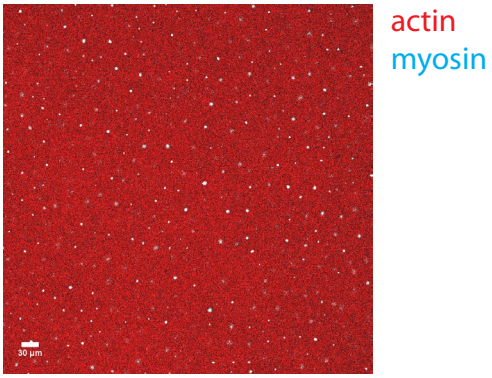

Figure A1: Confocal image of actin (red) and myosin (cyan) in the absence of crosslinks ([actin] = 12 μM, R_M = 0.01, t ~ 2 h after the initiation of actin polymerization). Myosin motors form small foci, which are separated approximately 30 μm apart.

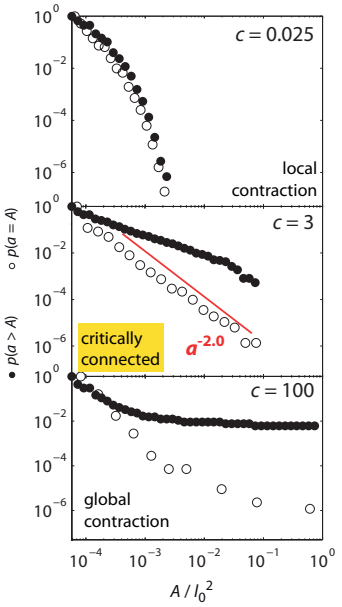

Figure A2: Simulated histogram (open circles) and corresponding cumulative probability distribution (closed circles) of cluster areas, a / l_0^2, for the three conditions shown in the main text, Fig. 3d-f. Solid red lines denote a power law with exponent −2.0.

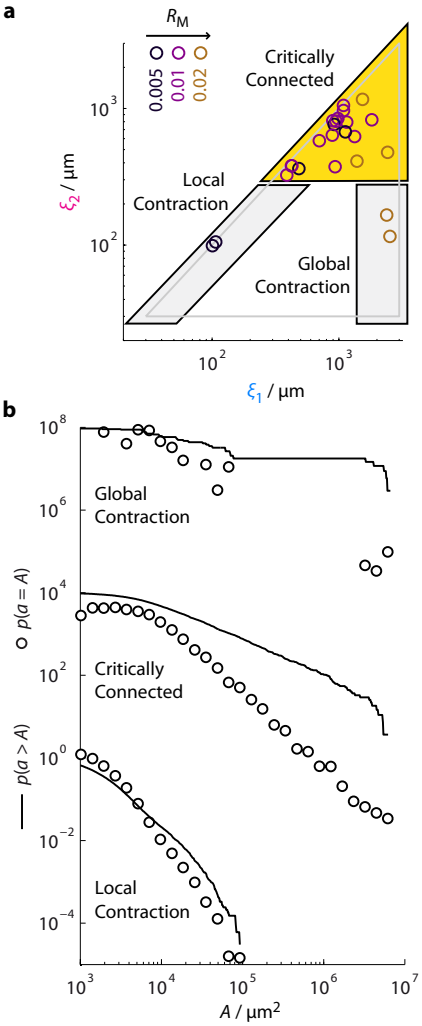

Figure A3: Increased myosin activity results in smaller clusters. **a**: Scatter plot of samples with different R_M in ξ_1-ξ_2-space (see legend, top left). Crosslink concentration is constant ($R_F = 0.02$). Boxes delimit different regimes: local contraction ($\xi_1 < 300$ µm), critically connected ($\xi_1 \geq 300$ µm and $\xi_2 \geq 300$ µm), and global contraction ($\xi_1 \geq 1500$ µm and $\xi_2 < 300$ µm). **b**: Histogram (circles) and corresponding cumulative probability distribution (solid lines) of cluster areas, a / µm^2, for the three regimes. For the critically connected regime, data across more than two orders of magnitude are consistent with a power-law distribution with an exponent of –1.90 ± 0.06 ($p = 0.12$, $a_{min} = (20 \pm 8)\ 10^3$ µm^2).

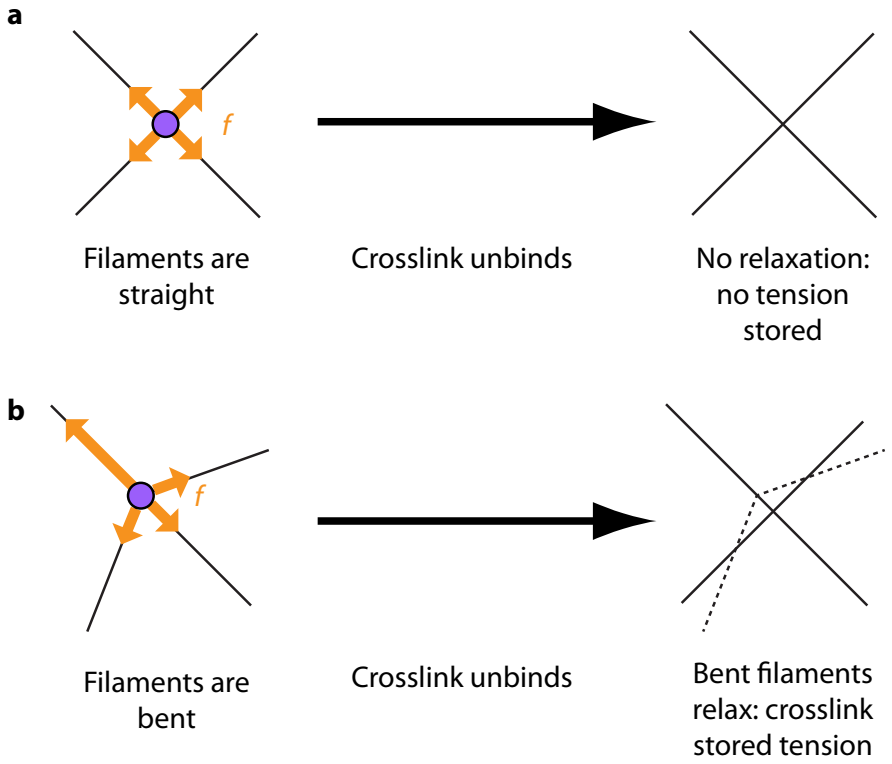

Figure A4: Bent filaments induce tension on crosslinks. **a**: Two straight filaments (black lines) are crosslinked (purple circle) at their intersection. If forces (orange arrows) are balanced, the crosslink experiences zero tension. This is evident because if the crosslink unbinds (right), no relaxation occurs. **b**: A straight filament and a bent filament are crosslinked. Although forces are balanced, the crosslink here experiences tension. This is evident because if the crosslink unbinds (right), the bent filament relaxes to a straight conformation.

Algorithm for determining cluster size. We developed a MATLAB algorithm to determine sizes of contracting clusters from time-lapse images of contractile actomyosin networks. Actin filaments and myosin motors were fluorescently labeled to appear in separate channels. In short, this technique begins with the final frame of acquisition (Fig. A5a), determines clusters, and tracks the expansion of these clusters back in time until the first frame of acquisition. The result is a decomposition of the initial network into clusters.

Step 1: the final acquired image from the actin channel (Fig. A5b) was median-filtered with a radius of 1px (Fig. A5c). This step filters out noise.

Step 2: the median-filtered image was thresholded using Otsu's method (Otsu, 1975) (Fig. A5d). The result of this step is a binary image of only black or white pixels. Contiguous groups of white pixels are called connected components. Each connected component corresponds to a cluster of actin and myosin.

Step 3: the final acquired image from the myosin channel (Fig. A5e) was also median filtered with a radius of 1px (Fig. A5f).

Step 4: the median-filtered image was thresholded using Otsu's method (Fig. A5g), again yielding a black-and-white image of connected components that correspond to clusters of actin and myosin.

Step 5: the thresholded image was morphologically opened (successive dilation and erosion) using a 1-px-radius-disk as a structuring element (Fig. A5h). This step serves as an additional filter, removing connected components smaller than the structuring element.

Step 6: connected components from step 5 were assigned to connected components from step 2 (Fig. A5i). Note that the connected components from step 2 (actin) are usually large, and contain many smaller connected components from step 5 (myosin). Without this step, the disjoint connected components from step 5 could be erroneously treated as separate clusters.

Step 7: domains were defined around each cluster, using the MATLAB function bwdist, which performs a distance transform (Fig. A5j). This step decomposes the entire image into a Voronoi-like diagram, where domain boundaries occur halfway between connected components.

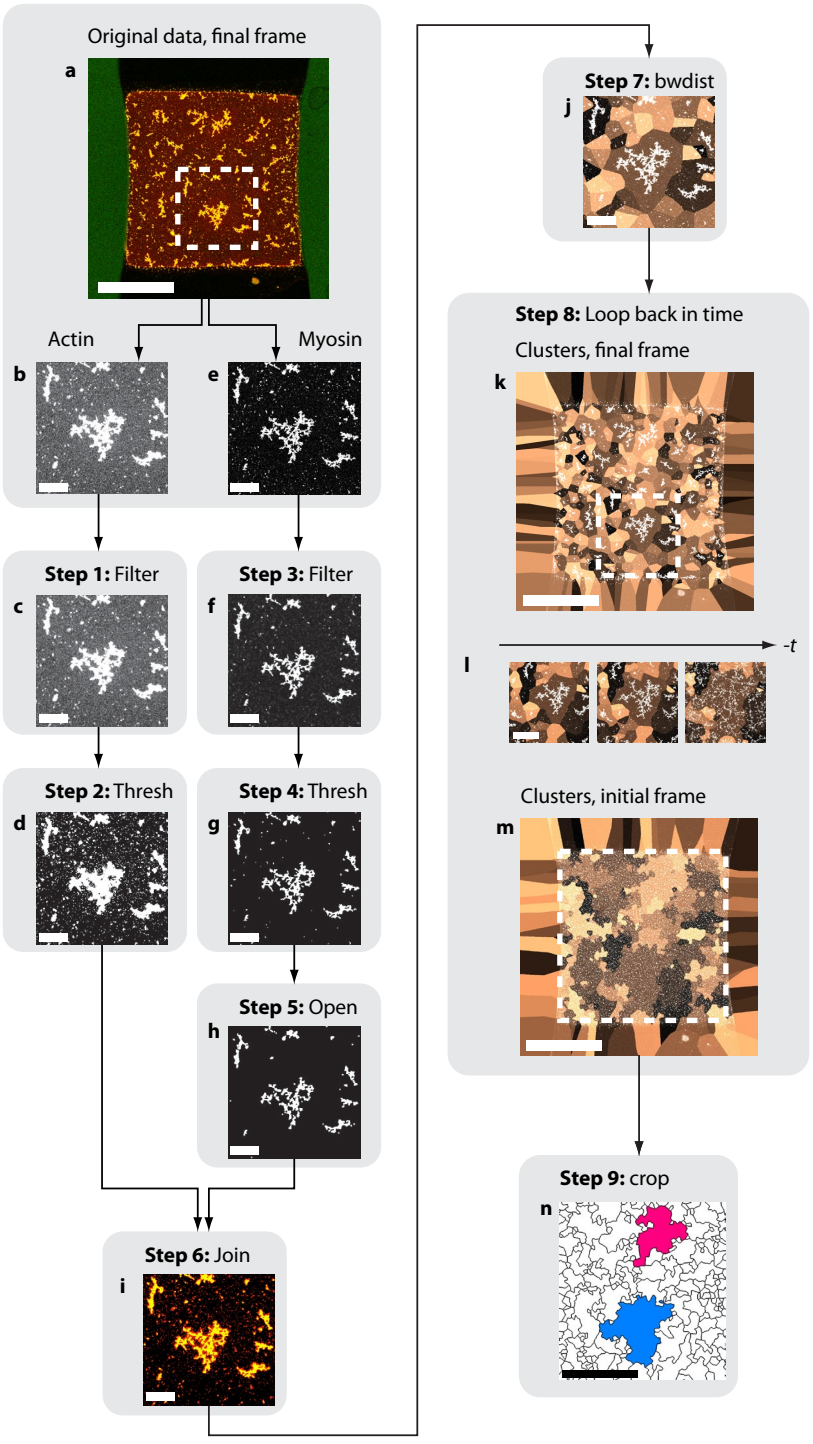
Original data, final frame
a
Actin
Myosin
b
e
Step 1: Filter
Step 3: Filter
c
f
Step 2: Thresh
Step 4: Thresh
d
g
Step 5: Open
h
Step 6: Join
i
Step 7: bwdist
j
Step 8: Loop back in time
Clusters, final frame
k
-t
l
Clusters, initial frame
m
Step 9: crop
n

Step 8: steps 3-7 were repeated for the myosin channel, starting with the final acquired frame (Fig. A5k), looping through successive acquired images backwards in time (Fig. A5l), and finally arriving at the first acquired frame (Fig. A5m). The end result is the first acquired frame, where the actin and myosin signals are uniformly distributed, and decomposed into clusters. During the loop, steps 3-7 were unchanged, except for step 6: myosin connected components were joined not by using actin connected components, but by the domains from the previous iteration of step 7.

Step 9: finally, the image of domains produced from step 7 of the final loop was cropped to the largest rectangle contained by the network.

Figure A5. Cluster-size algorithm. **a**: Final image of a time-lapse acquisition of a contractile actomyosin network (t = 80 min). Alexa-594-actin is shown in red, DyLight-488-myosin in green. [actin] = 12 μM, R_F = 0.02, R_M = 0.02. **b**: Close-up of the actin channel, corresponding to dashed box, *a*. **c**: Median filter of *b*. **d**: Otsu threshold of *c*. **e**: Close-up of the myosin channel, corresponding to dashed box, *a*. **f**: Median threshold of *e*. **g**: Otsu threshold of *f*. **h**: Morphological opening of *g*. **i**: Superposition of *d* (red) and *h* (green). Note that some disjoint green clusters are contained within one large red cluster. In this case, they are treated as one large cluster. **j**: Superposition of original myosin signal (white) with domains (shades of beige), which result from a distance transform, implemented in MATLAB as the *bwdist* function. **k**: Myosin signal (white) and domains (shades of beige) for the entire sample before looping the algorithm, beginning with the final frame (t = 80 min). **l**: Close-up of *k* (dashed box) at three representative stages of loop progression as clusters expand in -t (from left to right: t = 20 min, 8 min, 4 min). **m**: Myosin signal and resulting clusters for the first acquired frame (t = 2 min). Note that myosin is distributed homogeneously across the entire network at the beginning of acquisition, and is fully decomposed into clusters. **n**: Clusters (outlined in black) after cropping to dashed box, *k*, with largest and second-largest clusters denoted in blue and pink, respectively. Scale bars: a: 1 mm, b-j: 200 μm, k: 1 mm, l: 500 μm, m: 1 mm.

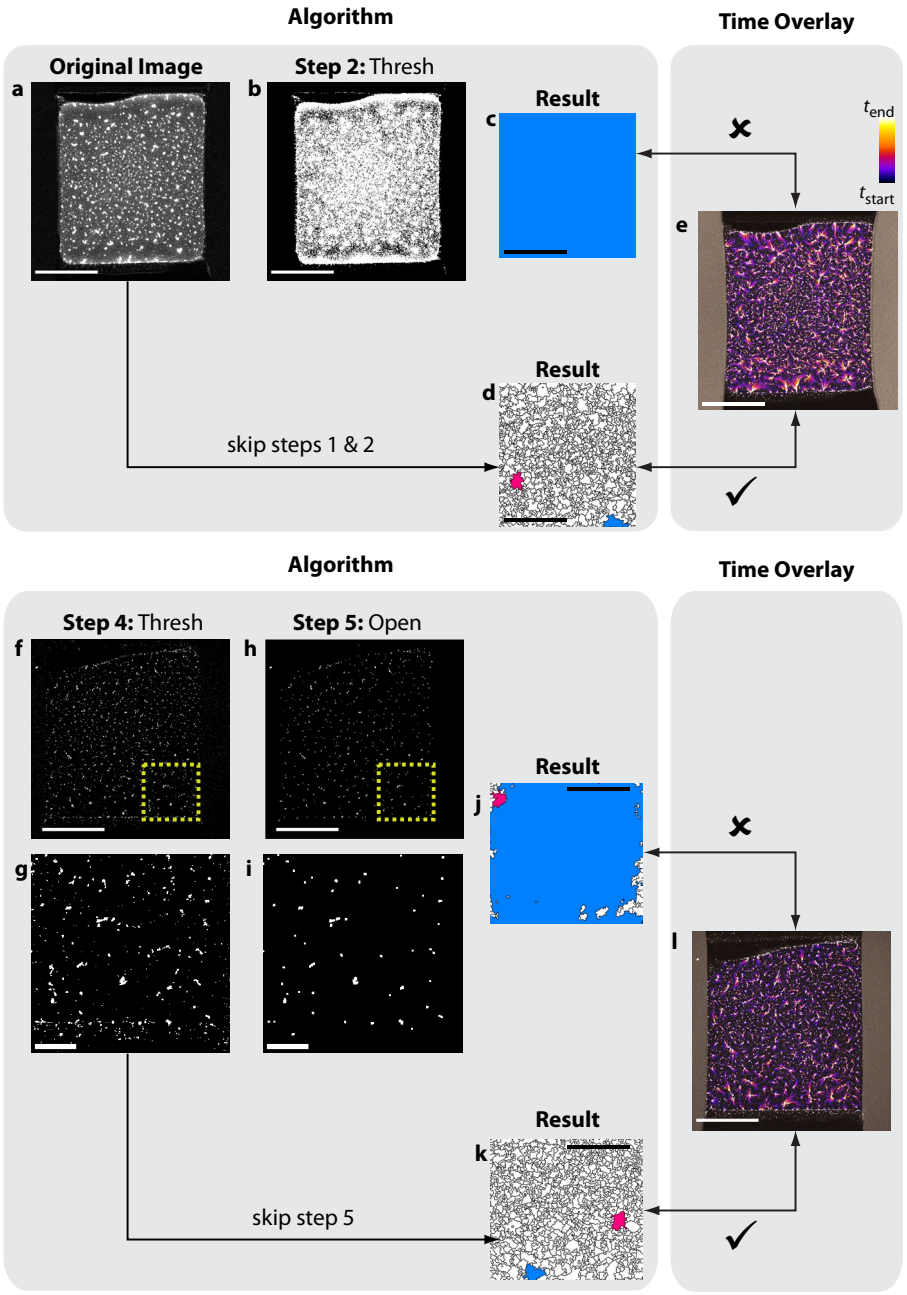

Figure A6. Two modifications of the cluster-size algorithm. **a-e**: First modification: skipping step 2 when it erroneously yields large, system-spanning connected clusters. **a**: Actin channel of original image (R_F

In two cases, adjustments to this routine were necessary. In one case, during step 2, Otsu's threshold sometimes yielded large connected components that spanned the image (Fig. A6a). This resulted in the network being erroneously represented as one large cluster (Fig. A6b). This artifact was eliminated by choosing a more restrictive threshold (Fig. A6c), which resulted in accurate domains (compare panels d and e). In another case, during step 5, morphological opening sometimes filtered out small, dim clusters (Fig. A6f). This led to their corresponding domains to disappear, and small, neighboring clusters were reported as bigger clusters (Fig. A6g). This artifact was eliminated by omitting step 5 (Fig. A6h), yielding accurate domains (compare panels i and j).

Adjustment of domains. We performed two types of adjustments to the cluster decompositions produced by our algorithm. First, we removed long edge domains from our analysis. These domains could

---

= 0.01, R_M = 0.01, local contraction regime). **b**: Result of step 2. Note that the thresholded image does not resemble the individual clusters visible in the original image. **c**: Result of continuing the algorithm, which erroneously represents the sample as one large cluster. **d**: Result of the algorithm, skipping steps 1 and 2. Note that this image correctly represents individual clusters. **e**: Overlay of acquired data, where color corresponds to time (calibration bar, top right). t_{start} = 1 min; t_{end} = 20 min. Note that this image qualitatively captures cluster evolution, and is obtained independently of the cluster-size algorithm. Comparing to panels *c* and *d* shows that panel *d* more accurately represents true cluster size. **f-l**: Second modification: skipping step 5 when it removes small, dim myosin clusters. **f**: Result of step 4 (R_F = 0.01, R_M = 0.01, local contraction regime). **g**: Close-up of *f*, green dashed box. **h**: Result of step 5. **i**: Close-up of *h*, green dashed box. Note that morphological opening removes very small clusters. **j**: Result of continuing the algorithm, which erroneously joins together many small clusters in one large cluster. **k**: Result of the algorithm, skipping step 5. Note that this image correctly represents individual clusters. **l**: Time overlay, as in *e*. t_{start} = 2 min; t_{end} = 30 min. Comparing to panels *j* and *k* shows that panel *k* more accurately represents true cluster size.


Time Overlay
Result of Algorithm
Corrected
t_{end}
t_{start}
$R_F = 0.02$
$R_M = 0.005$
$\xi_1 = 2135$ µm
$\xi_2 = 488$ µm
$\xi_1 = 2387$ µm
$\xi_2 = 163$ µm
$R_F = 0.02$
$R_M = 0.005$
$\xi_1 = 2281$ µm
$\xi_2 = 580$ µm
$\xi_1 = 2435$ µm
$\xi_2 = 456$ µm
$R_F = 0.02$
$R_M = 0.005$
$\xi_1 = 2205$ µm
$\xi_2 = 716$ µm
$\xi_1 = 2535$ µm
$\xi_2 = 141$ µm
$R_F = 0.05$
$R_M = 0.01$
$\xi_1 = 2036$ µm
$\xi_2 = 531$ µm
$\xi_1 = 2300$ µm
$\xi_2 = 337$ µm
$R_F = 0.05$
$R_M = 0.01$
$\xi_1 = 1996$ µm
$\xi_2 = 573$ µm
$\xi_1 = 2304$ µm
$\xi_2 = 622$ µm

be the result of enhanced interactions with the edge of the confining geometry, in addition to internal driving by myosin activity. We first search for domains that touch the border of the cropping rectangle (Fig. A5m, dashed line). We next compute the major and minor axis of the ellipse that has the same normalized second central moment of each domain, as well as the orientation of the major axis. Finally, we consider edge domains which satisfy the following two conditions: (i) the major-axis-to-minor-axis ratio is greater than two; (ii) the major axis is oriented along the edge that the domain touches to within 45°. (Condition ii is dispensed for corner domains that touch two edges.) Edge domains that satisfy these two conditions are then omitted from the sums in the definition of ξ_1 and ξ_2, as well as when plotting distributions.

Second, we compensated for fast clusters. Sometimes the displacement of a cluster between two successive frames was greater than the half-way distance to a neighboring cluster. Clusters would then leave their own domain and erroneously enter neighboring domains. This artifact mostly affected networks in the global contraction regime, where the global build-up of stress led to fast relaxation events. This artifact cannot be addressed by modifying the algorithm. We therefore manually corrected contraction domains to accurately reflect network evolution. A total of five corrections were performed, all of which are reported in Fig. A7.

These two adjustments to domain size affect our results for the global contraction regime. This is evident by inspecting the effect of the two adjustments on cluster size distributions (Fig. A8a). However, the local contraction and critically connected regimes are largely unaffected. The power-law exponents determined from experiment are robust to the two adjustments described above (Fig. A8b).

Figure A7: Manual correction of five experiments. True sample dynamics is depicted in the time overlay (first column). For these five experiments, the algorithm produces excessively large domains (second column). Upon careful visual inspection of the original data, erroneous domains were manually corrected to their apparent true size (third column). Scale bar 1 mm.

a

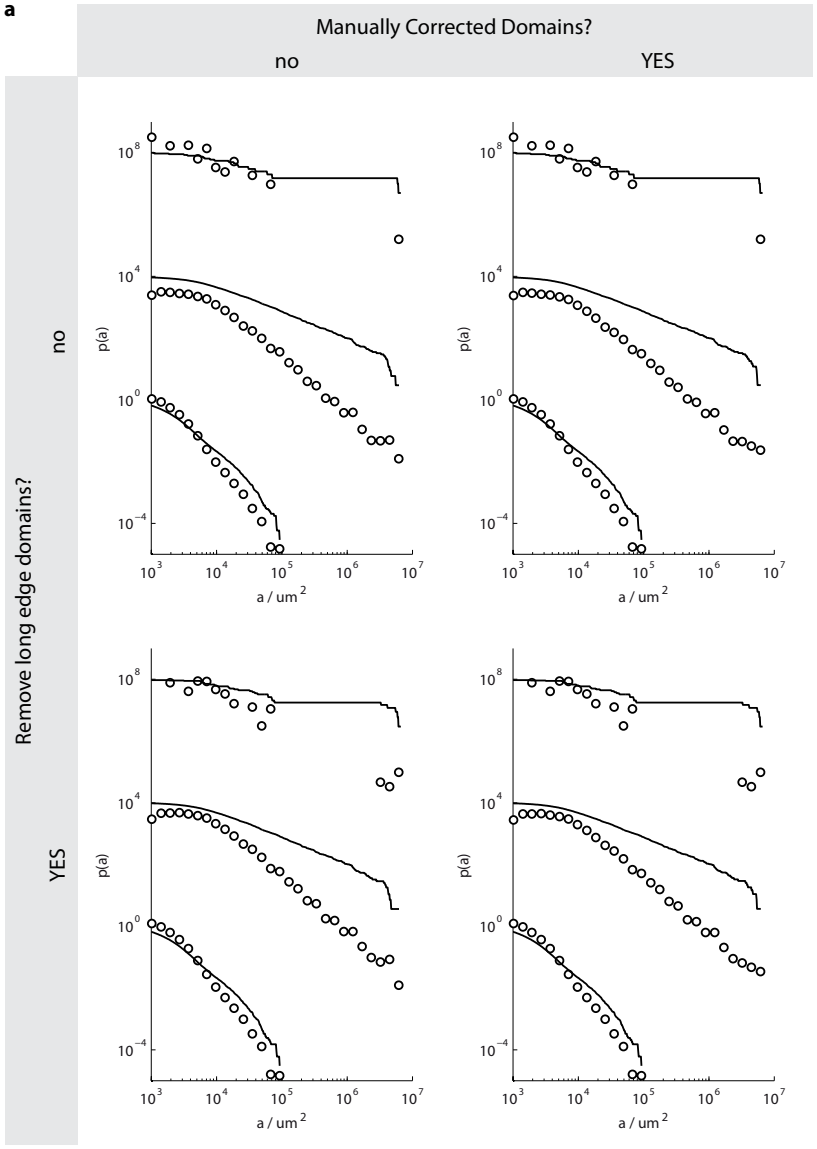

b

Remove long edge domains?	Manually corrected domains?	Power-law exponent	a_{min} / 10^3 µm^2	*p*
no	no	1.93 ±0.07	75.1 ±19.5	0.44
no	YES	1.91 ±0.07	73.0 ±19.4	0.40
YES	no	1.92 ±0.06	75.1 ±17.1	0.50
YES	YES	1.91 ±0.06	75.1 ±16.9	0.52

Statistical analysis of domain sizes. In order to determine whether cluster size distributions were consistent with a power law, we employed a recently developed, rigorous statistical analysis (Clauset et al., 2009). This technique first fits observed data to a power law, determining both the best exponent and best lower cut-off. The lower cut-off is the minimum value above which the power law is fitted. It then compares the observed dataset with multiple synthetic datasets (generated from a power-law distribution using the best fit parameters) by computing the Kolmogorov-Smirnov statistic, which quantifies the "distance" between a dataset and the true power-law distribution. Finally, it computes a p-value, which is defined as the fraction of synthetic datasets whose distance is greater than the observed dataset. Therefore, larger p-values correspond to an increased likelihood that the observed dataset is consistent with a power law. A power law can be ruled out for $p < 0.1$.

Percolation model. Our model is based on three-dimensional network of N straight filaments of length L placed in a W x W x W box. The filaments are placed such that their position and orientation is uniformly distributed. Two filaments are considered to be intersecting if the shortest distance between them is less than a certain value which is taken to be of the order of size of the cross link. At this intersection these two filaments can be connected by a freely hinging crosslink. The probability that such a crosslink exists is denoted by p. Periodic boundary conditions are assumed in all directions. The line density NL / W^3 is obtained from the experiments, and estimated to be ~20 μm^{-2}. Our simulations show that the connectivity percolation occurs in the vicinity of p=0.33.

Figure A8: Results from modifying algorithm output. **a**: Distributions of cluster sizes (R_M = 0.01) that result when either removing long edge domains (rows) or manually correcting domains (columns). Distributions are divided according to global contraction (top), critically connected (center), and local contraction (bottom) (see main text, Figure 2).

5.7 Methods

Protein Preparation. Monomeric (G-) actin and myosin II were purified from rabbit psoas skeletal muscle (Soares e Silva et al., 2011b). G-actin was purified with a Superdex 200 column (GE Healthcare, Waukesha, WI, USA) and stored at −80 °C in G-buffer (2 mM tris-hydrochloride pH 8.0, 0.2 mM disodium adenosine triphosphate, 0.2 mM calcium chloride, 0.2 mM dithiothreitol). Myosin II was stored at −20 °C in a high-salt storage buffer with glycerol (25 mM monopotassium phosphate pH 6.5, 600 mM potassium chloride, 10 mM ethylenediaminetetraacetic acid, 1 mM dithiothreitol, 50% w/w glycerol). Creatine phosphate disodium and creatine kinase were purchased from Roche Diagnostics (Indianapolis, IN, USA), all other chemicals from Sigma Aldrich (St. Louis, MO, USA). Magnesium adenosine triphosphate was prepared as a 100 mM stock solution using equimolar amounts of disodium adenosine triphosphate and magnesium chloride in 10 mM imidazole pH 7.4. Myosin II was labeled with Alexa Fluor 488 NHS ester (Invitrogen, Paisley, UK); actin was labeled with Alexa Fluor 594 carboxylic acid, succinimidyl ester (Soares e Silva et al., 2011b). Recombinant mouse fascin was prepared from T7 pGEX *E. coli* (Gentry et al., 2012).

Sample Preparation. Fresh myosin solutions were prepared by overnight dialysis into myosin buffer (20 mM imidazole pH 7.4, 300 mM potassium chloride, 4 mM magnesium chloride, 1 mM dithiothreitol) and used within four days. All frozen protein stocks (actin, myosin, fascin) were clarified of aggregated proteins upon thawing at 120,000 g for at least 5 min and used within four days. The proteins' concentrations in the supernatant were determined by measuring the solution absorbance at 280 nm with a NanoDrop 2000 (ThermoScientific, Wilmington, DE, USA) and using extinction coefficients, in M^{-1} cm, of 26600 (actin (Pardee and Spudich, 1982)), 249000 (myosin (Margossian and Lowey, 1982)) and 66280 (fascin, computed from amino acid sequence (Artimo et al., 2012)). Fluorescently labeled proteins were mixed with unlabeled proteins to yield a 10% molar ratio of dye to protein. During sample preparation, myosin and Alexa-488-myosin were mixed at high salt and then mixed into a tube containing fascin and buffer. This solution was mixed into a second tube containing actin and Alexa-594-actin to

initiate polymerization and immediately inserted into glass flowcells passivated by poly-L-lysine-polyethylene-glycol (Surface Solutions AG, Dübendorf, Switzerland).

Samples were mixed to yield a final buffer composition of 20 mM imidazole pH 7.4, 50 mM potassium chloride, 2 mM magnesium chloride, 1 mM dithiothreitol, and 0.1 mM adenosine triphosphate (ATP). Furthermore, 1 mM trolox, 2 mM protocatechuic acid, and 0.1 μM protocatechuate 3,4-dioxygenase were added to minimize photobleaching. The ATP level was held constant by addition of 10 mM creatine phosphate disodium and 0.1 mg mL^{-1} creatine kinase. The actin concentration was held constant at 12 μM (0.5 mg mL^{-1}). Freshly mixed actoymyosin solutions were loaded onto polyethylene-glycol-passivated flowcells with a geometry of 2.5 x 2.5 x 0.1-mm^3 and sealed with either Baysilone silicone grease (Bayer, Leverkusen, Germany) or uncured PDMS (Dow Chemicals, Midland, MI, USA). The time evolution of the network structure was observed with a Nikon PlanFluor 4x objective (NA 0.13), which allows the network to fit entirely within the objective's field of view.

Image Analysis. Cluster sizes were determined by a customized algorithm, implemented in MATLAB. Time-lapse images of contracting actomyosin networks were analyzed, starting from the final acquired frame. Cluster evolution, determined from Voronoi diagrams of myosin foci, was tracked by looping the algorithm backwards in time (see Appendix).

Definition of ξ_1 and ξ_2. For experimental results, we measure the areas a_i of the initial network that contract together, which we define as clusters. We define ξ_1 as the weighted mean of cluster sizes l_i (square root of area), in analogy to the definition of the correlation length from percolation theory (Stauffer and Aharony, 1994):

$$\xi_1 := \Sigma_i \, l_i \, a_i^2 \, / \, \Sigma_i \, a_i^2.$$

This length scale is dominated by the largest cluster. We furthermore define ξ_2 in analogy to percolation theory:

$$\xi_2 := \Sigma'_i \, l_i \, a_i^2 \, / \, \Sigma'_i \, a_i^2,$$

where Σ'_i denotes summation over all clusters except for the largest cluster, as well as long edge clusters (see Appendix). This length scale is dominated by the second-largest cluster.

For simulation results, ξ_1 and ξ_2 are given by the square root of the harmonic-averaged area of the largest and second largest clusters, respectively, over 10-100 disorder realizations for each set of parameters.

Preparation of flow cells. Glass flow cells were assembled by sandwiching strips of ParaFilm between a long cover slip (24 mm x 60 mm) and 2.5-mm-narrow glass strips which were manually cut from 40-mm-long cover slips. This yielded 2.5 x 2.5 x 0.1-mm^3-large chambers (corresponding to ~0.6 μL). All glass was cleaned with piranha solution, rinsed in MilliQ water, and stored in isopropanol. Assembled flow cells were then passivated by applying 1 M potassium hydroxide for 5 min, rinsing with MilliQ, drying with nitrogen, applying 0.2 mg mL^{-1} poly-L-lysine-polyethylene-glycol (Surface Solutions AG, Dübendorf, Switzerland) for 30 min, rinsing with MilliQ, and drying with N2.

Simulation. The values taken for the simulations are: the system size W=100, $k_{off,0} = 10$, $T_0 = 1$, $k_{on}\, d / \mu = 10$, $k = 1$. Buckling is implemented by vanishing force of a bond for a compression strain below 0.1. The stiffening is implemented by increase of the stretching constant by 100-fold for extension strain above 0.2.

Acknowledgements

Simulations were designed and performed by Misha Sheinman, Abhinav Sharma, and Fred MacKintosh (VU Amsterdam). We thank Marjolein Kuit-Vinkenoog, Magdalena Preciado-López, and Feng-Ching Tsai (AMOLF, Amsterdam, Netherlands) for help with purifications, Scott Hansen and Dyche Mullins (UC San Francisco, USA) for the fascin plasmid, Kota Miura (EMBL, Heidelberg, Germany) for the Temporal Color Code ImageJ plugin, Dirk-Jan Spaanderman and Henk-Jan Boluijt for assistance with the cover art of this chapter, and Chase Broedersz (Princeton University, NJ, USA) for insightful discussions.

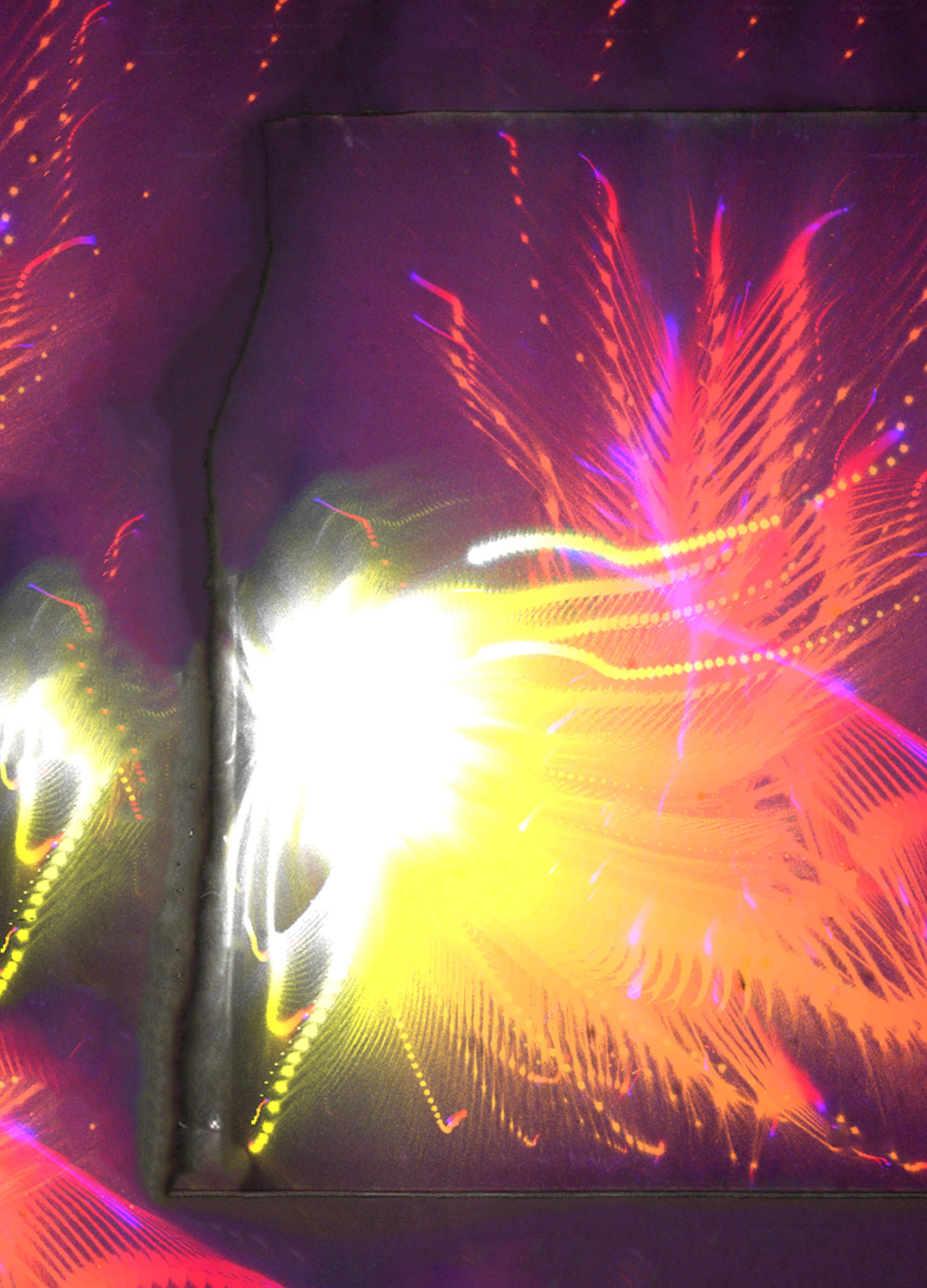


6

6. Phase behavior of contractile active gels

Cells and tissues can undergo remarkable shape changes which are driven by actively generated forces, such as pulling forces in the actin cytoskeleton generated by myosin motors. External biochemical signals are known to regulate the length scales over which these pulling forces act, but less is understood about how physical properties of the actin cytoskeleton affect these length scales. In order to provide insights into this question, we measure the length scale of contraction in reconstituted active gels composed of actin, skeletal muscle myosin II, and different crosslink proteins (fascin, fimbrin, and α-actinin). We vary motor activity by varying ATP and salt concentrations in the buffer, and vary network connectivity by varying actin filament density and length. Consistent with the results presented in Chapter 5, we find three contraction regimes: local, critical, and global. Increased network connectivity promotes larger-scale contraction, whereas increased myosin activity promotes rupture of contracting networks into many clusters. We summarize our data by proposing a phase-space diagram of connectivity-governed contractile active gels. At the end of the chapter, we report first data obtained with space- and time-resolved dynamic light scattering, probing the sample-age-dependent dynamics of contractile active gels. We simultaneously measure at four different scattering vectors and show that actomyosin networks exhibit a length-scale-dependent relaxation timescale. Furthermore, we find sudden bursts of microscopic de-correlation which occur just moments before contraction. Our data obtained for minimal active gels may help to interpret in vivo studies showing evidence of physical regulation of actomyosin contraction, for instance during cortical flows and cytokinesis.

6.1 Introduction

Cells and tissues can undergo remarkable shape changes which are driven by actively generated, internal forces. In order to accomplish this, cells rely on their cytoskeleton, an internal network of protein filaments which actively generates pushing and pulling forces. Pulling forces often result from myosin motor filaments, which harness chemical energy derived from ATP hydrolysis to pull actin filaments towards one another (Levayer and Lecuit, 2012). Although individual myosin motors are only ~0.1 μm in size and exert only ~pN forces (Finer et al., 1994; Howard, 2001), cells integrate the activity of many motors to produce nN contractile forces on cellular length scales. The most efficient example of this sort of force integration occurs in striated muscle cells, where contraction occurs on length scales that approach the length scale of the host organism. These contractions are mediated by a sarcomeric organization whose highly regular architecture allows efficient force transmission (Gautel, 2011; Huxley and Niedergerke, 1954; Huxley and Hanson, 1954).

Non-muscle cells lack sarcomeric organization, and have a much more dynamic and adaptive actin-myosin cytoskeleton than muscle cells (Vicente-Manzanares et al., 2009). Depending on cell state, nonmuscle cells generate contractile forces on varying scales. Myosin motors exert localized, short-length-scale pulling forces at the equator of dividing cells (Vavylonis et al., 2008) or in the rear of migrating cells (Kolega, 1998; Svitkina et al., 1997; Vicente-Manzanares et al., 2007). Cellular-length-scale pulling forces facilitate cytoplasmic chromosomal transport (Lénárt et al., 2005) or cortical polarizing flows in developing oocytes (Bray and White, 1988; Mayer et al., 2010). Epithelial sheets of myosin-rich cells coordinate contractions that drive shape changes over tissue length scales in developing embryos (Lye and Sanson, 2011; Martin et al., 2009; Rauzi et al., 2008) and healing wounds (Mandato and Bement, 2001; Sonnemann and Bement, 2013).

How is the length scale of contraction regulated? Cells exert tight control on myosin activity via regulatory enzymes and ligands coupled to reaction-diffusion networks, which establish spatial activation patterns (Bement et al., 2006; Goehring et al., 2011; Hall, 2012). Phosphorylation

of the regulatory light chain by multiple kinases induces a conformational change of nonmuscle myosin II from a folded inactive state to an opened active state, allowing binding to F-actin, ATPase activity, and assembly into filaments (Bresnick, 1999; Korn and Hammer, 1988). Single myosin motors are non-processive and cannot produce actin filament sliding or contraction (Kovács et al., 2003; Wang et al., 2003). However, they can assemble into filaments composed of typically 10-30 tail-to-tail associated myosins (Verkhovsky, 1993; Verkhovsky et al., 1995). These filaments are bipolar and processive, and thus capable of pulling on actin filaments of opposite polarity. Myosin assembly into filaments is further regulated through phosphorylation of the heavy chain. There are many additional regulatory mechanisms involving noncovalent interactions of myosins with other proteins such as tropomyosin (Bresnick, 1999; Gunning et al., 2005).

In addition to biochemical regulation, physical interactions can also contribute to regulation of the length scale of contraction, as evident from experiments on model systems reconstituted from purified proteins. Usually, these assays are based on three protein components: purified actin, purified myosin (generally skeletal muscle myosin II), and crosslink proteins to establish network connectivity. Together, these assays have established two minimal requirements for macroscopic contraction: a minimal motor activity and a minimal network connectivity (Bendix et al., 2008; Janson et al., 1991; Köhler et al., 2011a). Network connectivity depends on the concentration of crosslink molecules, which simultaneously bind two or more actin filaments, as well on the actin filament density and length. Minimum values of actin filament density (Köhler et al., 2011a) as well as crosslink density (Bendix et al., 2008; Köhler et al., 2011a) are required for contraction to occur. Several mechanisms may account for network contraction mediated by myosin motor activity. As shown experimentally (Murrell and Gardel, 2012; Soares e Silva et al., 2011b; Vogel et al., 2013) as well as theoretically (Dasanayake et al., 2011; Lenz et al., 2012b; 2012a), contraction can proceed via actin filament buckling. Alternatively, alignment or rearrangement of bundles and mobility of myosin II motor filaments may promote contraction (Dasanayake et al., 2011; Köhler et al., 2012). There is evidence that network contraction occurs only in an optimum window of crosslink density: in the absence of crosslinks,

myosin motors generate sliding forces which do not result in pulling (Humphrey et al., 2002; Le Goff et al., 2002b), yet, excessive crosslinks can inhibit contraction (Bendix et al., 2008; Janson et al., 1991; Köhler et al., 2012).

In vivo, the crosslink proteins that transmit myosin pulling forces are highly dynamic. They usually have dissociation rate constants in the μM-range and on-times of a few seconds (Courson and Rock, 2010). Moreover, their binding kinetics are responsive to forces. Usually, off-rates increase when a force is applied (Evans and Ritchie, 1997). However, some crosslink molecules such as filamin and α-actinin exhibit catch-bond behavior, with an off-rate that decreases when a force is applied (Ferrer et al., 2008; Yao et al., 2011; 2013). This raises the question how force-responsive binding kinetics of crosslinks will influence the contractile behavior of actomyosin networks as a function of motor activity and underlying network connectivity.

In order to answer this question, we investigated contractility of reconstituted actin-myosin networks crosslinked with fascin in Chapter 5 of this thesis. We showed that myosin motors contract and rupture these networks into clusters whose sizes are determined by an interplay between force-responsive binding kinetics of fascin crosslinks and motor activity. In the limit of low fascin concentration, networks show *local contraction*, with clusters whose typical sizes are far smaller than the system size. In the opposite limit of high fascin concentration, networks show *global contraction*, contracting entirely into one large cluster whose size approaches the system size. At intermediate crosslink densities, we observed an unexpectedly wide regime where networks contract into *large clusters*, characterized by a combination of small and large clusters with a scale-free size distribution. We proposed that this intermediate regime arises because above a critical network connectivity, motors not only contract the network but also reduce the connectivity of initially stable networks by promoting unbinding of fascin crosslinks. In combination with numerical simulations, our results suggested that the length scale of contraction is controlled by two main parameters: motor activity and network connectivity. However, we only varied two experimental parameters, motor density and crosslink density. Motor activity is also dependent on other factors such as motor processivity,

and network connectivity is also dependent on other factors such as actin filament density and length.

In this chapter, we experimentally test the generality of the proposed mapping of contractile "phase behavior" onto a phase space controlled by motor activity and network connectivity. We reconstitute minimal active gels from purified actin, skeletal muscle myosin II, and the crosslinks fascin, fimbrin, and α-actinin. We use different means to vary motor activity (by varying the level of ATP and the salt concentration) as well as different means to vary network connectivity (by varying actin filament density and length, and also by using different crosslink proteins). We measure the resulting length scales of motor-driven contraction by performing confocal microscopy of networks enclosed in customized flow-cells, which fit entirely in the field-of-view of a 4× microscope objective. We track the temporal evolution of the networks by time-lapse imaging and perform quantitative image analysis of cluster sizes. In Section 2, we present experimental results obtained for these reconstituted contractile active gels. In Section 3, we summarize our data by proposing a phase-space diagram of connectivity-governed contractile active gels.

6.2 Results

Modulating motor activity. In Chapter 5, we modulated the motor-generated forces in crosslinked actin-fascin networks by varying the concentration of motors. Here, we instead modulate the motor activity at constant motor density, by varying the monovalent potassium chloride (KCl) concentration. Increasing [KCl] is expected to weaken motor forces, since the binding affinity of myosin II for actin is reduced with increasing ionic strength (Brenner et al., 1982; Takiguchi et al., 1990), thus reducing motor processivity. The KCl concentration has also been reported to influence the size of myosin filaments (Davis, 1988; Kaminer and Bell, 1966; Katsura and Noda, 1973; Koretz, 1979;

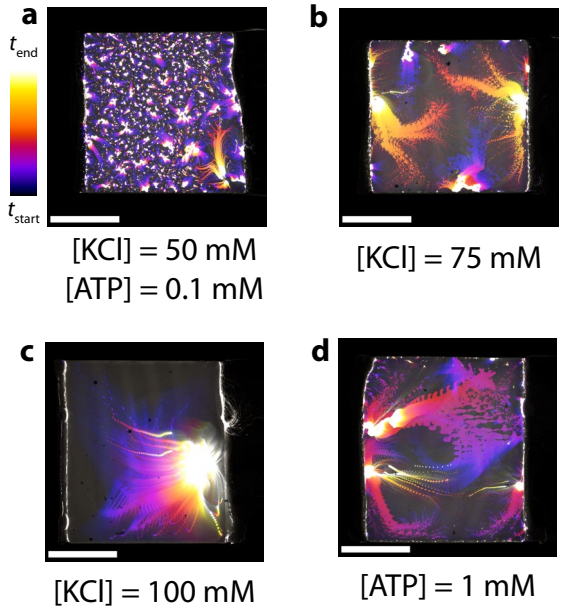

Figure 1. Lower motor activity increases the length scale of contraction. All images are time-overlay images where color corresponds to time (see calibration bar, below). Assays are performed at fixed initial network connectivity ([actin] = 12 μM and [fascin] = 260 nM) and motor density ([myosin] = 340 nM). **a**. Under reference conditions ([KCl] = 50 mM, [ATP] = 0.1 mM), networks contract into many clusters with a scale-free size distribution (see Chapter 4). **b**. Increasing [KCl] to 75 mM promotes larger-scale contraction. Moreover, we observe a second wave of contraction (reddish color). **c**. Increasing [KCl] further to 100 mM promotes macroscopic contraction. **d**. Increasing [ATP] to 1 mM increases the scale of contraction. For all panels, scale bars are 1 mm. Times (t_{start}, t_{end}) of color overlays, given as time after initiating actin polymerization: a: (30 sec, 6 min) b: (40 sec, 4 min) c: (11 min, 14 min) d: (40 sec, 6 min).

Pinset-Härström and Truffy, 1979; Pollard, 1982; Reisler et al., 1980). Myosin is generally stored in non-filamentous form in high-salt buffers (at least 300 mM KCl) and assembly is triggered by lowering the KCl concentration. The myosin filament size depends on [KCl] as well as

other buffer components, temperature, and the method of preparation (rapid dilution, gradual dilution, or dialysis). Here, we prepared myosin filaments by rapid dilution into a standard imidazole-based buffer, in which the filaments have an average length of 0.85 μm when formed at 50 mM KCl and 0.63 μm when formed at 150 mM KCl (Soares e Silva, 2011).

Figure 1 shows time-projections of movies of three different contractile networks, which all have the same initial network connectivity ([actin] = 12 μM, [fascin] = 260 nM). In the standard buffer with 50 mM KCl that is used throughout Chapter 5, motors rupture the network into many small clusters (Fig. 1a). In Chapter 5, we attributed this rupture to myosin activity. When we increase [KCl] to 75 mM, we again observe rupture into multiple clusters (Fig. 1b), but the clusters are larger than at 50 mM KCl. Strikingly, a further increase of [KCl] to 100 mM results in the entire network contracting to one large cluster (Fig. 1c). This observation is consistent with the model presented in Chapter 5, which predicts that reduced motor forces should reduce the ability of motors to break down network connectivity.

To independently test this interpretation, we performed an additional contraction assay in which we kept [KCl] = 50 mM as in the standard buffer, but increased the adenosine triphosphate (ATP) concentration to 1 mM. According to single molecule force measurements (Debold et al., 2005; Finer et al., 1994), the duty ratio of skeletal muscle myosin II is about 4% at mM levels of ATP, and ca. 4-fold larger at 0.1 mM ATP, which was used in the standard buffer used in Chapter 5. When we increase [ATP] to 1 mM, we again observe a marked increase in the sizes of contracting clusters (Fig. 1d) compared to the standard buffer conditions, consistent with a weaker influence of myosin motor forces on network connectivity.

To further investigate the effect of weakening motor activity, we also varied the KCl concentrations in networks that contract macroscopically in the standard buffer (Fig. 2a). This condition is attained by increasing the fascin concentration (from 260 nM in Fig. 1 to 1.2 μM in Fig. 2). When we increase [KCl] to 75 mM, we observe macroscopic network contraction, resembling the contraction at 50 mM KCl (Fig. 2b, top). However, increasing [KCl] further to 100 mM prevents contraction: the network remains static on macroscopic length scales (Fig. 2c, top).

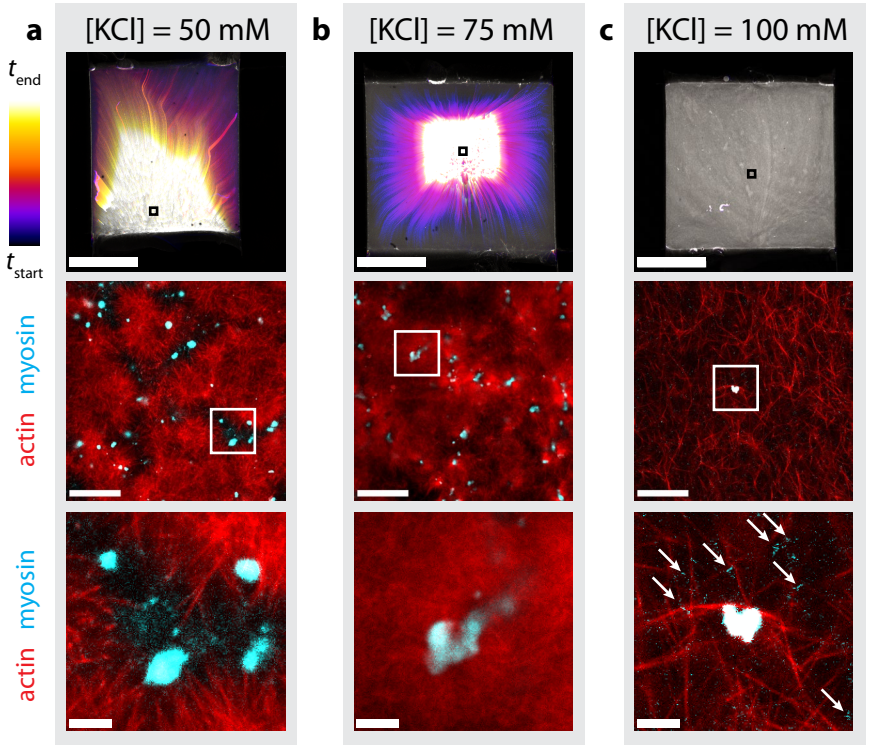

Figure 2. Degree of actin bundling around myosin foci depends on monovalent salt concentration. **a**. [KCl] = 50 mM. **b**. [KCl] = 75 mM. **c**. [KCl] = 100 mM. **Top row**. Time-overlay images of network contractions based on actin fluorescence. Color corresponds to time (calibration bar, left) and scale bars are 1 mm. Times (t_{start}, t_{end}) of color overlays, given as time after initiating actin polymerization: a: (45 sec, 6 min) b: (30 sec, 3 min) c: (1 min, 13 min). **Middle row**. Close-up of network structures corresponding to the areas indicated by the black squares in the top row. Actin is shown in red, myosin in cyan. Snapshots were acquired 2 hr after initiating actin polymerization. Scale bars 30 μm. **Bottom row**. Further close-up of network structures corresponding to the areas indicated by the white squares in the middle row. Note in panel C the presence of small myosin puncta, likely corresponding to individual myosin filaments (white arrows). Scale bars 5 μm. For all panels, [actin] = 12 μM, [myosin] = 120 nM, [fascin] = 100 nM.

Apparently, the motors are not sufficiently processive to cause network contraction.

To investigate how the network microstructure is influenced by variations in KCl concentration, we acquire confocal snapshots of the actomyosin networks 2 hr after initiating actin polymerization by a high-NA microscopy objective (middle and bottom row). For the standard KCl concentration of 50 mM, we find a heterogeneous network of clearly distinguishable actin bundles in the contracted network (Fig. 2a). This network is decorated with myosin foci of variable size, which appear alongside actin bundles but do not appear to be integrated in the network. Increasing [KCl] to 75 mM results in a finer meshwork of actin without pronounced actin bundles (Fig. 2b). Myosin foci appear to be integrated in the actin network, often surrounded by shell of locally enhanced actin fluorescence intensity indicative of local network condensation. The foci have similar sizes as at [KCl] = 50 mM, but they exhibit more irregular and non-convex shapes. Further increasing [KCl] to 100 mM, where the network does not contract, results in a homogeneous network of actin bundles (Fig. 2c). Large myosin foci seldom occur in these networks, although small puncta of myosin fluorescence (potentially single myosin filaments) are present all across the network (Fig. 2c, bottom, white arrows).

Rotating foci of myosin in dense actomyosin networks. During high-resolution imaging, we observed a striking phenomenon in strongly crosslinked contractile active gels (R_F = 0.1): about 5% of the myosin motor foci exhibited rotations within the dense actin networks formed after macroscopic contraction. Typical rotation speeds varied from 2–9 rotations per minute. With foci sizes varying from 2–6 μm (Fig. 3a), these rotation speeds correspond to linear speeds of approximately 0.1–1 μm s^{-1} at the surface, which is lower than the velocities of 3–4 μm s^{-1} reported for motor-driven sliding of actin filaments in gliding assays (Kron and Spudich, 1986). Some rotations continued uninterrupted with a well-defined rotational velocity, as shown in the first two and the last kymograph in Fig. 3b. These kymographs reveal regular patterns in foci trajectories. However, other foci exhibited pauses during rotation, as shown in the kymographs in columns 3–7, which reveal patches of regular patterns interspersed with straight sections indicating lack of movement. Foci were found to rotate both clockwise as well

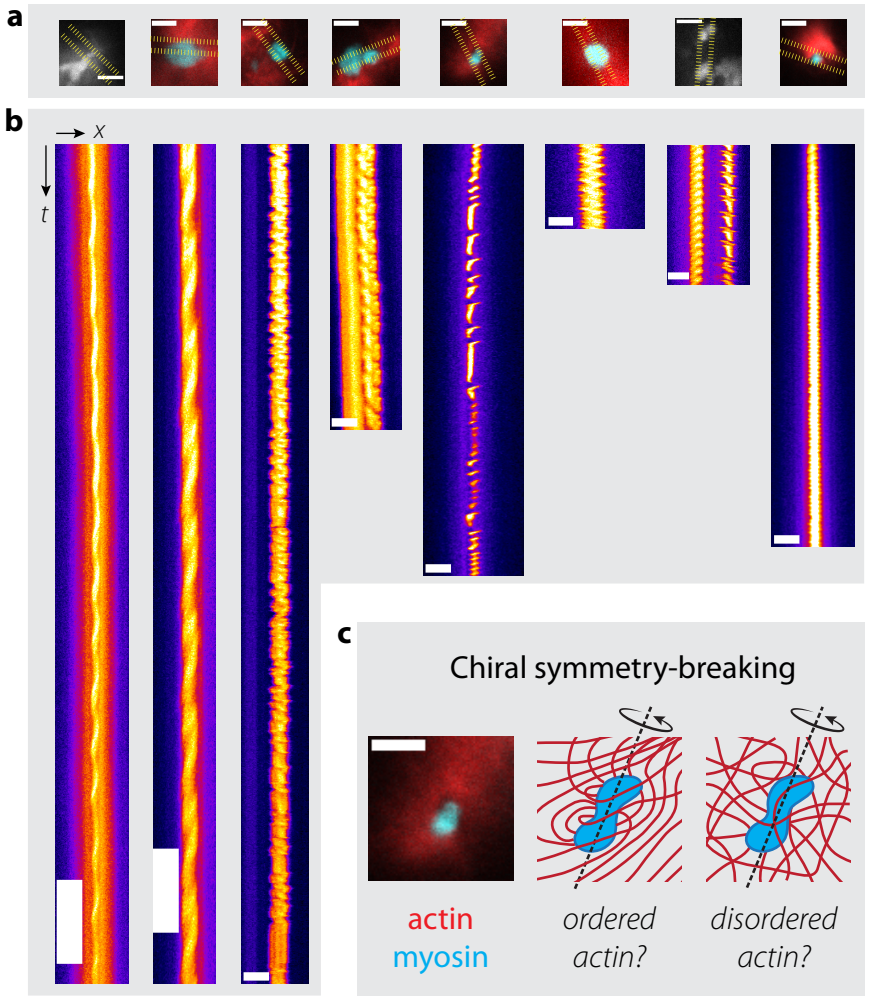

Figure 3. Rotating myosin foci. **a**. Snapshots of foci. Color images depict actin signal in red, myosin in cyan. Grayscale images depict myosin signal. Time, in minutes, after initiating actin polymerization, from left to right: 39, 25, 100, 46, 63, 70, 30, 3. Scale bars 5 μm. **b**. Kymographs. Horizontal direction: Fluorescence intensity of myosin along a line running through foci (between dashed yellow lines, panel a). Myosin intensity is shown in a "Fire" lookup table. Vertical direction: Time. Scale bars 5 μm x 10 s. Note that the first two columns were acquired at a 10x faster frame-rate.

as counterclockwise. However, foci were never observed to change rotation direction. The lack of preferred directionality is expected due to the apparent lack of an external axis from which left and right can be defined. Such an axis exists in developing embryos, where it is required to establish chiral symmetry breaking (Brown and Wolpert, 1990). Interestingly, we observed that preparing contractile networks in thin flow cells with a thickness of ~20 μm (see Methods) increased the likelihood of finding rotating foci.

Two potential scenarios could contribute to the rotation of myosin foci (Fig. 3 c). In one scenario, the actin filaments surrounding myosin foci are perfectly ordered, allowing motors on the surface of these foci to rotate processively along circular tracks of actin. In such a scenario, chiral symmetry breaking could arise from the inherent chiral pitch of actin filaments (Claessens et al., 2008; Shin et al., 2009). In a second scenario, actin filaments are disordered around myosin foci. Motors at the surface of the cluster would exert random forces, which could still give rise to rotations in the absence of actin filament chirality. This kind of behavior has been reported in suspensions of *Escherichia coli* bacteria in the presence of high concentrations of non-adsorbing polymers. Depletion interactions drive aggregation of bacteria into clusters, which were surprisingly observed to rotate around a single axis (Schwarz-Linek et al., 2012). Such rotations are understood to arise by hydrodynamics: bacterial flagella on the surface of the cluster exert randomly directed force dipoles on the surrounding fluid, which can give rise to uniaxial rotations. Whether such a mechanism could apply to rotating myosin clusters is not yet known.

Recent continuum models have begun to address the emergence of global chiral flows from local chiral activity (Fürthauer et al., 2012a; 2012b). Current evidence clearly points to the existence of a microscopic chirality arising from cytoskeletal components. Actin filaments exhibit a variable chiral pitch along the filament axis (Egelman et al., 1982; Galkin et al., 2010b), while fascin crosslinks appear to overtwist actin filaments by 1° per monomer (Claessens et al., 2008). Meanwhile, myosin motors have been shown to exhibit torques on actin filaments, evident from twirls with a left-handed pitch of ~1 μm in gliding assays (Beausang et al., 2008). A thorough understanding of how these effects can give rise to the rotations of myosin foci we report here currently remains

lacking. But such an understanding could help address the currently unanswered question of the origin of chiral symmetry breaking in developing embryos (Spéder et al., 2007). Mouse embryos have been shown to break symmetry by a leftward nodal flow (Nonaka et al., 2002), plausibly established by cilia pointed towards the posterior axis (Cartwright et al., 2004). Meanwhile, evidence from *Xenopus* (Adams et al., 2006; Levin et al., 2002) and chick (Adams et al., 2006) embryos demonstrate that ion pumps and channels are asymmetrically expressed, possibly resulting in L/R gradients in pH and membrane potential. The origin of this polarized expression remains elusive, though actin filaments or microtubules are thought to be essential (Qiu et al., 2005; Shibazaki et al., 2004). Perhaps most strikingly, myosin motors have been directly implicated in establishing chiral rotations in the genital disc of developing *Drosophila* embryos (Spéder et al., 2006). Mutants lacking myosin 1D surprisingly reverse the direction of rotation. Understanding how motor activity establishes such rotations remains poorly understood.

Modulating network connectivity. In Chapter 5, we modulated the network connectivity solely by varying the concentration of fascin crosslinks. However, network connectivity also depends on the concentration of actin filaments as well as their length. In semidilute solutions of long actin filaments, above the overlap concentration, steric entanglements can effectively act as crosslinks (MacKintosh et al., 1995). To test how actin concentration influences connectivity, we perform contraction assays at three different actin concentrations, keeping the myosin concentration and fascin concentration constant ([myosin] = 120 nM, [fascin] = 500 nM). At the largest actin concentration (12 μM), we observe macroscopic contraction, consistent with the high crosslink concentration and low motor density used (Fig. 4a). When we decrease the actin concentration to 6 μM, the network is instead ruptured into multiple large clusters, indicative of lower network connectivity (Fig. 4b). Further decreasing actin concentration to 3 μM results in the formation of many more, much smaller clusters (Fig. 4c), indicative of a further reduction of network connectivity.

To test the influence of filament length, which also influences connectivity, on network contraction, we polymerize actin in the presence of the protein gelsolin, which caps actin filaments at the barbed

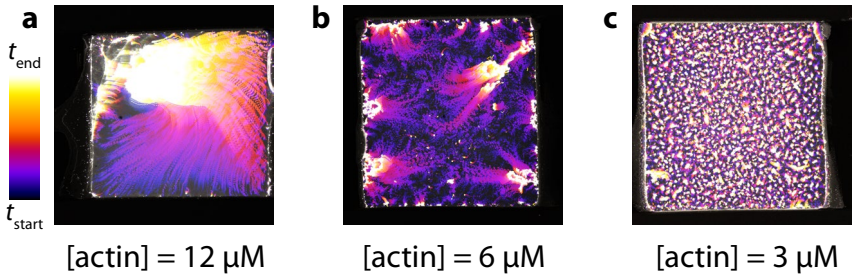

Figure 4. Reducing the network connectivity by decreasing the actin concentration causes network contraction into smaller clusters. **a**. Time-overlay image of a macroscopically contracting network ([actin] = 12 μM). Color corresponds to time (calibration bar, left. **b**. Decreasing [actin] to 6 μM. **c**. Decreasing [actin] further to 3 μM. For all panels, [myosin] = 120 nM, [fascin] = 500 nM. Times (t_{start}, t_{end}) of color overlays, given as time after initiating actin polymerization: a: (40 sec, 20 min) b: (1 min, 14 min) c: (1 min, 1.5 hr).

end. We use 120 nM gelsolin, which is expected to result in an average filament length of ~300 nm (Janmey et al., 1986). This drastic reduction in filament length abolishes network connectivity. Instead of a connected network, we observe isolated foci of myosin motors surrounded by a halo of actin filaments/bundles (Fig. 5a). The foci freely diffusive and coalesce to form larger foci when they collide, as demonstrated in the kymograph in Fig. 5b, where the arrow points to the coalescence event. The coalescence events are irreversible (Fig. 5c). This coalescence behavior is in marked contrast to the coalescence of actomyosin foci in the absence of gelsolin, where the actin filaments are sufficiently long to form a connected network (Fig. 5d). In connected networks, coalescing foci do not diffuse, but move in a directed manner towards one another at typical velocities of ~ 2 μm min^{-1} (Fig. 5e). In this case, coalescence is also irreversible (Fig. 5f).

Onset of network contraction in weakly-crosslinked contractile active gels. So far, we have investigated the effect of myosin-mediated network structure on large (mm) scales and identified the onset of large-scale network contraction as a function of motor and crosslink density. However, even at lower crosslink densities, we observe *local*

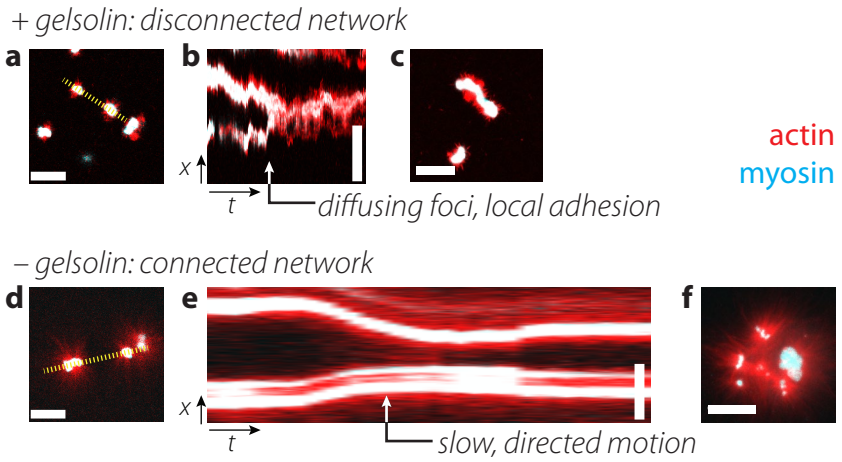

Figure 5. Shortening actin filament length by co-polymerizing with gelsolin results in disconnected actomyosin foci which freely diffuse and coalescence when they collide. **a**. In the presence of 120 nM gelsolin, foci of actin and myosin are freely diffusing in solution. [actin] = 12 μM, [myosin] = 120 nM, [fascin] = 260 nM. Scale bar 10 μm. **b**. Kymograph, as in b. Scale bar 10 μm x 20 sec. **c**. Snapshot of actomyosin foci after coalescence. **d**. In dense networks of long filaments ([actin] = 12 μM, no gelsolin, [myosin] = 120 nM, [fascin] = 120 nM), foci of actin and myosin are connected by a background meshwork of crosslinked actin filaments. Actin is shown in red, myosin in cyan. Scale bar 10 μm. **e**. Kymograph showing time along the horizontal direction and fluorescence intensity along the dashed yellow line from panel a along the vertical direction. Scale bar 10 μm x 20 sec. **f**. Maximum-*z*-projection over 17 μm of actomyosin foci after coalescence.

contraction into clusters that are only a few micrometers in size. This observation raises the question what is the minimum crosslink density required to initiate micron-scale contraction. To identify this onset, we perform confocal imaging of weakly crosslinked networks with a high-NA objective, 1 hr after initiating actin polymerization. In the absence of fascin crosslinks, we observe many small myosin foci (shown in blue) with sizes of a few μm (Fig. 6a, left). These foci are isolated and surrounded by an actin background network (shown in red) of

homogeneous density. Line scans across the foci show that the actin and myosin fluorescence intensity co-localize, but there is no obvious enrichment of actin around the myosin foci (Fig. 6a, right). When we add a small amount of fascin (R_F = [fascin] / [actin] = 0.001 and 0.002), we still observe small myosin foci without an obvious actin coat (see snapshots and line scans in Fig. 6b and c). However, when we increase R_F further to 0.005, the myosin foci are surrounded by a coat of actin (Fig. 6d, left), which is especially evident from the increasing width of the actin fluorescence signal in line scans (Figure 6d, right). Apparently, the threshold fascin crosslink density required to initiate local network contraction is around R_F = 0.005 for networks composed of [actin] = 12 μM and [myosin] = 120 nM. Increasing R_F to 0.01 results in foci with even thicker coats of accumulated actin (Fig. 6e).

In order to pinpoint the onset of local contraction, we plot the average thickness of the actin coat of myosin foci in each sample condition as a function of crosslink density. We quantify the coat thickness by fitting Gaussian peaks to line-scans of the actin and myosin fluorescence intensity, and taking the ratio of the standard deviations (peak widths) σ_a and σ_m of the actin and myosin peaks, respectively. Figure 6f summarizes the dependence of the width ratio σ_a / σ_m on fascin crosslink concentration. Up until R_F = 0.002, the width ratio is around 1, indicating that there is no network contraction. Above R_F = 0.002, the width ratio starts to increase above 1, indicating the onset of local contraction.

At the highest crosslink density in Fig. 6f (R_F = 0.01), we start to observe contractile coalescence of myosin foci. Time-lapse imaging reveals that contractile motions sometimes result in permanent coalescence (Fig. 7a), whereas at other times, foci initially move towards one another in a directed manner but ultimately do not succeed in joining (Fig. 7b). Close inspection of kymographs shows periods of unidirectional motion, as well as reversal events (see arrows in Fig. 7b).

Since weakly crosslinked networks ($R_F \leq 0.01$) contract only on a microscopic scale, we can measure their global viscoelastic properties by shear rheology. In the absence of motors and crosslinks, the actin networks have a low elastic modulus G' of ~0.1 Pa (Fig. 8), in agreement with previous studies (Xu et al., 1998). When we add motors but no crosslinks, G' is increased by a factor of 20, suggesting that the motors

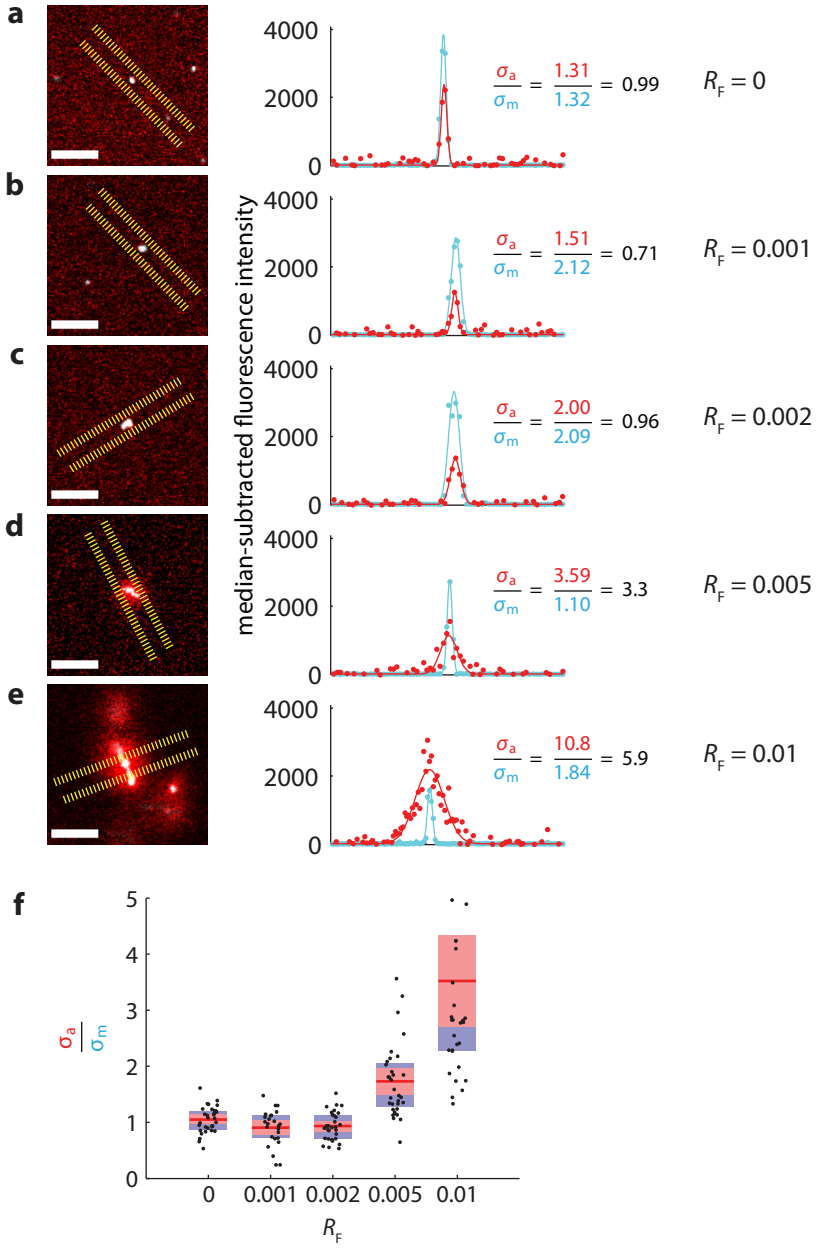

Figure 6. Accumulation of an actin coat onto myosin foci depends on fascin concentration. **Left Column**. Snapshots of actomyosin foci taken 1 hr after initiating actin polymerization. Scale bars 20 μm. **Right Column**. Fluorescence intensity of actin (red points) and myosin (cyan

themselves act as (transient) crosslinks. Adding a small number of crosslinks (R_F = 0.001) in the presence of motors results does not appreciably change *G'*. Interestingly, when we further increase the crosslink concentration, we observe a marked reduction of *G'*, which decreases approximately as $R_F^{-0.5}$. The reduced stiffness may originate from local condensation of the actin network around actomyosin foci, which reduces the actin (and myosin) concentrations in the background network.

Different crosslinks can affect the phase behavior of contractile active gels. So far we characterized the contractile behavior of active actin-myosin networks crosslinked by the actin-binding protein fascin. To test the generality of our results, we also test the ability of other physiological crosslink proteins to assist motor-driven contraction. When we crosslink networks with human α-actinin 2, we observe only local contraction over a broad range of α-actinin concentrations, up to 260 nM (Fig. 9a). However, increasing [α-actinin] to 560 nM results in a drastic change: the entire network contracts to one large cluster in a macroscopic contraction. This behavior is strikingly different from contractile active gels crosslinked by fascin, which exhibit a wide distribution of cluster sizes for intermediate crosslink concentrations.

---

points) along a line running through foci (between dashed yellow lines, left column). When foci are elongated (as in panel e), the line was chosen to run perpendicularly to focus axis. Solid lines denote fits of median-subtracted fluorescence data to Gaussian peaks. Text labels indicate values of the peak-width ratio σ_a / σ_m, defined as the ratio of the standard deviations σ_a and σ_m (given in pixels) from fitting actin and myosin line profiles, respectively. A value greater than one indicates the actin peak is wider than the myosin peak. **a**. R_F = 0. **b**. R_F = 0.001. **c**. R_F = 0.002. **d**. R_F = 0.005. **e**. R_F = 0.01. **f**. Box-plot of peak-width ratios σ_a / σ_m as a function of R_F. Points indicate individual foci (N = 32, 25, 30, 32, and 32 for R_F = 0, 0.001, 0.002, 0.005, and 0.01, respectively). Red lines denote mean ratio. Pink boxes denote 95% confidence interval (CI). Blue boxes denote interquartile range. Two datasets are statistically significantly different from each other ($p < 0.01$) if their CIs do not overlap.

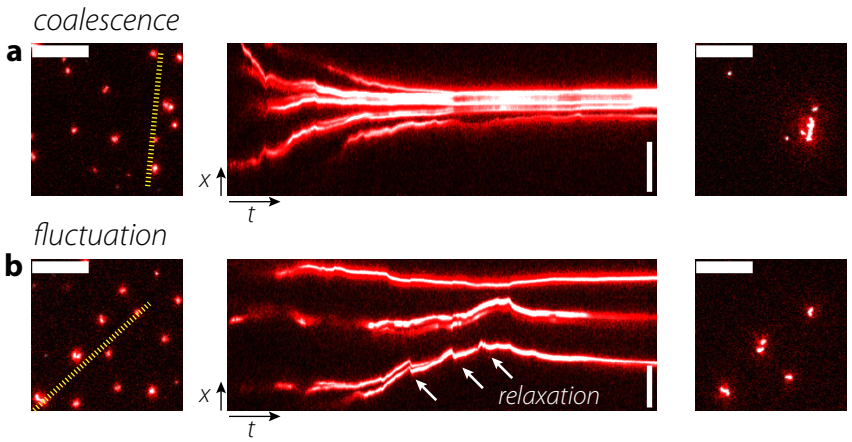

Figure 7. Fluctuation and coalescence of actomyosin foci showing snapshots of foci 50 sec after initiating actin polymerization (left column, scale bars 30 μm), kymographs with time along the horizontal direction and fluorescence intensity along the vertical direction (middle column, scale bars 30 μm x 20 sec), and snapshots of foci 18 min after initiating actin polymerization (right column, scale bars 30 μm). Kymographs are taken along the yellow dashed lines shown on the left. a. Fluctuation event showing motion of foci towards each other followed by relaxation. b. A coalescence event, where multiple foci merge to form a larger focus. In both cases, [actin] = 12 μM, [myosin] = 120 nM, [fascin] = 120 nM. Actin is shown in red, myosin in cyan.

When we crosslink networks with *Arabidopsis* fimbrin 2, we find local contraction at low concentrations of fimbrin (120 nM), larger clusters at 260 nM fimbrin, and macroscopic contraction at 560 nM fimbrin (Fig. 9b). These three contractile regimes qualitatively resemble the phase behavior we observed for contractile active gels crosslinked with fascin. When we crosslink actin networks with *Drosophila* septin complexes, we observe only local contraction, even at the highest concentration of septins we could attain in our assay (500 mM) (Fig. 9c). Furthermore, we crosslinked networks with 10 mM magnesium chloride ($MgCl_2$), which is known to drive attractive interactions between actin filaments by counterion condensation (Tang et al., 1996). Interestingly networks

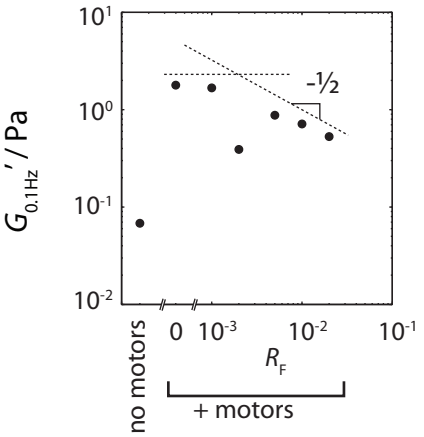

Figure 8. Apparent network stiffness decreases with increasing fascin concentration. Elastic shear modulus *G*' at 0.1 Hz is plotted against R_F = [fascin] / [actin] for experiments in the presence of motors ([myosin] = 120 nM) at a fixed actin concentration, [actin] = 12 μM. For comparison, one experiment in the absence of motors and fascin is plotted ("no motors", [actin] = 12 μM). For reference, dashed lines show $G' \sim R_F^0$ and $G' \sim R_F^{-1/2}$ scaling.

contracted macroscopically in the presence of magnesium chloride in a manner similar to physiological crosslinks.

In order to quantify the effect of α-actinin on the macroscopic phase behavior of contractile active gels, we determine cluster size using the techniques developed in Chapter 5. Figure 10a shows the result of this analysis for the four contractions shown in Figure 9a. For crosslink concentration ratios up to R_α = [α-actinin] / [actin], we find only small clusters. Increasing R_α to 0.05 results in one large cluster, with smaller clusters occurring at the boundary of the chamber. Figure 10b shows the average sizes of the largest (ξ_1) and second-largest (ξ_2) clusters as a function of R_α for twelve experiments. Plotting the results of all twelve experiments in ξ_1-ξ_2-space shows that most experiments occupy either the local-contraction or global-contraction regime (Fig. 10c). As expected, samples in the local-contraction regime exhibit short-tailed cluster size distributions, while samples in the global-contraction regime

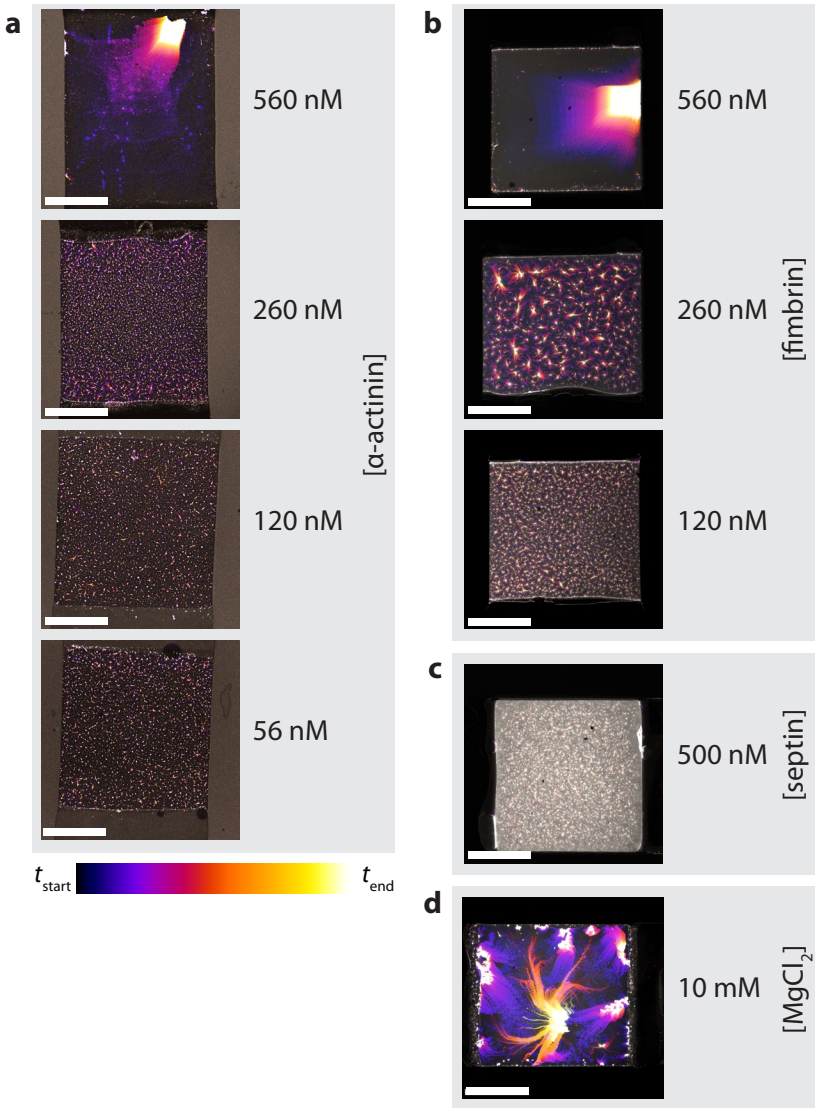

Figure 9. Contractions with different crosslinks. Time-overlays of contractile active gels with **a**. human α-actinin 2, **b**. *Arabidopsis* fimbrin 2, **c**. *Drosophila* septin hexameric complexes, and **d**. fascin with added $MgCl_2$. Color corresponds to time (calibration bar, below). Times (t_{start}, t_{end}) of color overlays, given as time after initiating actin polymerization, from top to bottom: a: (1 min, 27 min); (1 min, 20 min); (1 min, 17 min); (1 min, 12 min) b: (1 min, 12 min); (1 min, 19 min); (1 min, 8 min) c: (9 min, 44 min) d: (35 sec, 8 min). Scale bar 1 mm.

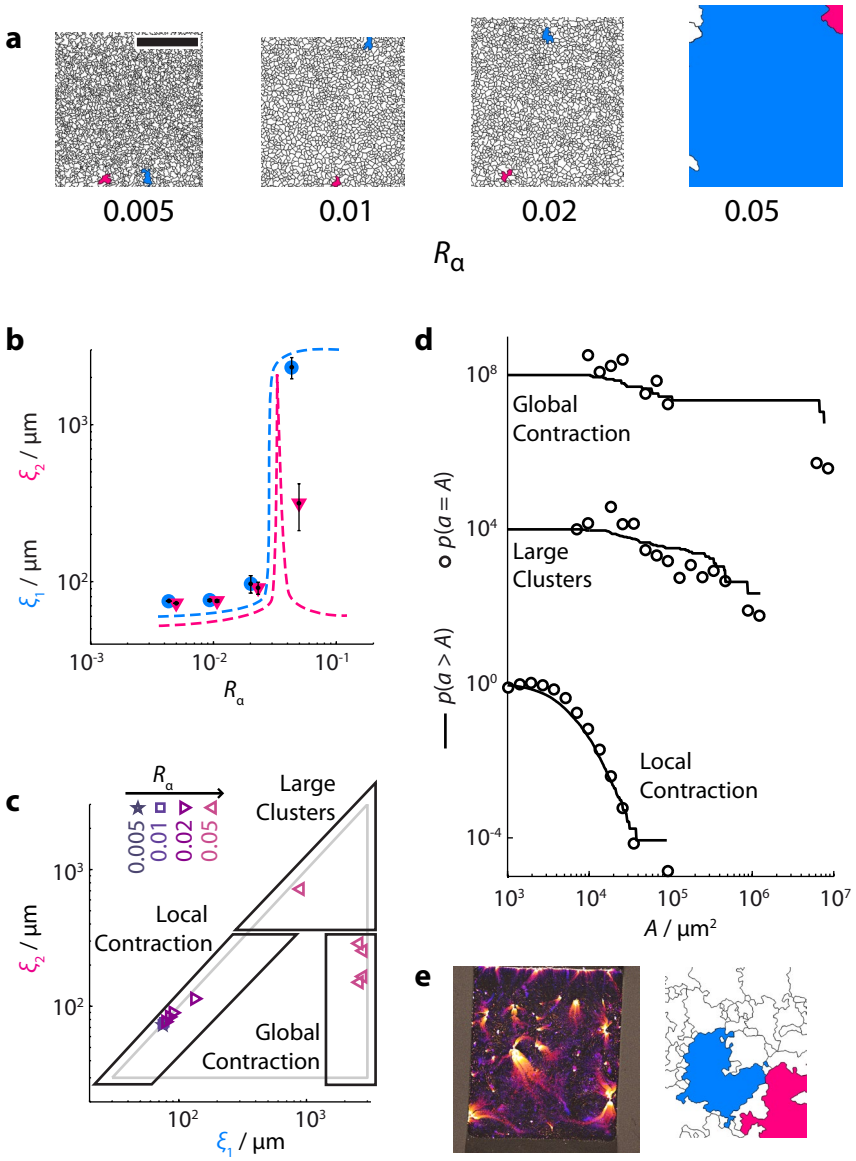

Figure 10. Contractions of networks crosslinked with α-actinin are characterized by a sharp boundary between local contraction for weakly crosslinked networks and global contraction for highly crosslinked networks. **a**. Result of cluster-size analysis for the four contractions shown in panel a of Figure 8. The largest cluster is shown in blue, the second-largest cluster is shown in pink. Scale bar 1 mm. **b**. Mean values

exhibit a bimodal cluster-size distribution with two well-separated length scales (Fig. 10d).

However, one sample prepared at $R_\alpha = 0.05$ did appear to exhibit clusters with a wide size distribution (Fig. 10e). This network was the only experiment performed with α-actinin that yielded $\xi_1 \sim \xi_2 \sim L$, where L is the system size. (see "Large Clusters", Fig. 10c). Its cluster size distribution is shown in Fig. 10d ("Large Clusters"), which shows a long-tailed distribution.

In order to investigate further the difference in macroscopic contractile phase behavior between fascin and α-actinin, we investigate its microscopic behavior. We perform experiments where we observe actomyosin-foci crosslinked with α-actinin in the presence of gelsolin. Surprisingly, α-actinin foci appear to exhibit foci where an actin core is surrounded by a myosin coat. This is in strong contrast to fascin foci, which exhibit a myosin core surrounded by an actin coat (Fig. 11).

---

of the sizes of the largest and second largest clusters, ξ_1 and ξ_2 respectively, as a function of R_α = [α-actinin] / [actin]. Error bars denote standard error of the mean for N = 1, 2, 3, and 5 experiments for R_α = 0.005, 0.01, 0.02, and 0.05, respectively. Dashed lines are guides to the eye. **c**. ξ_1-ξ_2-space with three regimes: local contraction, large clusters, and global contraction. Symbol color and shape corresponds to R_α (legend, top-left). Note that we observed a network with large clusters only once, in sharp contrast with fascin-crosslinked networks (Chapter 4). **d**. Cluster size distributions for the three regimes from panel c, represented as histograms (circles) and complementary cumulative probability distribution functions (lines).

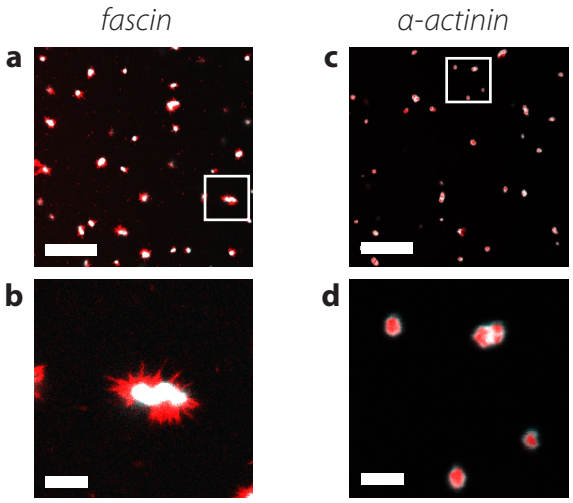

Figure 11. The organization of actin and myosin in freely-diffusing actomyosin foci formed in solutions of actin ([actin] = 12 μM) shortened with gelsolin ([gelsolin] = 120 nM) depend on the nature of the crosslink protein. **a**. Snapshot of actomyosin-gelsolin foci crosslinked by fascin (260 nM), acquired 40 min after initiation of actin polymerization. Scale bar 30 μm. Note that actin (in red) is on the outside of myosin (in cyan) foci. **b**. Close-up of the area indicated by the white box in panel a. Scale bar 5 μm. **c**. Snapshot of actomyosin-gelsolin foci crosslinked by α-actinin (560 nM), acquired 40 min after initiation of actin polymerization. Scale bar 30 μm. **d**. Close-up of the area indicated by the white box in panel c. Note that actin (in red) is sometimes on the inside. Scale bar 5 μm.

6.3 Discussion

Motor-driven patterning of actin-fascin networks. Our results for motor-driven actin-fascin networks complement a growing body of *in-vitro* work on this system.

First, a set of experiments by Backouche et al. (2006) focusing on well-connected (1 mg/ml) actin networks reported strikingly ordered patterns consisting of asters of actin-fascin bundles. These ordered patterns resemble previously reported asters and vortices of microtubules

driven by kinesin and dynein motor proteins (Nédélec et al., 1997), but are completely different from the disordered contractions reported in this thesis. This difference is likely a consequence of a difference in ionic strength of the buffers used in the two cases: Backouche et al. used a high KCl concentration (130 mM), whereas we used a low KCl concentration (50 mM). We showed in this chapter that the KCl concentration has a strong influence on the microstructure of actin-myosin-fascin networks as well as on the ability of motors to contract these networks. At low KCl concentration (50 or 70 mM), the actin networks are only partially bundled (in contrast to control samples with fascin but without myosin) and motors can efficiently contract the networks. At the highest KCl concentration studied here (100 mM), we observed that networks were more bundled, resembling control samples without myosin. Moreover, we found that contraction was inhibited (cf. Fig. 2). We propose that this KCl dependence is a consequence of changes in the binding affinity of myosin for F-actin, which determines the motor processivity. At low ionic strength, the motors are more processive and cause (more) forced-unbinding of fascin crosslinks, which inhibits actin bundling but promotes network contraction. At high ionic strength, the motors are less processive and leave actin bundles more intact (though at high myosin concentration, they are still capable of bundle disruption (Haviv et al., 2008)).

Second, a set of experiments on dilute (< 0.3 mg mL^{-1}) suspensions of actin-fascin bundles in a low-salt buffer by Köhler et al. (2011a) showed that driving by myosin motors can give rise to a dynamic steady state. Specifically, they observed clusters of bundles that continuously grow and shrink. Furthermore, they showed that these dynamic steady states can give rise to pulsatile collective transport modes (Köhler et al., 2011b). They ascribed this fascinating behavior to an interplay between motor-activity and forced crosslink unbinding, somewhat reminiscent of the mechanism we propose for rupture and contraction in highly connected (0.5 mg/ml) active contractile gels. At actin concentrations higher than 0.3 mg mL^{-1}, Kohler et al. observed network contraction instead of dynamic steady states (Köhler et al., 2011a; 2012), consistent with our observations. In a third set of experiments, by Schaller et al. (2011), quasi-2D layers of actin filaments were transported by nonprocessive myosin motors immobilized on a glass coverslip. This assay is a high-

density version of a conventional gliding assay. These authors were able to demonstrate the emergence of a frozen active steady state that consisted either of constantly rotating rings or collectively moving elongated fibers. This assay is different from our assay in different ways. First, the geometry is 2D, in contrast to our 3D conditions. Second, the motors are immobilized, whereas in our assay myosin filaments substantially reorganize in the course of network contraction, forming large foci. Prior work showed that myosin foci are particularly effective in driving network contraction by generating large compressive forces that cause actin filament buckling (Soares e Silva et al., 2011b).

Phase behavior of active contractile gels. In this chapter as well as Chapter 5, we performed experiments on contractile active gels in which we systematically varied network connectivity and motor activity. In Chapter 5, we focused on actin-fascin networks in which we varied fascin and myosin concentration but held other parameters (actin density and filament length, buffer conditions, ATP concentration) fixed. We discovered that the length scale of network reorganization due to motor-driven contraction depends sensitively on the physical properties of the network, in particular the network connectivity and motor activity. Based on the distribution of contracting cluster sizes, we identified three contraction regimes, which we indicate as local, critical, and global contraction regions. In this chapter, we showed that transitions between these three regimes can be achieved in different ways. The network connectivity increases with increasing actin filament length and density as well as increasing crosslink density, promoting larger-scale contraction. The myosin activity increases with decreasing ATP and salt concentration, promoting network contraction and rupture into multiple clusters.

Based on all our own data in combination with prior data on contractile actin-myosin networks, we propose a schematic phase space diagram of contractile active gels that summarizes the contractile behavior as a function of these two parameters (Fig. 12). We distinguish six different regimes: I. Dissipative networks; II. Local contraction; III. Critically connected networks; IV. Global contraction; V. Prestressed networks. O. Passive networks.

In the dissipative networks regime (region I), motor activity is high but connectivity approaches zero. In this regime, motors locally exert

pulling forces on actin filaments, but the lack of connectivity prevents build-up of contractile stress. Instead, motor-driven sliding results in mainly dissipative processes such as the dynamic cluster reorganization reported in dilute suspensions of actin-fascin bundles (below 0.3 mg mL^{-1} actin) (Köhler et al., 2011a) or the coalescence of freely diffusing actomyosin foci we report in Fig. 5. In the local contraction regime (region II), sufficient connectivity is present to allow motor-induced sliding of filaments to locally deform the surrounding network. At low crosslink concentrations, we observed that motors mostly induce contractile fluctuation events, whereas permanent coalescence events were rare (cf. Fig. 7). This agrees with previous findings: in the absence of (passive) crosslinks, motor activity fluidizes actin networks (Humphrey et al., 2002) and increases the apparent temperature (Le Goff et al., 2002a; Liverpool, 2003; Morozov and Pismen, 2010), and in weakly crosslinked networks motor activity mainly generates contractile fluctuations (Mizuno et al., 2008; Soares e Silva et al., 2011b; Stuhrmann et al., 2012). At high enough crosslink density, the interplay between connectivity and force can give rise to net contraction. Net contractile stresses may result from the asymmetry in the mechanical response of actin filaments, which support tension but not compression (Lenz et al., 2012a; 2012b; Murrell and Gardel, 2012; Soares e Silva et al., 2011b) or from active reorganization of motors in the network (Dasanayake et al., 2011). We showed that motors contract networks that are weakly crosslinked with fascin or fimbrin into clusters with a mean size that increases with increasing crosslink concentration, qualitatively consistent with earlier observations on networks crosslinked by biotin-neutravidin (Soares e Silva et al., 2011b).

In the critically connected regime (region III), motor activity contracts connected network to clusters with a scale-free size distribution. Experimentally, we have shown that this critical behavior occurs for contractile active gels crosslinked by fascin (cf. Chapter 5). We have also observed qualitatively similar behavior for gels crosslinked by fimbrin (cf. Fig. 9). Interestingly, networks crosslinked by α-actinin do not appear to exhibit robust critical behavior (cf. Fig. 9). Only one network assayed exhibited a broad distribution of cluster sizes, suggesting that α-actinin suppresses the robustness of critical behavior. We do not yet know why α-actinin produces a qualitatively different

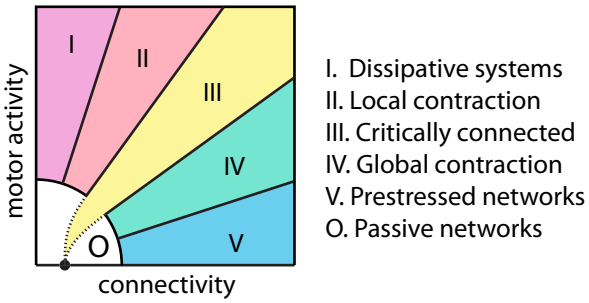

Figure 12. Proposed schematic phase diagram of active contractile actomyosin gels, showing six different phases and their proposed dependence on connectivity and motor activity. The conductivity percolation threshold in the absence of motor activity is shown as a black circle on the connectivity axis.

behavior. Possibly, the crosslink responds differently to an applied force than fascin and fimbrin. There are reports of catch-bond behavior of human α-actinin-4 (Yao et al., 2013; 2011) as well as rabbit skeletal-muscle α-actinin (Ferrer et al., 2008), but the force-responsiveness of the human α-actinin-2 used here is unknown. In contrast, there is strong evidence that fascin exhibits slip-bond behavior in response to motor-driven forces (Ishikawa et al., 2003). The geometry of the crosslink protein may also play a role: α-actinin forms actin bundles of mixed polarity whereas fascin and fimbrin are smaller crosslink proteins that form unipolar actin bundles (see below). Furthermore, the microscopic organization of the actomyosin foci appear to be different in the presence of α-actinin compared to fascin (cf. Fig. 11). In the presence of gelsolin, we observed that actomyosin foci had an actin core surrounded by a thin coat of myosin in the presence of α-actinin, whereas they have a myosin core and an actin shell in the presence of fascin. This difference in microscopic organization may contribute somehow to the difference in macroscopic phase behavior.

In the global contraction regime (region IV), connectivity is strong enough to allow motor activity across the entire network to uniformly contract it into one dense cluster. Finally, in the prestressed networks regime (region V), connectivity and/or network stiffness is too high to

allow motors to macroscopically deform the network. We did not find a prestressed regime with fascin, fimbrin, and human α-actinin-2, but this regime was reported for actin networks crosslinked by filamin or by α-actinin purified from chicken gizzard and also for human filamin A (Bendix et al., 2008; Janson et al., 1991; Koenderink et al., 2009).

A transition to the global contraction region (IV), likely from regions II or V, has been suggested by simulations accounting for correlated motor kicks (Wang and Wolynes, 2012a; 2012b). Although a contraction phase was evident above a certain connectivity threshold, the nature of the threshold itself remained poorly characterized. Our own experiments and numerical modeling revealed a scale-free cluster-size distribution that characterizes region III, which is consistent with a conductivity percolation transition (Stauffer and Aharony, 1994). Simulations of a crosslinked network of filaments internally stressed by contractile motor activity showed that force-induced crosslink unbinding is required in combination with a finite viscosity to obtain critical behavior (cf. Chapter 5). Interestingly, motor activity can drive networks with a wide range of initial conditions to this critical state, when either fascin or fimbrin is used as a crosslinker. This robustness may explain why the critically connected regime is experimentally accessible. The relationship between region III and the transition between regions IV and V has not yet been addressed.

At low fascin crosslink density, we observed a transition between regions I and II: specifically, we showed that at $R_F = 0.002$ and above, myosin foci accumulate a coat of actin (cf. Fig. 6), indicating that the network connectivity is high enough to allow for local network contraction. Furthermore, we found that G' decreases with increasing crosslink concentration, likely due to increased local compaction of the actin network into dense actomyosin foci. The transition from region I to region II may represent a rigidity percolation transition, similar to the rigidity percolation observed in passive actin networks as a function of crosslink density (Tempel et al., 1996).

In the limit of diminishing force and connectivity, we should expect networks that are not observably active (Region O). The physical properties of contractile active gels in this "passive regime" remain poorly understood experimentally. Previous experiments and theory have demonstrated an order-disorder transition which depends on a

critical motor activity in the presence of small amounts of permanent crosslinks (Peter et al., 2008; Smith et al., 2007). It will be interesting to investigate whether this transition relates to a boundary between region O and the other regions we propose.

We showed that modulating motor forces by addition of KCl and ATP allows transitioning between different contractile phases by influencing myosin motor activity. Both KCl and ATP affect myosin activity in several ways. Higher KCl concentrations decrease the binding affinity of myosin II to actin filaments (Brenner et al., 1982) and prevent sliding of actin filaments in gliding assays (Takiguchi et al., 1990). Furthermore, monovalent salts influence the size of myosin filaments (Davis, 1988; Kaminer and Bell, 1966; Katsura and Noda, 1973; Koretz, 1979; Pinset-Härström and Truffy, 1979; Pollard, 1982; Reisler et al., 1980). Myosin filament length has been shown to strongly affect contraction velocity in reconstituted actomyosin bundles (Thoresen et al., 2013). As discussed above, the KCl-dependence of myosin motor activity may explain why prior experiments on actin-myosin-fascin networks at high salt (130 mM KCl) gave rise to ordered patterns, including networks of actin bundles and asters (Backouche et al., 2006). We anticipate that these patterns are only possible when motor activity is weak enough to allow polar bundles of fascin to form and remain intact. At 100 mM KCl, we found that macroscopic contraction could be prevented and the actin networks consisted of bundles, qualitatively consistent with the study of Bakouche et al. performed at 130 mM KCl (Backouche et al., 2006). In contrast, we never find ordered patterns at intermediate salt concentrations (50 or 70 mM KCl) in the presence of any of the crosslinks we studied. Similarly, prior studies using biotin-neutravidin crosslinks also observed only disorganized actomyosin foci (Soares e Silva et al., 2011b). At 75 mM KCl, we found a fine meshwork of actin, rather than a network of well-defined bundles around myosin foci (cf. Fig. 2).

Increasing concentrations of ATP also reduce myosin processivity, but at the same time the ATP concentration influences the motor velocity. In dilute (<0.3 mg/ml) actin suspensions, an ATP concentration window of 0.05–0.1 mM was found to yield a maximum in motor-driven collective pulsatile behavior (Köhler et al., 2011b), consistent with experiments on glycerinated rabbit psoas fibers showing that

motor-induced tension was maximized at ATP concentrations of 0.05 mM (Cooke and Bialek, 1979). Higher ATP concentrations in these studies resulted in higher velocities but lower tensions, due to decreased binding affinity between myosin motors and actin filaments, which in turn decreases processivity and hence motor activity. Our results are consistent with this interpretation, where we found that added ATP shifted networks to the macroscopic contraction regime.

A number of microscopic effects could significantly alter the phase-space diagram we propose. The effect of different crosslink proteins on the phase behavior of contractile active gels remains poorly understood. A particularly interesting open question is the role of the geometry of crosslinks. In the absence of a connected network, myosin motors contract only filaments of opposite polarity (Reymann et al., 2012). In this light, it may appear surprising that actin-fascin and actin-fimbrin networks can contract, since both crosslinks are known to induce polar bundles of actin filaments (Courson and Rock, 2010; Ishikawa et al., 2003). Both proteins possess two actin-binding domains, which contain tandem calponin-homology domains in case of fimbrin (Klein et al., 2004) and β-trefoil domains 1 and 3 in case of fascin (Jansen et al., 2011). However, in a connected network, contraction does not necessarily require antiparallel filament pairs since the asymmetric force-extension behavior of actin filaments can break symmetry (Dasanayake et al., 2011; Lenz et al., 2012a; 2012b; Soares e Silva et al., 2011b). Indeed, recent contraction assays that directly compared the influence of fascin and cortexillin (which creates mixed polarity bundles) showed that networks in both cases contract above a critical crosslink density (Köhler et al., 2012). However, cortexillin-networks contracted more dramatically than fascin-networks (to 3% compared to 15% of the original volume), indicating a subtle influence of the type of crosslink used. We did not observe a clear difference between the degree of contraction of networks crosslinked by the polar crosslink fascin and fimbrin compared to the apolar crosslink α-actinin. However, we did observe a more narrow critical regime for α-actinin. It remains to be seen whether this is related to the geometry of α-actinin. In contrast to fimbrin and fascin, α-actinin possesses only one actin-binding domain, but it dimerizes to simultaneously bind two actin filaments and form crosslinks (Broderick and Winder, 2005). Alternatively, the binding

kinetics and the responsiveness to force may be different for the different crosslinks. Previous work has shown that human α-actinin 4 exhibits catch-bond behavior (Yao et al., 2013; 2011), which could drastically affect the propagation of myosin-induced contractile stresses.

The microscopic properties of myosin will also likely influence the contractile phase space diagram. Myosin motors were recently shown to cause rupture of actin filaments by introducing high-curvature bends (Murrell and Gardel, 2012; Vogel et al., 2013), which provides an additional mechanism to actively reduce the network connectivity in the course of myosin-driven network remodeling. Different isoforms of myosin have rather different processivities and velocities, which also strongly influences contractility of actin-myosin systems (Thoresen et al., 2013). Motors themselves may also introduce network connectivity, acting as active crosslinks, an effect which is probably particularly relevant for highly processive motors such as nonmuscle myosin IIB (Norstrom et al., 2010; Wang et al., 2003) and in highly connected networks due to the catch bond response of myosin to high loads (Guo, 2006; Luo et al., 2012). In isotropic networks, motors only cause contraction at extremely low ATP concentrations, a phenomenon known as superprecipitation (Mizuno et al., 2007). However, when actin filaments are pre-organized into bundles before motors are activated, motors can cause bundle contraction in the absence of crosslinks (Stachowiak et al., 2012; Thoresen et al., 2011; 2013).

In conclusion, we have shown that the physical properties of contractile active gels can tune the length scale of motor-driven contraction. There is evidence that physical interactions also contribute to regulation of actomyosin contraction during diverse physiological processes in living cells and organisms, in combination with biochemical regulation. For instance, recent observations of *Dictyostelium* amoeba showed that a cooperative interaction between motors and crosslinks aids mechanosensation (Kee et al., 2012; Luo et al., 2012; Ren et al., 2009). During cytokinesis in *Drosophila* S2 cells, cortical flows deliver myosin II to the cell equator, which contributes to local contractile ring formation in concert with biochemically regulated myosin activation and filament formation (Uehara et al., 2010). Large-scale cortical flows have also been shown to aid segregation of membrane-bound cell polarity factors in embryos (Goehring et al., 2011), and local contractions of the

actin-myosin cortex in hamster ovary cells have been shown to cause clustering of cell surface proteins (Goswami et al., 2008; Gowrishankar et al., 2012). These observations suggest a strong link between the physical properties of active gels and the regulation of the plasma membrane. Such a link could allow for a direct role for contractile active gels in the regulation of biochemical signaling networks (Bois et al., 2011; Goehring et al., 2011; Howard et al., 2011).

6.4 Methods

Protein Preparation. Monomeric (G-) actin and myosin II were purified from rabbit psoas skeletal muscle (Soares e Silva et al., 2011b). G-actin was purified with a Superdex 200 column (GE Healthcare, Waukesha, WI, USA) and stored at −80 °C in G-buffer (2 mM tris-hydrochloride pH 8.0, 0.2 mM disodium adenosine triphosphate, 0.2 mM calcium chloride, 0.2 mM dithiothreitol). Myosin II was stored at −20 °C in a high-salt storage buffer with glycerol (25 mM monopotassium phosphate pH 6.5, 600 mM potassium chloride, 10 mM ethylenediaminetetraacetic acid, 1 mM dithiothreitol, 50% w/w glycerol). Creatine phosphate disodium and creatine kinase were purchased from Roche Diagnostics (Indianapolis, IN, USA), all other chemicals from Sigma Aldrich (St. Louis, MO, USA). Magnesium adenosine triphosphate was prepared as a 100 mM stock solution using equimolar amounts of disodium adenosine triphosphate and magnesium chloride in 10 mM imidazole pH 7.4. Myosin II was labeled with Alexa Fluor 488 NHS ester (Invitrogen, Paisley, UK); actin was labeled with Alexa Fluor 594 carboxylic acid, succinimidyl ester (Soares e Silva et al., 2011b). Recombinant mouse fascin was prepared from T7 pGEX *E. coli* (Gentry et al., 2012). The mouse fascin plasmid was a kind gift from Scott Hansen and R. Dyche Mullins (UC, San Francisco). *Arabidopsis* fimbrin-2 tagged with GFP and 6xHis was prepared from T7 pET28 *E. coli*. Lysate from cells expressing GFP-His-Fim2 was clarified by centrifugation at 10,000 *g* and applied to Ni-NTA Agarose beads (GE

Healthcare). Eluted protein was stored in 20 mM imidazole, 50 mM potassium chloride, 5% sucrose, and 1 mM dithiothreitol. The fimbrin plasmid was a kind gift from Tijs Ketelaars (Wageningen UR). Human α-actinin 2 protein was a kind gift from Balász Visegrády (U Pécs).

Sample Preparation. Samples were mixed to yield a final buffer composition of 20 mM imidazole pH 7.4, 50 mM potassium chloride, 2 mM magnesium chloride, 1 mM dithiothreitol, and 0.1 mM adenosine triphosphate (ATP). Furthermore, 1 mM trolox, 2 mM protocatechuic acid, and 0.1 μM protocatechuate 3,4-dioxygenase were added to minimize photobleaching. Networks lacking protocatechuate 3,4-dioxygenase and protocatechuic acid contracted with a length scale that was indistinguishable from control experiments. The ATP level was held constant by addition of 10 mM creatine phosphate disodium and 0.1 mg mL^{-1} creatine kinase. The actin concentration was held constant at 12 μM (0.5 mg mL^{-1}) unless otherwise indicated. Freshly mixed actomyosin solutions were loaded into polyethylene-glycol-passivated flow cells with a square geometry measuring 2.5 x 2.5 x 0.1-mm^3 and sealed with either Baysilone silicone grease (Bayer, Leverkusen, Germany) or uncured PDMS (Dow Chemicals, Midland, MI, USA). The time evolution of the network structure was observed with a Nikon PlanFluor 4x objective (NA 0.13), which allows the network to fit entirely within the objective's field of view.

Rheology. Networks were sheared by a stress-controlled rheometer (Physica MCR 501, Anton Paar). Samples were polymerized at room temperature between a top cone plate (CP-20-1) and a bottom planar plate. A wet tissue was placed around the sample and a surrounding hood was lowered to maintain humidity. Network evolution was monitored by probing the samples at low strains (0.5 %, 0.5 Hz) for one hour. Next, network mechanical properties were probed by a frequency sweep (frequencies 1–0.01 Hz) using a strain amplitude 5% which was still within the linear viscoelastic regime.

Sample Preparation. Fresh myosin solutions were prepared by overnight dialysis into myosin buffer (20 mM imidazole pH 7.4, 300 mM potassium chloride, 4 mM magnesium chloride, 1 mM dithiothreitol) and used within four days. All frozen protein stocks (actin, myosin, fascin) were clarified of aggregated proteins upon thawing at 120,000 g for at least 5 min and used within four days. The proteins' concentrations in

the supernatant were determined by measuring the solution absorbance with a NanoDrop 2000 (ThermoScientific, Wilmington, DE, USA) and using extinction coefficients, in M^{-1} cm^{-1}, of 26600 (280 nm, actin (Pardee and Spudich, 1982)), 66280 (280 nm, fascin, computed from amino acid sequence (Artimo et al., 2012)), and 55000 (488 nm, GFP-fimbrin (McRae et al., 2005)). Fluorescently labeled proteins were mixed with unlabeled proteins to yield a 10% molar ratio of dye to protein. During sample preparation, myosin and Alexa-488-myosin were mixed at high salt and then mixed into a tube containing fascin and buffer. This solution was mixed into a second tube containing actin and Alexa-594-actin to initiate polymerization and immediately inserted into glass flow cells passivated by adsorption of poly-L-lysine-polyethylene-glycol (Surface Solutions AG, Dübendorf, Switzerland).

Preparation of flow cells. Glass flow cells were assembled by sandwiching strips of ParaFilm between a long cover slip (24 mm x 60 mm) and 2.5-mm-narrow glass strips which were manually cut from 40-mm-long cover slips. This yielded 2.5 x 2.5 x 0.1-mm3-large chambers (corresponding to ~0.6 μL). For thinner chambers (~20 μm), ParaFilm was first stretched before cutting into strips. All glass was cleaned with a base piranha solution (5:1:1 water to ammonium hydroxide to hydrogen peroxide), rinsed in MilliQ water, and stored in isopropanol. Assembled flow cells were then passivated by applying 1M potassium hydroxide for 5 min, rinsing with MilliQ, drying in a flow of N_2-gas, applying 0.2 mg mL-1 poly-L-lysine-polyethylene-glycol (Surface Solutions AG, Dübendorf, Switzerland) for 30 min, rinsing with MilliQ, and drying in a flow of N_2. Networks in passivated chambers are free to contract macroscopically (Fig. 13a, top). After the experiment, confocal stacks reveal that proteins are distributed homogeneously in the z-direction (Fig. 13a, bottom). However, in the presence of sticky, nonpassivated surfaces, networks do not contract macroscopically (Fig. 13b, top). Furthermore, surfaces appear to be uniformly coated in actin and myosin (Fig. 13b, bottom).

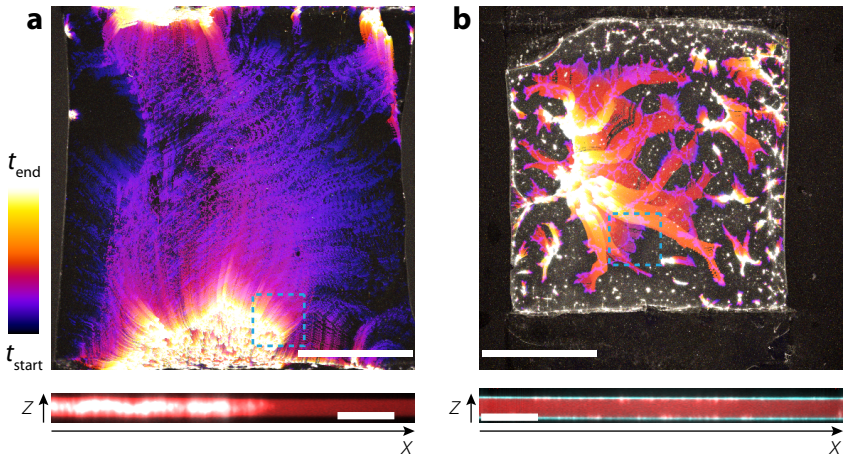

Figure 13. Sticky surfaces decrease the cluster size of contractile networks. **a**. A macroscopically-contracting network with passivated glass surfaces. **b**. A macroscopically-contracting network with non-passivated, sticky glass surfaces. **Top row**: Time-overlay images. Color corresponds to time (calibration bar, below). Scale bars 1 mm. Times (t_{start}, t_{end}) of color overlays, given as time after initiating actin polymerization: a. (1 min, 38 min), b. (1 min, 30 min). Bottom row: Average-y-projections of confocal stacks corresponding to dashed cyan boxes of top row. Vertical direction: z-direction, horizontal direction: x-direction. In sticky chambers, myosin is clearly localized on the bottom and top surfaces.

6.5 Outlook: Light scattering of contractile active gels

Until now we investigated the phase behavior of contractile active gels exclusively by optimal microscopy. However, the spatial resolution of images obtained by conventional fluorescence microscopy methods is limited by the diffraction of light. We are thus able to observe changes in network structure on micron and millimeter length scales, but we can obtain only limited insight into the microscopic processes that

determine the dynamics of networks before and during contraction. Here we investigate the dynamics of an active gel undergoing contraction using light scattering techniques, which can quantitatively probe the microscopic structure and dynamics of soft condensed matter systems (Pine, 2000). Light scattering techniques can probe a large sample volume, yielding better ensemble averages than standard microscopy techniques (Cipelletti and Weeks, 2010). However, the analysis of light scattering experiments assumes ergodic behavior (time averages correspond to ensemble averages), and therefore cannot accurately probe spatially heterogeneous or nonequilibrium samples. However, recent light scattering techniques have been developed to overcome this limitation by resolving (rather than averaging) data over time (Cipelletti et al., 2002), or over both time and space (Duri et al., 2009). Such space- and time-resolved techniques were employed to measure a decrease of the relaxation timescale as a function of sample age for actin networks crosslinked by fascin, which demonstrated out-of-equilibrium dynamics in networks previously assumed to be in equilibrium (Lieleg and Bausch, 2007).

In this Outlook Section, we employ these space- and time-resolved light scattering techniques to probe the sample-age-dependent dynamics of contractile active gels. We simultaneously measure four different scattering vectors and show that actomyosin networks exhibit a length-scale-dependent relaxation timescale. Furthermore, we find sudden bursts of microscopic de-correlation which occur just moments before contraction.

Phase behavior of contractile active gels. Actin networks were prepared with varying amounts of myosin and fascin and loaded into cylindrical glass NMR tubes with a 5-mm outer diameter and a wall thickness of 0.4 mm (see Methods). The dependence of contractile behavior on myosin and fascin concentrations is shown in Figure 14. Phase behavior was determined by visual inspection: stationary samples (blue) did not exhibit observable contractions and appeared clear or turbid. Clustered samples (green) exhibited small, ~1-mm-large clusters suspended throughout the sample, suggesting the existence of a background network that keeps clusters suspended. Samples that contracted macroscopically (pink) collapsed into one large, 2–3-mm-large cluster, which often remained suspended in the middle of the

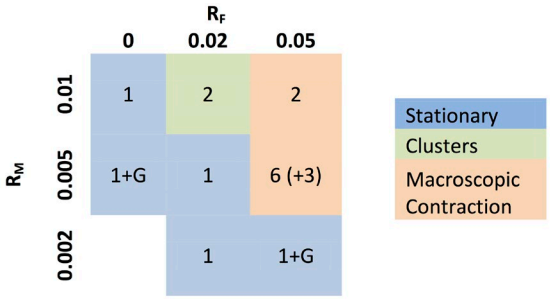

Figure 14. Contraction phase diagram as a function of fascin and myosin concentration (given by R_F = [fascin] / [actin] and R_M = [myosin] / [actin], respectively). Numbers indicate the number of experiments performed. Parentheses denote three additional experiments under altered conditions (150 mM KCl; no ATP, CP, CK; 1 mM ATP). "+G" denotes an additional goniometry measurements.

solution or attached to the sides of the tube. The phase behavior observed here is largely consistent with microscopy experiments. In particular, the existence of the cluster regime was also observed at R_F = 0.02 and R_M = 0.01, where the network broke up into many small clusters. Macroscopic contractions were also observed at R_F = 0.05 and R_M = 0.01. The only inconsistency with microscopy experiments occurred at R_F = 0.02 and R_M = 0.005. With microscopy we saw macroscopic contractions, whereas here we found a stationary sample.

Time-resolved dynamics. In order to probe microscopic dynamics of contractile active gels, we first measured speckle dynamics using the 4xCCD setup (see Methods). We compute the correlation function $c(t, \tau)$ between time-points t and $t+\tau$, where t is sample age and τ is lag time (see Methods). Figure 15 shows how $c(t, \tau)$ evolves for a sample that contracts macroscopically. At t = 0 s, just after the proteins are mixed, we find fast dynamics with relaxation times below 1 s, as evidenced by the correlation functions which take values close to zero for all time-lags. Up till $t \approx$ 2500 s (42 min), $c(t, \tau)$ increases, suggesting slower dynamics. Slower dynamics are consistent with the formation of a space-spanning network and may also reflect the build-up of stresses across the network due to tension driven by myosin motor activity. At t ≈ 2500–3000 s (42–50 min), $c(t, \tau)$ experiences a drop, suggesting a

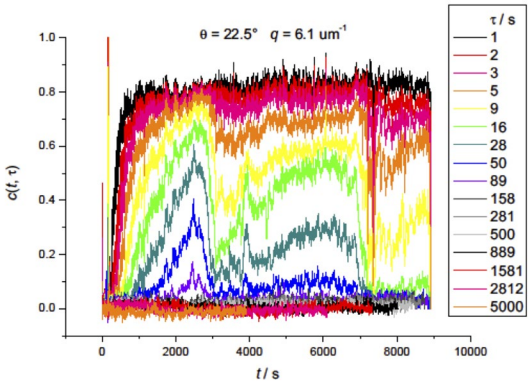

Figure 15. Correlation function $c(t,\tau)$ as a function of sample age t and lag time τ for $\theta = 22.5°$. Colored lines denote different values of τ (see legend, right) for all sample ages observed, up to 9000 s (2.5 h). Actin network (0.5 mg/ml) with $R_M = 0.01$ and $R_F = 0.05$.

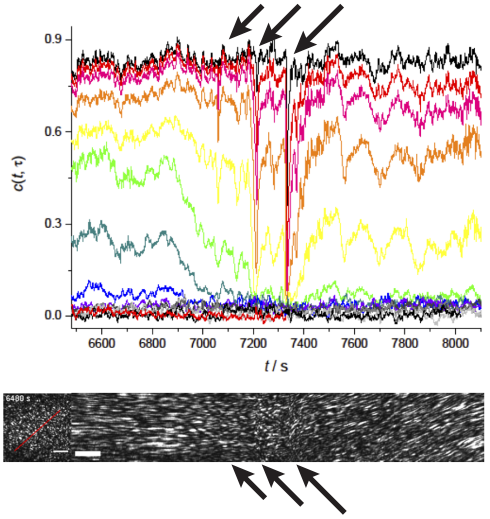

Figure 16. Correlation valleys in $c(t,\tau)$ arising from sudden network rearrangements. **Top row**: Close-up of Figure 15 for sample ages t = 6480–8100 s. **Bottom row, left**: Corresponding speckle pattern at 6480s. Scale bar 100 μm. **Bottom row, right**: Kymograph. Horizontal direction: sample age t = 6480–8100s. Vertical direction: speckle intensity along red line (bottom-left panel). Scale bar 30 μm x 100 s.

change in microscopic structure. The amount by which $c(t, \tau)$ drops depends strongly on lag time τ, and is maximal for $\tau \sim 28$s. At $t \approx$ 3000–72500 s (50 min–2 h), $c(t, \tau)$ remains constant, suggesting that the network remains in a steady state during this time. However, at $t \approx$ 7000–7400 s (2 h), we observe three sharp valleys in $c(t, \tau)$ (Fig. 16, top, black arrows). These valleys become progressively deeper, and are much narrower than the drops in correlation observed at t ≈ 2500 s. These valleys occur because speckle patterns undergo a sudden change. This is shown in the kymograph in Figure 16, bottom panel (black arrows). At $t \approx$ 6600–7000 s, before the three peaks, speckles appear as straight, horizontal streaks on the kymograph. This feature indicates that the microscopic structure of the network slowly rearranges on timescales that are comparable to the length of the streaks. However, the network remains stationary on a macroscopic scale. At t ≈ 7000–74000, the three valleys in $c(t, \tau)$ occur and the speckle pattern changes abruptly. This is evident in the kymograph, where existing horizontal streaks cease and new streaks begin. These abrupt changes in speckle pattern indicate a sudden rearrangement of the network. After these three peaks, at $t \approx$ 7400–8000, the speckles drifted globally, which is evident in the kymograph as slanted streaks. The global drift of speckles is very likely due to contraction, which results in a macroscopic drift of the network. After the experiment, a large cluster was indeed visible with the naked eye. The three sharp negative peaks may correspond to sudden events relating to an abrupt change in microscopic conformation: global loss of tension, detachment of the network from a boundary, etc.

Length-scale dependent dynamics. So far, we presented correlation function at one fixed scattering angle. We now turn our attention to data acquired simultaneously for four different scattering angles using four separate CCD detectors (Fig. 17). Qualitatively, we observe the same time evolution of the correlation functions at all angles. However, $c(t, \tau)$ decays faster with increasing scattering angle, which corresponds to smaller length scales.

In order to quantify relaxation times, we plot $g_2(\tau) - 1$ (Fig. 18a) and fit with a stretched exponential decay to extract the relaxation time τ_{relax} (see Methods). Performing this fit for all four scattering angles reveals that the relaxation time depends on scattering vector with a scaling relation of approximately $\tau_{relax} \sim q^{-0.7}$ (Fig. 18b). We do not yet

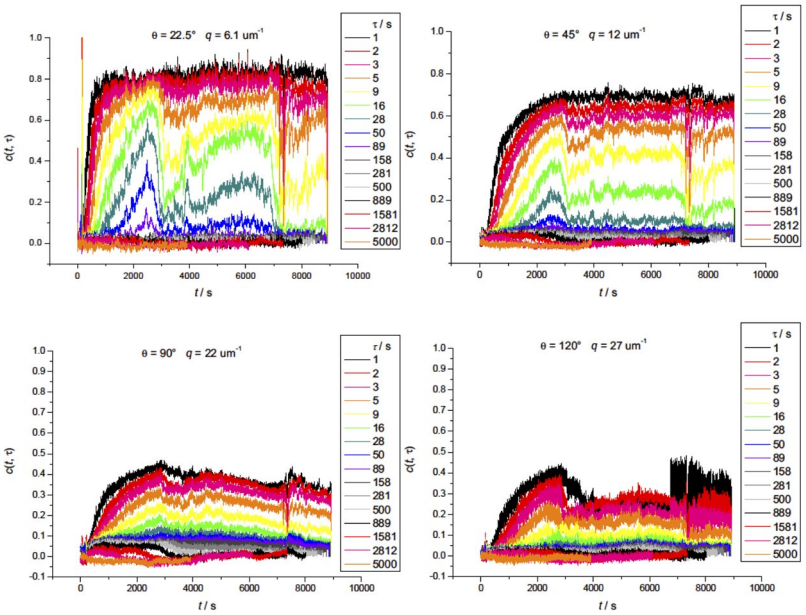

Figure 17. Correlation function $c(t,\tau)$ from Figure 15, acquired at different scattering angles θ: **Top-left**: θ = 22.5°. **Top-right**: θ = 45°. **Bottom-left**: θ = 90°. **Bottom-right**: θ = 120°.

know the physical origin of this scaling relation. Further measurements on networks prepared at different myosin and fascin concentrations will likely help to understand better how light scattering data may complement the microscopy results presented here and in Chapter 5.

Methods. Active gels were prepared under the following conditions: [actin] = 12 uM; [myosin] / [actin] = R_M = 0, 0.002, 0.005, 0.01; [fascin] / [actin] = R_F = 0, 0.02, 0.05; assay buffer (20 mM Imidazole pH 7.4, 50 mM KCl, 2 mM $MgCl_2$, 0.1 mM ATP, 10 mM creatine phosphate disodium, 0.1 mg/mL creatine kinase, 1 mM trolox, 5 mM protocatechuic acid). These conditions are identical to those used for microscopy, but a few experimental details are different: actin was resuspended from lyophilized powder without centrifugation to remove any oligomers, and was not fluorescently labeled, and we did not add the anti-photobleaching mix of protocatechuate-3,4-dioxygenase and protocatechuic acid. All buffer solutions were filtered through 0.22-μm filters to remove dust, which hampers light scattering measurements.

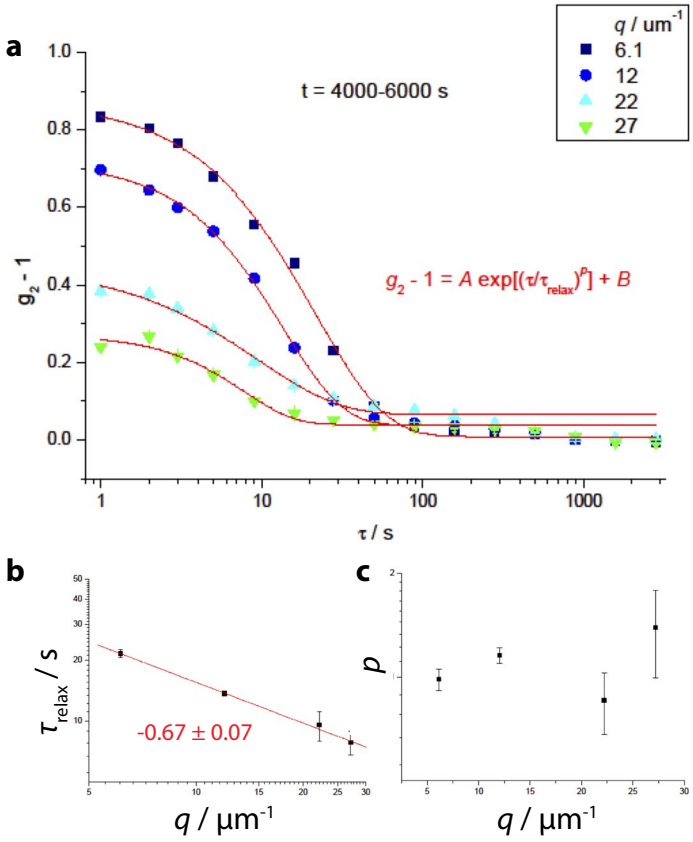

Figure 18. Quantifying relaxation time scales. **Top**: $g_2(\tau) - 1$, averaged over the time window $t = 4000–6000$ s for the four different angles shown in Figure 17. Red lines denote fits to a stretched exponential decay. **Bottom, left**: relaxation time τ_{relax} from fit versus scattering vector q. **Bottom, right**: exponent p from fit versus scattering vector q. Error bars denote standard error of the mean.

Networks were prepared by mixing a solution containing buffers, salts, myosins, and fascins. Polymerization of the network was initiated by mixing this solution with actin monomers. This mixture was subsequently loaded into a cylindrical glass NMR tube with a 5-mm outer diameter and a wall thickness of 0.4 mm.

4xCCD setup. We used a setup with 4 charge-coupled devices (henceforth "4xCCD setup") to measure space- and time-resolved scattering of an incident 532 nm laser collimated to a beam width of 1 mm. The sample is mounted in a metal housing with four holes drilled at 22.5°, 45°, 90°, and 120°. The four CCDs were mounted to capture speckle dynamics simultaneously at all four angles. Each CCD delivers space- and time-resolved information, and combining all four CCDs allows us to investigate length-scale dependent dynamics. The intensity of each pixel of the CCD corresponds to the microscopic conformation of a 3μm x 3μm x 1mm volume of the network. The value of 3 μm is determined by the size of the image projected on the CCD and was chosen to coincide with the average speckle size. The value of 1 mm is determined by the width of the beam.

CCD data acquisition was performed using a variable delay between images. Acquisitions were triggered with a user-programmable transistor-transistor logic (TTL) circuit. All CCDs were triggered simultaneously. We acquired pairs of images: the delay between two pairs of images varied from ~5ms to 1s using ¼-order-of-magnitude steps, scaled logarithmically; the delay between pairs was fixed at 1s. Image exposure time was ~1ms. We cycle through these logarithmically separated pairs of images continuously throughout the entire experiment.

Scattering intensity decreases for increasing scattering angle θ. In order to compensate for this intensity variation and ensure a roughly constant intensity on all four CCDs, we placed linear polarizers in front of the CCDs corresponding to 22.5° and 45°. We then adjusted the gain of the other two CCDs. We found that the scattering intensity of contracting samples increases over time; in order to minimize pixel saturation, we acquired data using the lowest possible gains.

CCD data processing: Before performing an experiment, we acquired so-called "dark data": ~100 images of each CCD with the laser switched on but no sample loaded. We averaged dark data over space and frames to obtain the contribution $<N_{back}>$ of the ambient background, which depends on the gain chosen for each CCD. We furthermore corrected for intensity variations due to the beam profile by calculating a normalization factor $N_{beam}(x,y)$ equal to the time-average over all frames acquired in an experiment. This average image usually results in a smooth image with features occurring only over long length scales,

corresponding to the background. However when sample dynamics was slow, these average image exhibited intensity variations on the length scale of a speckle. In these cases, we further spatially filtered the average image to smooth out features of speckle-length-scales. Therefore, given the signal $S(x, y, t)$ from the CCD, we compute the scattered laser intensity:

$$I(x, y, t) = \frac{S(x, y, t) - \langle N_{\text{back}} \rangle}{N_{\text{beam}}(x, y)}.$$

Correlation between two images A and B is defined as

$$c(A, B) = \frac{\langle AB \rangle}{\langle A \rangle \langle B \rangle} - 1,$$

where angular brackets denote an average over all pixels. Note that the correlation between an image A with itself, $c(A, A)$, can take on values less than one. This value depends on the pixel intensity distribution of image A. Well-resolved speckles exhibit a Chi-distribution and $c(A, A) \rightarrow 1$, whereas poorly-resolved speckles (which are observed when speckle dynamics are faster than the acquisition time, or when speckles are smaller than the pixel size) exhibit a Gaussian distribution and $c(A, A) \rightarrow 0$. The correlation function between two spatial conformations of speckle intensities is therefore given by

$$c(t, \tau) = \frac{\left\langle I(x, y, t) \cdot I(x, y, t + \tau) \right\rangle_{xy}}{\left\langle I(x, y, t) \right\rangle_{xy} \cdot \left\langle I(x, y, t + \tau \right\rangle_{xy}} - 1,$$

where angular brackets denote averages over all pixels of a given time frame. In order to extract relaxation times from $c(t, \tau)$, we average $c(t, \tau)$ over a time window in which it remains constant, yielding the quantity $g_2(\tau) - 1$:

$$g_2(\tau) - 1 = \langle c(t, \tau) \rangle_t,$$

where angular brackets denote a time average over the chosen time window. We then fit $g_2(\tau) - 1$ with a stretched exponential to recover

$$g_2(\tau) - 1 = Ae^{\left(\frac{\tau}{\tau_{\text{relax}}}\right)^p} + B.$$

Scattering angle θ and scattering vector q are related by

$$q = \frac{4\pi n}{\lambda} \sin\left(\frac{\theta}{2}\right),$$

where n is the index of refraction of the solvent (we use the refractive index of water, which is 1.33), and λ is the wavelength of the incident laser beam (here 532 nm).

Acknowledgements

Dynamic light scattering experiments were performed with Luca Cipeletti (U Montpellier). The Temporal Color Code ImageJ plugin was written by Kota Miura (EMBL, Heidelberg, Germany). Human α-actinin 2 protein was a kind gift from Balász Visegrády (U Pécs). *Arabidopsis* fimbrin 2 plasmid was a kind gift from Tijs Ketelaars (Wageningen UR). Mouse fascin plasmid was a kind gift from Scott Hansen and R. Dyche Mullins (UC San Francisco). We thank Marjolein Kuit-Vinkenoog, Magdalena Preciado-López, and Feng-Ching Tsai (AMOLF, Amsterdam, Netherlands) for help with purifications.

Summary

Polymers differ from many common solids. Crystalline solids can be thought of as a three-dimensional lattice of point-like atoms. Meanwhile, polymers can be thought of as lines of matter, or filaments. The filamentous shape of single polymer chains explains some of the unique material properties of polymer-based materials such as plastics. Cells, too, contain a special subclass of polymers called biological polymers. These polymers give cells mechanical strength, allowing them to resist external forces and maintain their shape. Biological polymers also give cells the fascinating ability to actively exert forces on their internal compartments as well as their environment. Understanding how cells resist and exert forces is essential in quantifying cell behavior.

The goal of this thesis is to better understand biological polymers inside cells. Most of our understanding of biological polymers comes from idealized experiments in an artificial, cell-free environment. Using this knowledge to explain the behavior of real cells remains challenging. In order to address this shortcoming, I have designed experiments of biological polymers confined to cellular dimensions, bent into rings, and driven by molecular motors.

In Chapters 2 and 3, I report experiments where biological polymers were confined to small chambers. The sizes of these chambers compares to the typical size of cells. Little is known about how polymers organize when packed into such confined spaces. I built customized chambers of different shapes to address how confinement influences biological polymers. In Chapter 2, I report experiments with liquid crystals of the rod-shaped virus bacteriophage fd which are confined to donut-shaped chambers. I wrote customized software to quantify the local alignment of the liquid crystal. This analysis reveals a striking pattern with three-fold symmetry. Existing continuum models, which

neglect rod size, cannot predict this pattern. But numerical simulations which account for rod size can. In Chapter 3, I report experiments of actin filament networks which were confined to rectangular chambers. I wrote customized software to quantify local alignment. Filaments align either along the diagonal or parallel to the longest edges. The results of both these chapters suggest that the boundary of a cell influences the alignment of its biological polymers.

In Chapter 4, I report experiments showing that septins bind to and bundle actin filaments. These results overthrow prevailing assumptions to the contrary. Surprisingly, growing actin filaments in the presence of septins lead to rings. I wrote customized software to quantify their curvature. We do not yet understand how these rings form. Existing models disagree with our findings. The results of this chapter suggest that septins can form actin rings inside cells—including the contractile ring which divides cells.

In Chapters 5 and 6, I report experiments with myosin motor proteins, which drive actin filaments. This driving leads to muscle-like contraction forces. Crosslink proteins are needed for contraction over long distances. But little is known about how crosslinks propagate force. I perform experiments with crosslinked, driven actin networks to address this question. In Chapter 5, I report that motors contract actin networks to clusters. I wrote customized software to determine cluster size. The size distribution of these clusters is scale-free, indicating critical behavior. Surprisingly, this behavior occurs more commonly than expected. Existing theories cannot predict this finding. But numerical simulations which account for motor forces and crosslink detachment predict it. In Chapter 6, I extend the results in Chapter 5. I compare the effect of different crosslinks and different methods of weakening motor force. The results of these chapters show that internal forces from myosin motors behave differently from external forces. They suggest that non-muscle cells exploit this fact to determine the distance of contractions.

As for all five research chapters, we currently lack analytical physical models to explain our results. Future theoretical work will likely overcome this. In doing so, we will better understand the physical forces that affect the biological polymers inside cells. This should allow researchers to better quantify how cells exert and resist forces.

Samenvatting

Polymeren zijn anders dan gewone vaste stoffen. Een driedimensionaal rooster van deeltjes is een goed model voor een kristalstructuur. Maar polymeren zijn eendimensionale strengen van materie, filamenten genoemd. Deze filamenteuze vorm zorgt voor de unieke eigenschappen van vele polymeren, zoals plastic. Ook cellen bevatten polymeren: zogenaamde biologische polymeren. Deze polymeren geven cellen mechanische rigiditeit. Zo kunnen cellen externe krachten weerstaan en hun vorm handhaven. Door middel van biologische polymeren kunnen cellen kracht uitoefenen op hun interne compartimenten en op hun omgeving. Inzicht in hoe cellen krachten weerstaan en uitoefenen is nodig om celgedrag te kunnen kwantificeren.

Het doel van dit proefschrift is om biologische polymeren in cellen beter te begrijpen. De meeste van onze kennis komt van geïdealiseerde experimenten in een kunstmatig, cel-vrij milieu. Met deze kennis kan men biologische polymeren in echte cellen moeilijk kwantificeren. Om dit tekort te verhelpen ontwierp ik experimenten met biologische polymeren die op cellulaire lengteschalen zijn ingesloten, in ringen zijn gebogen, en worden aangedreven door moleculaire motoreiwitten.

In hoofdstukken 2 en 3 beschrijf ik experimenten waar biologische polymeren in kleine ruimtes zijn ingesloten. De groottes van deze ruimtes komen overeen met de typische groottes van cellen. We weten weinig over hoe polymeren zich organiseren in dergelijke ruimtes. Ik maakte ruimtes met verschillende vormen om te begrijpen hoe insluiting polymeren beïnvloedt. In hoofdstuk 2 beschrijf ik experimenten met vloeibare kristallen van staafvormige fd-virussen, die in donut-vormige kamers zijn ingesloten. Ik ontwierp software om de lokale ordening van het vloeibare kristal te kwantificeren. Deze analyse laat een verrassende patroon van drievoudige symmetrie zien. Bestaande

continuümmodellen die de grootte van de staven verwaarlozen kunnen dit patroon niet voorspellen. Maar dat kan wel met numerieke simulaties die rekening houden met de grootte van de staven. In hoofdstuk 3 beschrijf ik experimenten met actinefilamenten die in rechthoekige kamers zijn opgesloten. Ik ontwierp software om de lokale ordening te kwantificeren. Filamenten liggen of langs de diagonaal of parallel met de langste kanten van de rechthoek. De resultaten van deze hoofdstukken suggereren dat de grens van een cel de ordening van zijn biologische polymeren kan beïnvloeden.

In hoofdstuk 4 beschrijf ik experimenten die laten zien dat het eiwit septine actine-filamenten bindt en bundelt. Deze resultaten verwerpen eerdere aannames die het tegenovergestelde suggereerden. Verrassend is dat actine in de aanwezigheid van septine ringen vormt. Ik ontwierp software om hun kromming te kwantificeren. Wij weten niet hoe deze ringen vormen. Bestaande modellen zijn in tegenspraak met onze bevindingen. De resultaten van dit hoofdstuk laten zien dat septine binnen cellen actineringen kan vormen—inclusief de contractiele ring die delende cellen insnoert.

In hoofdstukken 5 en 6 beschrijf ik experimenten waar het motoreiwit myosine actine-filamenten aandrijft. Deze aandrijving leidt tot inwaartse trekkrachten zoals in spieren. Gecrosslinkte eiwitten zijn nodig om samentrekkingen over lange afstanden uit te voeren. We weten weinig over hoe crosslinks inwaartse trekkrachten propageren. Ik voer experimenten uit met aangedreven, gecrosslinkte actine-netwerken om deze vraag te beantwoorden. In hoofdstuk 5 schrijf ik dat myosine actine-netwerken in klonten kunnen samentrekken. Ik ontwierp software om de grootte van klonten te kwantificeren. De distributie van deze klonten is schaalvrij, wat op een kritische proces duidt. Verrassend is dat dit vaker gebeurt dan verwacht. Bestaande modellen kunnen dit resultaat niet verklaren. Maar dat kan wel met numerieke simulaties die rekening houden met krachten van motoreiwitten en het loslaten van crosslinks. In hoofdstuk 6 breid ik het werk van hoofdstuk 5 uit. Ik vergelijk het effect van verschillende soorten crosslinks en verschillende manieren om motorkrachten te verzwakken. De resultaten van deze hoofdstukken laten zien dat de interne krachten uitgeoefend door myosines anders zijn dan externe krachten. Ze suggereren dat cellen dit feit gebruiken om de lengte van contracties te bepalen.

In alle vijf onderzoekshoofdstukken ontbreken analytische modellen die onze experimentele resultaten verklaren. Toekomstige theoretische modellen zullen deze tekortkoming verhelpen. Dan kunnen we de natuurkundige krachten die biologische polymeren beïnvloeden beter begrijpen. Dit zou ons helpen begrijpen hoe cellen krachten weerstaan en uitoefenen.

Met dank aan Martijn Wehrens en Joris Paijmans voor hun hulp met de nederlandse tekst.

References

Abercrombie, M. (1980). The Croonian Lecture, 1978: The Crawling Movement of Metazoan Cells. Proc Roy Soc B *207*, 129–147.

Adam, J.C., Pringle, J.R., and Peifer, M. (2000). Evidence for functional differentiation among Drosophila septins in cytokinesis and cellularization. Mol Biol Cell *11*, 3123–3135.

Adams, D.S., Robinson, K.R., Fukumoto, T., Yuan, S., Albertson, R.C., Yelick, P., Kuo, L., McSweeney, M., and Levin, M. (2006). Early, H+-V-ATPase-dependent proton flux is necessary for consistent left-right patterning of non-mammalian vertebrates. Development *133*, 1657–1671.

Alberts, B. (2008). Molecular Biology of the Cell (Garland Science).

Alvarado, J., Sheinman, M., Sharma, A., MacKintosh, F.C., and Koenderink, G. (2013). Molecular motors robustly drive active gels to a critically connected state. Submitted.

Ananthakrishnan, R., and Ehrlicher, A. (2007). The Forces Behind Cell Movement. Int J Biol Sci 3, 303–317.

Artimo, P., Jonnalagedda, M., Arnold, K., Baratin, D., Csardi, G., de Castro, E., Duvaud, S., Flegel, V., Fortier, A., Gasteiger, E., et al. (2012). ExPASy: SIB bioinformatics resource portal. Nucleic Acids Res *40*, W597–W603.

Atilgan, E., Wirtz, D., and Sun, S.X. (2006). Mechanics and dynamics of actin-driven thin membrane protrusions. Biophys J *90*, 65–76.

Atkins, P., and de Paula, J. (2009). Atkins' Physical Chemistry (OUP Oxford).

Backouche, F., Haviv, L., Groswasser, D., and Bernheim-Groswasser, A. (2006). Active gels: dynamics of patterning and self-organization. Phys Biol *3*, 264–273.

Barlan, K., Rossow, M.J., and Gelfand, V.I. (2013). The journey of the organelle: teamwork and regulation in intracellular transport. Curr Opin Cell Biol.

Bausch, A.R., and Kroy, K. (2006). A bottom-up approach to cell mechanics. Nat Phys *2*, 231–238.

Bawden, F.C., Pirie, N.W., Bernal, J.D., and Fankuchen, I. (1936). Liquid Crystalline Substances from Virus-infected Plants. Nature *138*, 1051–1052.

Beausang, J.F., Schroeder, H.W., 3rd, Nelson, P.C., and Goldman, Y.E. (2008). Twirling

of Actin by Myosins II and V Observed via Polarized TIRF in a Modified Gliding Assay. Biophys J *95*, 5820–5831.
Beise, N., and Trimble, W. (2011). Septins at a glance. J Cell Sci *124*, 4141–4146.
Bement, W.M., Miller, A.L., and Dassow, von, G. (2006). Rho GTPase activity zones and transient contractile arrays. Cytoskeleton *28*, 983–993.
Bendix, P.M., Koenderink, G.H., Cuvelier, D., Dogic, Z., Koeleman, B.N., Brieher, W.M., Field, C.M., Mahadevan, L., and Weitz, D.A. (2008). A quantitative analysis of contractility in active cytoskeletal protein networks. Biophys J *94*, 3126–3136.
Berens, P. (2009). CircStat: a MATLAB toolbox for circular statistics. J Stat Software *31*, 1–21.
Bernal, J.D., and Fankuchen, I. (1941). X-ray and crystallographic studies of plant virus preparations. III. J Gen Physiol *25*, 147–165.
Bernstein, M., and Rosenbaum, J.L. (1994). Kinesin-like proteins in the flagella of Chlamydomonas. Trends Cell Biol *4*, 236–240.
Bertin, A., McMurray, M.A., Grob, P., Park, S.S., Garcia, G., Patanwala, I., Ng, H.L., Alber, T., Thorner, J., and Nogales, E. (2008). Saccharomyces cerevisiae septins: supramolecular organization of heterooligomers and the mechanism of filament assembly. Proc Natl Acad Sci USA *105*, 8274–8279.
Bertin, A., McMurray, M.A., Thai, L., Garcia, G., Votin, V., Grob, P., Allyn, T., Thorner, J., and Nogales, E. (2010). Phosphatidylinositol-4,5-bisphosphate promotes budding yeast septin filament assembly and organization. J Mol Biol *404*, 711–731.
Bertrand, O.J.N., Fygenson, D.K., and Saleh, O.A. (2012). Active, motor-driven mechanics in a DNA gel. Proc Natl Acad Sci USA *109*, 17342–17347.
Betz, T., Koch, D., Lu, Y.-B., Franze, K., and Käs, J.A. (2011). Growth cones as soft and weak force generators. Proc Natl Acad Sci USA *108*, 13420–13425.
Bialek, W., Cavagna, A., Giardina, I., Mora, T., Silvestri, E., Viale, M., and Walczak, A.M. (2012). Statistical mechanics for natural flocks of birds. Proc Natl Acad Sci USA *109*, 4786–4791.
Bischofs, I.B., Klein, F., Lehnert, D., Bastmeyer, M., and Schwarz, U.S. (2008). Filamentous Network Mechanics and Active Contractility Determine Cell and Tissue Shape. Biophys J *95*, 3488–3496.
Bois, J., Jülicher, F., and Grill, S. (2011). Pattern Formation in Active Fluids. Phys Rev Lett *106*, 028103.
Bolhuis, P., and Frenkel, D. (1997). Tracing the phase boundaries of hard spherocylinders. J Chem Phys *106*, 666–687.
Bonthuis, D., Meyer, C., Stein, D., and Dekker, C. (2008). Conformation and Dynamics of DNA Confined in Slitlike Nanofluidic Channels. Phys Rev Lett *101*, 108303.
Bork, P., Sander, C., and Valencia, A. (1992). An ATPase domain common to prokaryotic cell cycle proteins, sugar kinases, actin, and hsp70 heat shock proteins. Proc Natl Acad Sci USA *89*, 7290–7294.
Borukhov, L., Bruinsma, R., Gelbart, W., and Liu, A. (2005). Structural polymorphism of the cytoskeleton: A model of linker-assisted filament aggregation. Proc Natl Acad Sci USA *102*, 3673–3678.
Bowne-Anderson, H., Zanic, M., Kauer, M., and Howard, J. (2013). Microtubule

dynamic instability: A new model with coupled GTP hydrolysis and multistep catastrophe. Bioessays *35*, 452–461.
Brangwynne, C.P., Koenderink, G.H., MacKintosh, F.C., and Weitz, D.A. (2008). Nonequilibrium microtubule fluctuations in a model cytoskeleton. Phys Rev Lett *100*, 118104.
Bras, W., Diakun, G.P., Díaz, J.F., Maret, G., Kramer, H., Bordas, J., and Medrano, F.J. (1998). The Susceptibility of Pure Tubulin to High Magnetic Fields: A Magnetic Birefringence and X-Ray Fiber Diffraction Study. Biophys J *74*, 1509–1521.
Bray, D., and White, J. (1988). Cortical flow in animal cells. Science *239*, 883–888.
Brenner, B., Schoenberg, M., Chalovich, J.M., Greene, L.E., and Eisenberg, E. (1982). Evidence for cross-bridge attachment in relaxed muscle at low ionic strength. Proc Natl Acad Sci USA *79*, 7288–7291.
Bresnick, A.R. (1999). Molecular mechanisms of nonmuscle myosin-II regulation. Curr Opin Cell Biol *11*, 26–33.
Bringmann, M., Landrein, B., Schudoma, C., Hamant, O., Hauser, M.-T., and Persson, S. (2012). Cracking the elusive alignment hypothesis: the microtubule-cellulose synthase nexus unraveled. Trends Plant Sci *17*, 666–674.
Broderick, M.J.F., and Winder, S.J. (2005). Spectrin, α-Actinin, and Dystrophin. In Advances in Protein Chemistry, A.J.M.S. David A D Parry, ed. (Academic Press), pp. 203–246.
Broedersz, C.P., Mao, X., Lubensky, T.C., and MacKintosh, F.C. (2011). Criticality and isostaticity in fibre networks. Nat Phys *7*, 983–988.
Brokaw, C.J. (1994). Control of flagellar bending: A new agenda based on dynein diversity. Cell Motil Cytoskeleton *28*, 199–204.
Brown, N.A., and Wolpert, L. (1990). The development of handedness in left/right asymmetry. Development *109*, 1–9.
Bryant, P.J. (1999). Filopodia: fickle fingers of cell fate? Curr Biol 9, R655–R657.
Burgess, S.A., Walker, M.L., Sakakibara, H., Knight, P.J., and Oiwa, K. (2003). Dynein structure and power stroke. Nature *421*, 715–718.
Bustamante, C., Marko, J., Siggia, E., and Smith, S. (1994). Entropic elasticity of lambda-phage DNA. Science *265*, 1599–1600.
Bustamante, C., Chemla, Y.R., Forde, N.R., and Izhaky, D. (2004). Mechanical processes in biochemistry. Annu Rev Biochem *73*, 705–748.
Buxbaum, R.E., Dennerll, T., Weiss, S., and Heidemann, S.R. (1987). F-actin and microtubule suspensions as indeterminate fluids. Science *235*, 1511–1514.
Byers, B. (1976). A highly ordered ring of membrane-associated filaments in budding yeast. J Cell Biol *69*, 717–721.
Camalet, S., Duke, T., Jülicher, F., and Prost, J. (2000). Auditory sensitivity provided by self-tuned critical oscillations of hair cells. Proc Natl Acad Sci USA *97*, 3183–3188.
Cameron, L., Svitkina, T., Vignjevic, D., Theriot, J., and Borisy, G. (2001). Dendritic organization of actin comet tails. Curr Biol *11*, 130–135.
Cartwright, J.H.E., Piro, O., and Tuval, I. (2004). Fluid-dynamical basis of the embryonic development of left-right asymmetry in vertebrates. Proc Natl Acad Sci USA *101*, 7234–7239.

Casamayor, A., and Snyder, M. (2003). Molecular dissection of a yeast septin: distinct domains are required for septin interaction, localization, and function. Mol Cell Biol *23*, 2762–2777.

Castellano, J.A. (2005). Liquid Gold (World Scientific Publishing Company).

Cavey, M., and Lecuit, T. (2009). Molecular Bases of Cell-Cell Junctions Stability and Dynamics. Cold Spring Harb Perspect Biol *1*, a002998.

Cēbers, A., Dogic, Z., and Janmey, P. (2006). Counterion-Mediated Attraction and Kinks on Loops of Semiflexible Polyelectrolyte Bundles. Phys Rev Lett *96*, 247801.

Chang, F., and Martin, S.G. (2009). Shaping fission yeast with microtubules. Cold Spring Harb Perspect Biol *1*, a001347.

Chaudhuri, O., Parekh, S.H., and Fletcher, D.A. (2007). Reversible stress softening of actin networks. Nature *445*, 295–298.

Chen, B., Li, A., Wang, D., Wang, M., Zheng, L., and Bartles, J.R. (1999). Espin contains an additional actin-binding site in its N terminus and is a major actin-bundling protein of the Sertoli cell-spermatid ectoplasmic specialization junctional plaque. Mol Biol Cell *10*, 4327–4339.

Chen, C.S., Mrksich, M., Huang, S., Whitesides, G.M., and Ingber, D.E. (1997). Geometric control of cell life and death. Science *276*, 1425–1428.

Chen, Z.Y. (1993). Nematic ordering in semiflexible polymer chains. Macromolecules *26*, 3419–3423.

Chhabra, E.S., and Higgs, H.N. (2007). The many faces of actin: matching assembly factors with cellular structures. Nat Cell Biol *9*, 1110–1121.

Choi, M., Santangelo, C., Pelletier, O., Kim, J., Kwon, S., Wen, Z., Li, Y., Pincus, P., Safinya, C., and Kim, M. (2005). Direct observation of biaxial confinement of a semiflexible filament in a channel. Macromolecules *38*, 9882–9884.

Cipelletti, L., and Weeks, E.R. (2010). Glassy dynamics and dynamical heterogeneity in colloids. arXiv 1009.6089.

Cipelletti, L., Bissig, H., Trappe, V., Ballesta, P., and Mazoyer, S. (2002). Time-resolved correlation: a new tool for studying temporally heterogeneous dynamics. J Phys Condens Matter *15*, S257–S262.

Claessens, M.M.A.E., Semmrich, C., Ramos, L., and Bausch, A.R. (2008). Helical twist controls the thickness of F-actin bundles. Proc Natl Acad Sci USA *105*, 8819–8822.

Claessens, M.M.A.E., Tharmann, R., Kroy, K., and Bausch, A.R. (2006). Microstructure and viscoelasticity of confined semiflexible polymer networks. Nat Phys *2*, 186–189.

Claessens, M.M.A.E., Bathe, M., Frey, E., and Bausch, A.R. (2006b). Actin-binding proteins sensitively mediate F-actin bundle stiffness. Nat Mater *5*, 748–753.

Clauset, A., Shalizi, C.R., and Newman, M.E.J. (2009). Power-Law Distributions in Empirical Data. SIAM Rev *51*, 661–703.

Cojoc, D., Difato, F., Ferrari, E., Shahapure, R.B., Laishram, J., Righi, M., Di Fabrizio, E.M., and Torre, V. (2007). Properties of the force exerted by filopodia and lamellipodia and the involvement of cytoskeletal components. PLOS One 2, e1072.

Cooke, R., and Bialek, W. (1979). Contraction of glycerinated muscle fibers as a function of the ATP concentration. Biophys J 28, 241–258.

Coppin, C.M., and Leavis, P.C. (1992). Quantitation of liquid-crystalline ordering in F-actin solutions. Biophys J *63*, 794–807.
Cornwell, J.F. (1984). Group theory in physics (Academic Press).
Corté, L., Chaikin, P.M., Gollub, J.P., and Pine, D.J. (2008). Random organization in periodically driven systems. Nat Phys *4*, 420–424.
Cosentino Lagomarsino, M., Tanase, C., Vos, J.W., Emons, A.M.C., Mulder, B.M., and Dogterom, M. (2007). Microtubule organization in three-dimensional confined geometries: evaluating the role of elasticity through a combined in vitro and modeling approach. Biophys J *92*, 1046–1057.
Costerton, J.W., Stewart, P.S., and Greenberg, E.P. (1999). Bacterial Biofilms: A Common Cause of Persistent Infections. Science *284*, 1318–1322.
Courson, D.S., and Rock, R.S. (2010). Actin Cross-link Assembly and Disassembly Mechanics for alpha-Actinin and Fascin. J Biol Chem *285*, 26350–26357.
D'Avino, P.P., Takeda, T., Capalbo, L., Zhang, W., Lilley, K.S., Laue, E.D., and Glover, D.M. (2008). Interaction between Anillin and RacGAP50C connects the actomyosin contractile ring with spindle microtubules at the cell division site. J Cell Sci *121*, 1151–1158.
Dammone, O., Zacharoudiou, I., Dullens, R., Yeomans, J., Lettinga, M., and Aarts, D. (2012). Confinement Induced Splay-to-Bend Transition of Colloidal Rods. Phys Rev Lett *109*, 108303.
Dasanayake, N.L., Michalski, P.J., and Carlsson, A.E. (2011). General mechanism of actomyosin contractility. Phys Rev Lett *107*, 118101.
Davenport, R.W., Dou, P., Rehder, V., and Kater, S.B. (1993). A sensory role for neuronal growth cone filopodia. Nature *361*, 721–724.
Davidson, A.J., Brown, C.V., Mottram, N.J., Ladak, S., and Evans, C.R. (2010). Defect trajectories and domain-wall loop dynamics during two-frequency switching in a bistable azimuthal nematic device. Phys Rev E *81*, 051712.
Davis, J.S. (1988). Assembly Processes in Vertebrate Skeletal Thick Filament Formation. Annu Rev Biophys Biophys Chem *17*, 217–239.
Davison, A.C., and Hinkley, D.V. (1997). Bootstrap Methods and Their Application (Cambridge University Press).
de Gennes, P.-G., and Prost, J. (1995). The Physics of Liquid Crystals (Clarendon Press).
de Gennes, P.-G. (1979). Scaling concepts in polymer physics (Cornell University Press).
Debold, E.P., Patlak, J.B., and Warshaw, D.M. (2005). Slip sliding away: load-dependence of velocity generated by skeletal muscle myosin molecules in the laser trap. Biophys J *89*, L34–L36.
Dehmelt, L., and Halpain, S. (2003). Actin and microtubules in neurite initiation: Are MAPs the missing link? Cytoskeleton *58*, 18–33.
Deshpande, S., and Pfohl, T. (2012). Hierarchical self-assembly of actin in micro-confinements using microfluidics. Biomicrofluidics 6, 034120.
Dickinson, R.B., Caro, L., and Purich, D.L. (2004). Force Generation by Cytoskeletal Filament End-Tracking Proteins. Biophys J *87*, 2838–2854.

Dijkstra, M., van Roij, R., and Evans, R. (2001). Wetting and capillary nematization of a hard-rod fluid: a simulation study. Phys Rev E *63*, 051703.
Dobbelaere, J., and Barral, Y. (2004). Spatial coordination of cytokinetic events by compartmentalization of the cell cortex. Science *305*, 393–396.
Dogic, Z., and Fraden, S. (2006). Ordered phases of filamentous viruses. Curr Opin Colloid Interface Sci 11, 47–55.
Dogic, Z., and Fraden, S. (2000). Cholesteric Phase in Virus Suspensions. Langmuir *16*, 7820–7824.
Dogic, Z., and Fraden, S. (2005). Phase Behavior of Rod-Like Viruses and Virus–Sphere Mixtures. In Soft Matter, Vol. 2: Complex Colloidal Suspensions, G. Gompper, and M. Schick, eds. (Weinheim, Germany: Wiley-VCH Verlag GmbH & Co. KGaA), pp. 1–86.
Dogic, Z., Purdy, K., Grelet, E., Adams, M., and Fraden, S. (2004). Isotropic-nematic phase transition in suspensions of filamentous virus and the neutral polymer Dextran. Phys Rev E *69*, 051702.
Dogterom, M., and Yurke, B. (1997). Measurement of the Force-Velocity Relation for Growing Microtubules. Science *278*, 856–860.
Dogterom, M., Kerssemakers, J.W., Romet-Lemonne, G., and Janson, M.E. (2005). Force generation by dynamic microtubules. Curr Opin Cell Biol *17*, 67–74.
Doi, M., and Edwards, S.F. (1978). Dynamics of concentrated polymer systems. Part 1.-Brownian motion in the equilibrium state. J Chem Soc Faraday Trans 2 74, 1789–1801.
Driscoll, M.K., McCann, C., Kopace, R., Homan, T., Fourkas, J.T., Parent, C., and Losert, W. (2012). Cell Shape Dynamics: From Waves to Migration. PLOS Comput Biol *8*, e1002392.
Dujardin, D.L., and Vallee, R.B. (2002). Dynein at the cortex. Curr Opin Cell Biol *14*, 44–49.
Dumont, S., and Mitchison, T.J. (2009). Force and Length in the Mitotic Spindle. Curr Biol *19*, R749–R761.
Duri, A., Sessoms, D., Trappe, V., and Cipelletti, L. (2009). Resolving Long-Range Spatial Correlations in Jammed Colloidal Systems Using Photon Correlation Imaging. Phys Rev Lett *102*, 085702.
Dzubiella, J., Schmidt, M., and Löwen, H. (2000). Topological defects in nematic droplets of hard spherocylinders. Phys Rev E *62*, 5081–5091.
Edwards, R.A., Herrera-Sosa, H., Otto, J., and Bryan, J. (1995). Cloning and expression of a murine fascin homolog from mouse brain. J Biol Chem *270*, 10764–10770.
Efron, B. (1987). Better Bootstrap Confidence Intervals. J Am Stat Assoc *82*, 171–185.
Egelman, E.H., Francis, N., and DeRosier, D.J. (1982). F-actin is a helix with a random variable twist. Nature *298*, 131–135.
Eggert, U.S., Mitchison, T.J., and Field, C.M. (2006). Animal Cytokinesis: From Parts List to Mechanisms. Annu Rev Biochem *75*, 543–566.
Ellis, R.J. (2001). Macromolecular crowding: obvious but underappreciated. Trends Biochem Sci *26*, 597–604.
Engqvist-Goldstein, Å.E.Y., and Drubin, D.G. (2003). Actin Assembly and Endocytosis:

From Yeast to Mammals. Annu Rev Cell Dev Biol *19*, 287–332.
Evans, E., and Ritchie, K. (1997). Dynamic strength of molecular adhesion bonds. Biophys J *72*, 1541.
Falzone, T.T., Lenz, M., Kovar, D.R., and Gardel, M.L. (2012). Assembly kinetics determine the architecture of α-actinin crosslinked F-actin networks. Nat Commun *3*, 861.
Fan, J., Saunders, M.G., Haddadian, E.J., Freed, K.F., La Cruz, De, E.M., and Voth, G.A. (2013). Molecular Origins of Cofilin-Linked Changes in Actin Filament Mechanics. J Mol Biol *425*, 1225–1240.
Fernandez-Gonzalez, R., Simoes, S. de M., Röper, J.-C., Eaton, S., and Zallen, J.A. (2009). Myosin II dynamics are regulated by tension in intercalating cells. Dev Cell *17*, 736–743.
Fernandez-Nieves, A., Vitelli, V., Utada, A., Link, D., Márquez, M., Nelson, D., and Weitz, D. (2007). Novel Defect Structures in Nematic Liquid Crystal Shells. Phys Rev Lett *99*, 157801.
Ferrer, J.M., Lee, H., Chen, J., Pelz, B., Nakamura, F., Kamm, R.D., and Lang, M.J. (2008). Measuring molecular rupture forces between single actin filaments and actin-binding proteins. Proc Natl Acad Sci USA *105*, 9221–9226.
Field, C.M. (2005). Characterization of anillin mutants reveals essential roles in septin localization and plasma membrane integrity. Development *132*, 2849–2860.
Field, C.M., and Alberts, B.M. (1995). Anillin, a Contractile Ring Protein That Cycles From the Nucleus to the Cell Cortex. J Cell Biol *131*, 165–178.
Field, C.M., and Lénárt, P. (2011). Bulk Cytoplasmic Actin and Its Functions in Meiosis and Mitosis. Curr Biol *21*, R825–R830.
Fielding, S.M., Cates, M.E., and Sollich, P. (2009). Shear banding, aging and noise dynamics in soft glassy materials. Soft Matter *5*, 2378–2382.
Finer, J.T., Simmons, R.M., and Spudich, J.A. (1994). Single myosin molecule mechanics: piconewton forces and nanometre steps. Nature *368*, 113–119.
Fink, J., Carpi, N., Betz, T., Bétard, A., Chebah, M., Azioune, A., Bornens, M., Sykes, C., Fetler, L., Cuvelier, D., et al. (2011). External forces control mitotic spindle positioning. Nat Cell Biol *13*, 771–778.
Fisher, C.I., and Kuo, S.C. (2009). Filament rigidity causes F-actin depletion from nonbinding surfaces. Proc Natl Acad Sci USA *106*, 133–138.
Fletcher, D.A., and Geissler, P.L. (2009). Active Biological Materials. Annu Rev Phys Chem *60*, 469–486.
Flory, P.J., and Abe, A. (1978). Statistical Thermodynamics of Mixtures of Rodlike Particles. 1. Theory for Polydisperse Systems. Macromolecules *11*, 1119–1122.
Fonck, E., Feigl, G.G., Fasel, J., Sage, D., Unser, M., Rufenacht, D.A., and Stergiopulos, N. (2009). Effect of Aging on Elastin Functionality in Human Cerebral Arteries. Stroke *40*, 2552–2556.
Footer, M.J., Kerssemakers, J.W.J., Theriot, J.A., and Dogterom, M. (2007). Direct measurement of force generation by actin filament polymerization using an optical trap. Proc Natl Acad Sci USA *104*, 2181–2186.
Founounou, N., Loyer, N., and Le Borgne, R. (2013). Septins Regulate the Contractility

of the Actomyosin Ring to Enable Adherens Junction Remodeling during Cytokinesis of Epithelial Cells. Dev Cell *24*, 242–255.
Fraden, S., Maret, G., and Caspar, D. (1993). Angular correlations and the isotropic-nematic phase transition in suspensions of tobacco mosaic virus. Phys Rev E *48*, 2816–2837.
Fraden, S., Maret, G., Caspar, D., and Meyer, R. (1989). Isotropic-nematic phase transition and angular correlations in isotropic suspensions of tobacco mosaic virus. Phys Rev Lett *63*, 2068–2071.
Frenkel, D. (1987). Onsager's spherocylinders revisited. J Phys Chem *91*, 4912–4916.
Fürthauer, S., Neef, M., Grill, S.W., Kruse, K., and Jülicher, F. (2012a). The Taylor–Couette motor: spontaneous flows of active polar fluids between two coaxial cylinders. New J Phys *14*, 023001.
Fürthauer, S., Strempel, M., Grill, S.W., and Jülicher, F. (2012b). Active chiral fluids. Eur Phys J E *35*, 89.
Furukawa, R., Kundra, R., and Fechheimer, M. (1993). Formation of liquid crystals from actin filaments. Biochemistry *32*, 12346–12352.
Furusawa, C., and Kaneko, K. (2012). Adaptation to Optimal Cell Growth through Self-Organized Criticality. Phys Rev Lett *108*, 208103.
Galanis, J., Harries, D., Sackett, D., Losert, W., and Nossal, R. (2006). Spontaneous Patterning of Confined Granular Rods. Phys Rev Lett *96*, 028002.
Galanis, J., Nossal, R., and Harries, D. (2010a). Depletion forces drive polymer-like self-assembly in vibrofluidized granular materials. Soft Matter *6*, 1026.
Galanis, J., Nossal, R., Losert, W., and Harries, D. (2010). Nematic Order in Small Systems: Measuring the Elastic and Wall-Anchoring Constants in Vibrofluidized Granular Rods. Phys Rev Lett *105*, 168001.
Galkin, V.E., Orlova, A., Kudryashov, D.S., Solodukhin, A., Reisler, E., Schröder, G.F., and Egelman, E.H. (2011). Remodeling of actin filaments by ADF/cofilin proteins. Proc Natl Acad Sci USA *108*, 20568–20572.
Galkin, V.E., Orlova, A., Salmazo, A., Djinovic-Carugo, K., and Egelman, E.H. (2010a). Opening of tandem calponin homology domains regulates their affinity for F-actin. Nat Struct Mol Biol *17*, 614–616.
Galkin, V.E., Orlova, A., Schröder, G.F., and Egelman, E.H. (2010b). Structural polymorphism in F-actin. Nat Struct Mol Biol *17*, 1318–1323.
Garcia, G., Bertin, A., Li, Z., Song, Y., McMurray, M.A., McMurray, M.A., Thorner, J., and Nogales, E. (2011). Subunit-dependent modulation of septin assembly: Budding yeast septin Shs1 promotes ring and gauze formation. J Cell Biol *195*, 993–1004.
Gardel, M.L., Shin, J.H., MacKintosh, F.C., Mahadevan, L., Matsudaira, P., and Weitz, D.A. (2004). Elastic behavior of cross-linked and bundled actin networks. Science *304*, 1301–1305.
Gardner, M.K., Charlebois, B.D., Jánosi, I.M., Howard, J., Hunt, A.J., and Odde, D.J. (2011). Rapid Microtubule Self-Assembly Kinetics. Cell *146*, 582–592.
Garlea, I., and Mulder, B. (2013) Personal Communication.
Garner, E.C., Campbell, C.S., Weibel, D.B., and Mullins, R.D. (2007). Reconstitution

of DNA Segregation Driven by Assembly of a Prokaryotic Actin Homolog. Science *315*, 1270–1274.
Gautel, M. (2011). The sarcomeric cytoskeleton: who picks up the strain? Curr Opin Cell Biol *23*, 39–46.
Gentry, B.S., Meulen, S., Noguera, P., Alonso-Latorre, B., Plastino, J., and Koenderink, G.H. (2012). Multiple actin binding domains of Ena/VASP proteins determine actin network stiffening. Eur Biophys J *41*, 979–990.
Gentry, B., Smith, D., and Käs, J. (2009). Buckling-induced zebra stripe patterns in nematic F-actin. Phys Rev E 79, 031916–11.
Gibaud, T., Barry, E., Zakhary, M.J., Henglin, M., Ward, A., Yang, Y., Berciu, C., Oldenbourg, R., Hagan, M.F., Nicastro, D., et al. (2012). Reconfigurable self-assembly through chiral control of interfacial tension. Nature *481*, 348–351.
Gilden, J.K., and Krummel, M.F. (2010). Control of cortical rigidity by the cytoskeleton: emerging roles for septins. Cytoskeleton *67*, 477–486.
Gilden, J.K., Peck, S., Chen, Y., and Krummel, M.F. (2012). The septin cytoskeleton facilitates membrane retraction during motility and blebbing. J Cell Biol *196*, 103–114.
Gisler, T., and Weitz, D. (1999). Scaling of the microrheology of semidilute F-actin solutions. Phys Rev Lett *82*, 1606–1609.
Gittes, F., Mickey, B., Nettleton, J., and Howard, J. (1993). Flexural rigidity of microtubules and actin filaments measured from thermal fluctuations in shape. J Cell Biol *120*, 923–934.
Glenney, J.R., Kaulfus, P., Matsudaira, P., and Weber, K. (1981). F-actin binding and bundling properties of fimbrin, a major cytoskeletal protein of microvillus core filaments. J Biol Chem *256*, 9283–9288.
Glotzer, M. (2005). The Molecular Requirements for Cytokinesis. Science *307*, 1735–1739.
Goehring, N.W., Trong, P.K., Bois, J.S., Chowdhury, D., Nicola, E.M., Hyman, A.A., and Grill, S.W. (2011). Polarization of PAR Proteins by Advective Triggering of a Pattern-Forming System. Science *334*, 1137–1141.
Goldmann, W.H., and Isenberg, G. (1993). Analysis of filamin and α-actinin binding to actin by the stopped flow method. FEBS Lett *336*, 408–410.
Goodson, H.V., Kang, S.J., and Endow, S.A. (1994). Molecular phylogeny of the kinesin family of microtubule motor proteins. J Cell Sci *107*, 1875–1884.
Goswami, D., Gowrishankar, K., Bilgrami, S., Ghosh, S., Raghupathy, R., Chadda, R., Vishwakarma, R., Rao, M., and Mayor, S. (2008). Nanoclusters of GPI-anchored proteins are formed by cortical actin-driven activity. Cell *135*, 1085–1097.
Gowrishankar, K., Ghosh, S., Saha, S., C, R., Mayor, S., and Rao, M. (2012). Active remodeling of cortical actin regulates spatiotemporal organization of cell surface molecules. Cell *149*, 1353–1367.
Graf, H., and Löwen, H. (1999). Phase diagram of tobacco mosaic virus solutions. Phys Rev E *59*, 1932–1942.
Green, N.M. (1990). Avidin and streptavidin. Method Enzymol *184*, 51–67.
Grelet, E., and Fraden, S. (2003). What Is the Origin of Chirality in the Cholesteric

Phase of Virus Suspensions? Phys Rev Lett *90*, 198302.
Griffith, A.A. (1921). The Phenomena of Rupture and Flow in Solids. Phil Trans R Soc Lond A *221*, 163–198.
Gruenbaum, Y., Wilson, K.L., Harel, A., Goldberg, M., and Cohen, M. (2000). Review: Nuclear Lamins—Structural Proteins with Fundamental Functions. J Struct Biol *129*, 313–323.
Guertin, D.A., Trautmann, S., and McCollum, D. (2002). Cytokinesis in eukaryotes. Microbiol Mol Biol Rev *66*, 155–178.
Guillot, C., and Lecuit, T. (2013). Adhesion Disengagement Uncouples Intrinsic and Extrinsic Forces to Drive Cytokinesis in Epithelial Tissues. J Mol Biol *24*, 227–241.
Gunning, B.E.S., and Steer, M.W. (1996). Plant Cell Biology (Jones & Bartlett Learning).
Gunning, P.W., Schevzov, G., Kee, A.J., and Hardeman, E.C. (2005). Tropomyosin isoforms: divining rods for actin cytoskeleton function. Trends Cell Biol *15*, 333–341.
Guo, B. (2006). Mechanics of actomyosin bonds in different nucleotide states are tuned to muscle contraction. Proc Natl Acad Sci USA *103*, 9844–9849.
Hagan, I.M. (1998). The fission yeast microtubule cytoskeleton. J Cell Sci *111*, 1603–1612.
Hagerman, P.J. (1988). Flexibility of DNA. Annu Rev Biophys Biophys Chem *17*, 265–286.
Hall, A. (2012). Rho family GTPases. Biochem Soc T *40*, 1378–1382.
Hall, P.A., and Russell, S.H. (2004). The pathobiology of the septin gene family. *204*, 489–505.
Halley, J.D., and Winkler, D.A. (2008). Critical-like self-organization and natural selection: Two facets of a single evolutionary process? BioSystems *92*, 148–158.
Harris, A., Wild, P., and Stopak, D. (1980). Silicone rubber substrata: a new wrinkle in the study of cell locomotion. Science *208*, 177–179.
Hartwell, L.H. (1971). Genetic control of the cell division cycle in yeast. IV. Genes controlling bud emergence and cytokinesis. Exp Cell Res *69*, 265–276.
Haviv, L., Gillo, D., Backouche, F., and Bernheim-Groswasser, A. (2008). A Cytoskeletal Demolition Worker: Myosin II Acts as an Actin Depolymerization Agent. J Mol Biol *375*, 325–330.
Helfand, B.T., Chang, L., and Goldman, R.D. (2003). The dynamic and motile properties of intermediate filaments. Annu Rev Cell Dev Biol *19*, 445–467.
Helfer, E., Panine, P., Carlier, M.-F., and Davidson, P. (2005). The Interplay between Viscoelastic and Thermodynamic Properties Determines the Birefringence of F-Actin Gels. Biophys J *89*, 543–553.
Herrmann, H., Bär, H., Kreplak, L., Strelkov, S.V., and Aebi, U. (2007). Intermediate filaments: from cell architecture to nanomechanics. Nat Rev Mol Cell Bio *8*, 562–573.
Hess, S., and Köhler, W. (1980). Formeln zur Tensor-Rechnung (Erlangen: Palm & Enke).
Heussinger, C. (2012). Stress relaxation through crosslink unbinding in cytoskeletal networks. New J Phys *14*, 095029.

Hill, T.L. (1981). Microfilament or microtubule assembly or disassembly against a force. Proc Natl Acad Sci USA *78*, 5613–5617.
Hinner, B., Tempel, M., Sackmann, E., Kroy, K., and Frey, E. (1998). Entanglement, elasticity, and viscous relaxation of actin solutions. Phys Rev Lett *81*, 2614–2617.
Hirokawa, N. (1998). Kinesin and Dynein Superfamily Proteins and the Mechanism of Organelle Transport. Science *279*, 519–526.
Hirst, L.S., Parker, E.R., Abu-Samah, Z., Li, Y., Pynn, R., MacDonald, N.C., and Safinya, C.R. (2005). Microchannel Systems in Titanium and Silicon for Structural and Mechanical Studies of Aligned Protein Self-Assemblies. Langmuir *21*, 3910–3914.
Holy, T.E., Dogterom, M., Yurke, B., and Leibler, S. (1997). Assembly and positioning of microtubule asters in microfabricated chambers. Proc Natl Acad Sci USA *94*, 6228–6231.
Holyst, R., and Poniewierski, A. (1987). Wetting on a spherical surface. Phys Rev B *36*, 5628–5630.
Hosek, M., and Tang, J.X. (2004). Polymer-induced bundling of F actin and the depletion force. Phys Rev E *69*, 051907.
Howard, J. (2001). Mechanics of Motor Proteins & the Cytoskeleton (Sinauer Associates).
Howard, J., Grill, S.W., and Bois, J.S. (2011). Turing's next steps: the mechanochemical basis of morphogenesis. Nat Rev Mol Cell Bio *12*, 392–398.
Howard, J. (1997). Molecular motors: structural adaptations to cellular functions. Nature *389*, 561–567.
Huber, F., Strehle, D., and Käs, J. (2012). Counterion-induced formation of regular actin bundle networks. Soft Matter *8*, 931.
Humphrey, D., Duggan, C., Saha, D., Smith, D., and Käs, J. (2002). Active fluidization of polymer networks through molecular motors. Nature *416*, 413–416.
Hussey, P.J., Ketelaar, T., and Deeks, M.J. (2013). Control of the actin cytoskeleton in plant cell growth. Annu Rev Plant Biol *57*, 109–125.
Huxley, A.F., and Niedergerke, R. (1954). Structural Changes in Muscle During Contraction: Interference Microscopy of Living Muscle Fibres. Nature *173*, 971–973.
Huxley, H., and Hanson, J. (1954). Changes in the Cross-Striations of Muscle during Contraction and Stretch and their Structural Interpretation. Nature *173*, 973–976.
Inoué, S., and Salmon, E.D. (1995). Force Generation by Microtubule Assembly/Disassembly in Mitosis and Related Movements. Mol Biol Cell *6*, 1619.
Isambert, H., and Maggs, A.C. (1996). Dynamics and Rheology of Actin Solutions. Macromolecules *29*, 1036–1040.
Isambert, H., Venier, P., Maggs, A.C., Fattoum, A., Kassab, R., Pantaloni, D., and Carlier, M.F. (1995). Flexibility of actin filaments derived from thermal fluctuations. Effect of bound nucleotide, phalloidin, and muscle regulatory proteins. J Biol Chem *270*, 11437–11444.
Ishijima, A., Kojima, H., Funatsu, T., Tokunaga, M., Higuchi, H., Tanaka, H., and Yanagida, T. (1998). Simultaneous Observation of Individual ATPase and Mechanical Events by a Single Myosin Molecule during Interaction with Actin.

Cell *92*, 161–171.
Ishikawa, R., Sakamoto, T., Ando, T., Higashi-Fujime, S., and Kohama, K. (2003). Polarized actin bundles formed by human fascin-1: their sliding and disassembly on myosin II and myosin V in vitro. J Neurochem *87*, 676–685.
Islam, M.F., Alsayed, A.M., Dogic, Z., Zhang, J., Lubensky, T.C., and Yodh, A.G. (2004). Nematic nanotube gels. Phys Rev Lett *92*, 088303.
Jammalamadaka, S.R., and Sengupta, A. (2001). Topics in Circular Statistics (World Scientific Publishing Company).
Janmey, P., Peetermans, J., Zaner, K., Stossel, T., and Tanaka, T. (1986). Structure and mobility of actin filaments as measured by quasielastic light scattering, viscometry, and electron microscopy. J Biol Chem *261*, 8357.
Jansen, S., Collins, A., Yang, C., Rebowski, G., Svitkina, T., and Dominguez, R. (2011). Mechanism of actin filament bundling by fascin. J Biol Chem *286*, 30087–30096.
Janson, L.W., Kolega, J., and Taylor, D.L. (1991). Modulation of contraction by gelation/solation in a reconstituted motile model. J Cell Biol *114*, 1005–1015.
Joglekar, A.P., Bloom, K.S., and Salmon, E.D. (2010). Mechanisms of force generation by end-on kinetochore-microtubule attachments. Curr Opin Cell Biol *22*, 57–67.
Joo, E., Surka, M.C., and Trimble, W.S. (2007). Mammalian SEPT2 is required for scaffolding nonmuscle myosin II and its kinases. Dev Cell *13*, 677–690.
Jülicher, F., Kruse, K., Prost, J., and Joanny, J.-F. (2007). Active behavior of the cytoskeleton. Phys Rep *449*, 3–28.
Kaminer, B., and Bell, A.L. (1966). Myosin filamentogenesis: Effects of pH and ionic concentration. J Mol Biol *20*, 391–401.
Kapur, J., Sahoo, P., and Wong, A. (1985). A new method for gray-level picture thresholding using the entropy of the histogram. Comput Vis Graph Image Process *29*, 273–285.
Kasza, K.E., Rowat, A.C., Liu, J., Angelini, T.E., Brangwynne, C.P., Koenderink, G.H., and Weitz, D.A. (2007). The cell as a material. Curr Opin Cell Biol *19*, 101–107.
Katsura, I., and Noda, H. (1973). Further Studies on the Formation of Reconstituted Myosin Filaments. J Biochem *73*, 245–256.
Kaur, H., Kumar, S., Singh, K., and Bharadwaj, L.M. (2011). Divalent cation induced actin ring formation. J Mol Biol *48*, 793–797.
Käs, J., Strey, H., Tang, J.X., Finger, D., Ezzell, R., Sackmann, E., and Janmey, P.A. (1996). F-actin, a model polymer for semiflexible chains in dilute, semidilute, and liquid crystalline solutions. Biophys J *70*, 609–625.
Kee, Y.-S., Ren, Y., Dorfman, D., Iijima, M., Firtel, R., Iglesias, P.A., and Robinson, D.N. (2012). A mechanosensory system governs myosin II accumulation in dividing cells. Mol Biol Cell *23*, 1510–1523.
Khokhlov, A.R., and Semenov, A.N. (1982). Liquid-crystalline ordering in the solution of partially flexible macromolecules. Physica A 112, 605–614.
Kiemes, M., Benetatos, P., and Zippelius, A. (2011). Orientational order and glassy states in networks of semiflexible polymers. Phys Rev E *83*, 021905.
Kinoshita, M., and Noda, M. (2001). Roles of septins in the mammalian cytokinesis machinery. *Cell Struct Func* 26, 667–670.

Kinoshita, M., Field, C.M., Coughlin, M.L., Straight, A.F., and Mitchison, T.J. (2002). Self- and actin-templated assembly of mammalian septins. Dev Cell *6*, 791–802.
Klein, M., Shi, W., Ramagopal, U., Tseng, Y., Wirtz, D., Kovar, D., Staiger, C., and Almo, S. (2004). Structure of the actin crosslinking core of fimbrin. Structure *12*, 999–1013.
Koenderink, G.H., Dogic, Z., Nakamura, F., Bendix, P.M., MacKintosh, F.C., Hartwig, J.H., Stossel, T.P., and Weitz, D.A. (2009). An active biopolymer network controlled by molecular motors. Proc Natl Acad Sci USA *106*, 15192–15197.
Koestler, S.A., Rottner, K., Lai, F., Block, J., Vinzenz, M., and Small, J.V. (2009). F- and G-actin concentrations in lamellipodia of moving cells. PLOS One 4, e4810.
Kolega, J. (1998). Cytoplasmic dynamics of myosin IIA and IIB: spatial "sorting" of isoforms in locomoting cells. J Cell Sci *111*, 2085–2095.
Korenbaum, E. (2002). Calponin homology domains at a glance. J Cell Sci *115*, 3543–3545.
Koretz, J.F. (1979). Effects of C-protein on synthetic myosin filament structure. Biophys J *27*, 433–446.
Korn, E.D., and Hammer, J.A., III (1988). Myosins of Nonmuscle Cells. Annu Rev Biophys Biophys Chem *17*, 23–45.
Kovács, M., Wang, F., Hu, A., Zhang, Y., and Sellers, J.R. (2003). Functional Divergence of Human Cytoplasmic Myosin II: Kinetic characterization of the non-muscle IIA isoform. J Biol Chem *278*, 38132–38140.
Köhler, S., and Bausch, A.R. (2012). Contraction mechanisms in composite active actin networks. PLOS One 7, e39869.
Köhler, S., Schaller, V., and Bausch, A.R. (2011a). Structure formation in active networks. Nat Mater *10*, 462–468.
Köhler, S., Schaller, V., and Bausch, A.R. (2011b). Collective Dynamics of Active Cytoskeletal Networks. PLOS One 6, e23798.
Köster, S., Steinhauser, D., and Pfohl, T. (2005). Brownian motion of actin filaments in confining microchannels. J Phys Condens Matter *17*, S4091–S4104.
Kratky, O., and Porod, G. (2010). Röntgenuntersuchung gelöster Fadenmoleküle. Recl Trav Chim Pays-Bas *68*, 1106–1122.
Kron, S.J., and Spudich, J.A. (1986). Fluorescent actin filaments move on myosin fixed to a glass surface. Proc Natl Acad Sci USA *83*, 6272–6276.
Kroy, K., and Frey, E. (1996). Force-Extension Relation and Plateau Modulus for Wormlike Chains. Phys Rev Lett *77*, 306–309.
La Cruz, De, E.M., Wells, A.L., Rosenfeld, S.S., Ostap, E.M., and Sweeney, H.L. (1999). The kinetic mechanism of myosin V. Proc Natl Acad Sci USA *96*, 13726–13731.
Laan, L., Pavin, N., Husson, J., Romet-Lemonne, G., van Duijn, M., López, M.P., Vale, R.D., Jülicher, F., Reck-Peterson, S.L., and Dogterom, M. (2012). Cortical Dynein Controls Microtubule Dynamics to Generate Pulling Forces that Position Microtubule Asters. Cell *148*, 502–514.
Lacroix, B., and Maddox, A.S. (2011). Cytokinesis, ploidy and aneuploidy. J Pathol *226*, 338–351.
Landau, L.D., Lifshitz, E.M., Kosevich, A.M., Pitaevskiĭ, L.P. (1986). Theory of Elasticity

(Butterworth-Heinemann).
Lapointe, J., and Marvin, D.A. (1973). Filamentous Bacterial Viruses VIII. Liquid Crystals of fd. Liq Cryst *19*, 269–278.
Lau, A.W.C., Prasad, A., and Dogic, Z. (2009). Condensation of isolated semi-flexible filaments driven by depletion interactions. Europhys Lett *87*, 48006.
Le Goff, L., Hallatschek, O., Frey, E., and Amblard, F. (2002a). Tracer Studies on F-Actin Fluctuations. Phys Rev Lett 89, 258101.
Le Goff, L., Amblard, F., and Furst, E.M. (2002b). Motor-driven dynamics in actin-myosin networks. Phys Rev Lett 88, 018101.
Leckband, D., and Israelachvili, J. (2001). Intermolecular forces in biology. Quart Rev Biophys *34*, 105.
Lecuit, T. (2004). Junctions and vesicular trafficking during Drosophila cellularization. J Cell Sci *117*, 3427–3433.
Lekkerkerker, H.N.W., and Tuinier, R. (2011). Colloids and the Depletion Interaction (Springer).
Lenz, M., Gardel, M.L., and Dinner, A.R. (2012). Requirements for contractility in disordered cytoskeletal bundles. New J Phys *14*, 033037.
Lenz, M., Thoresen, T., Gardel, M., and Dinner, A. (2012b). Contractile Units in Disordered Actomyosin Bundles Arise from F-Actin Buckling. Phys Rev Lett *108*, 238107.
Lettinga, M.P., Barry, E., and Dogic, Z. (2007). Self-diffusion of rod-like viruses in the nematic phase. Europhys Lett *71*, 692–698.
Levayer, R., and Lecuit, T. (2012). Biomechanical regulation of contractility: spatial control and dynamics. Trends Cell Biol *22*, 61–81.
Levin, M., Thorlin, T., Robinson, K.R., Nogi, T., and Mercola, M. (2002). Asymmetries in H+/K+-ATPase and Cell Membrane Potentials Comprise a Very Early Step in Left-Right Patterning. Cell *111*, 77–89.
Lénárt, P., Bacher, C.P., Daigle, N., Hand, A.R., Eils, R., Terasaki, M., and Ellenberg, J. (2005). A contractile nuclear actin network drives chromosome congression in oocytes. Nature *436*, 812–818.
Lieleg, O., and Bausch, A.R. (2007). Cross-linker unbinding and self-similarity in bundled cytoskeletal networks. Phys Rev Lett *99*, 158105.
Lieleg, O., Claessens, M., Heussinger, C., Frey, E., and Bausch, A. (2007). Mechanics of Bundled Semiflexible Polymer Networks. Phys Rev Lett 99, 088102.
Lieleg, O., Claessens, M.M.A.E., and Bausch, A.R. (2010). Structure and dynamics of cross-linked actin networks. Soft Matter *6*, 218–225.
Limozin, L., Bärmann, M., and Sackmann, E. (2003). On the organization of self-assembled actin networks in giant vesicles. Eur Phys J E *10*, 319–330.
Lin, G., Pister, K.S.J., and Roos, K.P. (2000). Surface micromachined polysilicon heart cell force transducer. J Microelectromech Sys *9*, 9–17.
Liverpool, T.B., Marchetti, M.C., Joanny, J.-F., and Prost, J. (2009). Mechanical response of active gels. Europhys Lett *85*, 18007.
Liverpool, T. (2003). Anomalous fluctuations of active polar filaments. Phys Rev E 67, 031909.

Lombillo, V.A., Stewart, R.J., and McIntosh, J.R. (1995). Minus-end-directed motion of kinesin-coated microspheres driven by microtubule depolymerization. Nature *373*, 161–164.
Lopez-Leon, T., Koning, V., Devaiah, K.B.S., Vitelli, V., Fernandez-Nieves, A., and A (2011). Frustrated nematic order in spherical geometries. Nat Phys *7*, 391–394.
Lopez-Leon, T., Bates, M.A., and Fernandez-Nieves, A. (2012). Defect coalescence in spherical nematic shells. Phys Rev E *86*, 030702.
Luck, D.J. (1984). Genetic and biochemical dissection of the eucaryotic flagellum. J Cell Biol *98*, 789–794.
Luo, T., Mohan, K., Srivastava, V., Ren, Y., Iglesias, P.A., and Robinson, D.N. (2012). Understanding the cooperative interaction between myosin II and actin cross-linkers mediated by actin filaments during mechanosensation. Biophys J *102*, 238–247.
Lye, C.M., and Sanson, B. (2011). Tension and Epithelial Morphogenesis in Drosophila Early Embryos. Curr Topic Dev Biol *95*, 145.
MacKintosh, F., Käs, J., and Janmey, P. (1995). Elasticity of semiflexible biopolymer networks. Phys Rev Lett *75*, 4425–4428.
Macosko, C.W. (1994). Rheology: principles, measurements, and applications (VCH).
Maier, W., and Saupe, A. (1958). Eine einfache molekulare Theorie des nematischen kristallinflüssigen Zustandes. Z Naturforsch A *13*, 564.
Majumdar, A., Newton, C., Robbins, J., and Zyskin, M. (2007). Topology and bistability in liquid crystal devices. Phys Rev E *75*, 051703.
Maly, I.V., and Borisy, G.G. (2001). Self-organization of a propulsive actin network as an evolutionary process. Proc Natl Acad Sci USA *98*, 11324–11329.
Mandato, C.A., and Bement, W.M. (2001). Contraction and polymerization cooperate to assemble and close actomyosin rings around Xenopus oocyte wounds. J Cell Biol *154*, 785–798.
Manor, U., and Kachar, B. (2008). Dynamic length regulation of sensory stereocilia. Seminars in Cell & Developmental Biology *19*, 502–510.
Marchetti, M.C., Joanny, J.-F., Ramaswamy, S., Liverpool, T.B., Prost, J., Rao, M., and Simha, R.A. (2012). Soft Active Matter. arXiv cond-mat.soft, 1207.2929.
Marenduzzo, D., Finan, K., and Cook, P.R. (2006). The depletion attraction: an underappreciated force driving cellular organization. J Cell Biol *175*, 681–686.
Margossian, S.S., and Lowey, S. (1982). Preparation of myosin and its subfragments from rabbit skeletal muscle. Method Enzymol *85 Pt B*, 55–71.
Martin, A.C., Kaschube, M., and Wieschaus, E.F. (2009). Pulsed contractions of an actin-myosin network drive apical constriction. Nature *457*, 495–499.
Martin, A.C., Gelbart, M., Fernandez-Gonzalez, R., Kaschube, M., Wieschaus, E.F., Martin, A.C., Gelbart, M., Fernandez-Gonzalez, R., Kaschube, M., and Wieschaus, E.F. (2010). Integration of contractile forces during tissue invagination. J Cell Biol *188*, 735–749.
Maruthamuthu, V., Sabass, B., Schwarz, U.S., and Gardel, M.L. (2011). Cell-ECM traction force modulates endogenous tension at cell–cell contacts. Proc Natl Acad Sci USA *108*, 4708–4713.

Maurer, S.P., Fourniol, F.J., Bohner, G., Moores, C.A., and Surrey, T. (2012). EBs Recognize a Nucleotide-Dependent Structural Cap at Growing Microtubule Ends. Cell *149*, 371–382.

May, R.C., and Machesky, L.M. (2001). Phagocytosis and the actin cytoskeleton. J Cell Sci *114*, 1061–1077.

Mayer, M., Depken, M., Bois, J.S., Jülicher, F., and Grill, S.W. (2010). Anisotropies in cortical tension reveal the physical basis of polarizing cortical flows. Nature *467*, 617–621.

McCord, R.P., Yukich, J.N., and Bernd, K.K. (2005). Analysis of force generation during flagellar assembly through optical trapping of free-swimming Chlamydomonas reinhardtii. Cell Motil Cytoskeleton *61*, 137–144.

McGrath, J.L., Eungdamrong, N.J., Fisher, C.I., Peng, F., Mahadevan, L., Mitchison, T.J., and Kuo, S.C. (2003). The Force-Velocity Relationship for the Actin-Based Motility of Listeria monocytogenes. Curr Biol *13*, 329–332.

McIntosh, J.R., Volkov, V., Ataullakhanov, F.I., and Grishchuk, E.L. (2010). Tubulin depolymerization may be an ancient biological motor. J Cell Sci *123*, 3425–3434.

McRae, S.R., Brown, C.L., and Bushell, G.R. (2005). Rapid purification of EGFP, EYFP, and ECFP with high yield and purity. Prot Expr Purif *41*, 121–127.

Medalia, O., Weber, I., Frangakis, A.S., Nicastro, D., Gerisch, G., and Baumeister, W. (2002). Macromolecular Architecture in Eukaryotic Cells Visualized by Cryoelectron Tomography. Science *298*, 1209–1213.

Mehta, A.D., Cheney, R.E., Rock, R.S., Rief, M., Spudich, J.A., and Mooseker, M.S. (1999). Myosin-V is a processive actin-based motor. Nature *400*, 590–593.

Mendes Pinto, I., Rubinstein, B., Kucharavy, A., Unruh, J.R., and Li, R. (2012). Actin Depolymerization Drives Actomyosin Ring Contraction during Budding Yeast Cytokinesis. Dev Cell *22*, 1247–1260.

Meyer, R.K., and Aebi, U. (1990). Bundling of actin filaments by alpha-actinin depends on its molecular length. J Cell Biol *110*, 2013–2024.

Meyers, M.A., and Chawla, K.K. (2009). Mechanical Behavior of Materials (Cambridge University Press).

Miao, L., Vanderlinde, O., Liu, J., Grant, R.P., Wouterse, A., Shimabukuro, K., Philipse, A., Stewart, M., and Roberts, T.M. (2008). The role of filament-packing dynamics in powering amoeboid cell motility. Proc Natl Acad Sci USA *105*, 5390–5395.

Mitchison, T.J. (1995). Evolution of a dynamic cytoskeleton. Philos Trans R Soc Lond B Biol Sci *349*, 299–304.

Mitra, S.K., and Kaiser, J.F. (1993). Handbook for Digital Signal Processing (John Wiley & Sons, Inc.).

Mizuno, D., Head, D.A., MacKintosh, F.C., and Schmidt, C.F. (2008). Active and passive microrheology in equilibrium and nonequilibrium systems. Macromolecules *41*, 7194–7202.

Mizuno, D., Tardin, C., Schmidt, C.F., and MacKintosh, F.C. (2007). Nonequilibrium mechanics of active cytoskeletal networks. Science *315*, 370–373.

Mogilner, A., and Oster, G. (1996). Cell motility driven by actin polymerization. Biophys J *71*, 3030–3045.

Mogilner, A., and Rubinstein, B. (2005). The physics of filopodial protrusion. Biophys J *89*, 782–795.
Mogilner, A., and Oster, G. (2003). Force generation by actin polymerization II: the elastic ratchet and tethered filaments. Biophys J *84*, 1591–1605.
Mora, T., and Bialek, W. (2011). Are biological systems poised at criticality? J Stat Phys *144*, 1–35.
Morozov, K.I., and Pismen, L.M. (2010). Motor-driven effective temperature and viscoelastic response of active matter. Phys Rev E *81*, 061922.
Mostowy, S., and Cossart, P. (2012). Septins: the fourth component of the cytoskeleton. Nat Rev Mol Cell Biol *13*, 183–194.
Mostowy, S., Janel, S., Forestier, C., Roduit, C., Kasas, S., Pizarro-Cerdá, J., Cossart, P., and Lafont, F. (2011). A role for septins in the interaction between the Listeria monocytogenes invasion protein InlB and the Met receptor. Biophys J *100*, 1949–1959.
Mostowy, S., Bonazzi, M., Hamon, M.A., Tham, T.N., Mallet, A., Lelek, M., Gouin, E., Demangel, C., Brosch, R., Zimmer, C., et al. (2010). Entrapment of Intracytosolic Bacteria by Septin Cage-like Structures. Cell Host & Microbe *8*, 433–444.
Mulder, P. (2012). Actin in Confined Spaces. Wageningen UR.
Mullins, R.D. (2010). Cytoskeletal mechanisms for breaking cellular symmetry. Cold Spring Harb Perspect Biol *2*, a003392.
Murrell, M.P., and Gardel, M.L. (2012). F-actin buckling coordinates contractility and severing in a biomimetic actomyosin cortex. Proc Natl Acad Sci USA *109*, 20820–20825.
Nédélec, F.J., Surrey, T., Maggs, A.C., and Leibler, S. (1997). Self-organization of microtubules and motors. Nature *389*, 305–308.
Nguyen, L.T., Yang, W., Wang, Q., and Hirst, L.S. (2009). Molecular dynamics simulation of F-actin reveals the role of cross-linkers in semi-flexible filament assembly. Soft Matter *5*, 2033–2036.
Nicastro, D., Schwartz, C., Pierson, J., Gaudette, R., Porter, M.E., and McIntosh, J.R. (2006). The Molecular Architecture of Axonemes Revealed by Cryoelectron Tomography. Science *313*, 944–948.
Nijenhuis, N., Mizuno, D., Spaan, J.A.E., and Schmidt, C.F. (2009). Viscoelastic response of a model endothelial glycocalyx. Phys Biol *6*, 025014.
Nishihama, R., Onishi, M., and Pringle, J.R. (2011). New insights into the phylogenetic distribution and evolutionary origins of the septins. Biol. Chem. *392*, 681–687.
Nonaka, S., Shiratori, H., Saijoh, Y., and Hamada, H. (2002). Determination of left-right patterning of the mouse embryo by artificial nodal flow. Nature *418*, 96–99.
Norstrom, M.F., Smithback, P.A., and Rock, R.S. (2010). Unconventional processive mechanics of non-muscle myosin IIB. J Biol Chem *285*, 26326–26334.
Oda, T., Makino, K., Yamashita, I., Namba, K., and Maéda, Y. (1998). Effect of the length and effective diameter of F-actin on the filament orientation in liquid crystalline sols measured by x-ray fiber diffraction. Biophys J *75*, 2672–2681.
Odijk, T. (1986). Theory of lyotropic polymer liquid crystals. Macromolecules *19*, 2313–2329.

Odijk, T. (1995). Stiff Chains and Filaments under Tension. Macromolecules *28*, 7016–7018.
Odijk, T., and Lekkerkerker, H.N.W. (1985). Theory of the isotropic-liquid crystal phase separation for a solution of bidisperse rodlike macromolecules. J. Phys. Chem. *89*, 2090–2096.
Oegema, K., Savoian, M.S., Mitchison, T.J., and Field, C.M. (2000). Functional analysis of a human homologue of the Drosophila actin binding protein anillin suggests a role in cytokinesis. J Cell Biol *150*, 539–552.
Oliver, T., Jacobson, K., and Dembo, M. (1995). Traction forces in locomoting cells. Cell Motil Cytoskeleton *31*, 225–240.
Omary, M.B., Ku, N.-O., Strnad, P., and Hanada, S. (2009). Toward unraveling the complexity of simple epithelial keratins in human disease. J Clin Invest *119*, 1794–1805.
Ono, S., Yamakita, Y., Yamashiro, S., Matsudaira, P.T., Gnarra, J.R., Obinata, T., and Matsumura, F. (1997). Identification of an Actin Binding Region and a Protein Kinase C Phosphorylation Site on Human Fascin. J Biol Chem *272*, 2527–2533.
Onsager, L. (1945). Theories and Problems of Liquid Diffusion. Ann NY Acad Sci *46*, 241–265.
Onsager, L. (1949). The effects of shape on the interaction of colloidal particles. Ann NY Acad Sci *51*, 627–659.
Otsu, N. (1975). A threshold selection method from gray-level histograms. IEEE Trans Syst Man Cybern Syst *9*, 62–66.
Ott, A., Magnasco, M., Simon, A., and Libchaber, A. (1993). Measurement of the persistence length of polymerized actin using fluorescence microscopy. Phys Rev E *48*, R1642–R1645.
Paluch, E., and Heisenberg, C.-P. (2009). Biology and Physics of Cell Shape Changes in Development. Curr Biol *19*, R790–R799.
Pan, F., Malmberg, R.L., and Momany, M. (2007). Analysis of septins across kingdoms reveals orthology and new motifs. BMC Evol Biol *7*, 103.
Pardee, J.D., and Spudich, J.A. (1982). Purification of muscle actin. Method Enzymol *85 Pt B*, 164–181.
Paredez, A.R., Assaf, Z.J., Sept, D., Timofejeva, L., Dawson, S.C., Wang, C.-J.R., and Cande, W.Z. (2011). An actin cytoskeleton with evolutionarily conserved functions in the absence of canonical actin-binding proteins. Proc Natl Acad Sci USA *108*, 6151–6156.
Peter, R., Schaller, V., Ziebert, F., and Zimmermann, W. (2008). Pattern formation in active cytoskeletal networks. New J Phys *10*, 035002.
Pfaendtner, J., La Cruz, De, E.M., and Voth, G.A. (2010). Actin filament remodeling by actin depolymerization factor/cofilin. Proc Natl Acad Sci USA *107*, 7299–7304.
Pine, D.J. (2000). Light scattering and rheology of complex fluids driven far from equilibrium. In Soft and Fragile Matter, M.E. Cates, and M.R. Evans, eds. (Bristol: SUSSP Institute of Physics).
Pinset-Härström, I., and Truffy, J. (1979). Effect of adenosine triphosphate, inorganic phosphate and divalent cations on the size and structure of synthetic myosin

filaments. J Mol Biol *134*, 173–188.
Pollard, T.D. (1982). Structure and polymerization of Acanthamoeba myosin-II filaments. J Cell Biol *95*, 816–825.
Pollard, T.D., and Borisy, G.G. (2003). Cellular Motility Driven by Assembly and Disassembly of Actin Filaments. Cell *112*, 453–465.
Poniewierski, A., and Holyst, R. (1988). Nematic alignment at a solid substrate: The model of hard spherocylinders near a hard wall. Phys Rev A *38*, 3721–3727.
Portran, D., Gaillard, J., Vantard, M., and Théry, M. (2013). Quantification of MAP and molecular motor activities on geometrically controlled microtubule networks. Cytoskeleton *70*, 12–23.
Prinsen, P., and van der Schoot, P. (2004). Continuous director-field transformation of nematic tactoids. Eur Phys J E 13, 35–41.
Prockop, D.J., and Kivirikko, K.I. (1995). Collagens: molecular biology, diseases, and potentials for therapy. Annu Rev Biochem *64*, 403–434.
Puech, N., Grelet, E., Poulin, P., Blanc, C., and van der Schoot, P. (2010). Nematic droplets in aqueous dispersions of carbon nanotubes. Phys Rev E *82*, 020702.
Purdy, K., and Fraden, S. (2004). Isotropic-cholesteric phase transition of filamentous virus suspensions as a function of rod length and charge. Phys Rev E *70*, 061703.
Purdy, K., Dogic, Z., Fraden, S., Rühm, A., Lurio, L., and Mochrie, S. (2003). Measuring the nematic order of suspensions of colloidal fd virus by x-ray diffraction and optical birefringence. Phys Rev E *67*, 031708.
Qiu, D., Cheng, S.-M., Wozniak, L., McSweeney, M., Perrone, E., and Levin, M. (2005). Localization and loss-of-function implicates ciliary proteins in early, cytoplasmic roles in left-right asymmetry. Dev Dyn *234*, 176–189.
Quint, D.A., and Schwarz, J.M. (2011). Optimal orientation in branched cytoskeletal networks. J Math Biol *63*, 735–755.
Rafelski, S.M., and Theriot, J.A. (2004). Crawling toward a unified model of cell mobility: spatial and temporal regulation of actin dynamics. Annu Rev Biochem *73*, 209–239.
Rauzi, M., and Lenne, P.-F. (2011). Cortical forces in cell shape changes and tissue morphogenesis. Curr Topic Dev Biol *95*, 93–144.
Rauzi, M., Verant, P., Lecuit, T., and Lenne, P.-F. (2008). Nature and anisotropy of cortical forces orienting Drosophila tissue morphogenesis. Nat Cell Biol *10*, 1401–1410.
Rayment, I., Holden, H., Whittaker, M., Yohn, C., Lorenz, M., Holmes, K., and Milligan, R. (1993). Structure of the actin-myosin complex and its implications for muscle contraction. Science *261*, 58–65.
Reisler, E., Smith, C., and Seegan, G. (1980). Myosin minifilaments. J Mol Biol *143*, 129–145.
Ren, Y., Effler, J.C., Norstrom, M., Luo, T., Firtel, R.A., Iglesias, P.A., Rock, R.S., and Robinson, D.N. (2009). Mechanosensing through cooperative interactions between myosin II and the actin crosslinker cortexillin I. Curr Biol *19*, 1421–1428.
Reymann, A.C., Boujemaa-Paterski, R., Martiel, J.L., Guerin, C., Cao, W., Chin, H.F., De La Cruz, E.M., Thery, M., and Blanchoin, L. (2012). Actin Network Architecture

Can Determine Myosin Motor Activity. Science *336*, 1310–1314.
Reymann, A.-C., Martiel, J.-L., Cambier, T., Blanchoin, L., Boujemaa-Paterski, R., and Théry, M. (2010). Nucleation geometry governs ordered actin networks structures. Nat Mater *9*, 827–832.
Rezakhaniha, R., Agianniotis, A., Schrauwen, J.T.C., Griffa, A., Sage, D., Bouten, C.V.C., van de Vosse, F.N., Unser, M., and Stergiopulos, N. (2012). Experimental investigation of collagen waviness and orientation in the arterial adventitia using confocal laser scanning microscopy. Biomech Model Mechanobiol *11*, 461–473.
Riseman, J., and Kirkwood, J.G. (1950). The Intrinsic Viscosity, Translational and Rotatory Diffusion Constants of Rod-Like Macromolecules in Solution. J Chem Phys *18*, 512.
Roberts, T.M., and Stewart, M. (2000). Acting like actin. The dynamics of the nematode major sperm protein (msp) cytoskeleton indicate a push-pull mechanism for amoeboid cell motility. J Cell Biol *149*, 7–12.
Roure, du, O., Saez, A., Buguin, A., Austin, R.H., Chavrier, P., Siberzan, P., and Ladoux, B. (2005). Force mapping in epithelial cell migration. Proc Natl Acad Sci USA *102*, 2390–2395.
Rubinstein, M., and Colby, R.H. (2003). Polymer Physics (OUP Oxford).
Salbreux, G., Charras, G., and Paluch, E. (2012). Actin cortex mechanics and cellular morphogenesis. Trends Cell Biol *22*, 536–545.
Sanchez, T., Kulic, I.M., and Dogic, Z. (2010). Circularization, Photomechanical Switching, and a Supercoiling Transition of Actin Filaments. Phys Rev Lett *104*, 098103.
Sanchez, T., Chen, D.T.N., DeCamp, S.J., Heymann, M., and Dogic, Z. (2012). Spontaneous motion in hierarchically assembled active matter. Nature *491*, 431–434.
Schaller, V., Weber, C.A., Hammerich, B., Frey, E., and Bausch, A.R. (2011). Frozen steady states in active systems. Proc Natl Acad Sci USA *108*, 19183–19188.
Schaus, T.E., Taylor, E.W., and Borisy, G.G. (2007). Self-organization of actin filament orientation in the dendritic-nucleation/array-treadmilling model. Proc Natl Acad Sci USA *104*, 7086–7091.
Schliwa, M., and Woehlke, G. (2003). Molecular motors. Nature *422*, 759–765.
Schnurr, B., Gittes, F., MacKintosh, F.C., and Schmidt, C.F. (1997). Determining microscopic viscoelasticity in flexible and semiflexible polymer networks from thermal fluctuations. Macromolecules 30, 7781–7792.
Schmidt, C.F., Baermann, M., Isenberg, G., and Sackmann, E. (1989). Chain dynamics, mesh size, and diffusive transport in networks of polymerized actin: a quasielastic light scattering and microfluorescence study. Macromolecules *22*, 3638–3649.
Schmoller, K.M., Lieleg, O., and Bausch, A.R. (2009). Structural and Viscoelastic Properties of Actin/Filamin Networks: Cross-Linked versus Bundled Networks. Biophys J *97*, 83–89.
Schmoller, K., Lieleg, O., and Bausch, A. (2008). Internal stress in kinetically trapped actin bundle networks. Soft Matter *4*, 2365–2367.
Schuyler, S.C., and Pellman, D. (2001). Microtubule "plus-end-tracking proteins": The

end is just the beginning. Cell *105*, 421–424.
Schwarz, U., and Safran, S. (2002). Elastic Interactions of Cells. Phys Rev Lett *88*, 048102.
Schwarz, U.S., and Gardel, M.L. (2012). United we stand - integrating the actin cytoskeleton and cell-matrix adhesions in cellular mechanotransduction. J Cell Sci *125*, 3051–3060.
Schwarz-Linek, J., Valeriani, C., Cacciuto, A., Cates, M.E., Marenduzzo, D., Morozov, A.N., and Poon, W.C.K. (2012). Phase separation and rotor self-assembly in active particle suspensions. Proc Natl Acad Sci USA *109*, 4052–4057.
Sedzinski, J., Biro, M., Oswald, A., Tinevez, J.-Y., Salbreux, G., and Paluch, E. (2011). Polar actomyosin contractility destabilizes the position of the cytokinetic furrow. Nature *476*, 462–466.
Seetapun, D., Castle, B.T., McIntyre, A.J., Tran, P.T., and Odde, D.J. (2012). Estimating the Microtubule GTP Cap Size In Vivo. Curr Biol *22*, 1681–1687.
Sellin, M.E., Sandblad, L., Stenmark, S., and Gullberg, M. (2011). Deciphering the rules governing assembly order of mammalian septin complexes. Mol Biol Cell *22*, 3152–3164.
Sheinman, M., Broedersz, C.P., and MacKintosh, F.C. (2012a). Nonlinear effective-medium theory of disordered spring networks. Phys Rev E *85*, 021801.
Sheinman, M., Broedersz, C., and MacKintosh, F. (2012b). Actively Stressed Marginal Networks. Phys Rev Lett *109*, 238101.
Sheterline, P., and Sparrow, J.C. (1994). Actin. Protein Profile *1*, 1–121.
Shibazaki, Y., Shimizu, M., and Kuroda, R. (2004). Body handedness is directed by genetically determined cytoskeletal dynamics in the early embryo. Curr Biol *14*, 1462–1467.
Shih, Y.-L., and Rothfield, L. (2006). The bacterial cytoskeleton. Microbiology and Molecular Biology Reviews *70*, 729–754.
Shin, H., Drew, K.R.P., Bartles, J.R., Wong, G.C.L., and Grason, G.M. (2009). Cooperativity and Frustration in Protein-Mediated Parallel Actin Bundles. Phys Rev Lett *103*, 238102.
Shin, J.H., Mahadevan, L., Waller, G.S., Langsetmo, K., and Matsudaira, P. (2003). Stored elastic energy powers the 60-microm extension of the Limulus polyphemus sperm actin bundle. J Cell Biol *162*, 1183–1188.
Shin, J.H., Tam, B.K., Brau, R.R., Lang, M.J., Mahadevan, L., and Matsudaira, P. (2007). Force of an actin spring. Biophys J *92*, 3729–3733.
Silverman-Gavrila, R., Hales, K.G., and Wilde, A. (2008). Anillin-mediated targeting of Peanut to pseudocleavage furrows is regulated by the GTPase Ran. Mol Biol Cell *19*, 3735–3744.
Singh, S., and Dunmur, D.A. (2002). Liquid Crystals: Fundamentals (World Scientific).
Sirajuddin, M., Farkasovsky, M., Hauer, F., Kühlmann, D., Macara, I.G., Weyand, M., Stark, H., and Wittinghofer, A. (2007). Structural insight into filament formation by mammalian septins. Nature *449*, 311–315.
Skau, C.T., Courson, D.S., Bestul, A.J., Winkelman, J.D., Rock, R.S., Sirotkin, V., and Kovar, D.R. (2011). Actin Filament Bundling by Fimbrin Is Important for

Endocytosis, Cytokinesis, and Polarization in Fission Yeast. J Biol Chem *286*, 26964–26977.
Sluckin, T.J., Dunmur, D.A., and Stegemeyer, H. (2003). Crystals That Flow — classic papers from the history of liquid crystals (London: Taylor & Francis).
Small, J.V., Herzog, M., and Anderson, K. (1995). Actin filament organization in the fish keratocyte lamellipodium. J Cell Biol *129*, 1275–1286.
Smith, D., Ziebert, F., Humphrey, D., Duggan, C., Steinbeck, M., Zimmermann, W., and Käs, J. (2007). Molecular motor-induced instabilities and cross linkers determine biopolymer organization. Biophys J *93*, 4445–4452.
Smith, M.B., Li, H., Shen, T., Huang, X., Yusuf, E., and Vavylonis, D. (2010). Segmentation and tracking of cytoskeletal filaments using open active contours. Cytoskeleton *67*, 693–705.
Soares e Silva, M. (2011). Structure and dynamics of active actin myosin networks : an in vitro perspective. VU University Amsterdam.
Soares e Silva, M., Alvarado, J., Nguyen, J., Georgoulia, N., Mulder, B.M., and Koenderink, G.H. (2011a). Self-organized patterns of actin filaments in cell-sized confinement. Soft Matter *7*, 10631.
Soares e Silva, M., Depken, M., Stuhrmann, B., Korsten, M., Mackintosh, F.C., and Koenderink, G.H. (2011b). Active multistage coarsening of actin networks driven by myosin motors. Proc Natl Acad Sci USA *108*, 9408–9413.
Somerville, C. (2006). Cellulose synthesis in higher plants. Annu Rev Cell Dev Biol *22*, 53–78.
Song, S., Landsbury, A., Dahm, R., Liu, Y., Zhang, Q., and Quinlan, R.A. (2009). Functions of the intermediate filament cytoskeleton in the eye lens. J Clin Invest *119*, 1837–1848.
Sonnemann, K.J., and Bement, W.M. (2013). Wound Repair: Toward Understanding and Integration of Single-Cell and Multicellular Wound Responses. In Annu Rev Cell Dev Biol, (Annual Reviews), pp. 237–263.
Speir, J.A., and Johnson, J.E. (2012). Nucleic acid packaging in viruses. Curr Opin Struc Biol *22*, 65–71.
Spéder, P., Ádám, G., and Noselli, S. (2006). Type ID unconventional myosin controls left-right asymmetry in Drosophila. Nature *440*, 803–807.
Spéder, P., Petzoldt, A., Suzanne, M., and Noselli, S. (2007). Strategies to establish left/right asymmetry in vertebrates and invertebrates. Curr Opin Gen Dev *17*, 351–358.
Spiegel, M.R. (1968). Vector Analysis (New York: McGraw-Hill).
Stachowiak, M.R., McCall, P.M., Thoresen, T., Balcioglu, H.E., Kasiewicz, L., Gardel, M.L., and O'Shaughnessy, B. (2012). Self-Organization of Myosin II in Reconstituted Actomyosin Bundles. Biophys J *103*, 1265–1274.
Starr, D., and Han, M. (2003). ANChors away: an actin based mechanism of nuclear positioning. J Cell Sci *116*, 211–216.
Stauffer, D., and Aharony, A. (1994). Introduction To Percolation Theory (Abingdon, UK: Taylor & Francis).
Storm, C., Pastore, J.J., MacKintosh, F.C., Lubensky, T.C., and Janmey, P.A. (2005). Nonlinear elasticity in biological gels. Nature *435*, 191–194.

Stossel, T.P., Condeelis, J., Cooley, L., Hartwig, J.H., Noegel, A., Schleicher, M., and Shapiro, S.S. (2001). Filamins as integrators of cell mechanics and signalling. Nat Rev Mol Cell Bio *2*, 138–145.

Stroobants, A., Lekkerkerker, H.N.W., and Odijk, T. (1986). Effect of electrostatic interaction on the liquid crystal phase transition in solutions of rodlike polyelectrolytes. Macromolecules *19*, 2232–2238.

Strzelecka, T.E., Davidson, M.W., and Rill, R.L. (1988). Multiple liquid crystal phases of DNA at high concentrations. Nature *331*, 457–460.

Stuhrmann, B., Soares e Silva, M., Depken, M., MacKintosh, F.C., and Koenderink, G.H. (2012). Nonequilibrium fluctuations of a remodeling in vitro cytoskeleton. Phys Rev E *86*, 020901(R).

Surka, M.C., Tsang, C.W., and Trimble, W.S. (2002). The mammalian septin MSF localizes with microtubules and is required for completion of cytokinesis. Mol Biol Cell *13*, 3532–3545.

Suzuki, A., Maeda, T., and Ito, T. (1991). Formation of liquid crystalline phase of actin filament solutions and its dependence on filament length as studied by optical birefringence. Biophys J *59*, 25–30.

Svitkina, T.M., Verkhovsky, A.B., McQuade, K.M., and Borisy, G.G. (1997). Analysis of the actin-myosin II system in fish epidermal keratocytes: mechanism of cell body translocation. J Cell Biol *139*, 397–415.

Svitkina, T.M., Bulanova, E.A., Chaga, O.Y., Vignjevic, D.M., Kojima, S.-I., Vasiliev, J.M., and Borisy, G.G. (2003). Mechanism of filopodia initiation by reorganization of a dendritic network. J Cell Biol *160*, 409–421.

Szeverenyi, I., Cassidy, A.J., Chung, C.W., Lee, B.T.K., Common, J.E.A., Ogg, S.C., Chen, H., Sim, S.Y., Goh, W.L.P., Ng, K.W., et al. (2008). The Human Intermediate Filament Database: comprehensive information on a gene family involved in many human diseases. Hum Mutat *29*, 351–360.

Takiguchi, K., Hayashi, H., Kurimoto, E., and Higashi-Fujime, S. (1990). In vitro motility of skeletal muscle myosin and its proteolytic fragments. J Biochem *107*, 671–679.

Takizawa, P.A., DeRisi, J.L., Wilhelm, J.E., and Vale, R.D. (2000). Plasma Membrane Compartmentalization in Yeast by Messenger RNA Transport and a Septin Diffusion Barrier. Science *290*, 341–344.

Tanaka, M., Rehfeldt, F., Schneider, M.F., Mathe, G., Albersdörfer, A., Neumaier, K.R., Purrucker, O., and Sackmann, E. (2005). Wetting and dewetting of extracellular matrix and glycocalix models. J Phys Condens Matter *17*, S649–S663.

Tanaka-Takiguchi, Y., Kinoshita, M., and Takiguchi, K. (2009). Septin-mediated uniform bracing of phospholipid membranes. Curr Biol *19*, 140–145.

Tang, J.X., Käs, J.A., Shah, J.V., and Janmey, P.A. (2001). Counterion-induced actin ring formation. Eur Biophys J *30*, 477–484.

Tang, J., and Fraden, S. (1995). Isotropic-cholesteric phase transition in colloidal suspensions of filamentous bacteriophage fd. Liq Cryst *19*, 459–467.

Tang, J., Wong, S., Tran, P., and Janmey, P. (1996). Counterion induced bundle formation of rodlike polyelectrolytes. Ber Bunsen Phys Chem *100*, 796–806.

Tarr, M., Trank, J.W., and Goertz, K.K. (1983). Effect of external force on relaxation kinetics in single frog atrial cardiac cells. Circ Res *52*, 161–169.
Tegenfeldt, J.O., Prinz, C., Cao, H., Chou, S., Reisner, W.W., Riehn, R., Wang, Y.M., Cox, E.C., Sturm, J.C., Silberzan, P., et al. (2004). The dynamics of genomic-length DNA molecules in 100-nm channels. Proc Natl Acad Sci USA *101*, 10979–10983.
Tempel, M., Isenberg, G., and Sackmann, E. (1996). Temperature-induced sol-gel transition and microgel formation in alpha -actinin cross-linked actin networks: A rheological study. Phys Rev E *54*, 1802–1810.
Theriot, J.A. (2000). The Polymerization Motor. Traffic *1*, 19–28.
Théry, M., Racine, V., Pépin, A., Piel, M., Chen, Y., Sibarita, J.-B., and Bornens, M. (2005). The extracellular matrix guides the orientation of the cell division axis. Nat Cell Biol *7*, 947–953.
Thomas, W.E., Vogel, V., and Sokurenko, E. (2008). Biophysics of catch bonds. Annu Rev Biophys *37*, 399–416.
Thompson, R.F., and Langford, G.M. (2002). Myosin superfamily evolutionary history. Anat Rec *268*, 276–289.
Thoresen, T., Lenz, M., and Gardel, M.L. (2011). Reconstitution of contractile actomyosin bundles. Biophys J *100*, 2698–2705.
Thoresen, T., Lenz, M., and Gardel, M.L. (2013). Thick Filament Length and Isoform Composition Determine Self-Organized Contractile Units in Actomyosin Bundles. Biophys J *104*, 655–665.
Tilney, L.G., and Portnoy, D.A. (1989). Actin filaments and the growth, movement, and spread of the intracellular bacterial parasite, Listeria monocytogenes. J Cell Biol *109*, 1597–1608.
Tilney, M.S., Tilney, L.G., Stephens, R.E., Merte, C., Drenckhahn, D., Cotanche, D.A., and Bretscher, A. (1989). Preliminary biochemical characterization of the stereocilia and cuticular plate of hair cells of the chick cochlea. J Cell Biol *109*, 1711–1723.
Tolić-Nørrelykke, I.M. (2008). Push-me-pull-you: how microtubules organize the cell interior. Eur Biophys J *37*, 1271–1278.
Tombolato, F., Ferrarini, A., and Grelet, E. (2006). Chiral Nematic Phase of Suspensions of Rodlike Viruses: Left-Handed Phase Helicity from a Right-Handed Molecular Helix. Phys Rev Lett *96*, 258302.
Tooley, A.J., Gilden, J., Jacobelli, J., Beemiller, P., Trimble, W.S., Kinoshita, M., and Krummel, M.F. (2009). Amoeboid T lymphocytes require the septin cytoskeleton for cortical integrity and persistent motility. Nat Cell Biol *11*, 17–26.
Torres-Sosa, C., Huang, S., and Aldana, M. (2012). Criticality Is an Emergent Property of Genetic Networks that Exhibit Evolvability. PLOS Comput Biol *8*, e1002669.
Tsai, F.C. (2013). PhD Thesis (to be published). VU University Amsterdam.
Tsakonas, C., Davidson, A.J., Brown, C.V., and Mottram, N.J. (2007). Multistable alignment states in nematic liquid crystal filled wells. Appl Phys Lett *90*, 111913
Tuma, M., and Gelfand, V.I. (1999). Molecular mechanisms of pigment transport in melanophores. Pigment Cell Res *12*, 283–294.
Uehara, R., Goshima, G., Mabuchi, I., Vale, R.D., Spudich, J.A., and Griffis, E.R. (2010).

Determinants of Myosin II Cortical Localization during Cytokinesis. Curr Biol *20*, 1080–1085.
Urban, E., Jacob, S., Nemethova, M., Resch, G.P., and Small, J.V. (2010). Electron tomography reveals unbranched networks of actin filaments in lamellipodia. Nat Cell Biol *12*, 429–435.
Vale, R.D. (2003). The Molecular Motor Toolbox for Intracellular Transport. Cell *112*, 467–480.
van der Schoot, P., and Odijk, T. (1992). Statistical theory and structure factor of a semidilute solution of rodlike macromolecules interacting by van der Waals forces. J Chem Phys *97*, 515.
van Hecke, M. (2009). Jamming of soft particles: geometry, mechanics, scaling and isostaticity. J Phys Condens Matter *22*, 033101.
van Mameren, J., Vermeulen, K.C., Gittes, F., and Schmidt, C.F. (2009). Leveraging single protein polymers to measure flexural rigidity. J Phys Chem B *113*, 3837–3844.
van Roij, R., Dijkstra, M., and Evans, R. (2000). Orientational wetting and capillary nematization of hard-rod fluids. Europhys Lett *49*, 350–356.
Vavylonis, D., Wu, J.Q., Hao, S., O'Shaughnessy, B., and Pollard, T.D. (2008). Assembly Mechanism of the Contractile Ring for Cytokinesis by Fission Yeast. Science *319*, 97–100.
Veatch, S.L., Cicuta, P., Sengupta, P., Honerkamp-Smith, A., Holowka, D., and Baird, B. (2008). Critical Fluctuations in Plasma Membrane Vesicles. ACS Chem Biol *3*, 287–293.
Vedula, S.R.K., Leong, M.C., Lai, T.L., Hersen, P., Kabla, A.J., Lim, C.T., and Ladoux, B. (2012). Emerging modes of collective cell migration induced by geometrical constraints. Proc Natl Acad Sci USA *109*, 12974–12979.
Verkhovsky, A.B. (1993). Non-sarcomeric mode of myosin II organization in the fibroblast lamellum. J Cell Biol *123*, 637–652.
Verkhovsky, A.B., Svitkina, T.M., and Borisy, G.G. (1995). Myosin II filament assemblies in the active lamella of fibroblasts: their morphogenesis and role in the formation of actin filament bundles. J Cell Biol *131*, 989–1002.
Verkhovsky, A.B., Chaga, O.Y., Schaub, S., Svitkina, T.M., Meister, J.-J., and Borisy, G.G. (2003). Orientational order of the lamellipodial actin network as demonstrated in living motile cells. Mol Biol Cell *14*, 4667–4675.
Versaevel, M., Grevesse, T., and Gabriele, S. (2012). Spatial coordination between cell and nuclear shape within micropatterned endothelial cells. Nat Commun *3*, 671.
Viamontes, J., and Tang, J. (2003). Continuous isotropic-nematic liquid crystalline transition of F-actin solutions. Phys Rev E *67*, 040701.
Viamontes, J., Narayanan, S., Sandy, A.R., and Tang, J.X. (2006a). Orientational order parameter of the nematic liquid crystalline phase of F-actin. Phys Rev E *73*, 061901.
Viamontes, J., Oakes, P.W., and Tang, J.X. (2006b). Isotropic to nematic liquid crystalline phase transition of F-actin varies from continuous to first order. Phys Rev Lett *97*, 118103.
Vicente-Manzanares, M., Zareno, J., Whitmore, L., Choi, C.K., and Horwitz, A.F.

(2007). Regulation of protrusion, adhesion dynamics, and polarity by myosins IIA and IIB in migrating cells. J Cell Biol *176*, 573–580.
Vicente-Manzanares, M., Ma, X., Adelstein, R.S., and Horwitz, A.R. (2009). Non-muscle myosin II takes centre stage in cell adhesion and migration. Nat Rev Mol Cell Biol *10*, 778–790.
Vignaud, T., Blanchoin, L., and Théry, M. (2012). Directed cytoskeleton self-organization. Trends Cell Biol *22*, 671–682.
Vignjevic, D., Yarar, D., Welch, M.D., Peloquin, J., Svitkina, T., and Borisy, G.G. (2003). Formation of filopodia-like bundles in vitro from a dendritic network. J Cell Biol *160*, 951–962.
Visscher, K., Schnitzer, M.J., and Block, S.M. (2000). Force production by single kinesin motors. Nat Cell Biol *2*, 718–723.
Vissers, T., van Blaaderen, A., and Imhof, A. (2011). Band Formation in Mixtures of Oppositely Charged Colloids Driven by an ac Electric Field. Phys Rev Lett *106*, 228303.
Vitelli, V., and Nelson, D.R. (2006). Nematic textures in spherical shells. Phys Rev E *74*, 021711.
Vogel, S.K., Petrasek, Z., Heinemann, F., and Schwille, P. (2013). Myosin motors fragment and compact membrane-bound actin filaments. eLife *2*, e00116.
Volkmer Ward, S.M., Weins, A., Pollak, M.R., and Weitz, D.A. (2008). Dynamic Viscoelasticity of Actin Cross-Linked with Wild-Type and Disease-Causing Mutant α-Actinin-4. Biophys J *95*, 4915–4923.
Vonna, L., Limozin, L., Roth, A., and Sackmann, E. (2005). Single-Filament Dynamics and Long-Range Ordering of Semiflexible Biopolymers under Flow and Confinement. Langmuir *21*, 9635–9643.
Vroege, G.J., and Lekkerkerker, H.N.W. (1992). Phase transitions in lyotropic colloidal and polymer liquid crystals. Rep Prog Phys *55*, 1241.
Wachsstock, D.H., Schwarz, W.H., and Pollard, T.D. (1993). Affinity of alpha-actinin for actin determines the structure and mechanical properties of actin filament gels. Biophys J *65*, 205–214.
Walczak, C.E., and Heald, R. (2008). Mechanisms of Mitotic Spindle Assembly and Function. In International Review of Cytology, K.W. Jeon, ed. (Academic Press), pp. 111–158.
Wang, F., Kovács, M., Hu, A., Limouze, J., Harvey, E.V., and Sellers, J.R. (2003). Kinetic Mechanism of Non-muscle Myosin IIB: Functional Adaptations for Tension Generation and Maintenance. J Biol Chem *278*, 27439–27448.
Wang, S., and Wolynes, P.G. (2012a). Active contractility in actomyosin networks. Proc Natl Acad Sci USA *109*, 6446–6451.
Wang, S., and Wolynes, P.G. (2012b). Tensegrity and motor-driven effective interactions in a model cytoskeleton. J Chem Phys *136*, 145102.
Weber, C., Schaller, V., Bausch, A., and Frey, E. (2012). Nucleation-induced transition to collective motion in active systems. Phys Rev E *86*, 030901.
Weeks, E., Crocker, J., Levitt, A., Schofield, A., and Weitz, D. (2000). Three-dimensional direct imaging of structural relaxation near the colloidal glass transition. Science

287, 627–631.
Weichsel, J., and Schwarz, U.S. (2010). Two competing orientation patterns explain experimentally observed anomalies in growing actin networks. Proc Natl Acad Sci USA *107*, 6304–6309.
Weichsel, J., Herold, N., Lehmann, M.J., Kräusslich, H.-G., and Schwarz, U.S. (2010). A quantitative measure for alterations in the actin cytoskeleton investigated with automated high-throughput microscopy. Cytometry *77A*, 52–63.
Weichsel, J., Urban, E., Small, J.V., and Schwarz, U.S. (2012). Reconstructing the orientation distribution of actin filaments in the lamellipodium of migrating keratocytes from electron microscopy tomography data. Cytometry *81A*, 496–507.
Weirich, C.S., Erzberger, J.P., and Barral, Y. (2008). The septin family of GTPases: architecture and dynamics. Nat Rev Mol Cell Biol *9*, 478–489.
Weisel, J.W. (2008). Enigmas of Blood Clot Elasticity. Science *320*, 456–457.
Wiesner, S. (2003). A biomimetic motility assay provides insight into the mechanism of actin-based motility. J Cell Biol *160*, 387–398.
Wong, G.C.L., Lin, A., Tang, J.X., Li, Y., Janmey, P.A., and Safinya, C.R. (2003). Lamellar phase of stacked two-dimensional rafts of actin filaments. Phys Rev Lett *91*, 018103.
Wyart, M., Liang, H., Kabla, A., and Mahadevan, L. (2008). Elasticity of floppy and stiff random networks. Phys Rev Lett *101*, 215501.
Xu, C., and Prince, J.L. (1998). Snakes, shapes, and gradient vector flow. IEEE Trans Image Process *7*, 359–369.
Xu, J., Schwarz, W., Kas, J., Stossel, T., Janmey, P., and Pollard, T. (1998). Mechanical properties of actin filament networks depend on preparation, polymerization conditions, and storage of actin monomers. Biophys J *74*, 2731–2740.
Yamakita, Y., Ono, S., Matsumura, F., and Yamashiro, S. (1996). Phosphorylation of Human Fascin Inhibits Its Actin Binding and Bundling Activities. J Biol Chem *271*, 12632–12638.
Yang, C., and Svitkina, T. (2011). Visualizing branched actin filaments in lamellipodia by electron tomography. Nat Cell Biol *13*, 1012–1013.
Yao, N.Y., Becker, D.J., Broedersz, C.P., Depken, M., MacKintosh, F.C., Pollak, M.R., and Weitz, D.A. (2011). Nonlinear viscoelasticity of actin transiently cross-linked with mutant α-actinin-4. J Mol Biol *411*, 1062–1071.
Yao, N., Broedersz, C., Depken, M., Becker, D., Pollak, M., MacKintosh, F., and Weitz, D. (2013). Stress-Enhanced Gelation: A Dynamic Nonlinearity of Elasticity. Phys Rev Lett *110*, 018103.
Yen, J.C., Chang, F.J., and Chang, S. (1995). A new criterion for automatic multilevel thresholding. IEEE Trans Image Process *4*, 370–378.
Yin, S., Zhang, X., Zhan, C., Wu, J., Xu, J., and Cheung, J. (2005). Measuring Single Cardiac Myocyte Contractile Force via Moving a Magnetic Bead. Biophys J *88*, 1489–1495.
Zemel, A., De, R., and Safran, S.A. (2011). Mechanical consequences of cellular force generation. Curr Opin Solid St M *15*, 169–176.
Zhang, H.P., Be'er, A., Florin, E.L., and Swinney, H.L. (2010). Collective motion and

density fluctuations in bacterial colonies. Proc Natl Acad Sci USA *107*, 13626–13630.

Zhang, J., Kong, C., Xie, H., McPherson, P.S., Grinstein, S., and Trimble, W.S. (1999). Phosphatidylinositol polyphosphate binding to the mammalian septin H5 is modulated by GTP. Curr Biol *9*, 1458–1467.

Zheng, L., Sekerková, G., Vranich, K., Tilney, L.G., Mugnaini, E., and Bartles, J.R. (2000). The deaf jerker mouse has a mutation in the gene encoding the espin actin-bundling proteins of hair cell stereocilia and lacks espins. Cell *102*, 377–385.

Zimmerberg, J., and Kozlov, M.M. (2005). How proteins produce cellular membrane curvature. Nat Rev Mol Cell Biol *7*, 9–19.

Zimmermann, K., Hagedorn, H., Heuck, C.C., Hinrichsen, M., and Ludwig, H. (1986). The ionic properties of the filamentous bacteriophages Pf1 and fd. J Biol Chem *261*, 1653–1655.

“Il semble que la perfection soit atteinte non quand il n’y a plus rien à ajouter, mais quand il n’y a plus rien à retrancher.”